VISUALIZING PARTICLE AND PORE ARRANGEMENTS IN DRY-PRESSED SPRAY-

DRIED ALUMINA (Al$_2$O$_3$) AS A FUNCTION OF PROCESSING PARAMETERS

by

IAN PATRICK MAHER

A dissertation submitted to the

School of Graduate Studies

Rutgers, The State University of New Jersey

In partial fulfillment of the requirements

For the degree of

Doctor of Philosophy

Graduate Program in Materials Science and Engineering

Written under the direction of

Dr. Richard A. Haber

And approved by

_____

_____

_____

_____

New Brunswick, New Jersey

October 2019

ABSTRACT OF THE DISSERATION

Visualizing Particle and Pore Arrangements in Dry-Pressed Spray-Dried Alumina (Al_2O_3) as a

Function of Processing Parameters

By IAN PATRICK MAHER

Dissertation Director:

Richard A. Haber

Variability in green bulk density in ceramic green bodies has been a continuing issue in the ceramic processing industry. Dry-pressing of ceramic powders is a widely used process due to its low cost, high production rates, and shape forming abilities. Spray-drying is the most widely used granulation technique for large production of dry-pressed ceramics. One mechanism that can cause variation in green bulk density is inadequate cohesion of the spray-dried granules during compaction. Organic binders are needed to create temporary adhesion and strength prior to the firing process. The mechanical properties of the binder and the morphology of the spray-dried granules govern the compaction behavior of the granules and the resultant green bulk density of the compacted body. Determining the roles and processing parameters that may lead to microstructural uniformity in processing dry-pressed green compacts will help narrow the problem of green bulk variation during processing. These parameters may include the type of organic binders, aqueous slurry characteristics prior to spray-drying, and pressing conditions. Visualizing this issue during the processing stage of green dry-pressed alumina is the focus of this dissertation and proves a need in the ceramic industry.

Alumina (Al_2O_3) is an important material in the technical ceramics industry due to its favorable thermal, mechanical, and electrically insulating properties. As previously stated, spray-drying is the most widely used granulation technique for large production of dry-pressing ceramics. This candidate system and granulation process were solely investigated for this dissertation. The effects that processing parameters have during the spray-drying process on the morphology of spray-dried granules promoted the understanding of how granule characteristics effect the compaction behavior of the granules and the rearrangement of the particles that comprise them. This provided an understanding of what granule characteristics promote or inhibit microstructural uniformity. The processing roles that were varied included the viscosity, the type and percentage of organic binder, and the specific gravity of the slurry. Alumina granules were compacted at various uniaxial pressures and characterized using a field emission scanning electron microscope (FESEM).

The solids loading of the alumina slurries affected the generated density of the spray-dried granules. The binder amount, binder type, and viscosity of the alumina slurries affected the droplet formation of the atomized slurry, and therefore, the generated morphology of the spray-dried granule. The acrylic emulsion binder resulted in spray-dried granules with a higher density and uniform internal structure when compared to the polyvinyl alcohol binder system whose internal structure consisted of an abundance of hollow coring, or microstructural voids, remaining after the spray-drying process. In comparison, the higher percentage of polyvinyl alcohol binder resulted in the lowest spray-dried granule densities and resulted in a higher degree of hollow coring occurring. This difference was noted in the resultant compacted microstructures of the compacted green

bodies as well, with a higher degree of microstructural uniformity formed from the green compacts processed with the acrylic emulsion binders. The generated voids within the polyvinyl alcohol binders were difficult to remove during compaction, leaving behind closed porosity and a higher degree of microstructural defects within the visualized compacted microstructure. Moisture content was added to these granules in hope to remove these defects. Since moisture is a plasticizer for polyvinyl alcohol, the moisture content softened the granule and resulted in the removal of these defects. A higher degree of microstructural uniformity was visualized as a function of compaction moisture. However, adding moisture content could affect the overall density distribution within the alumina compact, therefore, microstructural analysis in three dimensions was necessary. In terms of compaction behavior, the density of the granules affected the initial fill density but the morphology and binder type affected the overall knitting behavior and compaction rate of the generated granules.

A three-dimensional layering method was developed to stack two-dimensional FESEM micrographs in three-dimensions to visualize the microstructural characteristics of varying processing parameters. This method resulted in an accurate micron sized measurement to calculate the material removal based on the depths of micro-hardness indentations with a confocal laser scanning microscope throughout the varying removed layers. However, this method was time sensitive, generating small volumes in a matter of weeks. This method was compared to micro X-ray computed tomography (CT) data analyses. The FESEM method resulted in higher resolution three-dimensional microstructures of a finite volume whereas the micro X-ray CT analysis was sufficient to visualize the particle and pore arrangements throughout the full compact at a resolution

twelve times lower. This lower resolution resulted in depleting the overall microstructural information gained. Even though the micro X-ray CT data was sufficient to visualize the particle and pore arrangements as well as the density distribution throughout the whole green alumina compact, the three-dimensional FESEM microstructures gained the closed porosity and sub-micron information needed to be able to better characterize these green alumina compacts. Similar visualization results were obtained for the three-dimensional microstructures in comparison to the two-dimensional microstructural characterization analysis. The higher degree of polyvinyl alcohol binder resulted in a higher degree of microstructural defects and density distributions throughout the compact. The highest degree of uniformity was visualized from the compacts processed with the acrylic emulsion binder and the added moisture content to the polyvinyl alcohol polyvinyl alcohol spray-dried granules.

Image processing techniques were implemented on both data analyses to threshold the micrographs into a binary image that distinguished the micrographs into material and porosity based on pixel intensity on a greyscale. The porosity segmented analysis for the three-dimensional FESEM method returned similar results to the geometric porosity calculated from the geometric density measurements. Due to the lower resolution capabilities, the segmented porosity calculations obtained from the micro X-ray CT data were an underestimation in comparison to the geometric porosity measurements. Mercury porosimetry proved difficult to conduct as the green alumina compacts would break during mercury intrusion. This technique was insufficient in characterizing the porosity of soft, green alumina compacts even at slow intrusion rates. That is why the image processing and characterization techniques used for this dissertation are valuable in characterizing green

ceramic microstructures. The sub-micron and density distribution information gained throughout both visualization techniques can be used as a tool to understand what processing parameters as a function of what ceramic forming method will promote microstructural uniformity in the unfired state and more reliable ceramic parts.

The work completed in this dissertation involved analyzing the compaction behavior of granulated alumina as a function of processing parameters and visualizing the microstructural variations that comprised the final green microstructure. This dissertation developed and determined methods to understand particle and pore arrangements in dry pressed alumina green compacts. To understand this phenomenon, visualizing the internal structure of the green compacts in both two and three dimensions promoted the understanding of distinguishing what process parameters produce fewer green bulk microstructural variations. The improved microstructural characterization techniques accomplished in this work provided an improved method of characterizing green microstructures to help guide improved outcomes in ceramic processing.

ACKNOWLEDGEMENTS

Getting a Ph.D. in engineering is not for the light hearted. There are times the research goes well and there are times you feel like pulling out your hair and asking yourself "Why did I do this to myself?" However, at the end of the day, the reward of completing your own individual research and achieving the title "Doctor of Philosophy" is worth the rollercoaster ride that is categorized by graduate school.

My first acknowledgement must go to Dr. Haber, my advisor. None of this would be possible without his confidence in taking a stubborn college graduate that did not want anything to do with graduate school and eventually convincing me to accept an offer to become a student within his research group. I vividly remember the initial conversation we had in his office when he offered me a position within his group before I graduated undergraduate. I was shocked and couldn't believe I was being offered a fully funded graduate education. I remember thinking "Doesn't he know that I am not good enough to accomplish this?" I was speechless but stubbornly declined the offer. A few more months went by after working as a laboratory manager within the group, still at Rutgers, and eventually he wore me down and convinced me that graduate school was a great opportunity. Most importantly however, he convinced me that I was smart enough to accomplish the degree, something I never thought possible in myself. Three and a half years later and here we are. I can't thank him enough for his guidance, wisdom, and motivation along this rollercoaster ride.

To my outside committee member, Dr. Michael Normandia, thank you for all of your support and advice along the way. The numerous meetings we had on research as well as just advice on life meant a great deal to me. I would also like to thank him as well as Dr.

I would like to thank Laura for her unending support throughout my years at Rutgers. Distinctly the time we shared an office when I was a laboratory manager. She helped convince me to take on this next chapter of graduate school and would tell me over and over, "things happen for a reason". I especially have to thank Michelle for putting up with my perpetual stubbornness over the years. I can't thank her enough for all of the conversations and advice she has offered me. She is the research group mom, her care and

kindness for all of us is foremost to all of the other work she does for the group. Without her, nothing would get done. Thank you for everything.

To the Haber group; Sukanya, Vlad, Atta, Chawon, Berra, Tyler, Kanak, Vince, Joe, Anthony, Metin, Zeynep, Michael, Bruce, Azmi, Mark, Mustafa, Sweta, and Kent, thank you all for making this rollercoaster ride enjoyable. Especially to my officemates Vince, Joe, Mark, Sweta, and Mustafa. Fiber Optics 107 has felt like a home and I can't thank them enough for that.

There is one graduate student that deserves his own acknowledgement and that is Mustafa. Mustafa has been my brother throughout graduate school. His friendship and unending support has been overwhelming to say the least. I cannot wait to see where life takes him next, he is going to do amazing things and I wish him the best.

To my undergraduate research assistants over the years; James, Meera, Ojaswi, Salman, Ashley, Sweta, Frank, Joyce, Vats, Zahra, and Denise, thank you all. I want to thank them their help in accomplishing my research tasks, especially with cleaning the spray-dryer numerous times with a great attitude when we all knew it is not an enjoyable task.

The love and support I received from my friends throughout my studies has been incredible, especially Steve and Patrick. Thank you both for being there for me. I have to thank everyone in my family. First, I have to thank my parents, Peter and Jean, for their everlasting love and support throughout my life. I can't thank them both enough for everything they have sacrificed for myself as well as my siblings. To my two sisters, Jaci and Kelsey, and my brother-in-law Nick, thank you for your love and support over these past few years, I love you all. Thank you to my new extended family, my father and mother-

in-law Scott and Donna, my new siblings Tyler, Abigail, and Michael. I can't thank you enough for your love and support.

I couldn't conclude my acknowledgements without thanking the most important person in my life, and that is my wife Kiersten. She is my light and without her love and support over the years I would not have been able to accomplish this degree. She is the only person I would have wanted to share this crazy rollercoaster ride with over the past few years. I cannot wait to see what life has in store for us next. I love you with all my heart.

TABLE OF CONTENTS

xii

LIST OF TABLES

LIST OF FIGURES

NOMENCLATURE AND DEFINITIONS

The following vocabulary will be used as nomenclature for this thesis proposal [1-4].

- *Agglomerate* – several particles held together by weak cohesive forces.

- *Agglomeration* – formation of aggregates via physical (van der Waals, hydrophobic) or electrostatic forces; the resulting structure is called an agglomerate.

- *Angle of Repose* – the angle to the horizontal assumed by the surface of a poured heap of powder at rest.

- *Binder* – provides considerable green strength for handability after formation and prior to sintering the ceramic body.

- *Deflocculant/Dispersant* – a substance which when present in small amounts facilitates the dispersion of aggregates to form a stable suspension.

- *Dry Pressing* – the simultaneous uniaxial compaction and shaping of a granular powder with small amounts of water and/or organic binders during confined compressions in a die.

- *Fine Particle* – State of subdivision implying that the particles have average dimensions lying roughly between 1 µm and 100 µm.

- *Flocculation* – Formation of aggregates in a suspension mediated by polymeric species, either attached to the particles or free in the suspending medium; the resulting structure is called a floc, while the polymer additive is termed a flocculant; polymer bridging is a flocculation process.

- *Flowability* – the ease with which a powder flows; usually expressed as an index.

- *Granule* - state of subdivision generally referring to dry particulates with dimensions lying in the 50 µm to 200 µm range; for instance, produced by spray-drying for ease of handling during subsequent consolidation processes.

- *Granulation* – intentional agglomeration of primary particles to form a spherical cluster of particles referred to as granules.

- *Green Density* – the apparent density of a green compact.

- *Intergranular Pores* – pores in between granule remnants that persist after compaction.

- *Interparticle Pores* – pores in between particles within an agglomerate.

- *Particle* – a discrete element of material regardless of its size.

- *Plasticizer* – liquid that can be added to the binder composition to prevent brittleness in the dry body.

- *Powder* – dry collection of particulates with a macroscopic consistency.

- *Primary Particle* – smallest identifiable subdivision in a particulate system; primary particles may also be sub units of aggregates.

- *Sieving* – the operation of determining the size distribution of particles in a powder by using a series of sieves (woven wire with regularly spaced aperture of uniform size). Sieve and screen can be used interchangeably. Wet sieving is sieving particles with the aid of a liquid.

- *Slurry/Suspension* – a liquid in which solid particles are dispersed.

- *Tap Density* – the mass per unit volume of a powder that has been placed in a specified container and has been settled under specified conditions by mechanical action.

- *Well-Dispersed* – a state that describes a stable suspension in which the minimum particle size has been achieved; operationally defined by the observance of a constant (minimum) particle size distribution during the dispersion process.

- *Wet Milling* – the grinding of materials with sufficient liquid solvent to form a slurry.

1. INTRODUCTION

Microstructural variability in ceramic green bodies has been a known issue within the ceramic processing world. Dry-pressing of ceramic powders is a widely used process due to its low cost, high production rates, and shape forming abilities. Fine ceramic particles typically achieve high-density parts at lower temperatures and times due to enhanced sintering kinetics. However, fine particles do not flow due to the interparticle attractive forces, which are greater than the force of gravity. This reason is what hinders die filling uniformity and the green (non-sintered) bulk consistency of the compacted ceramic.

To improve the flowability of fine ceramic particles, a granulation technique is desirable. In dry-pressing, agglomerated powders are created in the form of flowable granules. Spray-drying is the most widely used granulation technique for large production of dry-pressed ceramics. A key requirement during the compaction process is a uniform density distribution of primary ceramic granules, without which causes variations in green bulk density. A desired uniform green microstructure shows no remnants of the agglomerated granules and a uniform density distribution. If granule remnants remain, intergranular pores will persist within the microstructure after densification, thus depleting the reliability of the ceramic's properties. Large pores that persist throughout the sintered microstructure can become stress concentrators and cause failures during production. A major challenge in dry-pressing ceramics is processing a flaw free green microstructure that will return a highly reliable sintered ceramic. Different factors in the processing of compacted green bodies lead to microstructural variations that are difficult to account for. These factors may include the aqueous slurry processing parameters prior to spray-drying,

the type of organic binder, and the granule characteristics and properties during the compaction process.

To form reliable dry-pressed ceramics, characterization and evaluation of the ceramic green microstructure is necessary. The issue that arises is an absence of sufficient analytical techniques needed to characterize the microstructure of the green ceramic compacts. Uematsu *et al.* [5] and Saito *et al.* [6, 7] have been successful in developing methods using optical microscopy and confocal laser scanning microscopy (CLSM) respectively to analyze the internal structures of granules and compacted green bodies. A limitation for these techniques is the inability to characterize specimens greater than 0.5 mm [5-29]. Hondo *et al.* [30-32] has developed a method to use micro-X-ray computed tomography (micro-CT) to visualize density gradients and large pore evaluation within compacted bodies. Unfortunately, this method showed it is unable to characterize microstructural variations less than one micron. It has been stated that it is impossible to prepare samples with a scanning electron microscope (SEM) to achieve high-resolution microstructure analysis of the compacted green ceramics [7, 13, 27]. Visualization of spray-dried granules and compacted green bodies obtained by a high resolution SEM will be beneficial in understanding what process parameters influence microstructural uniformity during the compaction process. Having the capabilities to visualize green microstructural variations in three-dimensions will aid in improving the processing of ceramics. This can only benefit research areas such as modeling of binder removal through porous mediums by understanding pore channel networks and residual defect formations as a function of processing parameters. Coupling the improved visualization techniques of

these phenomena with experimental results will improve processing and formation of materials.

This dissertation will describe a novel characterization method to visualize green alumina ceramics with the use of a field emission scanning election microscope with 2-D and 3-D visualization methods. Aqueous alumina slurries will be prepared by ball milling, evaluating the effect of slurry characteristics prior to spray-drying on the morphology and characteristics of the generated spray-dried granules. The resulting uniaxial dry-pressed alumina compact's microstructure will be evaluated in both 2-D and 3-D to attempt to compare varying process parameters on the generated dry-pressed green alumina compact's microstructure.

2. BACKGROUND

2.A. Defects in Compacted Ceramic Microstructures

The quality and state of the green microstructure strongly influences the microstructure in the final sintered body. The most common defect in compacted bodies is large intergranular porosity. Poor die filling and inconsistencies in granule packing lead to a non-uniform density distribution. After the forming process, if any large intergranular pores exist, they will not be removed during the sintering process. These large pores are detrimental to the reliability of the sintered ceramic and are considered flaws. They also act as local stress concentrators and reduce the strength of the body. The concentration of the applied stress propagates and causes fracture. The size and shape of these flaws dictate how the stress concentration behaves and propagates throughout the body. After the forming process, if a non-uniform density distribution is obtained, it will create regions of low and high densities, which will result in differential sintering, causing higher dense regions sintering away from lower dense regions. Differential shrinkage may occur as well and internal stresses will form causing flaws and microstructural defects. To control the reliability of the ceramic and to avoid stresses during the densification process, a uniform density distribution and green microstructure is desired [9].

Initially, to achieve a uniform microstructure, sufficient die filling must occur prior to the compaction process. The flowability of powder can be controlled by intentionally granulating the fine primary particles to ensure that sufficient die filling occurs. Granulating is commonly done with fine powders that are to be die pressed. The flowability of granules is controlled by the granule size distribution, density of powder, and morphology of granules. These techniques are used to understand how granule morphology

affects the die filling process [33]. Testing the flowability of granulated ceramic powders can be accomplished by measuring the flow rate or the angle of repose. The angle of repose must be less than or equal to 40º to ensure desired flowability [2]. Reed has suggested granules larger than 40 µm flow well for dry-pressing [34].

Granulating improves die filling, however, the challenge is to remove granule remnants during the compaction process, otherwise, large flaws may persist. Removing these remnants is essential in obtaining a uniform distribution of small pores throughout the compacted body. Densification occurs when two particles approach each other's centers. Thermodynamics controls this process and is why the use of fine powders is preferred. Fine powders enhance sintering kinetics due to greater particle – particle contacts, which, improves the diffusion process [35]. A pore coordination number is the number of particles that surround individual pores [36]. For every material, a critical pore number exists that depends on the materials dihedral angle, which for oxides is typically 150 degrees [36]. For pores to shrink, the pore coordination number must be less than the critical pore coordination value. Therefore, pores between particles within the granules will disappear during sintering but large intergranular pores and pores that remain within agglomerated granules cannot be removed during the compaction process, and therefore, will persist throughout sintering. A schematic illustrating this behavior is shown below in Figure 1.
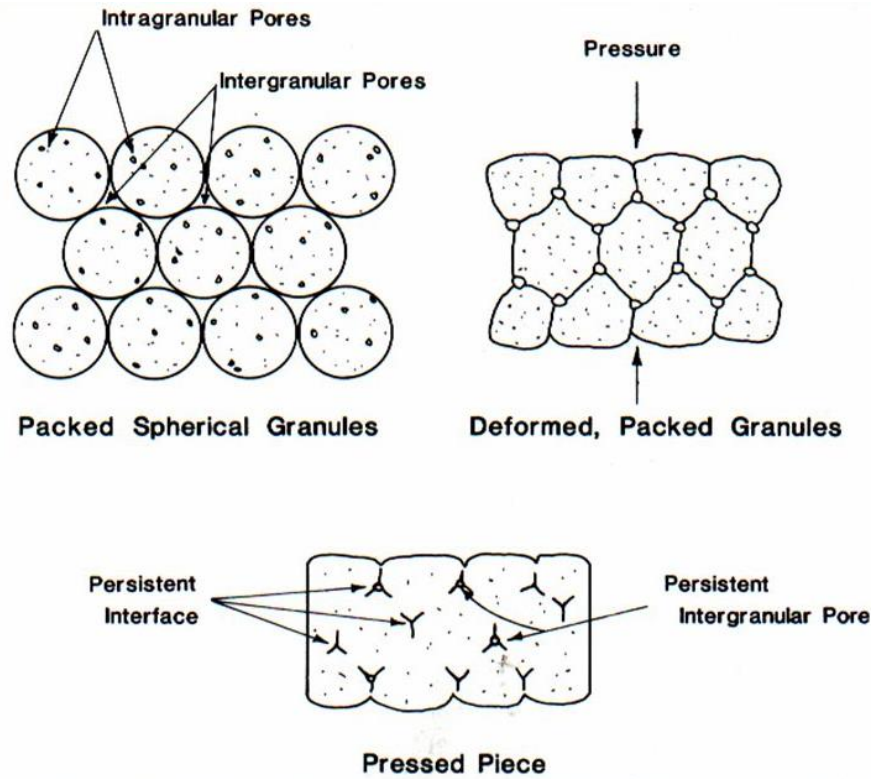
Figure 1. A schematic of what occurs when granule remnants persist throughout the microstructure during compaction, causing intergranular porosity to remain [34].

2.B. Spray-Drying Process

Spray-drying is the most commonly used granulation technique for dry-pressing ceramics and will be the sole technique investigated for this dissertation. This technique is the process by which a fluid feed material (typically termed "slurry") containing primary ceramic powder, water, organic binders, and dispersant are transformed into dry granules by atomizing the feed slurry into droplets within a hot drying medium [37]. This technique produces free-flowing granulated powder that is desired for dry-pressing.

2.B.1. Effects of Slurry Parameters

Ceramic slurry characteristics have major effects on the characteristics of spray-dried granules. Any variations during processing of the slurry can cause variations within the internal structure of generated granules. The ceramic solid content dictates the amount of granulated powder generated. A drawback to a high solids loading slurry would be an increased viscosity. This increase is disliked due to the dilatant behavior of the slurry during atomization which would cause the slurry to be impossible to atomize. An increase in the viscosity of the slurry will result in coarser droplets being formed and generating granules of a greater density. Factors that contribute to an increased viscosity include specific gravity of the slurry, dispersant amount, binder type, binder amount, and the temperature of the slurry.

To obtain a low viscosity and high solids loading slurry, the use of a dispersant is needed for the system to become deflocculated by countering the attractive van der Waals forces among the particles with repulsive electrical forces. Dispersants are also used to prevent agglomeration of the powder within the slurry during the milling process. Any

agglomeration that occurs at this stage can cause defects in the formed granules that may persist into the final ceramic body [4]. To guarantee the spray-dried granule characteristics remain constant, the behavior and characteristics of the slurry are crucial [10, 24].

The formation of uniform, spherical shaped granules are ideal for dry-pressing to produce a uniform green ceramic compact. The slurry characteristics can promote or diminish uniform formation of spray-dried granules due to the rheology of entering ceramic slurry. These characteristics may include the dispersed state, surface tension, and the viscosity of the aqueous ceramic slurry. These characteristics may affect the formation of droplets entering the drying chamber. Lukasiewicz [38] reported that the average droplet size atomized into the drying chamber is proportional to the slurry's viscosity and surface tension and inversely proportional to the mass ratio of the atomized air to the feed material. Coalescence of drying droplets can produce spray-dried granules with irregular shapes or clusters of smaller granules [34].

It has been proposed that a relationship between apparent surface tension and granule shape exists [39]. The levels of organics added to the ceramic slurry can have a direct effect on the surface tension and therefore the viscosity of the slurry. These parameters coupled together control the size and shape of the generated spray-dried granules [2, 3].

To parallel this observed behavior, Takahashi *et al.* [40] investigated the effects of dispersant levels within SiN_4 slurries and how this relates to the compaction behavior of spray-dried granules. Well-dispersed slurries formed hard and dense granules that retained their shape throughout the compaction process. Flocculated slurries formed soft and lower dense granules that were easier to deform. Shinohara *et al.* [13] discovered that well-

dispersed slurries resulted in irregular shaped granules that formed dimples on the outside surface, which were hard and not easily deformable. Bertrand *et al.* [41, 42] investigated well-dispersed and flocculated slurries of both alumina and zirconia and found similar results.

These results agree with the results mentioned by Walker and Reed [39], that the mobility of the solid particles during the drying process and the mobility of the particles within the ceramic suspension are correlated. A diagram showing this behavior is shown below in Figure 2. Zainuddin *et al.* [24] investigated the internal structure of spray-dried granules from flocculated and well-dispersed slurries with the use of cross polarized light. This research found that the flocculated granules consisted of loosely packed, randomly oriented particles where as well-dispersed granules consisted of densely packed particles that were oriented along the granule surface.
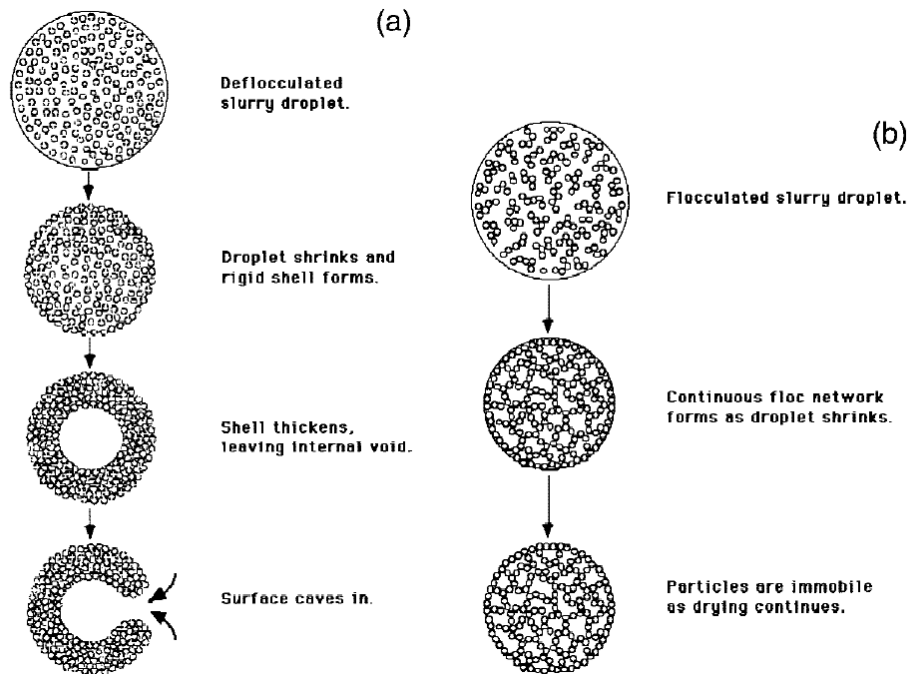
Figure 2. Model of granule formation for (a) well-dispersed and (b) flocculated slurry [39].

2.B.2. Binders and Plasticizers

Organic binders are used to impart the plasticity required to form green compacts with a high green strength and handability during production. Organic binders are polymer chains that bind the particles together within an agglomerated spray-dried granule. The strength of the binder dictates the adhesion properties during granule compaction to obtain a uniform microstructure. The binder must be soft to allow the granule to deform and knit to the other granules, however, a drawback to a soft binder is the creation of low green strength compacts that cannot be handled [10, 24]. The strength of the binder is governed by its temperature. The binder's mechanical properties at low temperatures are elastic and as temperatures increase, the polymer goes through a glass transition (T_g) to a viscoelastic region. Temperatures below $0.75T_g$ will cause binders to become brittle, therefore compaction must take place above the glass transition temperatures [43].

2.B.2.a. Polyvinyl Alcohol

Polyvinyl alcohol (PVA) is an organic binder typically used for its high green strength and handability during compaction [44]. The glass transition temperature of PVA is typically in the range of 75˚C to 85˚C, therefore the organic binder must be plasticized to be practical for compaction purposes. Plasticizing the organic binder is a technique used to lower the T_g of the binder so compaction can occur at most temperatures. Typical plasticizers include glycerin, low molecular weight polyethylene glycol (PEG), and water [4]. Moisture can be used as a plasticizer with spray-dried granules that have been prepared with PVA. Higher levels of moisture will be adsorbed by the PVA binder, lowering the T_g of the binder and the granule yield point during compaction [45]. However, this can become a problem for manufacturing plants due to the sensitivity of water, controlling the

humidity during the process, as well as a "caking" behavior causing the granules to adhere or stick to the compaction dies. Therefore, it becomes impractical during production to incorporate moisture during the compaction process. Also, incorporating PVA organic binders within the aqueous slurry to be spray-dried can increase the viscosity thus having to decrease the solids loading of the prepared slurry. Otherwise, if the increased viscosity of the slurry is not countered by reducing the solids loading, the system would not be able to spray-dried due to its high viscosity and dilatant behavior [44].

Another concern with PVA is the organic binder being water soluble causing binder migration during the spray-drying process. When used during processing of aqueous slurries, PVA ionizes and is adsorbed weakly on the particles due to hydrogen bonding and creates free PVA chains within the suspension. This free PVA can migrate during the evaporation stage of spray-drying process and create a segregated binder layer that hinders densification during compaction due to the binder layer supporting stress [19].

Zhang *et al.* [46] attempted to mitigate the segregation of PVA binder to the surface of the granule by adsorbing PVA onto the surface of the ceramic powder. Adsorption was a slow process and decreased as temperatures increased. However, the PVA binder was not fully desorbed at higher temperatures therefore PVA segregation can be limited prior to spray-drying.

2.B.2.b. Polyethylene Glycol

As previously stated, plasticizing the organic binder is a technique used to lower the T_g of the binder so compaction can occur at most temperatures. Plasticizers are termed as liquid oligomers, structurally similar to the binder, therefore, able to infiltrate in between the binder molecules to lubricant them. This added plasticizer causes the binder's polymer

chains to slide past each other. This allows the system to withstand strain without actually cracking by controlling the strength of the binder during compaction. Plasticizers, in turn, prevent brittleness of the binder in a dried compact, thus, obtaining a stronger green state.

A typical plasticizer used with PVA is a low molecular weight polyethylene glycol (PEG) and will be the plasticizer used for this dissertation [4]. The T_g depends on the molecular weight of the polymer, ranging from -95˚C to -15˚C for low to high molecular weight polymers respectively [3]. Walker *et al.* have found that green strength increased with the use of an amorphous PEG binder when compared to a PVA binder [47]. Walker et al. examined the fracture surface of the compacts and found that the compacts made with PEG showed no granule remnants in the microstructure whereas the PVA compacts showed granule remnants persisting throughout the microstructure. These remaining remnants weaken the body, causing the fracture path to go around the granules and the intergranular boundaries rather than through the granules [47]. Contradicting Walker's results, Wu *et al.* [44] showed that an amorphous PEG binder resulted in green bodies that were weaker than green bodies containing the same amount of PVA and acrylic emulsion binders.

PEG is also water soluble, similar to PVA, however it does not increase the viscosity of the processed aqueous slurry as PVA does. Other concerns that arise with the use of PEG is causing a foaming slurry during processing and volatilizing the organic binder if operating temperatures are too high during the spray-drying process [3].

2.B.2.c. Polyacrylic Emulsion Binders

Polyacrylic acid (PAA) is used for its high green strength and good pressibility without plasticization [44]. Acrylic emulsion binders consist of a dispersion of polymer

particles in a range of 0.05 to 0.5 µm in water [3]. Due to the organic binder being an emulsion, it has a lower viscosity than an aqueous solution of PVA. Therefore, one can achieve a higher solids loading aqueous slurry at a lower viscosity prepared with a PAA binder than an aqueous slurry prepared with a PVA binder. Acrylic polymers must be hydrophilic to remain dispersed in water, therefore acrylic emulsion binders are insensitive to changes in humidity where as PVA binders are very sensitive to humidity and moisture changes, plasticizing the organic binder and lowering its T_g. Different proportions of acrylic polymers can modify the T_g of the acrylic binder. Acrylic binders with a high T_g have shown to have faster granular flow and higher green strength. Lower T_g binders have been found to result in higher green density and granule deformation at lower pressures with reduced springback [3].

A concern that arises with the use of PAA is the coagulation of the binder through aggressive stirring or ball milling [3]. This occurs due to reducing the emulsion particle size during aggressive milling or stirring, where to a point, there is not enough surfactant to cover the surface area of the emulsion particles therefore coagulating the system. To inhibit shearing the emulsion, careful measures must be taken such as gentle mixing or addition of the acrylic emulsion binder into the system. PAA creates repulsive forces when ionized and disperses the particles in a stabilized suspension. When ionized, the PAA ions adsorb onto the particles prohibiting movement within the suspension during the evaporation stage of spray-drying. This allows PAA to distribute uniformly within the internal structure of the spray-dried granule due to inhibiting binder migration during the spray-drying process [3].

Tanaka *et al.* [19, 21] discovered that granules formed with PAA binder result in a lower yield stress during compaction that densifies quicker compared to granules processed with PVA. PAA resulted in a more uniform microstructure with increased sintered strength compacted to compacts made from PVA. Zainuddin *et al.* [22] discovered that it is possible for PAA to form segregated binder layers when an amount of free PAA ions do not absorb fully on the particles at a maximum binder content value. As binders are needed for handability during manufacturing, visualizing pore channels three-dimensionally will improve predictive modeling for binder removal to determine the optimal heating profile for each system preventing structural failure and internal pressure induced crack propagation.

2.B.3. Effects of Operating Parameters

Operating parameters during the spray-drying process include the atomization pressure, slurry feed rate entering the nozzle, the inlet and outlet temperatures. During the atomization stage, with the increase in atomization air pressure within the nozzle and a constant slurry feed rate, the droplet size will decrease forming finer granules. Increasing the slurry feed rate with all other parameters kept constant will generate larger granules. The operating inlet temperature will affect the rate of evaporation of the entering droplets at a constant airflow rate. An increased evaporation rate may result in granules of lower density due to the formation of higher porosity structures. The outlet temperature will affect the moisture content of the generated granules leaving the drying chamber [37].

Lukasiewicz [38] summarized the production of spray-drying and determined the slurry characteristics govern the granule morphology and bulk density achieved. Operating

parameters govern the droplet size and evaporation rate during drying. Hotta *et al.* [12] investigated the effect that the size of a spray-dryer may have on the internal structure and morphology of the granules. The smaller laboratory spray-dryer produced a smaller average granule size with smaller internal defects. Due to these results associating the operating parameters of the spray-drying process to the initial droplet size and thus the overall granule size obtained, this dissertation will focus primarily on the slurry characteristics and what roles govern granule morphology of the generated spay-dried granules.

2.B.4. Atomization and Droplet Drying

During the spray-drying process, three major stages occur [48]. Ceramic slurry atomization into fine droplets is considered stage one. Stage two occurs when these atomized droplets become exposed to a drying medium of hot air inside the drying chamber. Rapid water evaporation occurs during this stage due to the large ratio of surface area to the volume of droplets [38]. The final stage occurs when dried granules are separated from the drying chamber and are collected.

There are three different atomization techniques used for spray-drying which include rotary, pressure, and two-fluid (pneumatic) atomization [38]. For this dissertation, a two fluid atomization technique will be the focus and sole technique investigated. During two fluid atomization, the ceramic slurry is fed through an orifice at a low pressure and is atomized by the use of a high velocity stream of compressed air at a specific pressure [48].

The atomization pattern of the droplets entering the spray-dryer has an effect on the droplet drying time, degree of moisture removal, and the formation of powder on the

chamber walls. There are three groups of airflow patterns after atomization: co-current, counter-current, and mixed flow. Mixed flow, or a combination of counter and co-current airflow patterns, will be the primary pattern investigated during this dissertation. This airflow pattern exists when the atomization nozzle is located at the base of the spray-dryer and the hot air enters at the top of the chamber. The nozzle creates a fountain type atomization, spraying the droplets towards the top of the chamber near the entrance of the hot air [3]. Schematics of the different atomization patterns are shown below in Figure 3 shared by Lukasiewicz [38].

Walker and Reed [39] investigated the difference between mixed flow and co-current atomization effects on the morphology of the spray-dried granules internal structure and found that the difference in spray-drying atomization did not affect the degree of hollow coring or morphology within the granules.
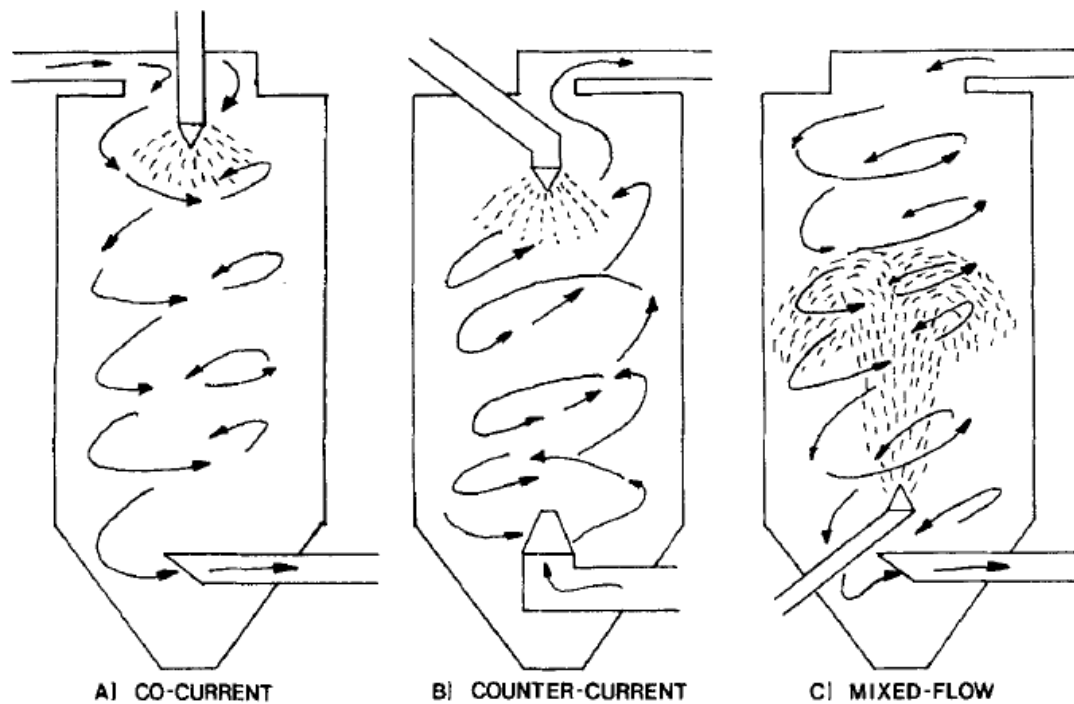
Figure 3. Droplet atomization patterns used in spray dryers [38].

Surface tension of the aqueous ceramic slurry forms spherical droplets entering the drying chamber due to spheres having the lowest surface area per unit volume. The surface tension depends on the amount of deflocculant and binder type within the slurry. The lower the surface tension, the smaller size of droplets form. In contrast, the higher the surface tension of the slurry, the more difficult it becomes to atomize the slurry [2, 3].

After the slurry is atomized into the drying chamber, droplets form and the stages of droplet drying begin. First, the droplets enter the drying chamber and the maximum evaporation rate, or constant rate drying period, begins. The heat is transported to the liquid from the atmosphere and the evaporated liquid is then transported into the surrounding atmosphere until moisture migrates from the interior of the droplet rapidly enough to maintain surface saturation. The drying rate of the droplets depends on the temperature of the liquid within the droplet as well as the temperature, humidity, and flow rate of the drying air within the drying chamber.

Ultimately, a critical moisture content is achieved where the droplet surface can no longer be kept saturated by moisture migration and thus the falling rate period begins. Eventually the entire surface becomes unsaturated and the drying plane for evaporation changes from the exterior to the interior of the droplet. A decreasing drying rate now takes precedence. This phenomenon causes solids to escape the solution at the surface of the droplet and a crust forms around the droplet. The drying rate effects the thickness of the formed crust. The droplet is now in a constant drying period where shrinkage occurs. Further drying and evaporation of the liquid depends solely on the permeability of the surface's crust [2, 38, 49]. A high initial drying rate will lead to the formation of larger

granules that consist of thin shells and a low density. A low initial drying rate will lead to the formation of smaller granules of a higher density that consist of thick shells [2].

2.B.5. Internal Defects within Spray-Dried Granules

Binder migration is a common defect that occurs during granule formation due to the use of water-soluble organic binders. As the water evaporates within the droplet, the binder migrates to the surface of the granule and forms a layer. This creates a non-uniform binder distribution within the structure of the granule that affects the compaction behavior of the agglomerate due to the formation of a tough surface layer. During compaction, this increase in granule strength will promote the formation of large intergranular pores and remnant granule structures within the microstructure [38, 50].

Another common issue developed during the formation of spray-dried granules is hollow coring within the agglomerated powder. There are many proposed reasons as to why this phenomenon occurs [37, 38]. One reason is attributed to air entrapment within the slurry. Air entrapment creates a low specific gravity slurry and thus, low-density granules. A de-airing step usually takes place prior to spray-drying to account for this issue [34]. Another proposed reason is the migration of particles during the drying stage. Particles may become carried to the surface of the droplet, along with the liquid and organic binders, due to capillary responses occurring during evaporation. If a surface layer of binder forms around the droplet and creates a low permeable barrier for evaporation to take place, moisture becomes entrapped within the droplet due to the impedance of evaporation. Therefore, as the droplet is drying within the chamber, the moisture boils inside the droplet

and causes a ballooning effect within the granule resulting in the formation of an empty void.

It has been difficult to visualize these issues as they occur. Uematsu *et al.* [5, 10] has visualized binder migration after spray-drying with the use of an optical microscope and immersion liquid. Zhang *et al.* [11] determined with the use of a computer modeling simulation that the initial binder concentration and size of atomized droplets govern the formation of segregated binder layers on the surface of the spray-dried granule. Walker and Reed [39] determined the mobility of particle rearrangement is governed by the droplet size and the difference in particle motion between well-dispersed and flocculated suspensions.

Liang *et al.* [51] further explored this phenomenon by modeling the droplet formation during spray-drying and relating slurry parameters to the formation of crust layers. Liang determined that the droplet size is dependent on the solid volume fraction within the slurry. Tsubaki *et al.* [52] evaluated the migration of particles and binder to the surface of granules based on the dispersed state of the suspension. Tsubaki found agreement with Walker and Reed [39] and determined that the mobility of particles within the flocculated structure determines the mobility of the particles during the drying period. It is not known what drives the formation of hollow cores within granules other than a combination of temperature, binder migration, and low-permeable barriers forming during the evaporation stage of the droplets.

2.C. Dry-Pressing

2.C.1. Granule Flow and Die-Filling

The first critical step in dry-pressing ceramics is obtaining a uniform die fill to avoid green bulk density variations in the final pressed ceramic. A reproducible and uniform die filling process is desired to produce consistent ceramic part densities, shapes, sizes, and microstructures. As previously stated, a granulation technique is implemented to produce free flowing agglomerated ceramic powder with good flowability.

A uniform granule density and size distribution is desired for dry-pressing. Irregular shaped granules may cause a bridging behavior during die filling that impeded granular flow within the die [34]. Size segregation occurring during the die filling process or delivery of the die to the press will result in part to part variation in fill density which will correlate to green bulk density variations in the pressed ceramic. Fine ceramic powders or granules could fall in between the die wall and punch which reduces the ability for air to escape during pressing, resulting in microstructural defects. A bimodal granule size distribution that incorporates many fines and coarse granules may show size segregation, however using a broad size distribution will not show this issue. For this dissertation, granule size distribution of 45 – 150 microns will be used to overcome this issue [2, 3].

2.C.2. Compaction Behavior

Research involving compaction behavior of ceramic powder and agglomerates dates back to the 1950's. Lukasiewicz and Reed [53] investigated the compaction response of agglomerated ceramics into the three stages of compaction. A typical compaction curve showing the three stages of compaction is shown below in Figure 4 [54, 55]. This curve

displays the relative density of the compact plotted against the logarithm of the compaction pressure. Compaction curves are used as a tool to understand the pressure necessary to achieve a respective green density. The three stages of compaction include granule flow and rearrangement (Stage I), granule deformation predominating (Stage II), and granule densification predominating (Stage III) [34].
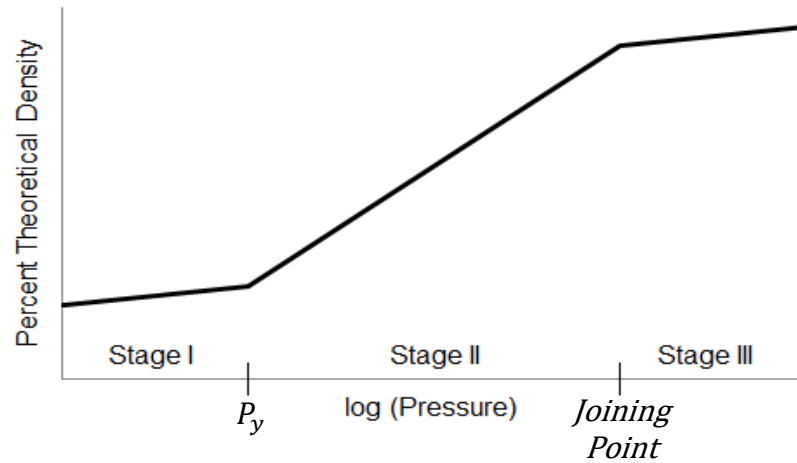
Figure 4. Compaction curve schematic showing the three stages of compaction [54, 55].

During Stage I, the granules achieve a maximum packing configuration that is dependent on the flowability of the spray-dried granules. The compaction process achieves its initial density purely by the die filling process. A vibrating stage can be administered to ensure complete granule rearrangement and increase the die-filled density to the corresponding tap density of the granules. During stage I, granules slide past each other and the slope of the curve is represented by the following equation [2, 3];

$$\frac{\rho_2 - \rho_1}{\log P_2 - \log P_1} \qquad\qquad 1$$

where ρ is density and P is pressure. As pressure is increased, the granules can no longer rearrange and deformation predominates. Granules reach a critical yield pressure (P_y) at

the transition from stage I to stage II. Density increases rapidly at this stage due to the fracture of granules. Large interstitial pores between granules begin to be removed. The dominant mechanism in stage II is the fracture of weak bonds within the agglomerates or sub-agglomerates [56]. The densification during this stage is represented by the following equation [34];

$$D_c = D_f + m \ln \left(\frac{P_a}{P_y} \right) \qquad\qquad 2$$

where D_c is the compact density at an applied pressure P_a, D_f is the initial fill density of the granules, P_y is the yield strength of the granules, and m is a compaction constant that depends on the deformability and packing of the granules [34]. The rate at which compaction occurs can dictate changes in the slope during stage I. Increasing the compaction rate will lower the slope by not allowing sufficient time for granules to rearrange and fill voids. This may cause density gradients within the compact, further lowering the slope during stage II [3].

The transition from stage II into stage III is termed the joining point and this is where densification begins to dominate the compaction process. Only a small change in density is achieved with increasing pressure. The separation of aggregates within sub-agglomerates, or the fracture of the strong bonds in the residual sub-agglomerates, is the dominant mechanism in stage III [56]. Lukasiewicz and Reed [53] state that in order to achieve well knitted granules, compacts must be processed at pressures roughly 1,000 psi above the joining point.

Messing *et al.* [57] automated a method to obtain compaction curves by use of a computer interface in the 1980's. This was obtained by the proposed method of tracking the position, or height, of the compact throughout the process as a function of the

compaction load. A crosshead displacement value of the compacting die punch as a function of the load applied was obtained. Using the crosshead position to calculate a relative density value and the load values to calculate the compaction pressure based on the compaction die parameters, one can create a plot for the compaction curve. This automated method allowed the user to actively monitor the crosshead position with the registered load so in-line monitoring of the compaction behavior was achieved. This automated method is the most realistic means of assessing compaction processes.

2.C.3. Factors Affecting Compaction Behavior

2.C.3.a. Mechanical Behavior of Spray-Dried Granules

Compaction behavior is dependent on the granule morphology and their respective characteristics [50]. Reed and Walker attributed that the granule yield point depends on the granule density and strength [58]. Segregated binder layers that form during compaction increase the granule critical yield point and inhibit densification at lower pressures [19]. Baklouti *et al.* [59] determined the resistance of the granules during compaction depends on the binder and its respective glass transition temperature. Frey *et al.* [60] investigated the compaction response of spray-dried alumina and determined that common plasticizers govern the compaction response and final porosity of the compact. The degree in which the organic binder is plasticized governs the compaction sensitivity of the ceramic and is an important aspect to consider when analyzing the compaction behavior of the spray-dried granules [34, 61].

Nies *et al.* [62] showed that compaction must occur above the T_g of the organic binder to promote densification. Moisture can be used as a plasticizer for certain water

soluble binders by softening and lowering the strength of the granule [17, 63]. Saito *et al.* [18] showed that absorbed moisture on the surface of spray-dried granules reduced the porosity and pore size within compacts. Greater green density values were achieved when using moisture due to moisture favoring intergranular bonding within the compact [64]. Tanaka *et al.* [64] discovered that the strength and density of compacts increased with increasing moisture content during compaction. This promoted transgranular fracture due to the increased intergranular bonding. Balasubramanian *et al.* [65] evaluated the use of an externally applied plasticizer of ethylene glycol monoethyl ether (EGME) on alumina granules. The externally applied plasticizer reduced defects during compaction due to the softer deformable nature of the granules, removing granule remnants more easily due to the greater knitting behavior. However, a reduction in green strength was observed by using an externally applied plasticizer than with granules without the plasticizer.

2.C.3.b. Ejection and Springback

Ejection of the compact from the pressing die relieves residual elastic strains from the pressing pressure. This phenomenon is called springback which can cause an expansion change in dimensions of the compact that can reach up to 0.5% after ejection [50]. Springback can become a major issue when dealing with processing parts that need tight dimension tolerances. To account for this issue, production times and cost will increase which ideally need to be minimized [2].

Springback is an outcome of stored elastic energy within the compact that is dependent on the elastic and viscoelastic components of the organic system [2]. Springback increases within compacts that have a higher degree of organic binders [3]. The glass transition temperature of these organic systems play a role in how the elastic and

viscoelastic response occurs within the compact. If compaction occurs below the T_g, the binder is elastic and springback will increase. When pressing above the T_g, the binder acts more like a liquid in a solid, deforming and adding little to the elastic springback of the compact [34, 61]. Lubricants and higher compaction pressures have also been known to increase the springback within compacts however lubricants are needed to enable the compact to be ejected from the die to reduce ejection pressure on the compact [4, 34].

Air entrapment can also cause springback due to air needing to be released during ejection. If air that is trapped within voids cannot escape through the pore interconnectivity or die wall and punch, it will become entrapped [66]. A slow compaction rate will prevent air entrapment during dry-pressing, reducing springback. Holding the compaction pressure as well will allow time for ceramic particles to rearrange, reducing the springback in the body [4]. Most air removal occurs during stage II of compaction. Reducing the pressure during this stage or incorporating pressure relief steps in the compaction process can limit springback and trapped air, as air removal is a function of volume reduction.

Niesz [50] evaluated the ceramic particles throughout the compaction process noting that each particle can act as a mini spring under high stress, and therefore due to the greater stored elastic energy, the particles bend and increase the extent of springback. Niesz also noted that particles shaped with sharp corners may promote particle interlocking causing springback to increase in the compact due to strain being stored in the bending of these particles [50].

2.C.3.c. Die-Wall Friction

During compaction, some fraction of the applied load is transferred to the die wall and the force produced from the die wall friction will cause pressure gradients and stress

within the compact [34]. Die friction can then cause density gradients within the ceramic compact, becoming a major issue during production [50]. To reduce shear stress due to die wall friction and the internal coefficient of friction due to the granules, lubricants are needed to allow the compact to be ejected [4]. Van Groenou [67] stated that isostatic pressure alone is not enough to remove the inhomogeneous microstructure that is caused by die wall friction. Lubricants can be added internally, mixed within a slurry along with the ceramic particles, or applied externally by coating the granules or applying the lubricant along the die wall. Both lubricants provide lubrication among the interaction between granules and the die wall. Internal lubricants and coated external lubricants will provide lubrication among the ceramic particles as well granule-granule interactions [4].

Lubricants only reduce die friction by the granules compacting along the die wall. Briscoe and Evans [68] proposed a model for die wall friction during compaction that stated it is governed by the interaction of lubricants and organic binders throughout the process. Balasubramanian *et al.* [69] saw no reduction in green strength or springback with the use of an internal lubricant, only reducing the particle-particle frictional forces within the granules.

2.C.4. Density and Stress Distribution

During compaction, the load is applied to the granules within the die and pressure is transmitted throughout the system causing the granules to move with the direction of the applied pressure. This distribution may not be uniform. Some fraction of the applied load is transferred to the die wall and the force produced from the die wall friction may cause pressure gradients and stress within the compact [34]. This stress variation can result in

compacts with density gradients. Single action uniaxial compaction consists of a fixed bottom punch and die with the top punch moving to compact the ceramic granules. Figure 5 shows the stress distribution during stage II of compaction for a single action uniaxial compaction process, the primary technique used for this dissertation.

Punch Motion

Begin Stage II   End Stage II

$$P_1 > P_2 > P_3 > P_4$$
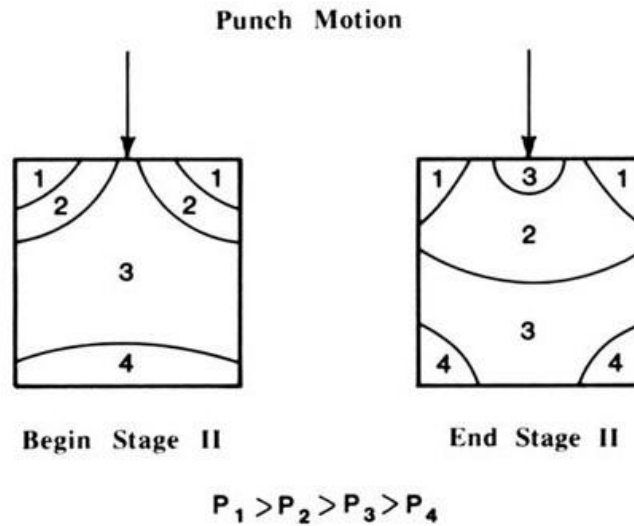
Figure 5. General pressure profiles during stage II for pressing using single action uniaxial compaction. Maximum compact density is localized at the top surface and decreases from the top to the bottom of the compact [34].

Adding a lubricant for this process can help maintain a uniform density distribution in the sample by improving the stress transmission and increasing the pressure near the bottom of the compact. DiMilia *et al.* [70] and Thompson [71] have stated that it is beneficial to add lubricants to the die wall rather than any other lubricating method to minimize density gradients within the compact. DiMilia also discussed decreasing the ratio of thickness to diameter to minimize density gradients by increasing the stress transmission during compaction. A larger diameter corresponds to a larger area to exert the applied force

and a smaller area contact between the die wall and powder. This places more pressure on the powder than the die wall, thus reducing die wall friction slightly [70].

2.C.5. Compaction Behavior Analysis

Compaction equations have been developed to interpret compaction curves by modeling various mechanisms of compaction based on the material system being compacted. These mechanisms can differ based on if the powder is agglomerated or not, and its respective porous nature and strength. The granule yield point is typically a range of values for granules of different sizes that experience different stress distributions [2]. Niesz and Bennett [72] have developed a relationship, first suggested by Duckworth [73] discussing Ryshkewitch's [74] paper on the strength of porous alumina and zirconia. Duckworth first suggested the following formula based on the experimental results of Ryshkewitch for the relative strength of agglomerates [73, 74]:

$$\sigma = \sigma_0 e^{-bP} \qquad\qquad 3$$

where σ is the strength of a porous body, σ_0 is the strength of a nonporous body of the same material, b is an empirical constant, and P is the porosity expressed as a fraction. The value of b correlates to the slope of the $\ln \sigma$ vs. P curve. Niesz [72] expressed this relationship in terms of pressure, replacing the strength terms to achieve:

$$P = P_0 e^{-bP} \qquad\qquad 4$$

Taking the logarithm of both sides:

$$\ln P = \ln P_0 - bP \qquad\qquad 5$$

Which gives the linear relationship of pressure versus the volume fraction of porosity. The logarithm of pressure is also linearly related to either the porosity, expressed as a

percentage, or density, either expressed as a fraction or a percentage of theoretical density [72].

Qualitatively, many researchers over the years have measured the critical yield point by drawing lines tangent to stages I and II and finding the point where they intersect [50, 58, 61, 65, 69, 75-77]. Mort *et al.* [78] further explored this technique with a mechanical tester. Mort took the crosshead displacement and force data and determined every point on a compaction curve has a corresponding x and y value. Calculating the first derivative between every point and repeating this process to obtain the second derivative, inflection points can be calculated. Smith [2] and Mort *et al.* [78] have stated that this method became more reproducible and accurate to calculate the granule yield point, however, the calculation is dependent on the data acquisition of the mechanical tester and the amount of data points analyzed on the compaction curve. Data transformation using a power transform equation, such as a box-cox transformation, can manipulate the data in a way to better estimate the critical yield pressure and joining point of compaction curves using this method. Since there exists a range of yield pressures for a broad granule size distribution, using the tangent line method is a faster and more efficient method to calculate the critical yield pressure of the granules as a collective whole. For this reason, it will be the primary method used in this dissertation. Finding a non-linear best fit line for the data over a respective pressure, the intersection of the two lines can be determined and thus the granule yield point.

Matsumoto [79] improved upon Messing's method of using a computer interface to track compaction behavior of the ceramic compact. Matsumoto cautioned that simply plotting the calculated results of pressure and density wasn't enough, and that machine

compliance factors were not taken into account during the compaction process. Matsumoto contributed the machine compliance factors to the following: the mechanical tester, the load cell, the compaction die, and the ceramic compact. Matsumoto assumed the compliances from the mechanical tester and compaction die were negligible. The ceramic compact's compliance was attributed to the springback of the compact, which Matsumoto considered negligible for his evaluation of compaction testing. Since the load cell is effectively a stiff spring, operating as a Hookean linear elastic spring, higher loads will result in higher displacement values, meaning the mechanical tester is not taking into account the displacement of the load cell during compaction testing. If one does not account for this issue, the apparent joining point observed will be uncorrected for machine compliance. This phenomenon is shown below in Figure 6.
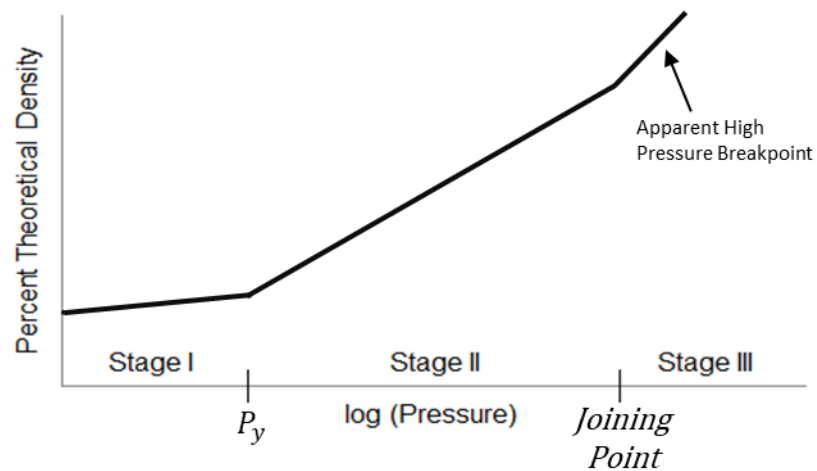
Figure 6. Compaction curve schematic uncorrected for machine compliance [55].

Matsumoto stated that to account for this issue, one must more accurately track the density values throughout the test [80]. Matsumoto used an unload-subtraction method to eliminate the elastic components of the crosshead by collecting the crosshead vs. load data

over a loading and unloading cycle during compaction testing. Highlighted in the equation below proposed by Mort *et al.* [78], Matsumoto found by using the difference between the loading (Z_{load}) and unloading (Z_{unload}) displacement values in accordance with the ejected compact's thickness (L_{final}), the elastic components of the machine were accounted for. Thus the density, or rather the net pellet thickness throughout the test (L), were more accurately represented.

$$L = L_{final} + Z_{load} - Z_{unload} \qquad\qquad 6$$

Mort improved upon this correction, taking into account die wall friction and elastic springback of the pellet during compaction. Mort stated that the total crosshead displacement during loading included the compaction of the ceramic plus the elastic deformation of the testing apparatus and elastic deflections of the ceramic compact (i.e. springback). Mort stated at the high pressure endpoint, or the maximum pressure on the compaction curve, the springback of the compact can be measured by the difference between an adjusted crosshead position and the thickness of the compact after ejection. To calculate for this adjusted crosshead displacement, Mort proposed collecting baseline data of the load and displacement for the compaction of an empty die. In doing this, the difference between the baseline displacement data of the empty die (Z_{base}) and the displacement data of the ceramic compact (Z_{load}) represents the thickness of the compact before elastic springback. The difference between these values at the high pressure endpoint, or P_{max}, is the measured springback at the maximum load during compaction, S_{max}, where L_{final} is the measured compact thickness after ejection [78].

$$S_{max} = 1 - \left.\frac{(Z_{load} - Z_{base})}{L_{final}}\right|_{P_{max}} \qquad\qquad 7$$

This equation supports correcting the high pressure endpoint of the compaction curve as shown in Figure 6. However, this is only taking into account the springback at the high pressure endpoint. Mort proposed mathematical models to allocate springback as a function of pressure. Mort proposed two models, linear and hybrid springback models. The linear model assumed a linear dependence between springback and pressure and is expressed in the equation below where P relates to the pressure of the compact throughout the compaction test and S is the springback calculated at that pressure [78].

$$S = \frac{P}{P_{max}} \times S_{max} \qquad 8$$

The second proposed model, the hybrid springback model, proposed mathematical models at intermediate pressures during compaction, based on the stages of compaction and deformation behavior of the ceramic material. Mort separated the springback relationship into two components, granule deformation and elastic deformation. Mort stated that during the initial stage of granule deformation, the springback is proportional to the granule compaction behavior. Therefore the springback component of granule deformation (S_{def}) for pressures above the critical yield pressure (P_y) is expressed by the equation below [78].

For $P>P_y$

$$S_{def} = S_{max} \times \frac{\log\left(\frac{P_{join}}{P_y}\right)}{\log\left(\frac{P_{max}}{P_y}\right)} \times \frac{\log\left(\frac{P}{P_y}\right)}{\log\left(\frac{P_{max}}{P_y}\right)} \qquad 9$$

For pressures above the joining point (P_{join}), the springback was modeled after the elastic deformation of the ceramic compact (S_{mod}) and is expressed in the equation below [78].

For $P > P_{join}$

$$S_{mod} = S_{max} \times \frac{\log\left(\frac{P_{max}}{P_{join}}\right)}{\log\left(\frac{P_{max}}{P_y}\right)} \times \frac{P - P_{join}}{P_{max} - P_{join}}$$

<div style="text-align:right">10</div>

The sum of the proposed components of the above springback models is the total springback over stages 2 and 3 during compaction [78].

$$S = S_{def} + S_{mod}$$

<div style="text-align:right">11</div>

For both the linear and hybrid springback models, the equation for the corrected compact thickness (*L*) accounted for springback is shown below [78].

$$L = \frac{Z_{load} - Z_{base}}{1 - S}$$

<div style="text-align:right">12</div>

Mort *et al.* [78] compared the unload-subtraction method to both of the proposed springback models and found that the hybrid springback model produced the most consistent results. The unload-subtraction method provided similar results at lower compaction pressures but exhibited systematic error at higher pressures due to die wall friction and the retardation of springback during unloading. Mort stated that both baseline correction methods were beneficial in analyzing the springback and die friction effects during compaction.

2.D. Image Analysis of Green Ceramic Microstructures

2.D.1. Liquid Immersion Method

Uematsu *et al.* [5] first developed the liquid immersion method (LIM) to understand the morphology of spray-dried granules. Alumina spray-dried granules were made transparent under an optical microscope by use of an immersion liquid to account for the refractive index of the alumina ceramic, which is n=1.76 [5]. Methylene iodide (n=1.74) and 2-bromonaphthalene (n=1.64) were tested since they have a similar refractive index of alumina [5]. The relative refractive indices of these liquids compared to alumina are R=1.01 for the former and 1.07 for the latter [5]. The interior structures of the spray-dried granules were examined to determine if they were solid or hollow [5, 9-19, 21, 23, 24].

This method proved to visualize the segregation of PVA binder within the internal structure of the granule. Zhang *et al.* [9] showed the distribution of PVA within the compacted body and how binder rich layers cause detrimental defects prior to sintering. Dry-pressed alumina green bodies were thinned by the use of a grinding sandpaper to less than 0.5 mm in thickness and an immersion liquid was used to visualize the uniformity of the compacted microstructure. Regions of high and low density were then differentiated based on the binder distribution within the granules, and thus, the compacted green body [5, 8, 12-14, 16, 18, 31]. It was found that large intergranular pores form in between the remnant structures of the compacted granules that have PVA rich layers on the surface. These pores persisted and formed detrimental defects within the sintered body. Density gradients also formed within the compacted body. Once the binder rich layers were removed during the sintering process, regions of low density formed along granule boundaries [8, 9, 13, 14, 16, 19, 31].
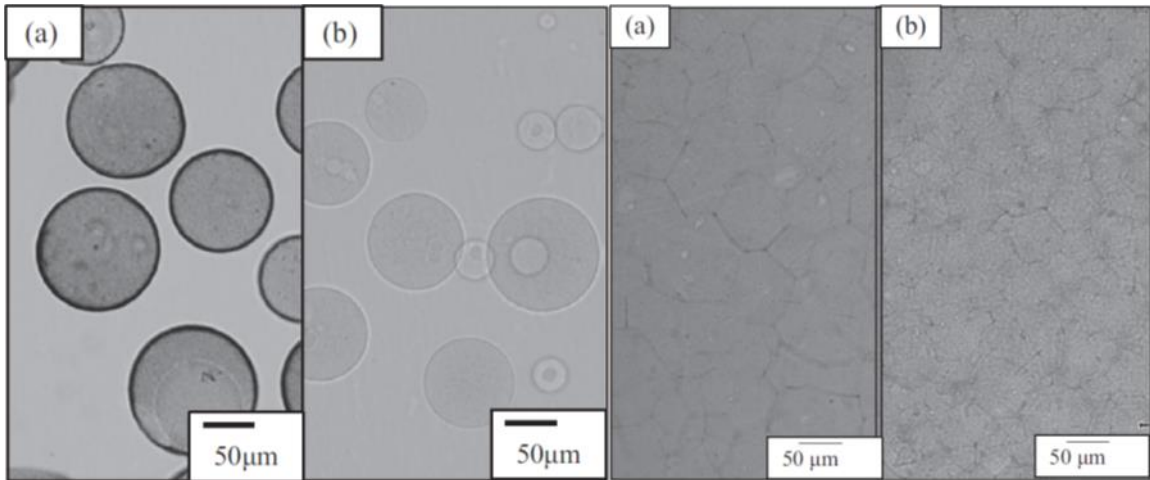
Figure 7. (Left) Images taken using LIM showing the PVA binder distribution within spray-dried granules (a) before and (b) after binder burnout. (Right) Compacted microstructure (a) before and (b) after binder burnout showing intergranular pores and low density [31].

Uematsu *et al.* [15] coupled infrared microscopy with the liquid immersion method to improve the capability with other ceramics. Silicon nitride, for example, has a refractive index of n=2.05, and all available immersion liquids to be used are toxic and unstable, therefore using a longer wavelength light source, such as infrared light, can be helpful for observation [15]. Due to the stronger light source, the thickness of specimens to be observed could be increased and 2 mm was achieved compared from 0.5 mm with an optical microscope.

The availability of immersion liquids for most ceramics with high refractive indices is low. This limitation and the process to thin specimens to roughly 0.5 mm are the limitations of the liquid immersion method. Its capabilities used for the visualization of binder segregation and internal structures of spray-dried granules has proven valuable in understanding how to create more reliable and uniform ceramic materials.
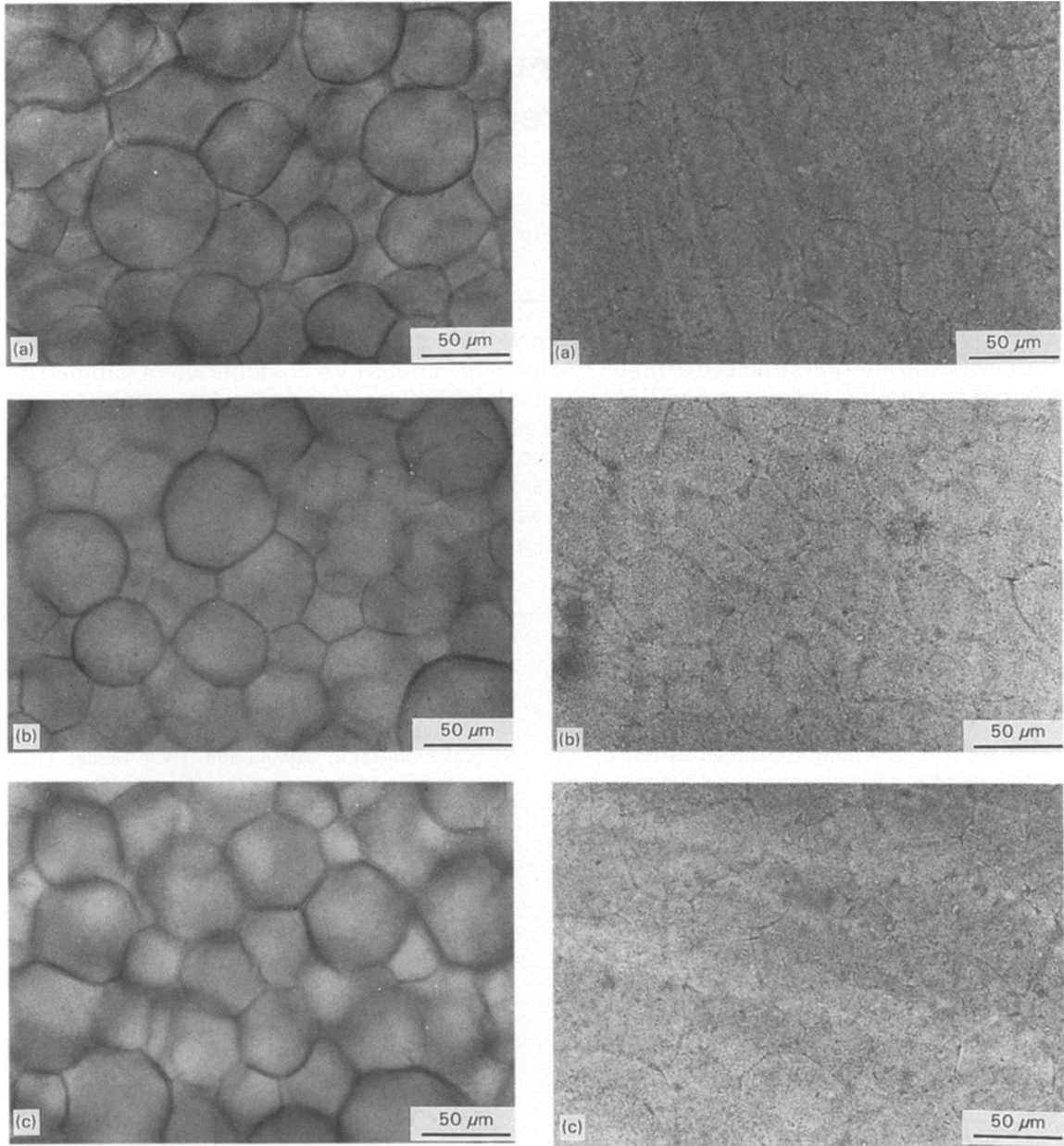
Figure 8. Optical microscope images obtained by LIM showing alumina compacts at various binder percentages (Left) before and (Right) after binder removal [9].

2.D.2. Confocal Laser Scanning Microscopy

Confocal laser scanning microscopy (CLSM) is an improved method that uses a fluorescent dye and an immersion liquid within a green compact. Confocal laser scanning microscopy (CLSM) uses a fluorescent dye and an immersion liquid within a green ceramic compact. A laser is used as a light source and is made parallel with a beam expander. The light is then directed towards an objective lens by a half mirror. The parallel light is converged by the objective lens to a focal point. The laser excites the fluorescent dye within the immersion liquid and the dye then absorbs the laser light and emits fluorescent light of a longer wavelength than the laser. The emitted light is made parallel again by passing through the objective lens and other light that is emitted is made with convergent light. Only the parallel light emitted from the focal point can pass through the pinhole and reach the detector after the laser light is removed through a filter. Then the emitted fluorescent light is reconstructed by use of a computer and an image of the focused region is obtained [7]. Dark regions correspond to areas where the fluorescent dye could not impregnate and bright regions correspond to porosity.

Saito *et al.* [7] has stated that this method can show the smallest features of roughly 0.4 microns, which is an improvement from the liquid immersion method. With this method, low density regions were shown to form at granule boundaries after binder burnout [6]. This method has also shown the processing effects of different relative humidity atmospheres on the compaction behavior of spray-dried granules and the resulting green microstructure [7, 26]. Brighter contrast regions show the effect PVA segregation has on the microstructure of the green compact, forming detrimental intergranular porosity. Homogeneous microstructures formed with higher relative humidity percentages resulted

in higher strength and reliable ceramics [26]. Tanaka *et al.* [25] investigated the difference between ball milled and agitated ball milled processing in terms of producing spray-dried granules. It was shown that ball milled granules resulted in a higher percentage of agglomerates and aggregates within the granule compared to agitated ball milled. Kato *et al.* [27] investigated the stages of compaction using this method by tapping granules within a die by use of a high refractive index resin and fluorescent dye in an attempt to visualize the behavior of spray-dried granules deforming in the initial stage of compaction at a pressure of 2 MPa. It was found difficult to quantify the deformation process using this method.
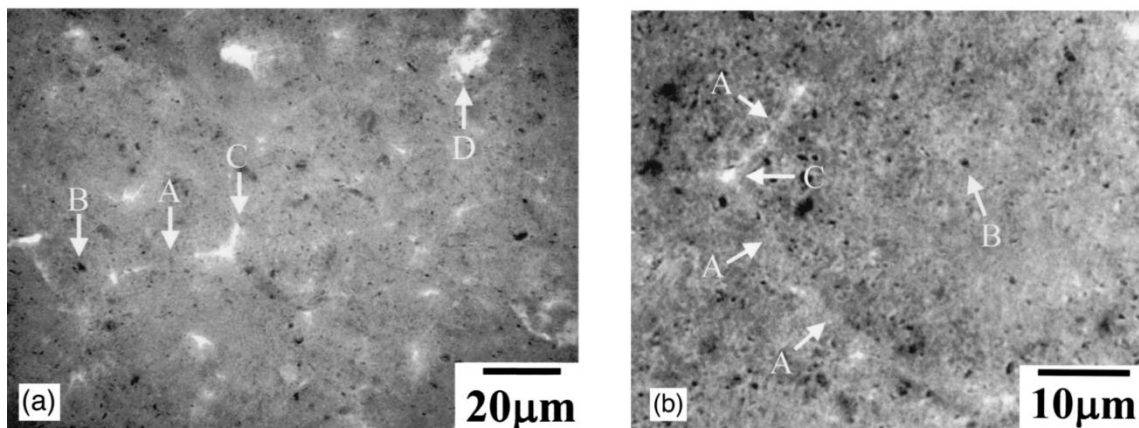
Figure 9. CLSM image of an alumina compact after binder removal showing (a) boundary regions of granules, (b) large particles or agglomerates, (c) triple junctions between granules, and (d) large pores [6].

The limitations of this method are the same as the liquid immersion method previously discussed. This method resolves heavily on the use of an immersion liquid with a high enough refractive index to characterize the green compacted ceramic. Alumina is heavily investigated due to its easily accessible refractive index for analysis [6, 7, 25-28].

Compacted green ceramics also have to be thinned to less than 0.2 mm for this method, which restrict the capabilities on a larger scale three-dimensionally [7].
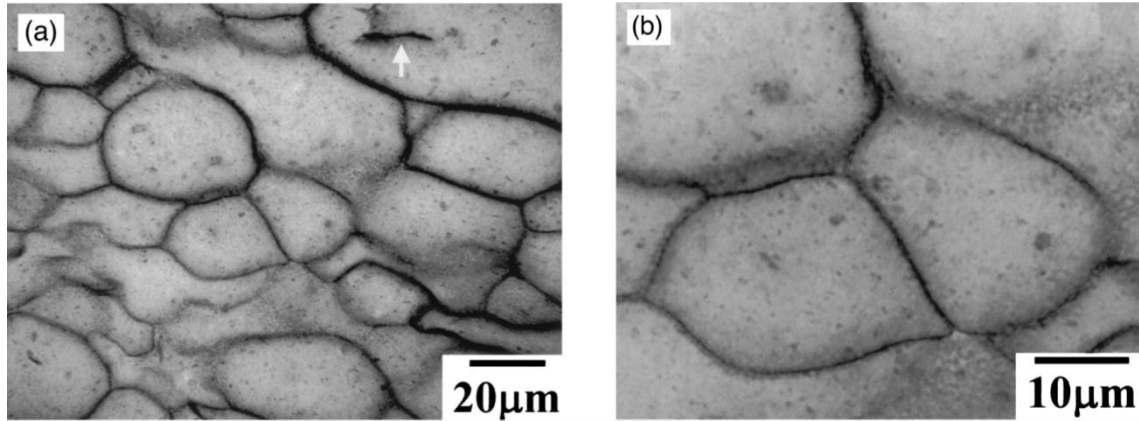
Figure 10. Image generated from CLSM showing PVA binder distribution within compacts [6].

2.D.3. Micro X-ray Computed Tomography

Micro X-ray computed tomography (micro X-ray CT) is a non-destructive characterization tool that has been recently used to visualize the internal structure of materials [30, 31]. In conventional devices, X-rays are generated by directing electrons produced in a cathode at a target, typically made of copper or tungsten. The deceleration of these electrons against the target occurs and kinetic energy is lost in the form of X-rays by the decelerating radiation. When these X-rays hit matter, any X-rays are absorbed by the sample being investigated or are collected by the detector. Differential absorption occurs when there are different materials being investigated that have different absorption characteristics causing a contrast difference in the image. The amount of X-ray photons that are absorbed depends on the material density ρ, atomic number Z, and the beam energy E. The following equation generalizes the X-ray attenuation of X-rays absorbed by a material where I is the emerging X-ray intensity, I_0 is the incident X-ray intensity or

intensity after reaching the material, μ is the X-ray attenuation coefficient, and *dt* represents the differential thickness the X-rays passed through the sample [81]:

$$I = I_0 \, exp^{\int -\mu(t,E)dt}$$

13

The X-rays that are collected by the detector are then converted into visible light by the detector coupled with a photodiode, which converts the visible light into current. The current is then analyzed by a computer and a digital image is produced. A reconstruction process is then administered by a pixel-based approach on the digital images with the use of a filtered back projection method. All of the generated images are filtered in the frequency domain and are converted using Fourier transforms. The data is then reconverted to the real domain and a back projection algorithm is administered to the filtered data in order to obtain a 3-dimensional tomographic rendered image [81].

The quality of the final rendered image is subject to the limitations and errors associated with the reconstruction algorithms. The major limitations of this characterization method include spatial resolution due to the lack of contrast obtained between phases that have similar attenuation coefficients. The spatial resolution is determined by the detector resolution and the focal spot size, typically around $0.5 - 5.0$ μm. The highest resolution is usually obtained with a smaller sample size or scanned area. Micro X-ray CT has difficulty distinguishing between material or phases with a similar attenuation coefficient, unable to provide sufficient information [81]. Computed tomography is typically used for macroscopic pore quantification [82]. For use with porous ceramic samples, a micro-X-ray CT would have difficulty distinguishing between loose packing structures and sub-micron porosity due to similar attenuation coefficients.

Dies *et al.* [83] investigated the moisture effects during compaction with this technique. Spray-dried granules were stored at varying relative humidity levels prior to compaction. Their respective densities were calculated by the final length measurement after compaction. Density distributions throughout the compacted green body were examined. Granules stored under no humidity resulted in a greater uniformity throughout the compacted body when compared to spray-dried granules stored at 98% relative humidity, which resulted in the greatest density but had a greater difference of density variations throughout the microstructure. The most uniform structure resulted from granules stored at a relative humidity level of 60%. A similar study was completed by Cottrino *et al.* [84] where density heterogeneity was highlighted by manipulating the compaction behavior of the spray-dried granules due to varying moisture and binder percentages of the granules prior to compaction.

Eckhard *et al.* [85] attempted to evaluate the porosity percentage of alumina spray-dried granules in the size range of 45 to 160 μm with the use of micro and nano X-ray computed tomography. The micro X-ray CT was not successful due to the maximum resolution of the device being 7 μm. Porcelain granules, in the size range of 400 to 500 μm were then evaluated with the micro X-ray CT, and evaluation of the micro-porosity was still difficult and couldn't be achieved. Nano X-ray CT, maximum resolution of 2 μm, was then attempted on alumina spray-dried granules with hollow cored internal structures and is shown below in Figure 11. Even though this method showed higher resolution, it is still difficult to interpret the images to evaluate the micro-porosity [85]. The technology centered around Micro X-ray Ct is quickly improving and in the next few years, this type

of analysis might be possible. However, there still exists the difficulty in understanding and discerning what one visualizes with a typical microscope in two-dimensions.
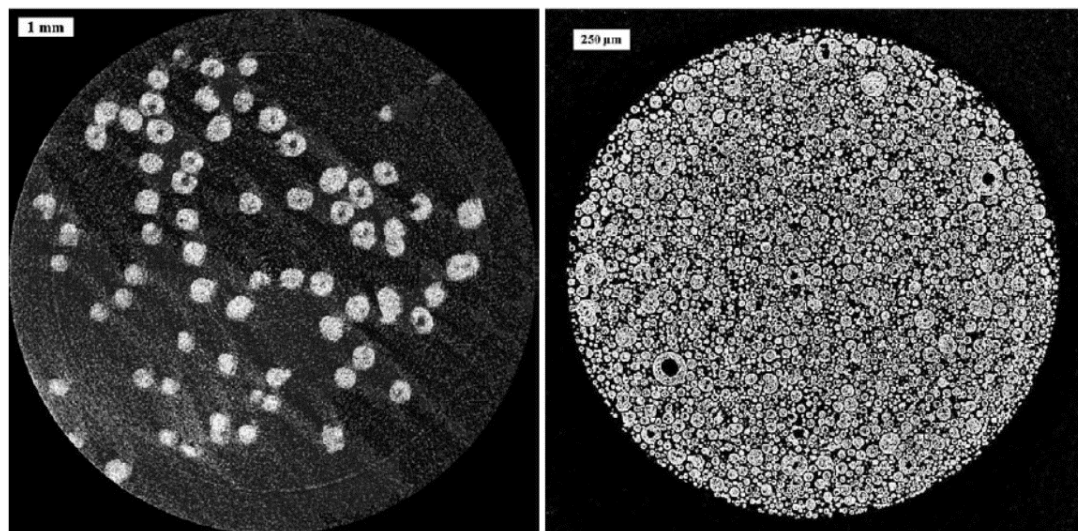
Figure 11. (Left) Micro X-ray CT of porcelain granules. (Right) Nano X-ray CT of alumina granules [85].

As previously stated, with the use of micro X-ray CT large pores and loose packing structures within the ceramic compact are difficult to distinguish due to the similar degrees of X-ray absorbency and attenuation coefficients [86]. To investigate a solution to this phenomena, Hondo *et al.* [30] used potassium iodide was used as a contrast media. Hondo was able to visualize areas of low density regions within green ceramics down to a resolution of one micron and generated a three-dimensional rendering of the characterized ceramic, shown below in Figure 12 [30]. Hondo went on to evaluate the growth behavior of large pores during sintering with the use of micro X-ray CT and was able to show heterogeneous densification occurs due to large pore growth and non-uniform granule remnant shrinkage [31, 32].
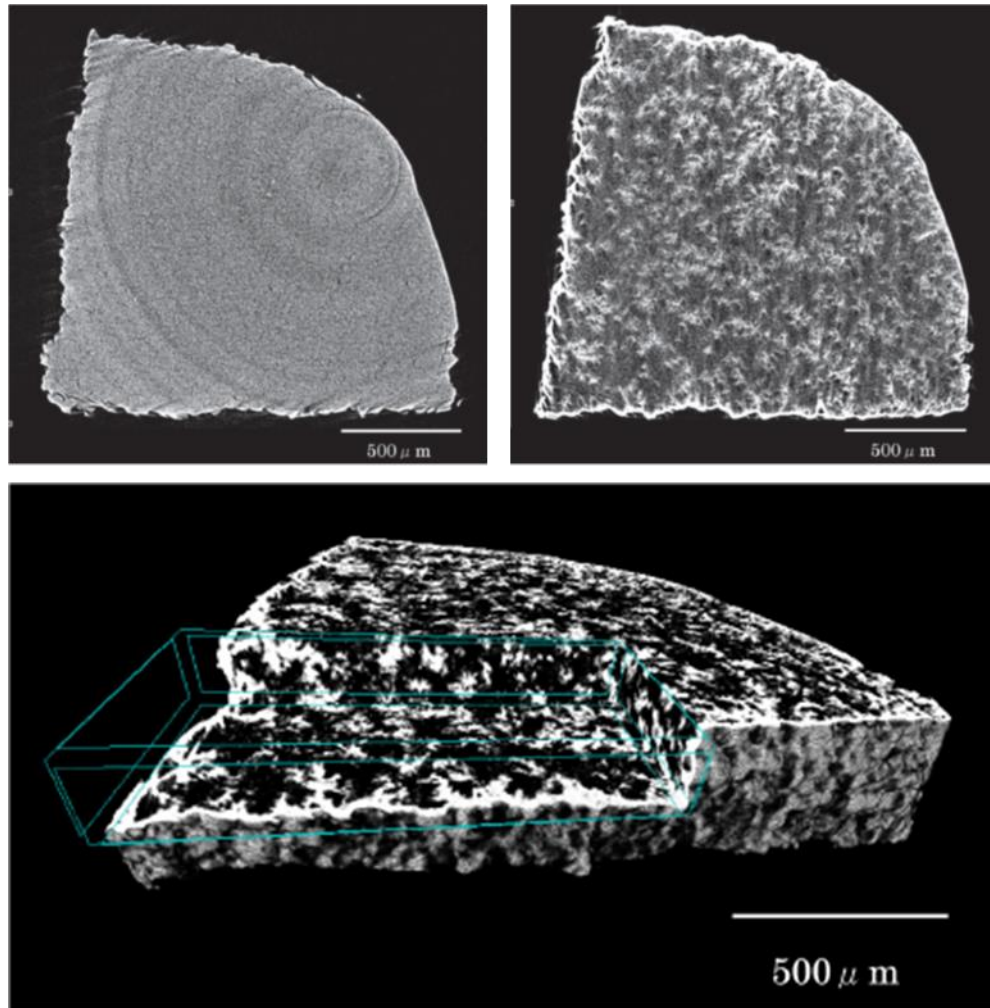
Figure 12. X-ray CT generated image (Left) before and (Right) after use of potassium iodide. Low magnification three-dimensional pore networks were obtained [30].

2.D.4. Scanning Electron Microscopy

Higher resolution microstructure images of porous ceramic materials are possible to achieve by use of an SEM, however, limitations must be overcome. Due to the porous nature of the green ceramic, a conductive surface must be implemented to mitigate charging effects while obtaining microstructure images. Methods exist for this purpose such as sputtering a nanolayer thickness of a conductive material such as gold on the

sample's surface prior to microstructural characterization or using other conductive materials such as carbon tape or silver paste. These methods can be used to obtain microstructural characterization of spray-dried granules as well as the surface and fracture surface of green compacts [5, 9, 12-19, 21-24].

To gain more microstructural information on the internal structure of porous ceramics, a method to evaluate the cross-section of the sample has to be enforced. Mechanical sectioning is a conventional method used to expose the cross section or internal structure of materials for microstructural characterization. The porous ceramic is infiltrated within an embedding agent, typically an epoxy resin. Then the infiltrated ceramic is mechanical sectioned by means of mechanical polishing [82].

This process may cause issues to arise on the surface of the mechanically polished sample, creating artifacts such as pullouts or loosely bound ceramic particles. Ceramic particles that are loosely bound within the embedding epoxy may smear on the surface of the sample, inhibiting proper microstructural characterization. Due to the soft nature of the sample, it is quite apparent that mechanically polishing could cause more harm on the sample's surface if not properly infiltrated. It has also been noted that the organic binder species within spray-dried granules may become overpowered by the embedding matrix of the epoxy and therefore difficult to visualize the binder distribution within the porous ceramic. If this cannot be overcome, sufficient characterization of the internal structure of spray-dried granules or porous ceramics is impractical [82]. For this reason, producing an image of a flat surface truly representative of the sample's microstructure proves difficult.

Höhn *et al.* [82] developed a method to visualize the internal structure of spray-dried granules with the use of an ion mill, or ion beam. Höhn attributed using an ion mill

as a gentle method to expose the internal structure of highly porous ceramics without introducing mechanical damage. Due to a major disadvantage of focused ion beam (FIB) systems only milling away a few μm^2 in only a short period of time, it becomes insufficient for quantitative analysis. In this study, Höhn analyzed the organic binder distribution within the spray-dried granules by use of a broad ion beam technique, using a dual argon source ion beam that can be directed either in field or selectively accelerated or decelerated by a specifically applied DC field onto the surface of the sample. This allows to an adequate removal of material for microstructural characterization of the internal structure of the spray-dried granules. A FESEM was used that was a dual beam unit with a FIB that was used for finer sample preparation. Energy dispersive X-ray spectroscopy (EDS) was also implemented to analyze regions of the organic binder on the spray-dried granules for chemical analysis. Five model granules were investigated for this study. The granules were glued onto a sample holder in preparation in the equatorial plane of the ion beam and were milled to expose their internal structure. The setup for this test can be seen below in Figure 13 [82].

Höhn observed that the granules spray-dried at a higher viscosity value resulted in solid granules with loose primary particle packing. Spray-dried granules spray-dried at similar viscosity levels but a varying degree of solids loading resulted in an internal structure that showed both hollow cores and solid granules but with a higher degree of particle arrangement [82].
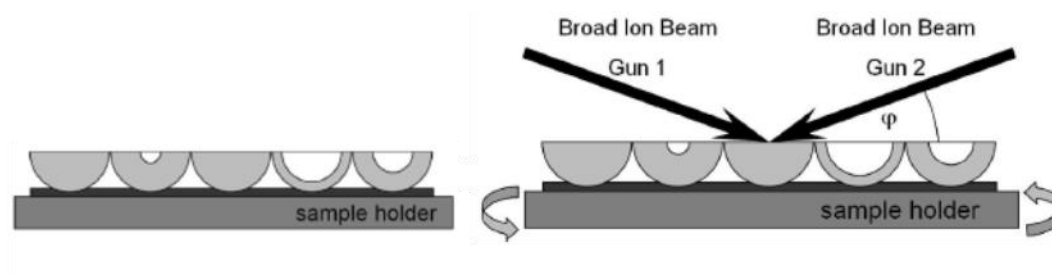
Figure 13. (Left) Test setup for microstructural characterization, adhering the granules to the sample holder with an adhesive. (Right) Schematic illustrating the ion milling process [82].

Visualizing the binder distribution was difficult for these granules and EDS analysis showed an abundance of organic binder at the surface or crust of the sample. To further examine the potential of visualizing and evaluating the organic binder additives, Höhn spray-dried granules with higher levels of organic additives, zinc stearate (5.0 wt. %) and an acrylic emulsion binder (Duramax B-1000, 7.5 wt. %). The internal structure of the zinc stearate granules showed a uniform and homogeneous distribution of the binder species. However, the zinc stearate showed up as of flake like agglomerated structures within the spray-dried granules. The acrylic binder showed evidence of inhomogeneous distribution when compared to the zinc stearate granules. Microstructures of these granules are shown in Figure 14 and Figure 15 [82].
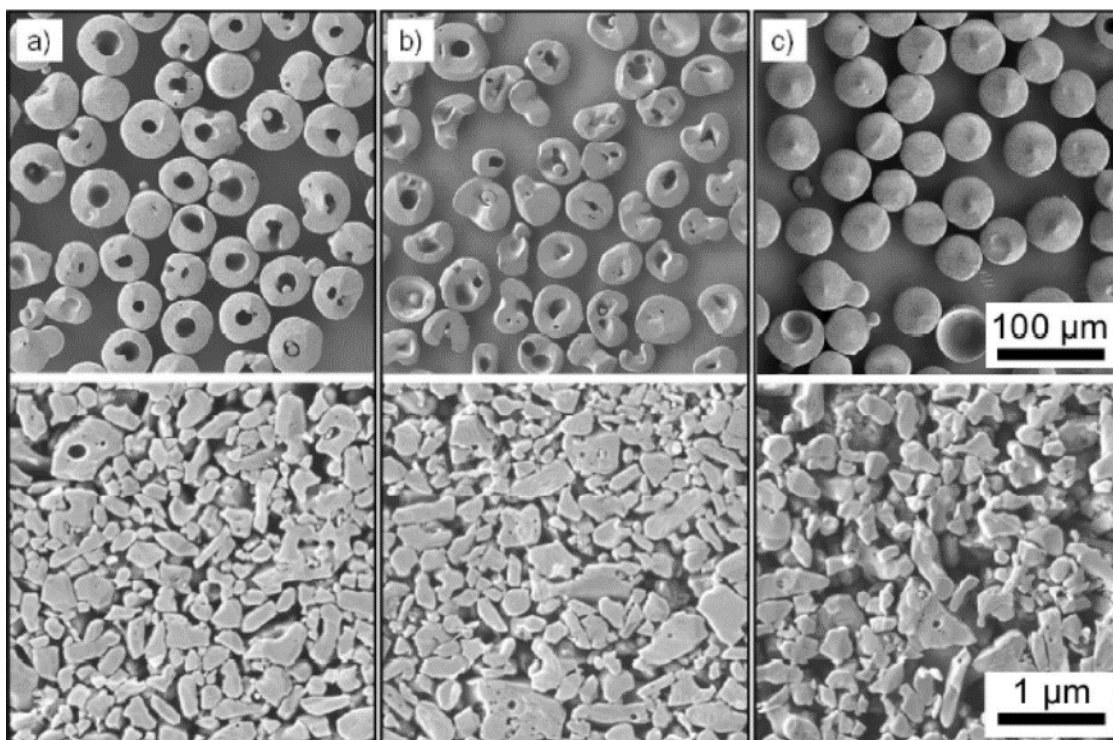
Figure 14. FESEM images of internal structures of alumina granules spray-dried at (a) 71.2 wt. % (b) 50.2 wt. % and (c) 62.1 wt. % solids with a high dispersant concentration compared to the previous two cases [82].
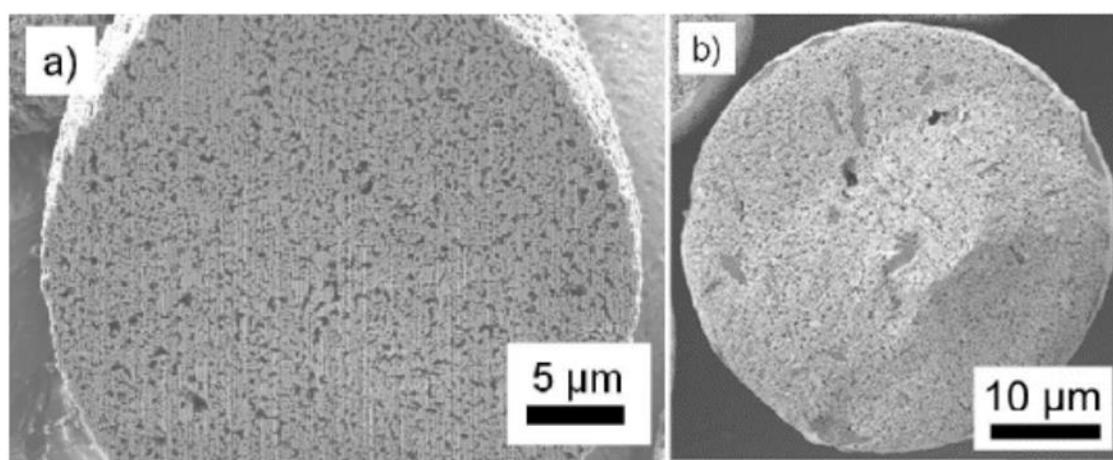
Figure 15. FESEM images of the internal structure of alumina granules spray-dried at (a) 49.9 wt. % solids with an acrylic emulsion binder and (b) 44.4 wt. % solids with a zinc stearate binder [82].

During the ion beam sample preparation, Höhn stated over heating of the specimen could occur and result in evaporation or sublimation. This occurrence could alter the characterization of the organic binder species, and must be controlled to temperatures below 100˚C. To achieve this boundary condition during sample preparation, adaptation of the removal rate of the ion beam, introducing pauses in preparation with the ion beam, or cooling the sample holder during the milling process could be attempted [82].

Höhn also conducted quantitative image analysis of the obtained ion milled FESEM images. However, due to deeper specimen regions being included in the grayscale detection process, an epoxy resin was used to infiltrate the granules. Infiltrated samples were mechanically polished with the use of a silicon carbide grinding paper down to 8 μm and ion milled with the previously stated method. Quantitative image analysis yielded similar results as mercury porosimetry results [82].

Eckhard *et al.* [85, 87] used Höhn's ion beam method to gain more detailed information on the influence of the granule internal structure on the mechanical properties of the spray-dried granules. Eckhard [85] used the FESEM images of granules over a size range of 45 to 160 μm to generate an image analysis method to quantify and compare porosity measurements with conventional methods such as mercury porosimetry. Mercury porosimetry can be helpful when analyzing the microstructure's total porosity, average pore size and pore distribution, however, interpretation of the data can become questionable when differentiating between the intragranular and intergranular porosity [82]. The average porosity obtained through mercury porosimetry was too low compared to theoretical results, around 45% porosity. Eckhard measured the diameter of the spray-dried granules as well as the void, or hollow core size, to determine percentage of

homogeneous or hollow. Comparing these results with calculated mercury porosimetry results showed promising results for porosity determination and analysis. Eckhard [87] also generated a particulate model to evaluate the mechanical properties of the spray-dried granule based on the particulate internal structure observed with the use of FESEM images obtained from the ion mill method.

Ku [54] developed a method of using Electron Microscopy Science's (EMS) Spurr Low Viscosity Kit epoxy to successfully infiltrate interparticle pores within ceramic powder without causing dispersion or breakage throughout the process. This epoxy can be heated up to lower the viscosity of the epoxy prior to infiltration. The epoxy is vacuum infiltrated into the prepared sample, holding the vacuum to ensure full infiltration is achieved. This epoxy resin hardens when exposed to temperatures above 70˚C for a time of 8 hours. Alazzawi *et al.* [88] has shown that this infiltration method can be used to successfully infiltrate green titanium dioxide extrudates for microstructural characterization with the use of a FESEM and charge mitigation techniques. Alazzawi used two dimensional image segmentation, attributing the pixels in obtained grayscale images from the FESEM to evaluate the porosity as a function of extrusion velocity.

Maher *et al.* [89] recently published using this method to successfully infiltrate spray-dried alumina granules to visualize their internal structure by mechanical polishing the infiltrated samples down to 0.05 μm with use of a diamond suspension. The polished samples were then ion milled by using the flat mill method on a Hitachi IM4000 ion mill with a specific voltage over a constant time and rotation speed. Using this epoxy for mechanical sectioning and ion milling proved sufficient to visualize the internal structure of the porous alumina without artifacts or pullouts on the surface. Green dry-pressed

alumina was then analyzed using the same infiltration epoxy, and was successful in infiltrating submicron and interparticle pores within the green compact [89]. Using this embedding epoxy also allowed visualization of the organic binder distribution within the spray-dried granules and green dry-pressed microstructure. This will be the primary method of visualizing the green microstructures investigated in this dissertation to visualize the particle and pore arrangements in dry-pressed spray-dried alumina in both two and three dimensions.

3. METHOD OF ATTACK

The goal of this dissertation centers on visualizing the particle and pore arrangements in dry pressed alumina as a function of processing parameters to form a fundamental relationship of experimental and visualization results to improve the characterization capabilities of compacted green microstructures. The processing parameters that were controlled included the slurry properties and granule characteristics prior to compaction. In meeting this goal, five primary objectives were met.

3.A. Objective 1: Spray-Drying and Processing of Granules

To examine the processing effects of compacted alumina, the appropriate candidate system for spray-drying alumina granules was determined. This included the appropriate organic binder system coupled with a specific particle size of alumina.

3.A.1. Slurry Selection, Processing, and Characterization for Spray-Drying

A16SG Alumina (Almatis GmbH, Frankfurt, Germany) was the commercial powder investigated. This was chosen due to its fine and narrow particle size distribution. A 21 wt. % aqueous solution of Selvol PVA (Sekisui, Dallas, TX) was the chosen binder system due to its wide use within industry for spray-drying alumina, availability in a solution form, and low cost. A 300 molecular weight PEG (Acros Organics, Bridgewater, NJ) was the chosen plasticizer. The chosen dispersant was Darvan 821A ammonium polyacrylate (Vanderbilt Minerals, Gouverneur, NY). The ratio of PVA to PEG was 2:1. Two different amounts of organic binder based on the solids weight of alumina were examined, 3.0 wt. % and 5.0 wt. %. Acrylic binders were also investigated to compare the difference among the binder distribution during the spray-drying process as well as comparing the type of organic binder effect on the compacted green microstructure and green strength of the dry-

pressed alumina. The chosen acrylic binders for this research were Duramax B-1000 and B-1022 (The Dow Chemical Company, Midland, MI) [2]. The ratio of Duramax B-1000 to B-1022 was 2:1 [2]. An emulsion stabilizer, Triton X-405 (Acros Organics, Bridgewater, NJ) was added to the acrylic aqueous slurries at 1.0 wt. % based on the total weight of acrylic binders in the system [2]. This candidate system was used to investigate and visualize the binder segregation during the spray-drying process in attempt to understand how it effects the compaction behavior and characteristics of the generated granules.

Aqueous alumina slurries were processed by ball milling. The milling process was monitored to ensure a uniform particle size after ball milling. Particle size was tested for all milled slurries by a light scattering particle sizer, Malvern MasterSizer 3000 (Malvern Instruments, Malvern, UK). Slurries were then characterized by specific gravity and viscosity prior to spray-drying. Three different viscosities were examined: 100, 250, and 400 cP at 50 wt. % solids. Two varying specific gravity slurries were examined: 50 wt. % (32 vol. %) and 60 wt. % solids (41 vol. %) solids at 400 cP viscosity for comparison. All viscosities were measured using a Brookfield LVDVIM viscometer at a speed of 20 rpm and an RV03 spindle size (Brookfield Ametek, Middleborough, MA).

As to ensure a well-dispersed suspension, the pH of the system was tested to account for any effects the dispersed state of the slurry may have had on the orientation of the particles during the spray-drying process. This was conducted by with a Fisher Scientific Accumet Basic AB15 pH meter (Fisher Scientific, Hanover Park, IL). To evaluate the dispersed state of the processed slurry, a fineness of grind (FOG) gauge, or Hegman scale, was used. A FOG gauge is a technique used to characterize the dispersed state of a suspension by scraping the suspension across a series of micron sized grooves,

acting as a scale, to visualize if any agglomeration is occurring within the suspension or slurry. The equipment used for this analysis was a Labman TIDAS (Labman, Middlesbrough, UK) which is an automated FOG gauge that uses a high resolution camera at a shallow angle to capture a histogram of the particle distribution after the test. This histogram is then analyzed by an algorithm to produce a sample rating of the dispersed state of the slurry. Using an automated equipment removes human error associated with this technique. The characterization of the alumina slurries was conducted to aid in the understanding of what slurry properties govern the characteristics of the spray-dried granules and the knitting characteristics of the granules during compaction.

3.A.2. Processing of Spray-Dried Granules

Alumina slurries were pumped into a mixed-flow fountain nozzle in a laboratory scale minor plant spray-dryer, a Niro Atomizer (Niro Inc. Colombia, MD). A Watson Marlow 323S model three roll peristaltic pump was the primary pump used for feeding the slurry into the drying chamber of the spray-dryer (Watson Marlow, Wilmington, MA). A dual headed pump system was used to reduce the pulsation of the slurry entering the spray-dryer. The alumina slurries with varying specific gravities and viscosities were spray-dried at a constant slurry pump feed rate, atomization air pressure, and temperature to ensure no other parameters prior to spray-drying were altered other than the slurry characteristics.

3.B. Objective 2: Compaction Behavior of Spray-Dried Granules

Compaction behavior of the granules were examined and investigated as a tool to understand if there were any differences in adhesion characteristics of the alumina granules based on the various processing parameters altered prior to spray-drying.

3.B.1. Spray-Dried Granule Characterization

The granule size distribution, bulk density, shape of granules, moisture content, and binder content of the spray-dried granules for all the varying slurry parameters were investigated. Initially, the moisture content of the as-received spray-dried granules was tested using an Arizona Instruments Computrak 2000 moisture analyzer (Arizona Instruments LLC, Chandler, AZ). The organic binder content was tested using a TA Instruments TGA/DSC Q600 (TA Instruments, New Castle, DE). The shape of the spray-dried granules was visualized and examined by use of a Keyence VHX-5000 advanced optical microscope (Keyence Corporation, Osaka, Japan). Understanding what governs the granule characteristics as a function of the spray-drying process parameters aided in the understanding of how the granules behaved during the compaction process.

3.B.2. Uniaxial Compaction Testing

Compaction behavior of the granules was examined and investigated as a tool to understand if there were any differences in adhesion characteristics of the alumina granules based on the various processing parameters altered prior to spray-drying.

A specific granule sieve size was analyzed to account for any variation that the granule size may have caused on the compaction behavior of the alumina granules. Compaction tests were conducted using an Instron model 5982 universal mechanical tester (Instron Corporation, Norwood, MA) at a specific uniaxial load of 10 kN in a compaction die with an 8.5 mm diameter. The effect of moisture was also investigated to understand how it affects the compressibility of the granules. The T_g of PVA lowers as moisture is added to the granule. Moisture acts as a plasticizer and softens the granules, lowering the critical yield pressure during compaction. Granules at moisture contents of dry, 2.0 wt. %,

4.0 wt. %, and 6.0 wt. % with an accuracy of +/- 0.25% were compacted to a uniaxial load of 10 kN. The granules used for the moisture study were all spray-dried at the same viscosity and specific gravity to keep everything constant except the moisture content of the granules (50 wt. % at 250 cP viscosity). Moisture was calculated by weight loss using the Arizona Instruments Computrak 2000 system.

3.B.3. Compaction Behavior Analysis

Compaction curves were analyzed for the various spray-dried granules formed as a function of processing parameters (i.e. viscosity, specific gravity, binder percentage, type of organic binder, and moisture content). Compaction curves were calculated using the weight of the alumina sample as a function of the change in volume, or change in height, during the compressive test. The hybrid-springback baseline correction method proposed by Mort *et al.* [78] was used to calculate the thickness of the compact throughout the compaction test. This method corrected the thickness of the pellet by accounting for springback and die friction throughout the compaction test. The weight of the alumina pellet was calculated as the de-binded weight of the sample after compaction was completed. This was to calculate the theoretical density of alumina to compare accurately between various binder percentages and moisture contents. The critical yield pressure of the granules for various processing parameters was determined by using a linear regression method by fitting semi-log equations to determine the stages of compaction [55]. This was to aid in the understanding of what slurry processing parameters and their respective granule morphologies had an impact on the crush strength of the granules.

3.B.4. 3 Point Modulus of Rupture Green Strength Testing

To evaluate the mechanical properties of the compacted alumina bodies, three-point modulus of rupture tests were conducted. Compacted bodies of alumina were processed at a size of 6 mm in thickness, 55 mm in width, and 101.5 mm in length. The two varying binder systems of an acrylic emulsion binder and a polyvinyl alcohol binder were tested, spray-dried at the same viscosity (250 cP) and specific gravity (50 wt. %). Moisture content was also evaluated, testing the green strength as a function of moisture. The acrylic binder granules were compacted at dry and 2.0% moisture, as acrylic binders are not moisture sensitive and there was no need to go to a higher moisture percentage. The PVA granules were compacted at dry, 2.0%, 4.0% and 6.0% held to an accuracy of +/- 0.25%. The reason behind this was to evaluate the mechanical properties and knitting behavior of the two different binders as a function of moisture. These samples were compacted at a uniaxial pressure of 40 MPa using a Carver Press (Carver Inc., Wabash, IN).

3.C. Objective 3: 2-D Microstructural Characterization of Processed Alumina

To visualize the alteration of processing parameters on the formation of spray-dried alumina as well as its impact on the compaction characteristics and microstructure of the system, spray-dried alumina granules and dry-pressed compacts were characterized by the use of a Zeiss Sigma field emission scanning electron microscope (FESEM) (Carl Zeiss Microscopy GmbH, Oberkochen, Germany).

3.C.1. Granule and Compacted Alumina Microstructural Preparation

Due to the porous microstructure of the green alumina granules and compacts, an infiltration epoxy that infiltrated sub-micron pores was needed. Spurr Low Viscosity Kit

(Electron Microscopy Sciences, Hatfield, PA) epoxy resin was used to embed the green body prior to mechanical polishing. This epoxy resin allowed infiltration within the interparticle pores without dispersion or breakage.

The infiltrated samples were mechanically polished down to 0.05 µm using a Buehler AutoMet 250 polisher (Buehler, Lake Bluff, IL) and ion milled using a Hitachi IM4000 ion mill (Hitachi Ltd., Tokyo, Japan). For the final step in preparation for characterization, since the alumina samples were porous, techniques were used to mitigate charging with the use of a FESEM. These techniques included the use of conductive materials such as silver paste, carbon tape, and a nanolayer of sputtered gold.

3.C.2. Green Microstructural Characterization

To gain a better understanding of what processing variations have on the morphology and compaction of spray-dried alumina, methods to better analyze the green microstructures of both granules and compacted alumina were determined using a FESEM. To visualize the morphology differences of spray-dried granules as a function of processing parameters, the cross sections of the spray-dried granules were characterized using a FESEM. In an effort and attempt to better understand the compressibility of the alumina granules along a compaction curve, granules were compacted at various pressures along their respective compaction curves to visualize the stages of compaction. Compacted samples were visualized to understand what processing parameters may have affected the microstructural uniformity in a compacted green body and compaction behavior. To evaluate the knitting behavior of the spray-dried granules, the fracture surfaces of the green samples were characterized and evaluated.

3.D. Objective 4: 3-D FESEM Visualization Method

3.D.1. Background: 3-D Micro-Hardness Indentation Method

To fully understand microstructural variations and pore arrangements within green ceramics, visualizing three-dimensional green microstructures was necessary. Developing a method to obtain high resolution microstructural images using a FESEM would be beneficial to visualize particle and pore interconnectivity on the micro and macro level of green ceramic materials. To achieve this, a sectioning technique needed to be administered to remove a certain level of material while being able to measure the calculated depth loss in between each layer.

The first thought was using a specific geometry, such as a pyramid or a sphere, to calculate the difference between each layer. Then, micro-hardness indentation became an idea. After the load of indentation is removed, there exists a fixed depth of the indent on the material that if known, can be used to determine the depth loss in between each layer. Vickers indents have a square or pyramid geometry as shown below in Figure 16.
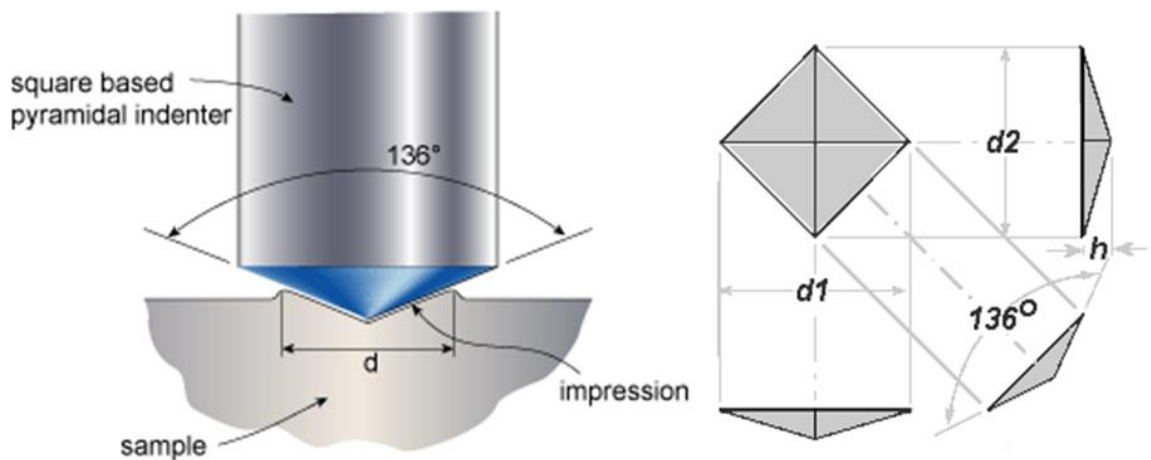
Figure 16. Schematic of a Vickers indentation.

Using the geometry of the indenter tip, the penetrated depth of the indent can be calculated by using the equations below.

$$h = \frac{d}{2\sqrt{2}\tan\left(\frac{136°}{2}\right)} \qquad\qquad 14$$

However, this equation represents the calculated depth of the indent under load, or during the indentation process. Once the load is removed, the material exhibits elastic recovery or relaxation. Therefore, the calculated depth under load is not the true depth of the indentation once the load has been removed. This phenomenon is shown below in Figure 17. A diagram of a loading and unloading curve during indentation is shown below in Figure 18, portraying the unloaded depth of the indent after the relaxation of the material [90].
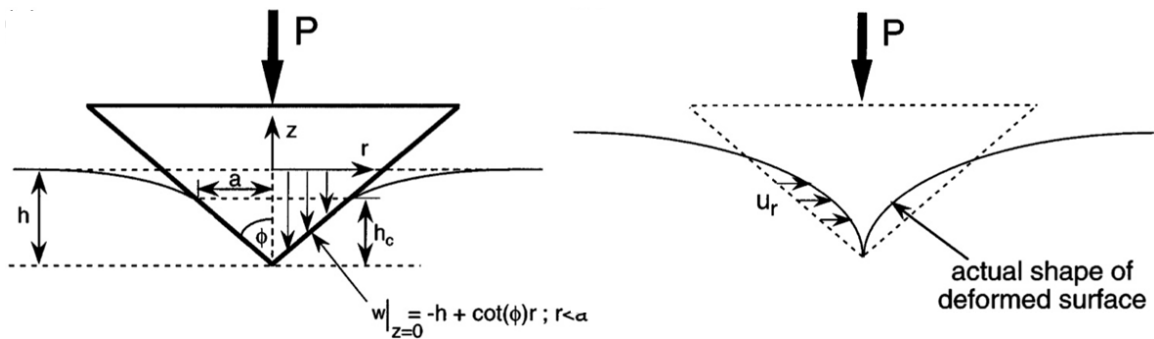
Figure 17. Schematic of material relaxation and elastic recovery [90].
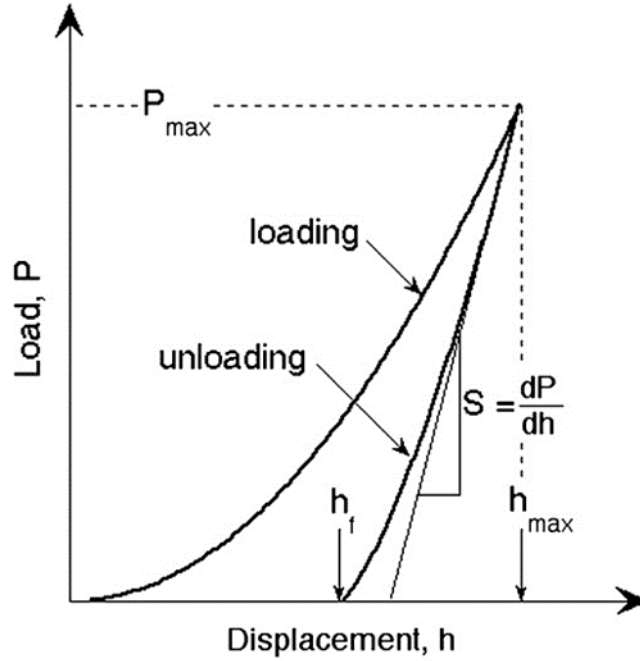
Figure 18. Schematic of loading and unloading curve during indentation [90].

Oliver and Pharr [91] developed a relationship between the indentation load *P* and the indenter penetration depth *h* by the indentation contact stiffness *S* = *dP/dh*, or evaluating the unloading curve. This relationship involved evaluating and calculating the projected contact area of the indent *A* and the elastic constants of the material, the elastic modulus *E* and Poisson's ratio *v* of the material. The corrected depth can be calculated by the equation below [91].

$$S = \frac{dP}{dh} = \frac{2}{\sqrt{\pi}} \frac{E}{(1 - v^2)} \sqrt{A}$$

15

Many researchers have improved upon this relationship and have attempted to correct for this calculation by using instrumentation to monitor the loading and unloading curve during the indentation process [90, 92, 93]. It has been stated that this equation can be used for any indenter size. Hay *et al.* [90] used finite element and analytical results to

propose corrections to this equation that incorporate the angle of the indenter and Poisson's ratio of the half included angle of the indenter. This equation can be re-written with the correction factor β

$$S = \frac{dP}{dh} = \beta \frac{2}{\sqrt{\pi}} \frac{E}{(1 - v^2)} \sqrt{A} \tag{16}$$

where β is equal to

$$\beta = \pi \frac{\left[\frac{\pi}{4} + 0.1548 \cot \theta \frac{(1 - 2v)}{4(1 - v)}\right]}{\left[\frac{\pi}{4} - 0.8312 \cot \theta \frac{(1 - 2v)}{4(1 - v)}\right]^2} \tag{17}$$

and θ is the half included angle of the indenter, which, for Berkovich indents equals 70.32° and for Vickers indents equals 68°. Oliver and Pharr [93] used improved testing equipment and advanced understanding of the elastic and plastic contact mechanics to re-write the stiffness correction equation with the effective elastic modulus as follows

$$S = \frac{dP}{dh} = \beta \frac{2}{\sqrt{\pi}} E_{eff} \sqrt{A} \tag{18}$$

E_{eff} is defined by

$$\frac{1}{E_{eff}} = \frac{1 - v^2}{E} + \frac{1 - v_i^2}{E_i} \tag{19}$$

where E and v are the elastic constants of the sample, elastic modulus and Poisson's ratio respectively, and E_i and v_i are the elastic constants of the indenter. The effective modulus takes into account the fact that elastic displacements occur in both the tested sample, and the indenter tip [92, 93].

These equations with a gained understanding of the mechanics involved during indentation can allow the user to more accurately calculate the hardness value of the

material by the shape and stiffness correction equations. However, this allows one to measure the depth of the indent after the load has been removed. If one were to section a portion of a material away, these equations would not assist in calculating the depth loss. Using an instrument to accurately measure the change in height of the indent, or the depth loss, between each layer was the most ideal path forward. A Keyence VKX-1050 confocal laser scanning microscope was the instrument used for this method. This microscope has a lateral resolution of 5 nm and z-measurement accuracy determined by the equation below, where L is the measured depth in microns.

$$\frac{0.2 + L}{100 \ \mu m} \qquad\qquad 20$$

Therefore, a height of 50 µm would have an accuracy of +/- 0.5 µm. In order to image the same area of the sample on the FESEM, the indents acted as registration marks during the process.

3.D.2. 3-D Layering Method via Conventional Mechanical Polishing

A three-dimensional destructive layering technique to obtain microstructural images using the FESEM was developed. This method dealt with using a destructive polishing method to calculate the depth of the polishing layer lost (z-displacement between layers). The geometry of Vickers micro-indents was used along with a target holder with 20 µm precision while mechanical polishing the compacted samples to cross correlate the accuracy of the layer polished off. Vickers indents were placed using a Buehler Wilson VH3300 (Buehler, Lake Bluff, IL). The depth of the indents was measured using a Keyence VK-X1050 confocal laser scanning microscope (Keyence Corporation, Osaka, Japan).

To do this, a registration material was needed to accurately place indents around the sample. This registration material needed to have a similar hardness and polishing

behavior of the green compacted alumina to not cause artifacts on the surface of the sample, such as pullouts.

3.D.3. 3-D Compact Infiltration and Preparation

The compacted alumina samples and the registration material were prepared for mechanical polishing and microstructural characterization by infiltration using Spurr Low Viscosity Kit (Electron Microscopy Sciences, Hatfield, PA) epoxy resin. After the polishing process was completed, Vickers indents were placed around the sample on the registration material's surface. At this point, the polished samples were imaged on the FESEM. Once microstructural characterization was completed, another polishing procedure was implemented to take layers off the sample's surface, ensuring that no excessive breakage occurred during polishing. This process was repeated for multiple layers of four compacted samples of various processing parameters. These samples included a PAA compact (acrylic emulsion binder), a PVA compact, a PVA sample compacted at 6.0% moisture, all three with 3.0 wt. % organic binder spray-dried at 250 cP and 50 wt. % solids loading. The fourth sample was a PVA compact processed with 5.0 wt. % organic binder, spray-dried at 400 cP and 50 wt. % solids loading. The uniaxial compaction pressure for all samples was 175 MPa. These four samples were evaluated in attempt to visualize the microstructure and pore arrangements between two different binder systems, two different organic binder amounts, and moisture used as a plasticizer to visualize possible density gradient formations.

3.D.4. 3-D Microstructural Characterization

In between each polishing layer, microstructure images using the FESEM were taken. The registration material and indents were used to find the same microstructural area

of the compacts with ease. The FESEM's stage navigation system was used to know the x and y displacement values in between each image taken. The samples were prepared by using conductive materials to mitigate charging.

3.D.5. 3-D Microstructural Reconstruction and Analysis

After obtaining two-dimensional FESEM images, FEI's Avizo, a three-dimensional reconstruction software, was used to obtain three-dimensional images of dry-pressed alumina (FEI Houston Inc., Hillsboro, OR). Images were stitched and layered by displacement measurements from the laser microscope to form a framework of high-resolution three-dimensional FESEM images of a compacted green alumina microstructure. Layers of 5 – 10 µm were determined to be the maximum layered thickness to account for the visualization needed to gather all the information for particle and pore interconnectivity of the green alumina compact.

3.E. Objective 5: Relating Processing Parameters to Visualization Results

This objective dealt with quantifying the visualization results in terms of the various processing parameters. Understanding the occurrence of various processing phenomena three-dimensionally will aid the understanding of better ceramic processing. For this dissertation, it involved understanding what phenomena during the slurry preparation, spray-drying, and dry-pressing of alumina granules correlated to microstructural uniformity and improved reliability of alumina ceramics. Three-dimensional visualization promoted the understanding of what parameters dictate microstructural uniformity or the formation of density gradients within compacted ceramics. Large intergranular voids, pore networks, and the formation of residual defects were explored to understand what

parameters dictate different microstructural characteristics. Within this objective, the primary task involved contrasting two-dimensional data with three-dimensional data analyses. Density and porosity results were contrasted with conventional methods such as mercury porosimetry and micro X-ray CT. A Micromeritics AutoPore V was the mercury porosimeter used (Micromeritics Instruments Corporation, Norcross, GA) and a Bruker SkyScan 1172 was the micro X-ray CT used for this work (Bruker, Billerica, MA). The spatial resolution information gained with the FESEM 3-D image was compared to the X-ray CT results.

4. OBJECTIVE 1: Spray-Drying and Processing of Granules

4.A. Experimental Procedures

Initially, a dispersant curve was completed to determine the weight percentage of dispersant necessary to obtain the viscosity range of 400 to 100 cP desired for the varying slurries. Figure 19 shows the dispersant curves for the respective slurries. Aqueous alumina slurries were processed by ball milling in one gallon Nalgene containers. Three varying sizes of cylindrical and spherical alumina media were used that consisted of 60% coarse (20 mm diameter), 30% medium (12 - 18 mm diameter), and 10% fine (6 – 8 mm diameter). The alumina media filled up to a third of the Nalgene container volume, another third being attributed to the aqueous slurry, and the final third attributed to air [1]. Table 1 lists the percentages of each material used in its respective slurry and the desired slurry parameters prior to spray-drying.

Two different batches of A16 Almatis alumina powder were used in the aqueous slurries. Light scattering particle size analysis was conducted on the two powders to ensure that the powders had the same particle size prior to processing the slurries using Malvern's MasterSizer 3000. Each powder's particle size is shown in Figure 20. The alumina and deionized water were ball milled initially for sixteen hours with a constant percentage of 0.1 wt. % dispersant based on the alumina solids weight.

After the ball milling process was completed, the aqueous alumina slurries were de-aired in a vacuum desiccator for half an hour. Due to the issue of coagulating the acrylic emulsion binder, after the aqueous alumina slurries were ball milled, small amounts of the binder were added at a time and hand mixed slowly as to not cause coagulation to the aqueous system. Once all of the binder was added to the slurry, it was mixed on a magnetic

stir plate for ten minutes at a low speed of 125 rpm. To keep the process consistent and to not cause a foamy slurry due to excessive ball milling, the PVA and PEG were added after the ball milling process as well. The volume and density of the slurries was used to determine the amount of binder weight to add based on the alumina weight within the slurry. The final amount of dispersant was added along with the binders to drop the viscosity to the desired range prior to spray-drying. The Darvan 821A ammonium polyacrylate dispersant was added to the slurry in a 50/50 volume solution of dispersant and deionized water [94]. The aqueous slurry was then mixed using an IKA-WERKE RW16 Basic (IKA Works Inc., Wilmington, NC) propeller mixer for ten minutes at a speed of 950 rpm.
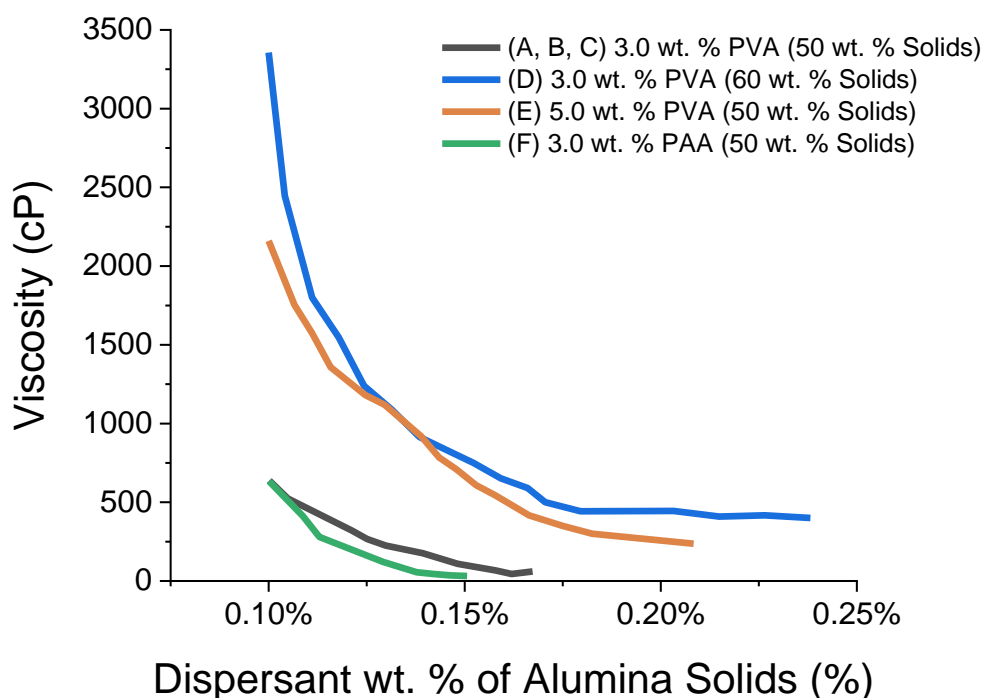
Figure 19. Viscosity response for the four varying alumina slurries with increasing levels of dispersant.

Table 1. Slurry parameters and weight percentages used during the processing of the four
varying types of slurries analyzed for this dissertation.

(A, B, C) 3.0 wt. % PVA (50 wt. % Solids Loading of Al_2O_3)

	A16SG Al_2O_3	Deionized Water	Darvan 821A	PEG	PVA
Wt. %	50.00 %	48.45 %	0.05 %	0.50 %	1.00 %
Vol. %	31.64 %	66.53 %	0.06 %	0.61 %	1.16 %
Wt. % of Al_2O_3	100.0 %	96.88 %	0.10 %	1.00 %	2.00 %

(D) 3.0 wt. % PVA (60 wt. % Solids Loading of Al_2O_3)

	A16SG Al_2O_3	Deionized Water	Darvan 821A	PEG	PVA
Wt. %	60.00 %	38.13 %	0.06 %	0.60 %	1.20 %
Vol. %	41.04 %	56.59 %	0.08 %	0.80 %	1.50 %
Wt. % of Al_2O_3	100.0 %	63.55 %	0.10 %	1.00 %	2.00 %

(E) 5.0 wt. % PVA (50 wt. % Solids Loading of Al_2O_3)

	A16SG Al_2O_3	Deionized Water	Darvan 821A	PEG	PVA
Wt. %	50.00 %	47.45 %	0.05 %	0.83 %	1.67 %
Vol. %	31.71 %	65.28 %	0.06 %	1.02 %	1.93 %
Wt. % of Al_2O_3	100.0 %	94.88 %	0.10 %	1.67 %	3.33 %

(F) 3.0 wt. % Acrylic (PAA) (50 wt. % Solids Loading of Al_2O_3)

	Al_2O_3	Water	Darvan 821A	B-1000	B-1022	Triton X-405
Wt. %	50.00 %	48.43 %	0.05 %	1.00 %	0.50 %	0.02 %
Vol. %	31.59 %	66.40 %	0.06 %	1.28 %	0.65 %	0.02 %
Wt. % of Al_2O_3	100.0 %	96.85 %	0.10 %	2.00 %	1.00 %	0.03 %

Alumina slurries were characterized by specific gravity and viscosity within two
hours after ball milling was completed. After adding the final dispersant amount, the
slurries were let sit for ten minutes prior to characterization. Viscosity values were tested
using a viscometer (Brookfield - LVDV1M). This test was held to an accuracy of +/- 25
cP. All of the slurries were pre-sheared with a propeller mixer at a speed of 200 rpm for
one minute. The slurry was then left to sit on the counter for one minute before
characterization. The slurry was the tested with the viscometer at a speed of 20 rpm and an

RV03 spindle size. After testing for one minute on the viscometer, the viscosity value was recorded. The temperature of the slurry was also recorded for every viscosity test measured.
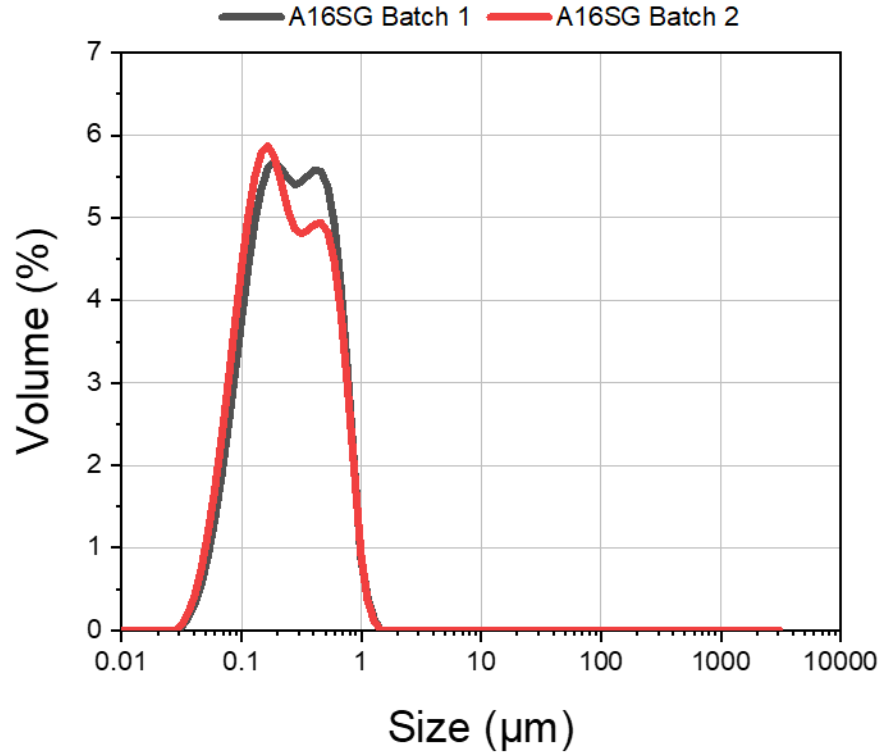
Figure 20. Light scattering particle size analysis of the two batches of Almatis A16SG alumina powder used for this dissertation.

Table 2. Malvern's MasterSizer 3000 light scattering particle size measurements for batches 1 and 2 of Almatis A16SG alumina used in this dissertation followed by the typical values Almatis advertises for their A16SG powder.

Almatis A16SG	D_{10}	D_{50}	D_{90}
Batch 1	0.10	0.27	0.66
Batch 2	0.09	0.24	0.68
Typical (Almatis)	NA	0.50	2.00

After viscosity measurements, specific gravity measurements were conducted using a 25 mL specific gravity bottle and the equation below. An electric thermometer was used to monitor the temperature of water and measurements to an accuracy of +/-0.25°C were used.

$$SG = \frac{Density\ of\ Slurry}{Density\ of\ Water\ at\ 20°C} \qquad 21$$

Light scattering particle size tests for all milled slurries were conducted using Malvern's MasterSizer 3000. An average of five tests per milled slurry were acquired with an absorption index of 0.01, the solvent's (deionized water) refractive index of 1.33, and alumina's refractive index of 1.76. To ensure a well-dispersed suspension, the pH of the system was tested to account for any effects the orientation of the particles had during spray-drying. The pH of each slurry was tested once per liter of slurry using a Fisher Scientific Accumet Basic AB15 pH meter. This pH meter was calibrated for each day of use. Also, analysis using a Labman TIDAS automated FOG gauge was administered. The two varying solids loading slurries were analyzed to visualize the dispersed state of the two slurries after processing using a FOG gauge groove range from 0 to 25 μm. Three tests were conducted for each of the two varying solids loading slurries at 50 and 60 wt. % alumina. The dispersant concentration was kept constant at 0.10 wt. % on the alumina solids loading weight. This was to evaluate the ball milling process at the same parameters used during the processing for all of the slurries.

Alumina slurries were pumped into a mixed-flow fountain nozzle within a laboratory minor plant, a Niro Atomizer, spray-dryer. An image and schematic of the spray-dryer is shown in Figure 21. A dual three roll peristaltic pump was the primary pump used for feeding the slurry into the drying chamber of the spray-dryer. A dual pump system

was used to reduce the pulsation of the slurry entering the drying chamber from the peristaltic pump by altering the two pump heads. Alumina slurries were spray-dried with a drying temperature of 150˚C. The atomization air pressure was kept constant at 1.5 Bar. The peristaltic pump speed was kept at a constant speed of 35 rpm, which relates to the alumina slurries pumping at a rate of around four liters per hour. Deionized water was pumped into the drying chamber once the spray-dryer reached operating temperature. Water was pumped for five minutes before beginning the spray-drying process. Once the five minutes were over, the peristaltic pump's tube was removed from the deionized water until the water was completely pumped through the nozzle.

The alumina slurries were then pumped and spray-dried. There was a 250 μm inline filter placed on the inlet tube of the spray-dryer nozzle to diminish the occurrence of any coagulation or agglomeration during the pumping of the slurry. This filter size was used based on previous research experience that used the same spray dryer, in attempt to diminish agglomeration during the pumping process. Inline filters smaller in size resulted in clogging of the pump line and inefficient processing times [2, 3].

The slurries were mixed at a low speed on a magnetic stir plate during the spray-drying process and this speed was kept constant for all slurries used in this study. Spray-dried granules were obtained in glass jars below the drying chamber (coarse granules) and the cyclone (fine granules) as shown in Figure 21. Once the glass jars became filled, the jars were sealed, covered with paraffin film, and then replaced on the spray-dryer. Each processing parameter was spray-dried on the same day, cleaning the spray-dryer, nozzle, and cyclone thoroughly before the next processing parameter was processed later. This was to ensure no contamination of the obtained granules occurred.
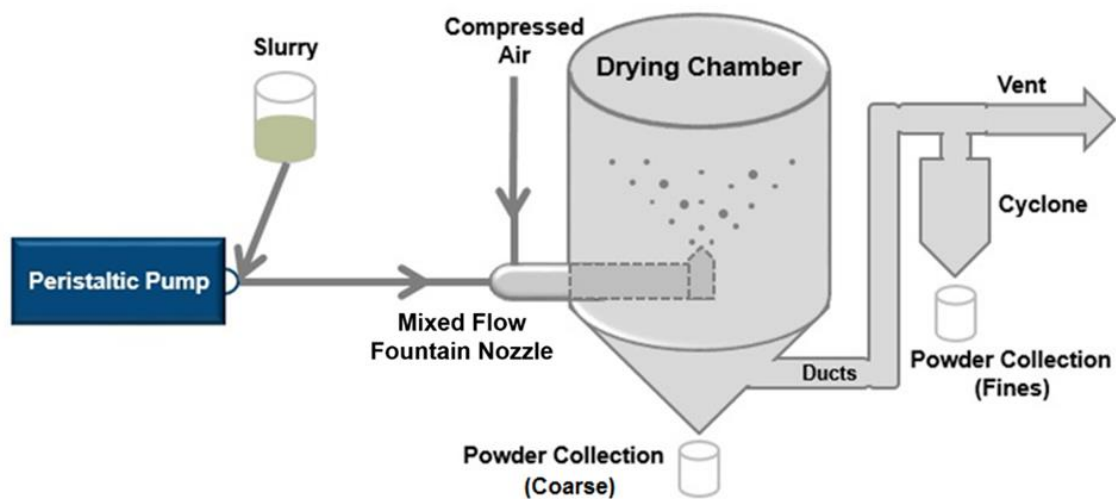
Figure 21. (Top) Schematic drawing of the Niro Atomizer Laboratory Minor Plant and (Bottom) the actual Niro Atomizer used for this dissertation.

4.B. Results and Discussion

  The light scattering particle size data for all of the processed slurries is shown below in Figure 22 and Table 3. Two slurries were processed for each of the varying process parameters. The values shown below are an average of two tests administered to each liter of slurry. Each test conducted was an average of five analyses, therefore, the values shown are an average of all ten tests conducted for each varied process parameter.

  The slurries processed with PVA (A – E) showed similar d_{value} measurements, therefore, the assumption was made that the grinded particle size was uniform for all of the processed slurries. The slurries processed with an acrylic emulsion binder (F) had d_{values} that shifted to the coarser end. The assumption made for this behavior was likely due to a possible degree of coagulation that occurred during the testing when adding the slurries into the instrument.

  The slurry characteristics prior to conducting the spray-drying process are shown in Table 4. The values shown are an average of two tests across the two liters of slurries processed for this dissertation. The specific gravity for all of the slurries processed at 50 wt. % solids loading of alumina (A – C, E – F) returned similar values around of 1.60. The temperature of the water used for the calculations from equation 21 averaged 19.0 ˚C ± 0.3 over ten tests. These values were measured using a digital thermometer with an accuracy of ± 1.0 ˚C and were deemed within the acceptable range for this analysis.

  The viscosity values were all within the desired range of ± 25 cP. The list of viscosity values included: 100 cP (A), 250 cP (B), and 400 cP (C) for 3.0 wt. % PVA and a solids loading of 50 wt. % alumina; 400 cP for 3.0 wt. % PVA and a solids loading of 60 wt. % alumina (D); 250 cP for 5.0 wt. % PVA and a solids loading of 50 wt. % alumina

(E); and 250 cP for 3.0 wt. % of the acrylic emulsion binder and a solids loading of 50 wt.

% (F). The temperatures of each of the tested slurries varied from 21 - 24 ˚C. These

temperatures were all measured during the viscosity measurement prior to spray-drying.

The temperatures were within the desired range of room temperature, 20 – 25 ˚C. It was

attributed that the temperature variation was not significant enough to vary the viscosities

out of the desired range of ± 25 cP and was considered negligible.
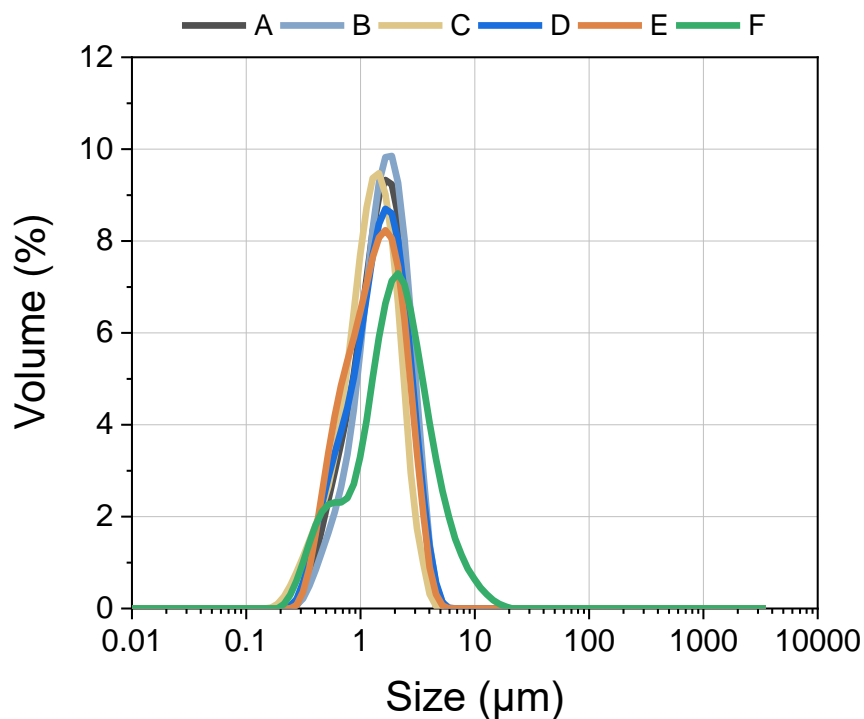
Figure 22. Light scattering particle size data acquired at an absorption index of 0.01 and a
refractive index of alumina at 1.76 for all six varying slurries evaluated. Values
shown are for an average of ten tests across two liters per varying slurry.

Table 3. Particle size analysis comparing the d_{values} for all six varying slurries evaluated. Values shown are an average of ten tests across two liters for each.

Slurry	D_{10}	D_{50}	D_{90}
A – Average	0.73 ± 0.17	1.59 ± 0.21	2.94 ± 0.16
B – Average	0.80 ± 0.13	1.72 ± 0.14	3.14 ± 0.29
C – Average	0.63 ± 0.29	1.32 ± 0.09	2.50 ± 0.44
D – Average	0.66 ± 0.16	1.54 ± 0.23	2.99 ± 0.18
E – Average	0.65 ± 0.14	1.43 ± 0.31	2.85 ± 0.29
F – Average	0.61 ± 0.02	2.08 ± 0.04	5.19 ± 0.26

Table 4. Slurry characteristics for all of the six varying slurries evaluated prior to spray drying. Values shown are an average of two tests, one test per liter of slurry. The temperature values pertain to the temperature during the viscosity measurement.

Slurry	Specific Gravity	pH	Viscosity (cP)	Temperature (˚C)
A	1.59 ± 0.00	9.26 ± 0.01	104.30 ± 14.89	23.60 ± 0.64
B	1.60 ± 0.01	8.97 ± 0.04	248.70 ± 4.31	22.70 ± 0.42
C	1.58 ± 0.00	8.75 ± 0.15	402.40 ± 30.83	21.40 ± 0.50
D	1.79 ± 0.01	8.80 ± 0.06	404.60 ± 6.01	24.30 ± 0.21
E	1.61 ± 0.02	8.40 ± 0.04	255.20 ± 26.09	21.90 ± 0.78
F	1.60 ± 0.01	9.08 ± 0.00	234.60 ± 4.95	22.20 ± 1.06

Figure 23 below shows the relationship of the pH measurements versus the measured viscosity. The trend for all of the slurries at 3.0 wt. % binder exhibits a downward trend which was to be expected. The outlier of the six tested slurries was shown in the slurries processed at a solids loading of 50 wt. % alumina and the highest binder amount of 5.0 wt. % PVA. The reason behind this was attributed to the pH of the Sekisui PVA used, which based on the MSDS was close to a value of 6.0.
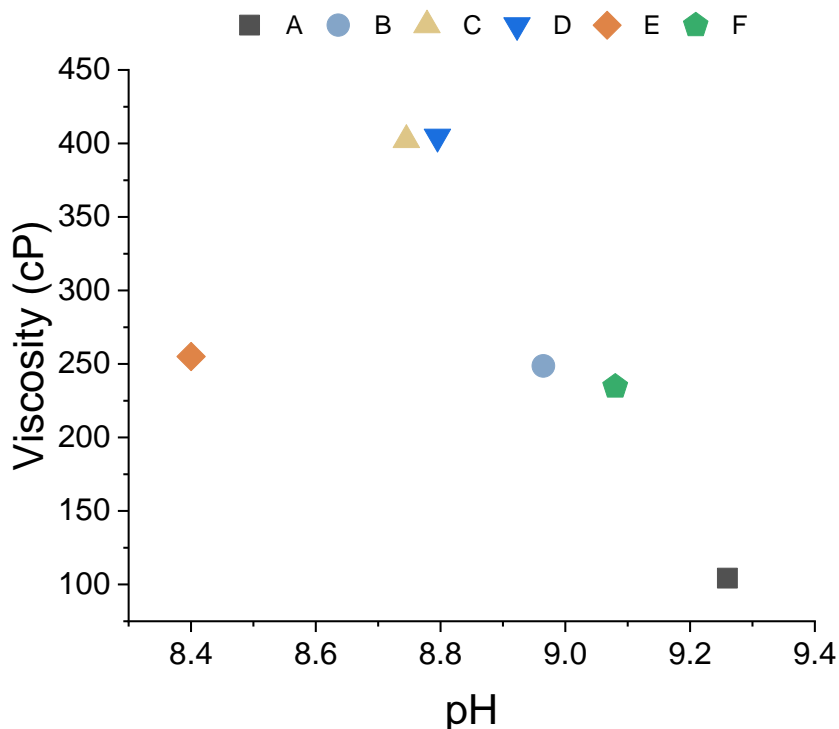
Figure 23. pH vs. viscosity relationship for all six varying slurries tested.

The degree of dispersion for the processed slurries was evaluated using a Labman TIDAS instrument. Two slurries were processed using the same ball milling procedure, one at a solids loading of 50 wt. % and the other at 60 wt. % alumina. The slurries were removed off the ball mill and the particle size and the fineness of grind gauge (FOG) analyses were conducted concurrently. The particle size distribution obtained from the MasterSizer is shown below in Figure 24 and the d_{values} are shown in Table 5. The distribution is similar to what was observed in Figure 22 and Table 3. Particle size analysis comparing the d_{values} for all six varying slurries evaluated. Values shown are an average of ten tests across two liters for each.. These results were compared to the information observed from the TIDAS unit, shown below in Figure 25. The histograms shown are from one of the three tests conducted for each solids loading slurry. This histogram was the

closest representation for the average of the three tests calculated. The average number of

agglomerates for the three tests are highlighted in Figure 26 for both of the solids loading

slurries evaluated.
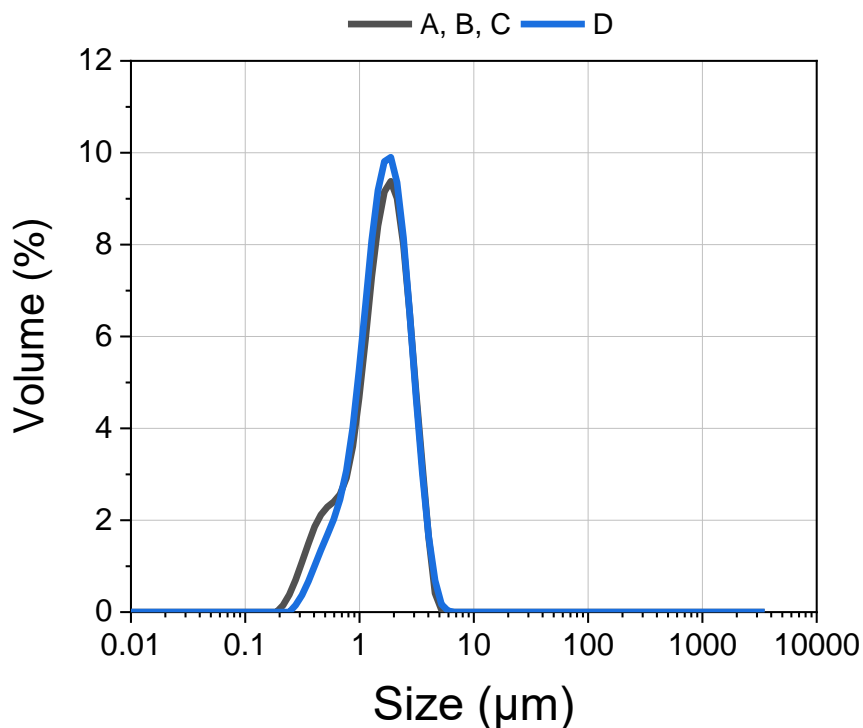
Figure 24. Light scattering particle size data acquired at an absorption index of 0.01 and a refractive index of alumina at 1.76 for the two solids loading slurries that were evaluated on the Labman TIDAS equipment. Values shown are for an average of five tests per slurry.

Table 5. Particle size analysis comparing the dvalues for the two solids loading slurries evaluated on the Labman TIDAS equipment. The values shown are for an average of five tests per slurry.

Slurry	D_{10}	D_{50}	D_{90}
A, B, C (50 wt. % Al_2O_3)	0.59 ± 0.05	1.70 ± 0.12	3.13 ± 0.21
D (60 wt. % Al_2O_3)	0.78 ± 0.08	1.74 ± 0.12	3.15 ± 0.20
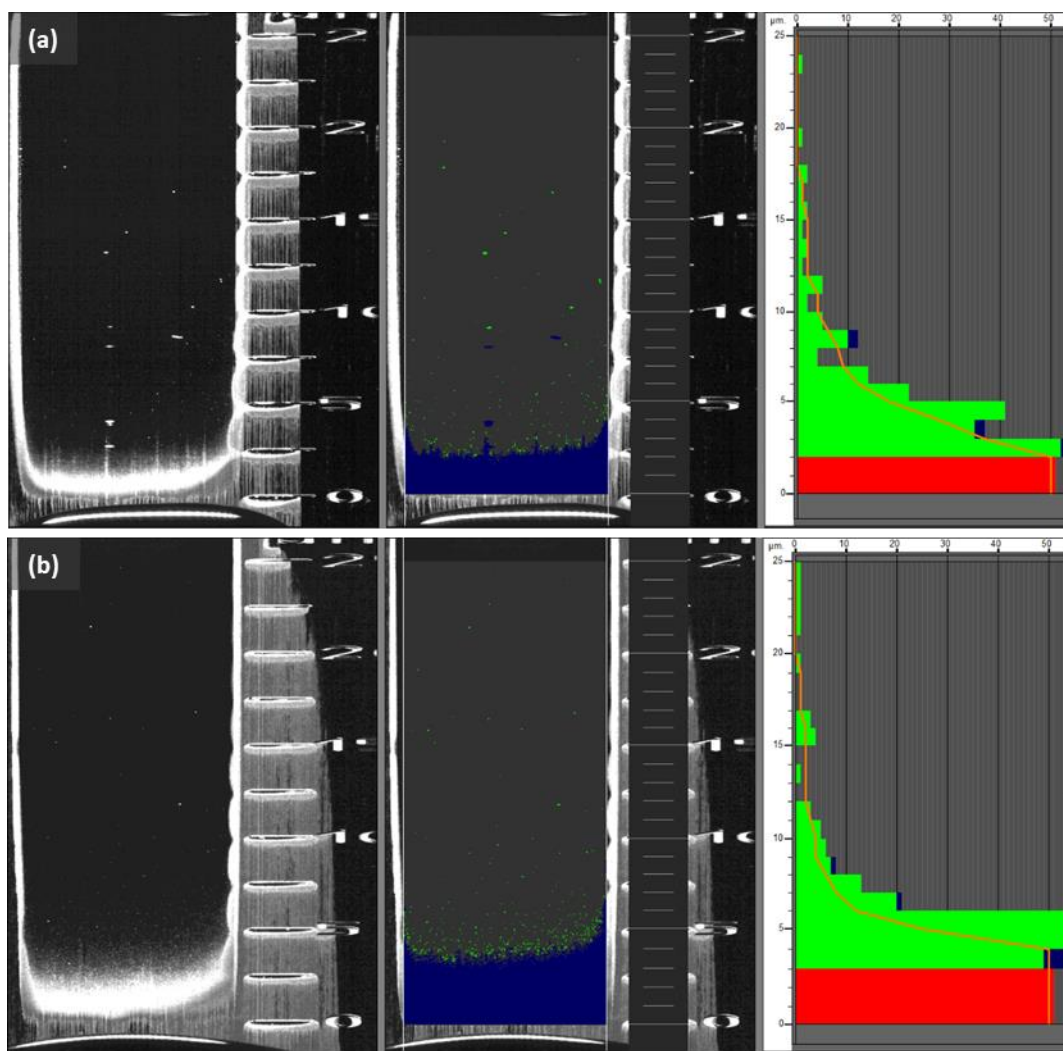
Figure 25. One test out of the three evaluated for each of the solids loading slurries using the Labman TIDAS instrument showcasing the histogram observed for each slurry (a) 50 wt. % and (b) 60 wt. %.

The information gained from the TIDAS analysis, or degree of agglomeration shown in Figure 26, shows a broader agglomerate distribution for the 50 wt. % alumina slurry when compared to the narrower distribution shown in the 60 wt. % slurry. Although the degree of agglomeration based on the number of agglomerates is mostly under 10 μm

for both cases, the broader distribution for the 50 wt. % slurry resulted in the highest degree of dispersion between the two cases evaluated. This is likely due to the higher solids loading of alumina particles within the suspension causing an increase in agglomeration or could be due to the processing conditions for both cases.
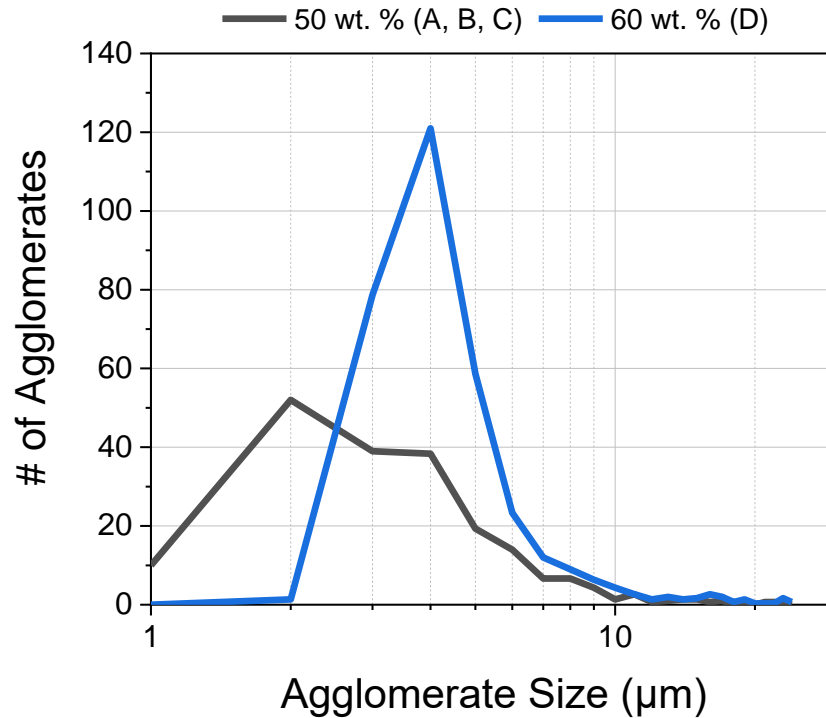
Figure 26. Labman TIDAS distribution for the varying solids loading slurries of 50 and 60 wt. %. The values shown are an average of three tests per slurry.

As discussed in Alazzawi *et al.* [95], Alazzawi investigated the capabilities of TIDAS analysis on a tape casted and stereolithography suspension. It was concluded that the TIDAS analysis can highlight and distinguish the degree of agglomeration in commercial suspensions for various processes. The results can be related to the processing conditions over various types of suspensions. For the results mentioned in this dissertation, the degree of agglomeration can be related to the dispersion state of the system prior to

processing and spray-drying of the alumina slurries. Comparing the various cases mentioned gained insight into the effect the solids loading had on the degree of agglomeration within the suspension prior to spray-drying.

4.C. Summary

This objective dealt with spray-drying alumina slurries at various slurry parameters. The slurry parameters that were varied included the viscosity and solids loading of the alumina suspensions as well as the organic binder type and amount of binder within the alumina suspensions. All measured slurry characteristics were kept within a certain accepted range. The milled particle size was attempted to be kept uniform across all of the six varying alumina slurries, highlighted in Table 1. The dispersed state for all of the suspensions was assumed to be well-dispersed based off of the TIDAS information observed and the constant ball milling process. The only variation was attributed to the effect the solids loading had on its representative number of measured agglomerates within the suspension. This was categorized as the effect solids loading had on the processing of the alumina slurries and the resultant spray-dried granules. The TIDAS data analyses were used as a visualization tool to visualize the degree of dispersion as a function of the alumina solids loading. The other major task of this objective centered on processing the alumina slurries at the specified slurry parameters to establish a fundamental relationship between the experimental results during the compaction analysis and microstructural visualization results of their resultant microstructures.

The viscosities of the alumina slurries were compared at values of 100, 250, and 400 cP for slurries with the same solids loading of alumina, binder type and amount of

PVA. These alumina slurries processed the spray-dried granules A through C respectively. The solids loading of the alumina slurries were compared at weight percentage values of 50.0 and 60.0 wt. %. for slurries with the same viscosity measurement of 400 cP and the PVA binder. These alumina slurries processed the spray-dried granules C and D respectively. The binder amount was compared at weight percentage values of 3.0 and 5.0 wt. % PVA binder based on the alumina solids weight. These slurries were processed with the same viscosity value of 250 cP and a solids loading of 50.0 wt. %. These alumina slurries processed the spray-dried granules B (3.0 wt. %) and E (5.0 wt. %). The binder type was the final slurry parameter altered and the PVA binder and acrylic emulsion binder were compared. These alumina slurries were processed with the same binder amount based off of the alumina solids weight, 3.0 wt. %, and were spray-dried at the same viscosity value of 250 cP and 50.0 wt. % solids loading. These alumina slurries processed the spray-dried granules B (PVA) and F (acrylic emulsion).

Varying the mentioned processing parameters during spray-drying was the initial step in developing a relationship between visualization and experimental results as a function of processing parameters. Determining what roles to vary and compare was essential in developing a relationship on what process parameters promote microstructural uniformity. Comparing the developed results to the compaction analysis and microstructural characterization of the processed alumina was necessary in continuing to develop this relationship.

5. OBJECTIVE 2: Compaction Behavior of Spray-Dried Granules

5.A. Experimental Procedures

Once the spray-drying process was completed, the spray-dried granules were characterized. Initially, the granule's moisture content was tested to understand the as-received moisture content from the spray-dryer. The moisture content was calculated by weight loss using the Arizona Instruments Computrak 2000 system, by heating up the granules to 115˚C and dwelling for 15 minutes. The granules should not exceed 115˚C due to the PVA binder starting to degrade at temperatures above 115˚C, therefore any weight loss during the test was accounted purely as moisture.

The size distribution of the generated granules was characterized next. This task required using a RO-TAP (W. S. Tyler, Mentor, OH) sieve shaker to sieve the spray-dried granules into varying sieve sizes. For this analysis, only the coarse as-received granules were analyzed, the fine granules received from the cyclone from the spray-dryer were discarded The sieve sizes used in this analysis are shown in Table 6. The cumulative mass percent finer (CMPF) was calculated for the sieve sizes used in this dissertation. This was to compare how the slurry characteristics had an effect on the generated granules sizes obtained during spray-drying.

Table 6. Sieve sizes used for the granule characterizations conducted in this dissertation.

U.S. Mesh Sieve Size	Micron Size (μm)
-100 Mesh	150 μm
+140 Mesh	106 μm
+170 Mesh	90 μm
+200 Mesh	75 μm
+230 Mesh	63 μm
+270 Mesh	53 μm
+325 Mesh	45 μm

Spray-dried granules were added into a 25 mL graduated cylinder to the maximum volume line. The dry weight of the graduated cylinder was taken to correct for the weight of the spray-dried granules added. The granules were added with the use of a funnel to ensure that there were no granules adhered to the wall of the graduated cylinder, altering the measured weight. The graduated cylinder was weighed containing the spray-dried granules at 25 mL of volume. The graduated cylinder was then placed on a vibrating table and the spray-dried granules were tapped for approximately 10 seconds. The final volume of the tapped spray-dried granules was taken. The granule weight and the final tapped volume were used in the equation below to calculate the tap density of the spray-dried granules based on the theoretical density of alumina ($\rho_{th} = 3.95$ gram/cm^3) for each of the various processing parameters. This test was repeated five times for each of the six varying spray-dried granules.

$$\rho_{tapped} = \frac{W}{V_T \times \rho_{th}} \times 100 \qquad\qquad 22$$

Carr's Index and Hausner Ratio were also calculated for the comparison amongst the varying six spray-dried granules. These equations are shown below equations in 23 and 24 respectively where V_B is the bulk volume, ρ_B is the bulk density, ρ_T is the tapped density, and V_T is the tapped volume of the spray-dried granules [54].

$$C = 100 \times \frac{V_B - V_T}{V_B} \qquad\qquad 23$$

$$H = \frac{\rho_B}{\rho_T} \qquad\qquad 24$$

The organic binder content was examined to correlate if the weight percentage of the organic binder added to the aqueous alumina slurry was the organic binder content

received within the generated spray-dried granules. The equipment used for this analysis was a TA Instruments DSC/TGA Q600. Spray-dried granules obtained from each processing parameter were added into an alumina crucible at a weight range between 15 to 20 mg. The granules were then heated up to 115˚C at a ramp of 50˚C per minute. The granules were dwelled at that temperature for 15 minutes to remove any moisture prior to the organic binder weight analysis. Then the program began to accept data from the Q600 and the granules were heated up to 700˚C at a rate of 3 ˚C per minute. The granules were dwelled at 700˚C for two hours to ensure all of the organic binder was removed through combustion. Then the granules were cooled down to room temperature. All of this testing occurred at a constant air flow of dry compressed air at 100 mL/min. The weight loss was then calculated from TA Universal Analysis 2000 software obtained from the TGA.

The size and shape of all six varying spray-dried granules was evaluated using a Keyence VHX-5000 optical microscope. The diameter and circularity for each varying granule was measured at a magnification of 500X. The spray-dried granules were adhered on carbon tape placed on an SEM stud to be able to distinguish the contrast difference between the black carbon tape and white alumina spray-dried granules. During the evaluation, the granules that were on the edge of the screen were removed from the image and any granules that appeared to be overlapping each other were separated. Five images were taken per varying spray-dried granule. The first 150 granules per varying granule were analyzed and an average value of circularity and diameter was calculated using the Keyence measurement software. The software uses the brightness of the image as a reference, then the granules are segmented from the background. Using the two-dimensional brightness pixel intensity, the segmented pixels are calculated based on the

pixel size per micron. The circularity of the granules is calculated as a ratio between the maximum and minimum diameter calculated per individual granule.

Compaction testing was conducted using a specific ratio of sieve sizes. This was to account for any variation granule size may cause on the compaction behavior of the alumina granules. The specific granule sieve sizes used for the compaction testing are shown in Table 6, using a 1:1 wt. ratio of all sieve sizes involved, not including granules +100 Mesh and -325 Mesh.

Compaction tests were conducted using a compaction die and an Instron universal mechanical tester. An 8.5 mm diameter uniaxial compaction die was used for all of the compaction testing for this thesis. A diagram of this compaction die is shown in Figure 27. Each test was compacted at a rate of 0.5 mm/min and the data acquisition rate was set to obtain data at every 2 N. The compaction die's walls and punches were cleaned with ethanol and coated in WD-40 as a lubricant prior to every test (WD-40 Company, San Diego, CA). A funnel was used to load the granules into the die to ensure to granules were not caked on the die wall during the test. Table 7 lists the spray-dried granules, processing parameters prior to spray-drying, and the moisture contents prior to each compaction test. A constant loading weight of the spray-dried granules was used for each compaction test to keep the thickness to diameter ratio (T/D) constant at 0.26 [78]. This weight was corrected for any of the granules that contained moisture prior to compaction, being respective to the weight of the granules at zero percent moisture. All of the granules were sealed in Nalgene containers with a paraffin film and placed in a desiccator when not being used. An average of three compaction tests was calculated for each of the varying spray-dried granules. Data points were acquired at every 2 N of force during the compaction run.

This was to ensure that taking the averages for three compaction runs for granules A through J was possible, as the calculated pressures per run would be similar, and the respective theoretical density calculation would be able to be compared and averaged for all three runs per granule.

Moisture was added by placing a thin layer of granules, roughly 100 grams, in an eight-inch sieve pan. These pans were added to an Associated Environmental Systems LH-1.5 humidity test chamber (Associated Environmental Systems, Acton, MA). Distilled water was used in the humidity chamber's tank. The humidity chamber controlled the temperature and relative humidity level within the chamber that were set to 25 ˚C and 95% respectively. Inside the chamber, there were three shelves and one pan was placed on each shelf.

After 30 to 60 minutes, the granules in each pan were tested. The moisture content was calculated by weight loss using an Arizona Instruments Computrak 2000 system, by heating up the granules to 115˚C and dwelling for 15 minutes. The moisture content was kept to an accuracy of ± 0.25 percent of the desired moisture value. If the granules fell within this range, they were removed from the humidity chamber and placed in a Nalgene container. These Nalgene containers were sealed with paraffin film and placed in a desiccator until they were needed. The moisture content was allowed to equilibrate by leaving the granules in their respective Nalgene containers for one week prior to being used. This was to ensure that any large variation in moisture content of the granules equilibrated before being used. The moisture content was re-evaluated before, during, and after compaction. Three moisture tests were conducted for each of the granules containing

moisture prior to compaction. Any granules tested for moisture percentage were discarded and not used during compaction.
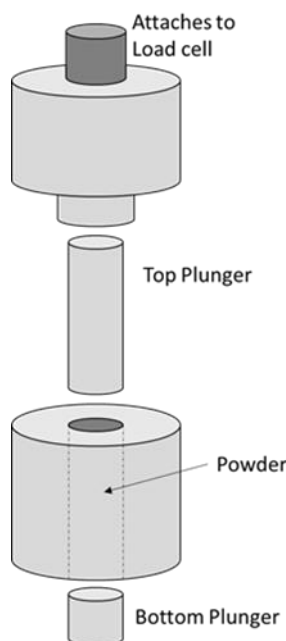
Figure 27. Schematic of the compaction die used for the uniaxial compaction analysis.

Table 7. A list of all ten spray-dried alumina granules evaluated for this research including the spray-drying characteristics (slurry parameters) and compaction parameters.

Granule	Viscosity	Solids (Al_2O_3)	Binder (Al_2O_3 Solids wt.)	Moisture Content
A	100 cP	50.0 wt. %	3.0 wt. % PVA	0.0 %
B	250 cP	50.0 wt. %	3.0 wt. % PVA	0.0 %
C	400 cP	50.0 wt. %	3.0 wt. % PVA	0.0 %
D	400 cP	60.0 wt. %	3.0 wt. % PVA	0.0 %
E	250 cP	50.0 wt. %	5.0 wt. % PVA	0.0 %
F	250 cP	50.0 wt. %	3.0 wt. % Acrylic (PAA)	0.0 %
G	250 cP	50.0 wt. %	3.0 wt. % PVA	2.0 %
H	250 cP	50.0 wt. %	3.0 wt. % PVA	4.0 %
I	250 cP	50.0 wt. %	3.0 wt. % PVA	6.0 %
J	250 cP	50.0 wt. %	3.0 wt. % Acrylic (PAA)	2.0 %

The compaction data was analyzed by the proposed mathematical models by Mort *et al.* [78] using the equations 7 through 12 in section 2.C.5. Initially, compaction runs of

an empty compaction die were conducted up to the high-pressure endpoint, or the maximum compaction pressure of 175 MPa. An average of five runs was calculated. A MATLAB code was used to fit all of the data into the same size data set, as Mort's mathematical models are dependent on the load and displacement values at single points of pressure. The MATLAB code used found the closest load value for each run and matched it up with its respective displacement value. This was to ensure comparison between the empty die compaction runs and the compaction tests for each of the spray-dried granules. Three compaction runs for granules A through J were conducted and their average was calculated by using the MATLAB code to get all of the data sets to the same size, matching the force values to their nearest neighbor for comparison and analysis. Then after calculating the density and pressure, the averages of these values were calculated and used for analysis. The MATLAB code used for is shown below.

```
fload = xlsread('Matlab.xlsx','load','B1:B6214');
fbase = xlsread('Matlab.xlsx','base','B1:B4411');

dload = xlsread('Matlab.xlsx','load','A1:A6214');
dbase = xlsread('Matlab.xlsx','base','A1:A4411');

FIT = bsxfun(@(x,y) abs(x-y), fbase(:), reshape(fload,1,[]));
[Abs, idxload] = min(FIT,[],2);

ForceResult = fload(idxload);
DisplacementResult = dload(idxload);
```

Both of Mort's linear and hybrid springback models were calculated for comparison. The final relative density of the compacts was calculated using the equation below [78].

$$RD = \frac{4W}{\pi d^2 L \rho_{th}}$$

25

where W is the weight of the de-binded compact, d is the diameter of the compact, L is the corrected compact thickness using Mort's springback models, and ρ_{th} is the theoretical density of alumina 3.95 grams/cm^3. The pressure was calculated based on the area of the compaction die. The log scale of the compaction pressure vs. relative density were plotted for each of the varying spray-dried granules.

The critical yield pressure and the joining point of the spray-dried granules were calculated by linear regression. The best fit semi-log equation was calculated tangent to the different stages of compaction in the form of equation 26 below. Each semi-log equation was fit to the data so the minimum correlation coefficient (R^2) was at least 0.985, to ensure empirically a sufficient linear fit was accomplished for each stage of compaction [55].

$$y = A \ln(x) + B$$

$$y = A_{StageI} \ln(x) + B_{StageI}$$

26

$$y = A_{StageII} \ln(x) + B_{StageII}$$

Finding the intersection between the two equations, the critical yield pressure and joining point for each varying spray-dried granule was calculated using equations 27 and 28 below [55].

$$\ln(x) = \left(\frac{B_{StageII} - B_{StageI}}{A_{StageI} - A_{StageII}} \right)$$

27

$$\sigma_{agglomerate} = exp^{\left(\frac{B_{StageII} - B_{StageI}}{A_{StageI} - A_{StageII}} \right)}$$

28

To evaluate the knitting behavior and adhesion characteristics of the granules during dry-pressing, green strength tests were conducted. Acrylic and PVA spray-dried granules were used to evaluate the difference between the two binder systems. The viscosity and solids loading of the slurries prior to spray-drying were kept constant at 20

cP and 50 wt. % (32 vol. %). Green strength as a function of moisture was also evaluated, compacting the PVA granules at a moisture content of dry, 2.0%, 4.0%, and 6.0%. The moisture was kept to an accuracy of ± 0.25% and was tested using the Computrak 2000 moisture analyzer. Acrylic granules were compacted at dry and 2.0%.

Granules were compacted to a specimen size of 6 mm in thickness, 55.0 mm in width, and 101.5 mm in length. This size was kept constant and the weight of the granules prior to compaction was corrected for granules containing moisture. The granule size was kept constant for all granules tested. Compacts were dried in an oven at 110˚C for a half hour. The dimensions and weight were measured after the compact cooled and then the compact was de-binded. Compacts were heated up to a temperature of 650˚C at a rate of 3˚C/min. Compacts were dwelled for 3 hours to ensure all of the binder was burnt off and removed. Compacts were then cooled down to room temperature slowly.

Within sixteen hours after the de-binding process was finished, compacts were placed in a desiccator for 30 minutes. Compacts were weighed and the dimensions were measured prior to testing. Compacts were fractured using the schematic shown in Figure 28, with the bottom span set to 80 mm. Tests were run at a rate of 0.5 mm/min. The force at break was recorded and the modulus of rupture fracture strength was calculated using the equation below where P is the force at break, L is the distance between the bottom supports, b is the width of the specimen, and d is the thickness. An average of three tests were conducted for the six varying granules tested.

$$MOR = \frac{3PL}{2bd^2}$$
29
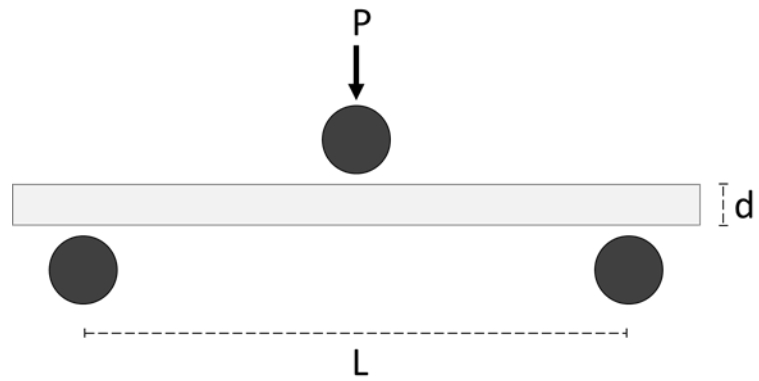
Figure 28. A 3-point modulus of rupture (MOR) schematic.

5.B. Results and Discussion

The initial moisture content measurements for the processed granules are shown in Table 8. The initial moisture of the granules straight from the spray-dryer ranged from 0.31 to 1.02 wt. %. These tests were conducted on the same day of granule processing. The granules were then sieved and exposed to air for a period of time, therefore prior to the tap density measurements, the moisture was removed. Table 9 lists the sieve analysis by weight calculated for each of the varying granules.

Table 8. The initial spray-dried granule moisture content tested on the same day as processing the granules as well as the moisture content tested during the tap density measurements after processing was completed. Values listed are for an average of six tests, one for each of the varying granules.

Granule State	Moisture (wt. %)
Initial (Straight out of the Spray-Dryer)	0.68 % ± 0.23
Prior to Tap Density Calculations	0.00 % ± 0.00

Table 9. Sieve analysis (wt. %) for all varying spray-dried granules.

Sieve Analysis of Spray-Dried Alumina Granules (wt. %)

	A	B	C	D	E	F
+100	14.46 %	42.49 %	21.99 %	28.11 %	12.42 %	19.04 %
+140	6.17 %	31.36 %	31.66 %	17.67 %	47.57 %	24.70 %
+170	10.88 %	8.87 %	12.56 %	8.67 %	8.92 %	11.31 %
+200	2.81 %	3.15 %	5.82 %	9.08 %	1.72 %	8.41 %
+230	1.74 %	5.03 %	7.91 %	6.36 %	2.74 %	9.00 %
+270	2.70 %	4.39 %	7.80 %	16.59 %	10.05 %	8.82 %
+325	61.24 %	4.71 %	12.28 %	13.53 %	16.57 %	18.73 %

A graph displaying the cumulative mass percent finer (CMPF) for each of the various slurry parameters (A – F) is shown in Figure 29. The largest outlier was attributed

to the granules spray-dried at 100 cP and 50 wt. % solids loading (A), exhibiting granule sizes that were 70% finer than 50 µm. This is likely due to the degree of dispersion of the slurries, affecting the droplet formation of the atomized slurries and therefore the droplet size during the process. The most linear trends were exhibited by the slurries processed at 50 wt. % solids loading and 250 cP with 3.0 wt. % acrylic emulsion binders (F). The slurries processed at 50 and 60 wt. % solids loading at a viscosity of 400 cP (C and D) showed a similar trend to the acrylic granules (F). Similar behavior was shown for the slurries spray dried at 250 cP and 50 wt. % solids loading with 3.0 and 5.0 wt. % PVA binder (B and E). However, these granules showed a higher degree of coarser granules when compared to granules the others. Therefore, following the trends observed, it seems the type of binder, degree of solids loading, and viscosity play a significant role in the droplet formation of the atomized slurries and thus the generated spray-dried granule size. This behavior is similar to what researchers have observed. Researchers have correlated the mobility of the solid particles within the ceramic suspension to the formation of droplets and generated spray-dried granule size and morphology [2, 3, 13, 24, 34, 38-42].

The measurements for tap density, binder weight concentration, Carr's compressibility index, and Hausner ratio are compared in Table 10. The tap density values are compared in Figure 31 for granules A through F. The values shown are for the de-binded weight of the alumina granules, and the theoretical density percentages are based on the theoretical density of alumina at 3.95 g/cm^3. The densest granules were exhibited from the F granules, processed with the acrylic emulsion binder. The reason behind this could be due to the acrylic binders being initially in emulsions that break during the drying stage of spray-drying, with the resultant organic species being insoluble. Therefore, binder

migration during the evaporation stage of spray-drying does not occur. Granules A through C showed similar density measurements when compared to each other. As these granules were spray-dried at the same specific gravity but with varying viscosity values, it showed that the viscosity was not a major contributor to the density of the spray-dried granules. Granules D, spray-dried at the higher solids loading of 60 wt. % alumina showed the second highest tap density measurements, slightly higher than granules A through C, but not by a considerable amount. The granules with the lowest density values were the E granules, spray-dried at the higher binder concentration of PVA at 5.0 wt. %. The reason behind this is likely die to the previously stated phenomenon of binder migration producing segregated binder layers and a possibility for the formation of hollow cores when compared to the other cases. Visualizing the cross section of the granules will gain us more qualitative analysis of the internal microstructures of these granules cases.

The binder concentrations were what was expected, granules A through D and F ranged from 2.95 to 3.14 wt. % binder and the E granules were 5.11 wt. % binder. Carr's compressibility index values and Hausner ratios were similar for all of the six varying slurries and proved that the spray-dried granules were free-flowing granules desired for dry-pressing. These values were what was expected for spray-dried agglomerated ceramic powder.

The size and shape of the spray-dried granules were examined using the Keyence optical microscope and the results are shown in Figure 32. Granules were adhered to carbon tape on an SEM stud for analysis. Five images were taken and segmented as shown for granules A through F. Spray-dried granules that were located along the edge of the image were removed for analysis. Using the microscope's measurement software, the circularity

and diameter of the granules were measured and compared. The first 150 granules over the five images taken were evaluated. The measurement software uses the brightness intensity as a reference to extract the segmented size and shape of the granule. Then, from the segmented pixel information and the pixel size, it measures the circularity by taking the maximum and minimum diameter value calculated for each granule. These values are shown in Table 11.
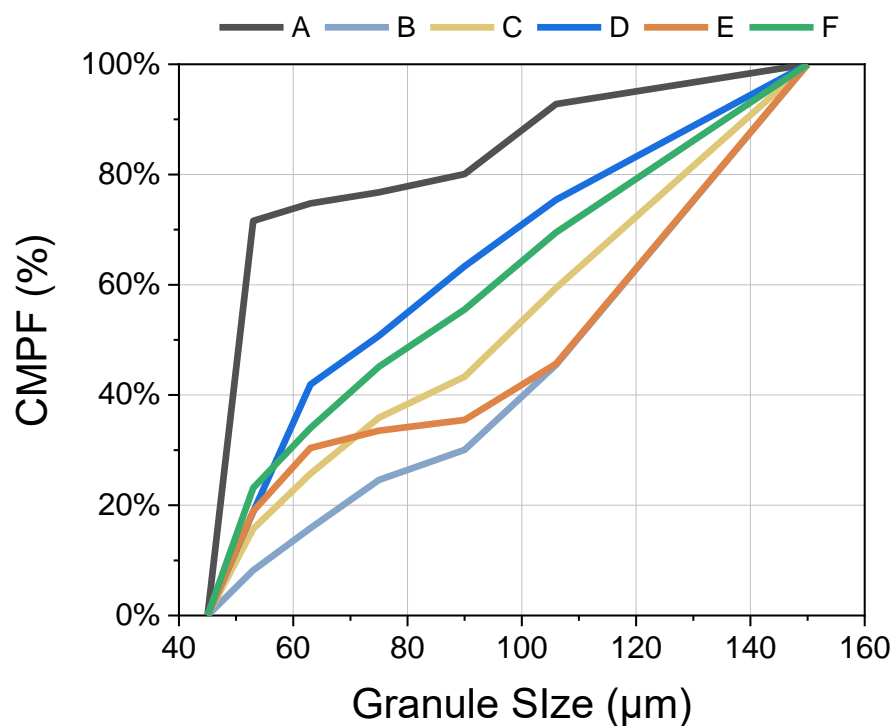
Figure 29. Cumulative mass percent finer (CMPF) displaying the sieve sizes used during this dissertation ranging from 45 – 150 µm.
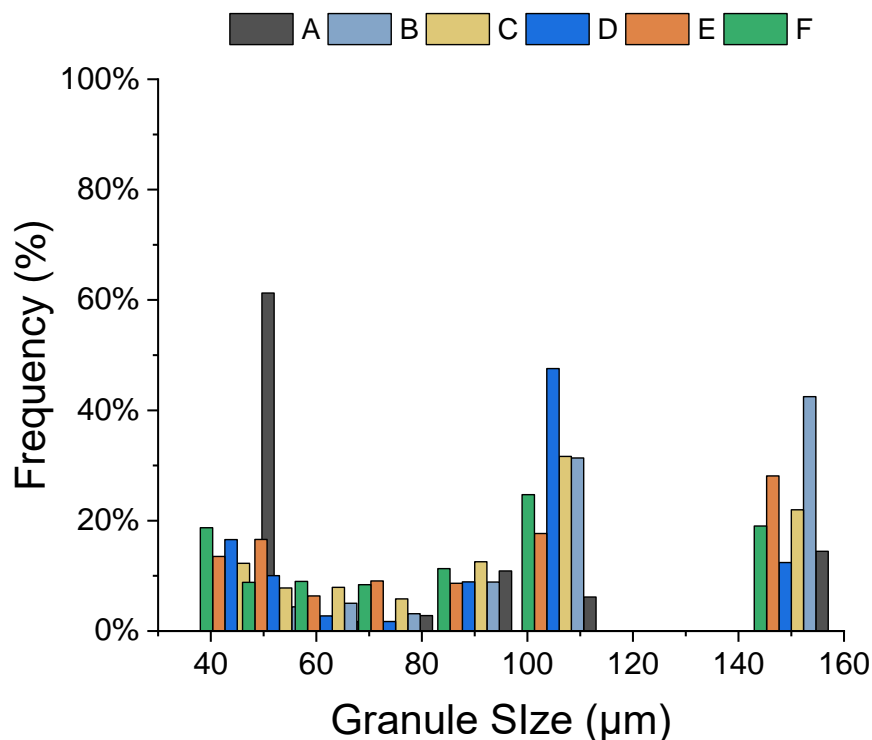
Figure 30. Weight percent plotted as a histogram of frequency percentage for the respective spray-dried granules and the sieve sizes used for this dissertation ranging from 45 – 150 μm.

Table 10. Spray-dried granule characteristics for the process parameters A – F comparing the tap density, binder wt. concentration, Carr's compressibility index, and Hausner ratio. Values listed are an average of five tests except for the binder wt. concentration which was an average of 3 tests.

Granule	Tap Density (% ρ_{th})	Binder Conc. (wt. %)	Carr's Index	Hausner Ratio
A	23.74 ± 0.26	2.95 ± 0.05	8.48 ± 0.91	1.09 ± 0.01
B	23.65 ± 0.12	3.09 ± 0.03	10.3 ± 1.28	1.12 ± 0.02
C	23.85 ± 0.31	3.07 ± 0.05	8.48 ± 1.34	1.09 ± 0.02
D	24.28 ± 0.20	3.14 ± 0.05	9.20 ± 1.36	1.11 ± 0.02
E	21.80 ± 0.63	5.11 ± 0.21	9.76 ± 1.22	1.10 ± 0.02
F	27.73 ± 0.65	2.99 ± 0.06	10.1 ± 0.91	1.11 ± 0.01
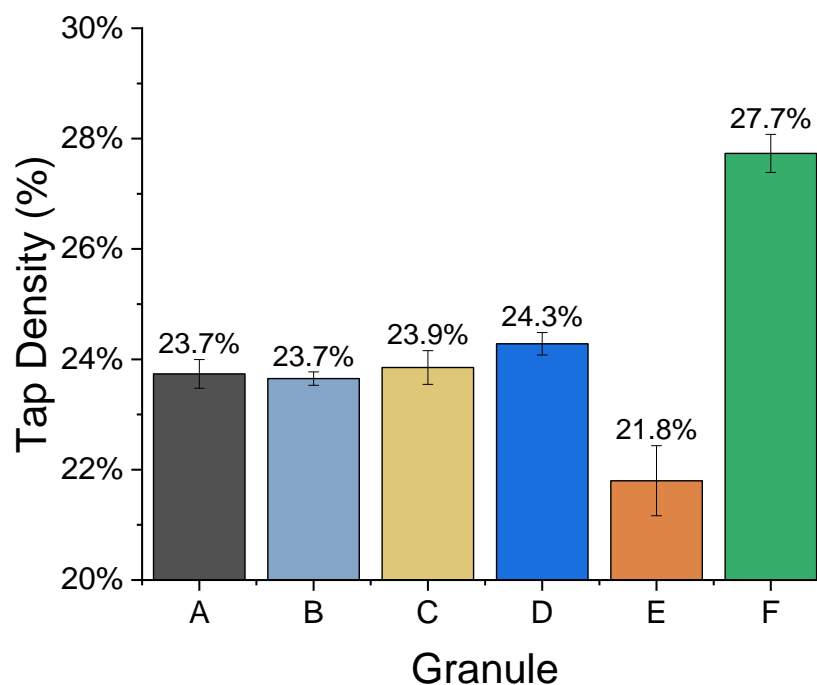
Figure 31. Tap density calculations for the six varying spray-dried granules.

Comparing the measured values from the Keyence software, the circularity for all of the six varying granules ranged from 0.60 to 0.69. The reason behind this could be due to the segmentation and extraction of the granules based on the pixel brightness. The measurement algorithm is based on the two-dimensional pixel brightness for each granule, therefore three-dimensional information is not being accounted for, only the two-dimensional orientation of the image taken. The A (100 cP) and B (250 cP) granules observed had a significant amount of satellites, showing that clustering of smaller atomized droplets occurred during the drying stage. Fewer satellites were observed in the C (400 cP) granules. The D (60 wt. % solids loading) and E (5.0 wt. % PVA) granules observed had seldom observed satellites on the granule surface and as one can see in Figure 32, had a higher degree of circularity than granules A through C. The acrylic granules, F, proved

difficult to analyze using this method as it proved difficult to adhere the granules to the carbon tape. As one can see, there very fewer granules shown within the image taken at the same magnification. This could be likely due to the process of adhering the granules to the carbon tape, not being sufficient enough for adhering the acrylic binder granules.
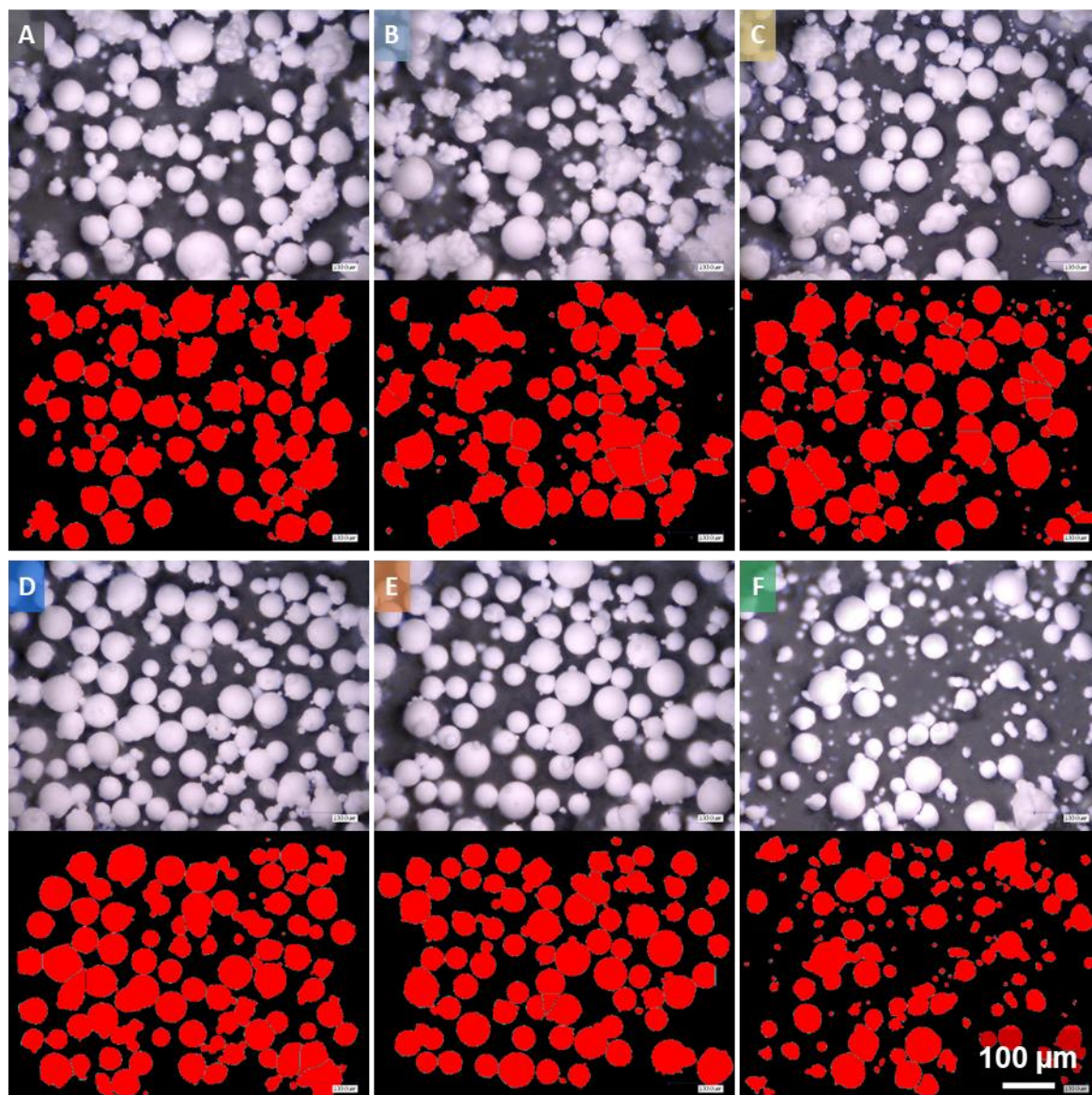
Figure 32. Optical images of the spray-dried granules and segmented images using the Keyence measurement software for granules A through F.

Table 11. Comparison of the measured diameter and circularity of spray-dried granules A through F using the Keyence optical microscope. Values shown are for an average of 150 granules.

Granule	Circularity	Max Diameter (µm)
A	0.67 ± 0.15	66.9 ± 20.6
B	0.60 ± 0.14	67.9 ± 23.1
C	0.68 ± 0.12	63.4 ± 21.4
D	0.69 ± 0.10	56.5 ± 16.3
E	0.65 ± 0.13	61.8 ± 19.8
F	0.61 ± 0.12	58.7 ± 18.4

Compaction curves were conducted for granules A through J. The transformation of the compaction data from the Instron to the linear and hybrid-springback models respectively, described in section 2.C.5, are highlighted in Figure 33. Evaluating the high-pressure end region, one can visualize a similar trend of the Instron data to the Linear springback transformation data. The hybrid-springback model varied from the other two analyses, removing the high-pressure end region discussed in the same mentioned section above and was the best transformation for compaction behavior analysis.

Compaction curve analysis was conducted for all ten granules up to a uniaxial pressure of 175 MPa. Three compaction runs were administered for each granule and the corresponding compaction curves are the representative average over the three runs. Figure 34 shows the compaction curve plot for granules A through J. Table 12 lists the respective densities at their respective compacted pressures for all ten granules, with the standard deviation listed for all three runs. The final compacted theoretical densities are shown in Figure 35. The densities were measured based on geometric density calculations and the de-binded weight of the compacts. The theoretical percentage was calculated based on the alumina's density of 3.95 g/cm^3. All of the compaction runs were conducted over a period

of two days. The temperature and humidity ranged from 22.9 – 24.9 ˚C and 10.8 – 18.1%

respectively on day one and 23.9 – 24.9 ˚C and 12.4 – 13.5 % on day two. These values

were measured using a digital thermometer and hygrometer located by the Instron

mechanical tester within the laboratory. These values did not vary a significant amount and

the atmosphere of the laboratory was deemed negligible throughout all conducted tests.

The critical yield pressure (P_y) and joining point (P_{join}) for each granule case, A

through J, were calculated by linear regression using equations 26 through 28 mentioned

in section 5.A. The ten granule cases were split into two regional groups for analysis based

on their compaction behavior. As the tangent lines used to calculate the intersection point

for this method govern the intersection point and thus the analysis, it was imperative to

analyze the regions based on the compaction behavior as well as compare amongst the

other granule cases. The granules were divided into two groups for the analysis, soft and

hard. As shown in Figure 34, granules A through E transitioned from stage I to stage II at

higher compaction pressures than granules F through J. For this reason, granules A through

E were categorized as hard and granules F through J were characterized as soft. Therefore,

the compaction regions needed to be representative of this behavior for the analysis. The

pressure regions and thus compaction data used to calculate the best fit line for the analysis

are listed in Table 13. The intersection point between regions one and two was used to

calculate the critical yield pressure (P_y) and the intersection point between regions two and

three were used to calculate the joining points (P_{join}) for each granule group. The R^2 values

for all best fit lines were above 0.98 and were acceptable. The calculated critical yield

pressures (P_y) and joining point (P_{join}) are listed below in Table 14 and Table 15

respectively as well as plotted in Figure 36 and Figure 37 respectively.
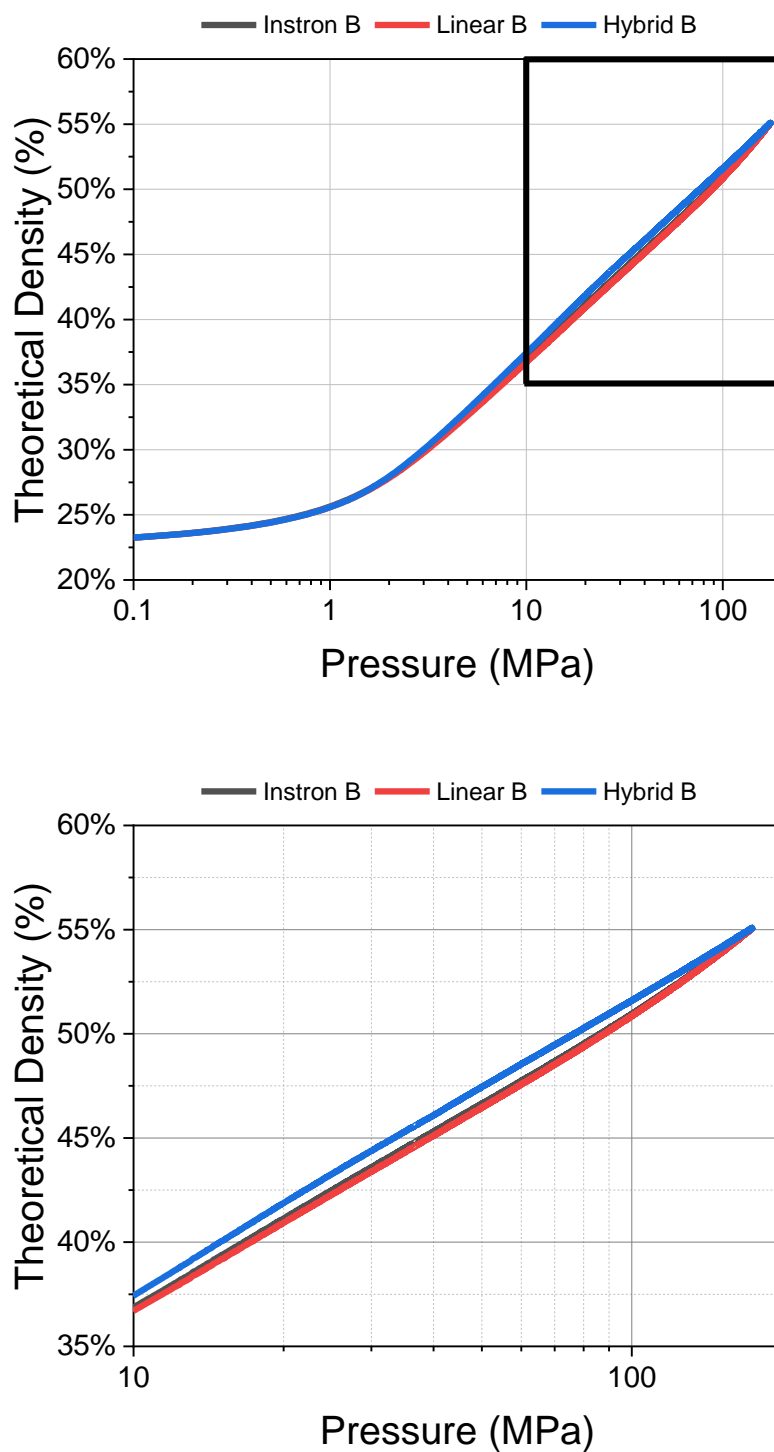
Figure 33. (Top) Compaction curves of B granules comparing the initial Instron data to the linear and hybrid springback model transformations. (Bottom) Highlighted region of the high-pressure end point (black box) comparing all three data sets.

It is important to note a comparison of this method to analyze the compaction curves to previous work done by Smith, Golomb, and Venugopal [2, 3, 55]. Although Smith and Golomb both evaluated the compaction curves using the hybrid-springback model proposed by Mort *et al.* [78], Smith and Golomb evaluated the compaction stages by taking the second derivative between the two points on the scatter plot to evaluate the inflection points of the curve. As noted in section 2.C.5, this method is strongly dependent on the data set collected, rather than the curve behavior on the plot. Venugopal used the same method as described in this work, the tangent line method, but with the unload-subtraction method proposed by Matsumoto [79, 80]. However, Venugopal used different pressure regions to evaluate the tangent lines of the curve as he was researching a different system and the aggregate breakdown of nanoparticulate titania. Although this analysis is similar to work previously conducted, the final analysis method has slight differences that are consequential to the accepted results when in comparison to the previous work.

Table 12. Theoretical density measurements at various pressures along the compaction curve. The values shown are an average of three density measurements showing the mean and standard deviation from the three compaction runs.

Granule	0.1 MPa	3.5 MPa	10.0 MPa	50.0 MPa	100.0 MPa	175 MPa
A	24.1 ± 0.4	32.4 ± 0.2	38.8 ± 0.2	47.1 ± 0.2	52.2 ± 0.1	55.5 ± 0.1
B	23.3 ± 0.4	30.9 ± 0.1	37.4 ± 0.2	47.5 ± 0.	51.6 ± 0.2	55.1 ± 0.2
C	23.4 ± 0.5	33.1 ± 0.1	39.7 ± 0.1	48.8 ± 0.1	52.4 ± 0.1	55.6 ± 0.1
D	23.3 ± 0.2	31.8 ± 0.3	38.8 ± 0.4	48.5 ± 0.4	52.2 ± 0.2	55.4 ± 0.1
E	21.2 ± 0.5	30.3 ± 0.1	37.3 ± 0.2	47.4 ± 0.3	51.3 ± 0.2	54.5 ± 0.1
F	27.6 ± 0.1	39.1 ± 0.2	43.7 ± 0.2	50.2 ± 0.1	53.3 ± 0.1	56.3 ± 0.2
G	23.4 ± 0.1	37.6 ± 0.3	43.3 ± 0.3	50.6 ± 0.1	53.7 ± 0.0	56.7 ± 0.0
H	23.7 ± 0.1	39.3 ± 0.1	44.8 ± 0.1	51.4 ± 0.1	54.4 ± 0.1	57.3 ± 0.1
I	24.0 ± 0.1	40.2 ± 0.2	45.4 ± 0.2	51.8 ± 0.1	54.7 ± 0.1	57.5 ± 0.1
J	28.2 ± 0.3	41.1 ± 0.1	45.9 ± 0.1	52.3 ± 0.1	55.2 ± 0.1	58.2 ± 0.1
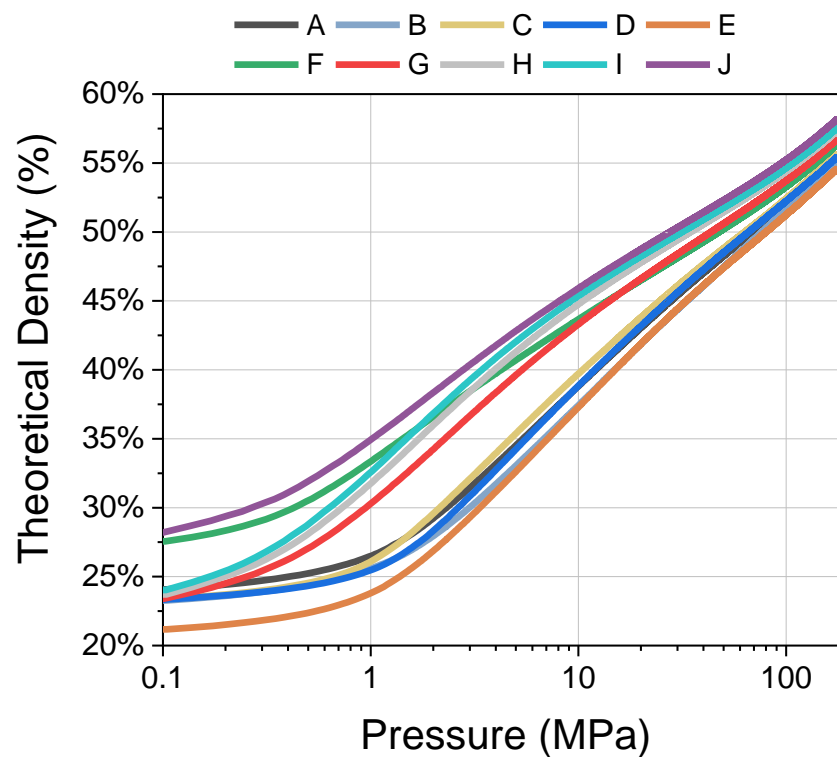
Figure 34. Compaction curve plots for granule A through J. The compaction plot is representative of an average of three compaction runs per granule.
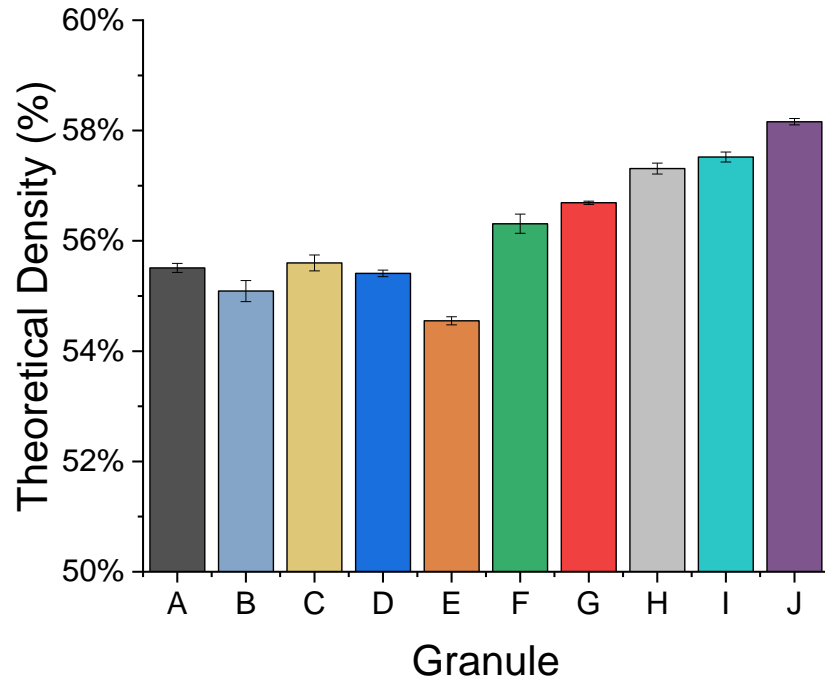
Figure 35. Theoretical density measurements of dry-pressed alumina granules for cases A through J compacted at a uniaxial compaction pressure of 175 MPa. Values shown are for an average of three compaction runs.

Table 13. Linear regression regions used to calculate the critical yield pressure and joining points broken into the two mentioned subgroups for the specific granules listed.

Granule Group	Region 1	Region 2	Region 3
Soft (A – E)	0.10 – 0.25 MPa	2.00 – 25.00 MPa	25.00 – 175.00 MPa
Hard (F – J)	0.10 – 0.15 MPa	0.75 – 5.00 MPa	15.00 – 25.00 MPa
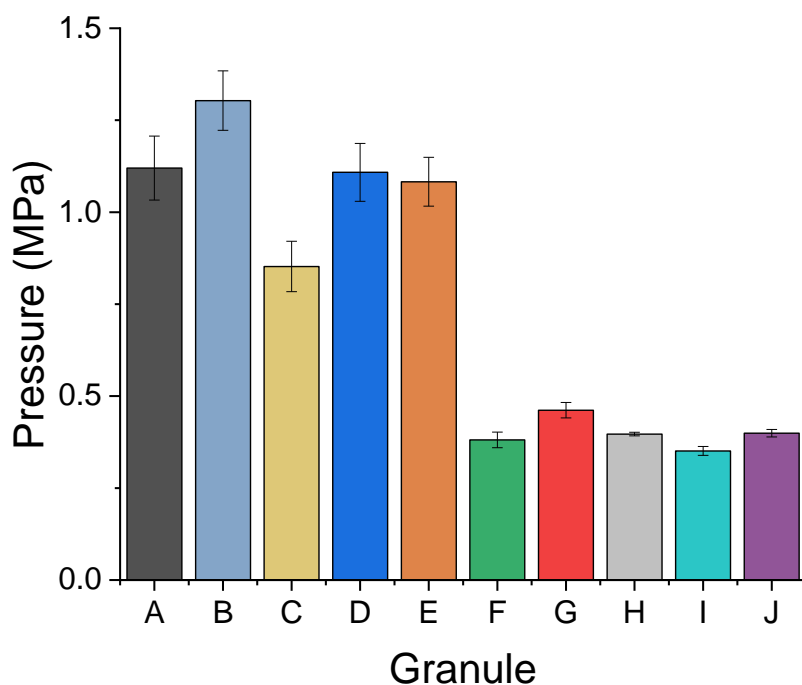
Figure 36. Critical yield pressures (Py) for granules A through J. Values shown are an
average of three compaction runs.

Table 14. Critical yield pressures (Py) for granules A through J are listed below comparing
the linear and hybrid springback model measurements. Values shown are an
average of three compaction runs.

Granule	Linear P_y Pressure (MPa)	Hybrid P_y Pressure (MPa)	ρ_{th} (%)
A	1.12 ± 0.09	1.12 ± 0.09	26.8
B	1.30 ± 0.08	1.30 ± 0.08	26.4
C	0.84 ± 0.07	0.85 ± 0.07	25.6
D	1.09 ± 0.08	1.11 ± 0.08	25.8
E	1.07 ± 0.07	1.08 ± 0.07	24.1
F	0.38 ± 0.02	0.38 ± 0.02	29.6
G	0.46 ± 0.02	0.46 ± 0.02	26.8
H	0.39 ± 0.01	0.40 ± 0.01	27.2
I	0.35 ± 0.01	0.35 ± 0.01	27.4
J	0.39 ± 0.01	0.40 ± 0.01	31.1
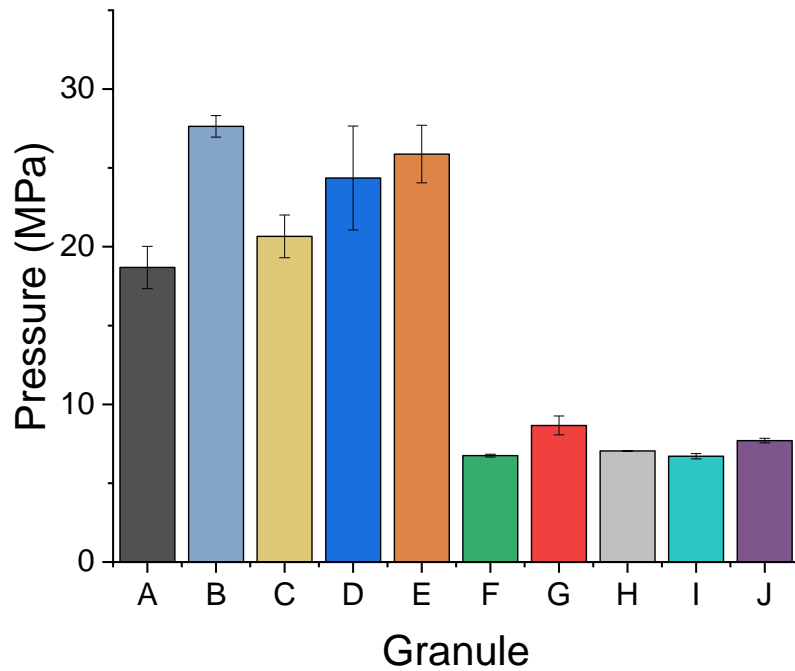
Figure 37. Joining point pressures (Pjoin) for granules A through J. Values shown are an
average of three compaction runs.

Table 15. Joining point pressures (Pjoin) for granules A through J are listed comparing the
linear and hybrid springback model measurements. Values shown are an average
of three compaction runs.

Granule	Linear P_{join} Pressure (MPa)	Hybrid P_{join} Pressure (MPa)	ρ_{th} (%)
A	49.5 ± 5.27	18.7 ± 1.34	26.8
B	39.3 ± 1.35	27.6 ± 0.68	26.4
C	76.2 ± 11.4	20.7 ± 1.35	25.6
D	103 ± 41.8	24.4 ± 3.30	25.8
E	85.5 ± 22.7	25.9 ± 1.82	24.1
F	5.92 ± 0.12	6.75 ± 0.09	29.6
G	8.42 ± 0.64	8.66 ± 0.60	26.8
H	6.84 ± 0.05	7.05 ± 0.03	27.2
I	6.44 ± 0.13	6.71 ± 0.17	27.4
J	7.37 ± 0.21	7.70 ± 0.14	31.1

The moisture contents prior to compaction for granules G through J are listed in Table 16. The table also includes the granules that the moisture was added to prior to compaction. For granules G through I, they were B granules compacted at their respective moisture contents. J granules were F granules compacted at 1.93 % moisture. There was no need to go higher in moisture content for the acrylic emulsion binders as moisture is not a plasticizer and they are insensitive to changes in moisture or humidity due to being hydrophilic [3].

Table 16. The moisture content calculated by weight loss for granules G through J.

Granule	Moisture Content (wt. %)	Original Granules	Binder
G	2.07 ± 0.20	B	PVA
H	3.98 ± 0.19	B	PVA
I	5.97 ± 0.22	B	PVA
J	1.93 ± 0.24	F	Acrylic Emulsion

The granules that achieved the highest densities at lower compaction pressures were granules F through J. Adding moisture to the B granules softened the granules and improved the densification rate during compaction. Comparing granules A through F in Figure 38, the acrylic emulsion granules (F) varied from all of the granules spray-dried with the PVA binder (A through E). The F granules had a higher tapped starting density within the compaction die and had a lower critical yield pressure when compared to the granules with the PVA binder. Therefore, the acrylic emulsion binder promoted higher density compacts at lower pressures when compared to the PVA granules. Comparing all of the PVA granules (A through E), their compaction rates varied in stages I and II, the dominating factor being the granule deformation and knitting behavior varying from each varying granule case. However, during stage III, the compaction rates across all of the

granules promoted similar final compacted density values, and thus, the granule densification behavior resulted in similar high-pressure end density measurements across all of the varying granule cases.
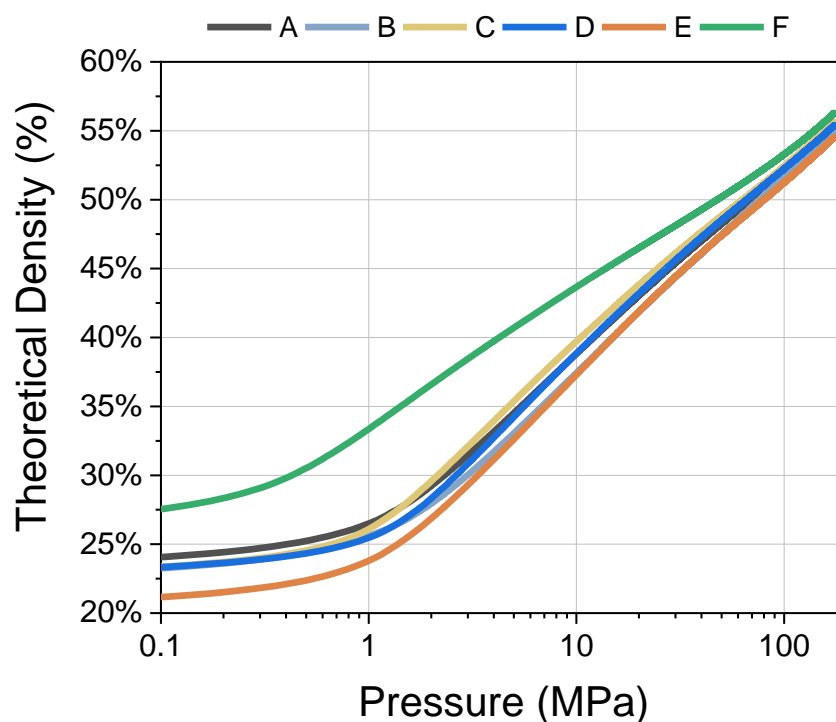
Figure 38. Compaction curve plot comparing all of the PVA granules (A through E) with the acrylic emulsion granules (F) compacted at 0.0 % moisture. The compaction plot is representative of an average of three compaction runs per granule.

Smith [2] also saw this behavior with varying the volume percentage of alumina in the slurries prior to spray drying with acrylic emulsion binders. Smith spray-dried alumina slurries at 43 and 53 vol. % and noted a final theoretical density variation between the two cases of 60 to 61% theoretical density respectively. Golomb [3] evaluated the compaction behavior of lubricants processed with acrylic emulsion binders and similar slurry parameters prior to spray-drying. Golomb concluded that the use of varying lubricants

slightly reduced the yield strength of the granules and altered the compaction characteristics in stages I and II. The pressing modulus was not greatly impacted at the end of the compaction runs compared across all of the cases. The varying lubricants did not significantly alter the final relative density values for all of the varying compacts as well, agreeing with the behavior noted in this dissertation.

Comparing the compaction characteristics when varying the viscosity of the slurries prior to spray-drying is highlighted in Figure 39. The compaction characteristics of the A granules (100 cP) versus the B granules (250 cP) resulted in a similar compaction behavior. The compaction rate throughout all of the tests seemed consistent with one another, only varying by the starting tap density within the compaction die and thus the resultant compacted density throughout the test. The compaction rate of the B granules increased around a pressure of 50 MPa, and the final density of the compact became similar to those of the A granules. The C granules, spray-dried at a viscosity of 400 cP, resulted in deformation and knitting at slightly lower pressures, promoting a faster compaction rate and knitting behavior during stages I and II. During stage III, the C granules compaction and densification rate decreased, resulting in similar final density measurements as the other two cases. As previously mentioned, during stage III, the granule densification behavior varies depending on the characteristics observed in stages II and III, however, eventually results in similar final density measurements across the granules with the same organic binder species. This phenomenon is likely due to the particle orientation and granule morphology of the spray-dried granules, altering the compaction characteristics across stages I and II but promoting similar end results during stage III due to the same organic binder species and thus the compaction densification behavior.
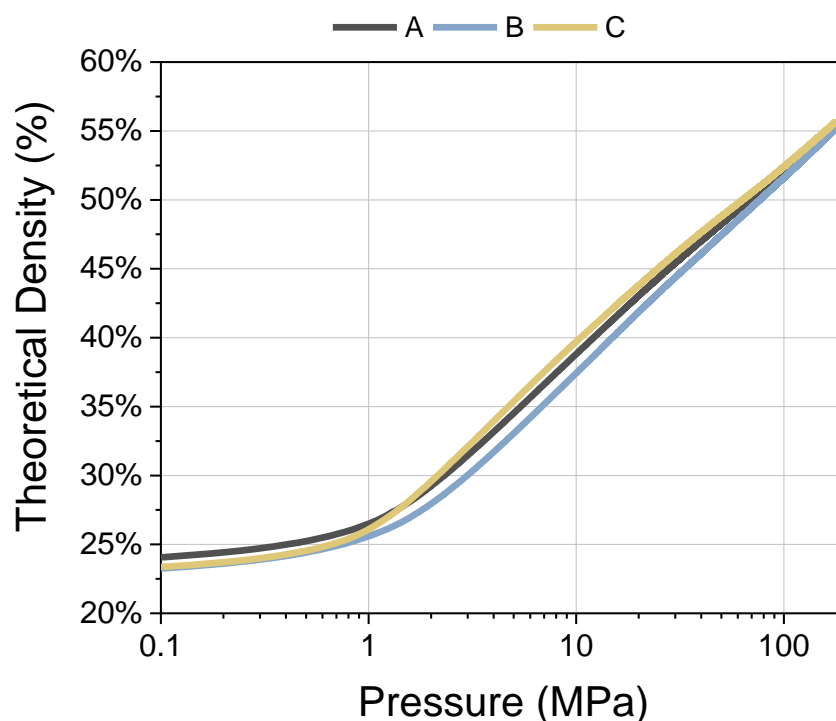
Figure 39. A compaction curve plot comparing the same specific gravity slurries (50 wt. % solids loading) but different viscosity values ranging from 100 cP (A), 250 cP (B), and 400 cP (C). The compaction plot is representative of an average of three compaction runs per granule.

Comparison of the specific gravity, or solids loading, of the alumina slurries prior to spray-drying is shown in Figure 40. The compaction characteristics are similar, only varying during stage II, or the deformation behavior of the granules. The C granules (50 wt. % alumina) showed a faster compaction rate and knitting behavior when compared to the D granules (60 wt. % alumina) during stage II. The critical yield pressure for the D granules was slightly shifted to the right when compared to the C granules. The reason behind this could be due to higher specific gravity or solids loading slurries promoting harder granules due to the particle orientation and granule morphology. The D granules

may have a lower degree of hollow coring due to the slurries having a higher specific gravity prior to spray-drying. Visualizing the microstructural cross sections of the spray-dried granules for a qualitative comparison will gain more information for the reasoning behind this behavior. However, the compaction rate and densification behavior in stages I and III were similar in comparison, with the only variation occurring with the compaction rate of the two granules differing during the transition from stage II to stage III. The C granules decreased in densification when compared to the D granules and the D granules increased in densification when compared to the C granules.
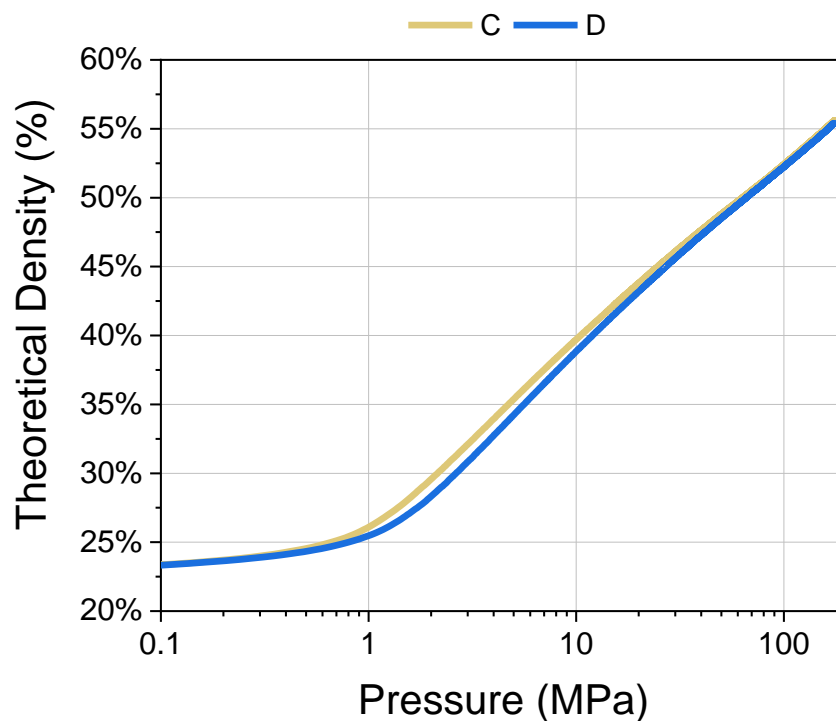
Figure 40. A compaction curve plot comparing the same viscosity value of the slurries (400 cP) but varying solids loading ranging from 50 wt. % (C) and 60 wt. % (D). The compaction plot is representative of an average of three compaction runs per granule.

Granules B and E were compared on a compaction scale and are shown in Figure 41. Theses slurries were spray-dried with the same type of PVA binder, but varied in the wt. % of the binder based on the alumina solids weight. The B granules were spray-dried with 3.0 wt. % PVA and the E granules were spray-dried with 5.0 wt. % PVA on the alumina solids weight. These cases were spray-dried at the same specific gravity and viscosity values (50 wt. % alumina and 250 cP). The compaction variation between the two granules occurred during stage I, granule flow and rearrangement. The tap densities of the E granules were the lowest observed, as previously mentioned. After the critical yield pressure of the granules was overcome and granule deformation dominated, the compaction rate and densification of the two granule cases were similar in comparison, only varying at the end of the compaction test and the final resultant density measurement of the E granules being less than the B granules. During stage III, the densification rate of the compacts processed with the E granules decreased. This behavior is likely due to the higher binder concentration producing thicker segregated binder layers of the PVA. The binder migrates to the surface of the alumina granules during the evaporation stage and produces and eggshell type layer on the surface. This segregated binder layer creates a different knitting and densification behavior in stage III, slightly diminishing densification.

Adding moisture content to the B granules was conducted and compared for granules G through I, their respective compaction curves shown in Figure 42 with their respective moisture contents listed in Table 16 as previously mentioned. The correlation observed was higher resultant compacted densities were achieved with increasing moisture content. Comparing granules H (3.98 % moisture) and I (5.97 % moisture), the compaction behavior and resultant final density measurements were similar. This suggests there is a

threshold of moisture affecting the knitting and deformation behavior of the granules. Comparing the granules compacted with no moisture content (B) with 2.07 % moisture (G), there was a significant increase in deformation and densification being promoted at lower compaction pressures. Adding moisture content softened the granules by lowering the glass transition temperature of the binder, decreased their respective critical yield pressures and joining points, and promoted higher resultant compacted densities.
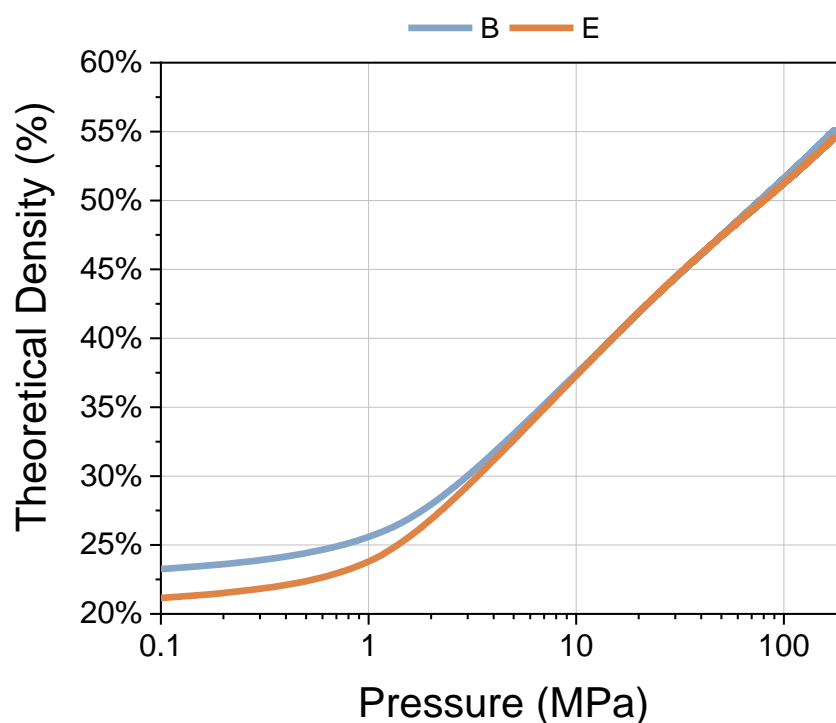
Figure 41. A compaction curve plot comparing the same solids loading and viscosity values (50 wt. % alumina and 250 cP) but varying the PVA binder concentration of 3.0 wt. % of the alumina solids (B) and 5.0 wt. % of the alumina solids (E). The compaction plot is representative of an average of three compaction runs per granule.
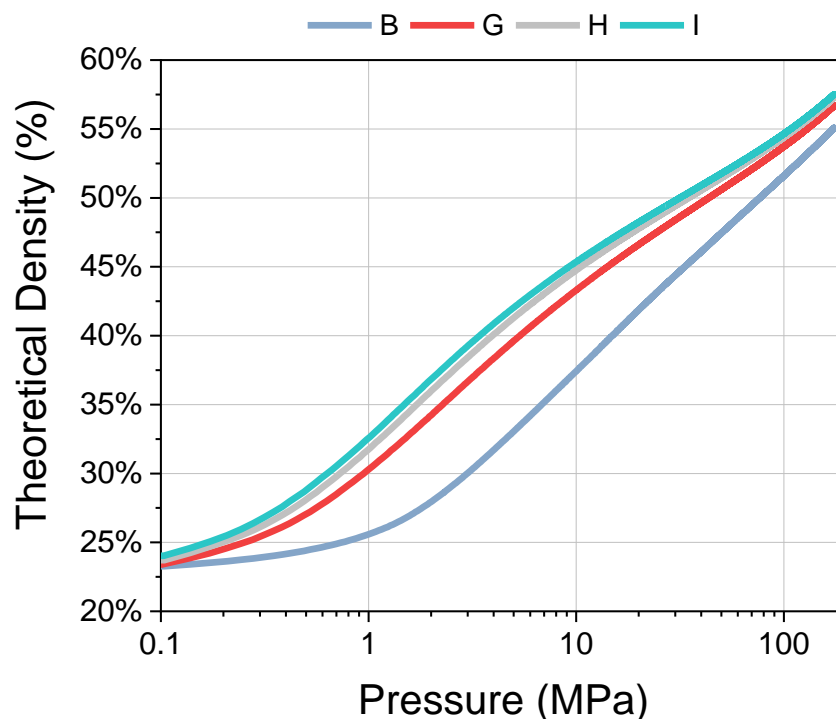
Figure 42. A compaction curve plot comparing the same solids loading and viscosity values (50 wt. % alumina and 250 cP) with granules compacted at varying moisture contents. The compaction plot is representative of an average of three compaction runs per granule.

The two varying types of binder used in this dissertation were compared on a compaction scale and their respective compaction curves are shown below in Figure 43. These granules were spray-dried at the same viscosity, solids loading, and binder amount (50 wt. % alumina, 250 cP, and 3.0 wt. % binder). There was a significant difference between the two binders, with the acrylic emulsion binder promoting higher compacted densities and densification rates at lower compaction pressures.

Adding 1.93 % moisture content to the F granules resulted in the highest compacted density measurements. As shown in Figure 44, the J granules resulted in the highest

compacted density values at a compaction pressure of 175 MPa. This is likely due to moisture promoting the knitting behavior of the granule and higher densification rates. However, it is possible density gradients may have formed within the compacts from those J granules with a moisture content of 1.93 wt. %. Coupling these results with the visualization results in objective three will gain more information on the resultant differences amongst the varying processing parameters.
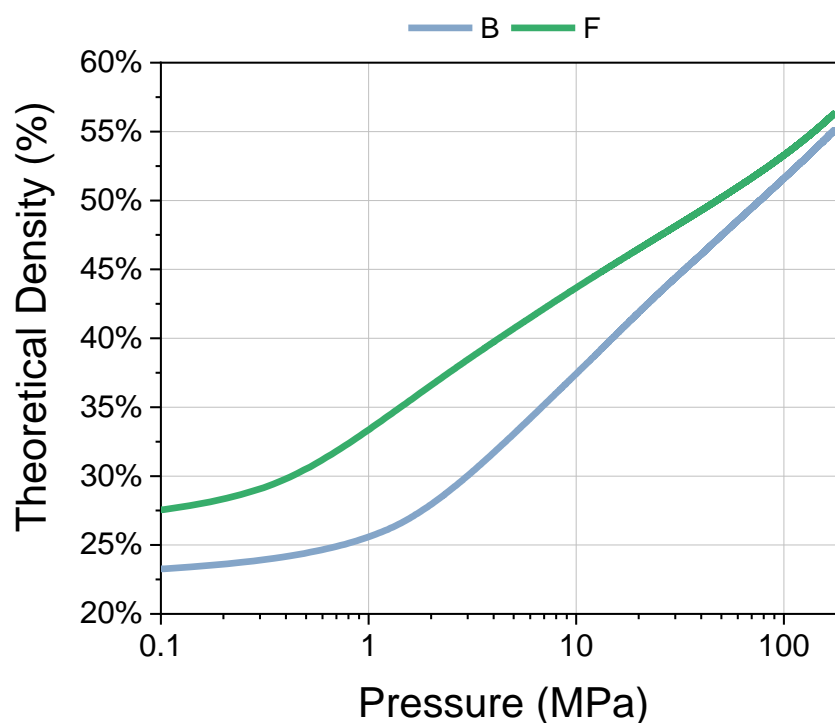
Figure 43. A compaction curve plot comparing the same solids loading, viscosity values, and binder amount (50 wt. % alumina, 250 cP, and 3.0 wt. % binder) with granules compacted with different types of binder; PVA (B) and an acrylic emulsion binder (F). The compaction plot is representative of an average of three compaction runs per granule.
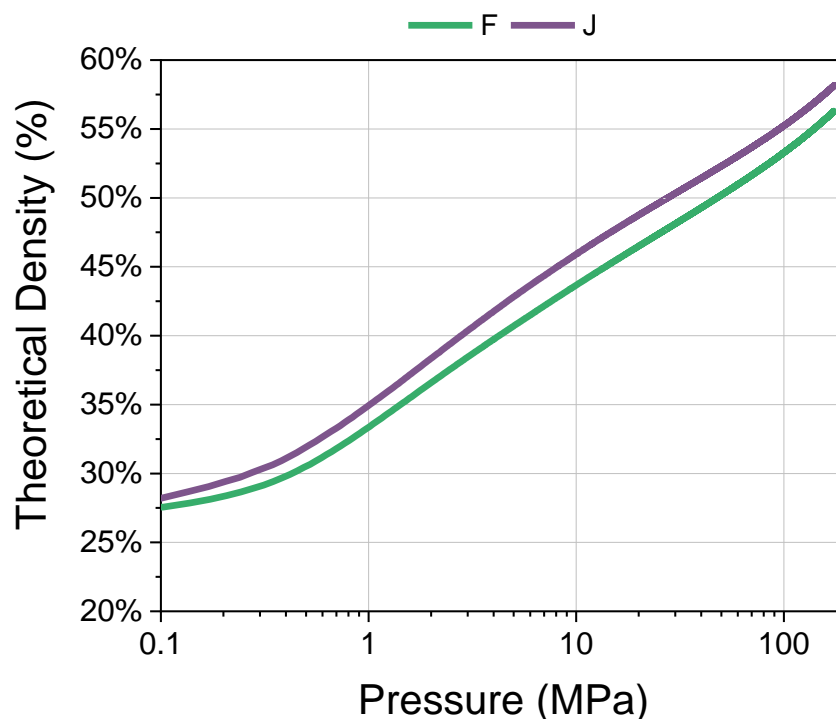
Figure 44. A compaction curve plot comparing the same solids loading, viscosity values, and binder (50 wt. % alumina, 250 cP, and an acrylic emulsion binder) with granules compacted at varying moisture contents; dry (F) and 1.93 % (J). The compaction plot is representative of an average of three compaction runs per granule.

The 3-point modulus of rupture (MOR) green (unfired) flexural strength was conducted on granules B and F as a function of moisture (G through J) to evaluate the strength of the two varying binder species and the role moisture plays during compaction for each granule case. The granules were compacted to a uniaxial pressure of 40 MPa and a specimen size (Length x Width x Thickness) of 101.5 x 55.0 x 6.0 mm. Alumina compacts were de-binded and evaluated using the fixture shown in Figure 45. The final de-binded geometric density was calculated based on the theoretical density of alumina (3.95 g/cm^3) and the resultant densities are shown in Figure 46. The 3-point green flexural strength

results are shown in Figure 47. Three samples were conducted per granule case, therefore the resultant density and flexural strength values are representative of an average of those three samples per granule case.
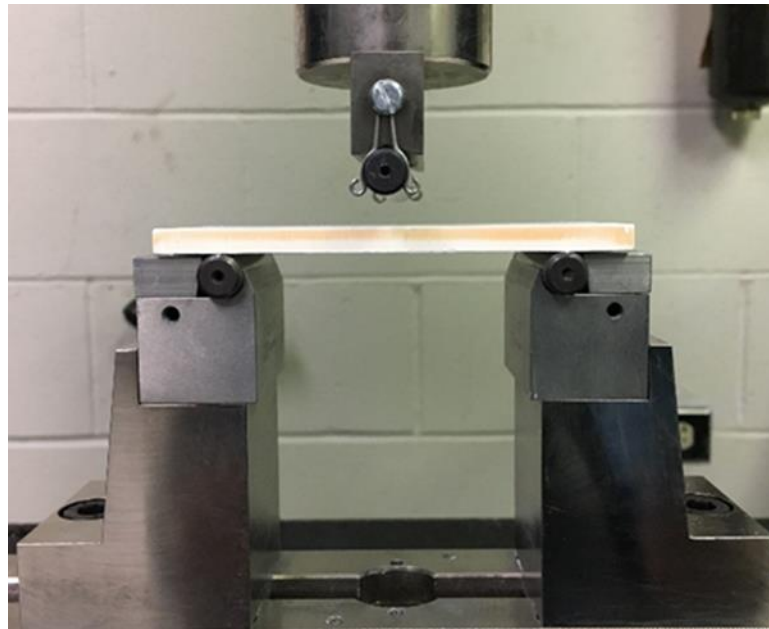
Figure 45. Instron 3-Point flexural fixture set at a span of 80.0 mm and conducted at a compaction rate of 0.5 mm/min.
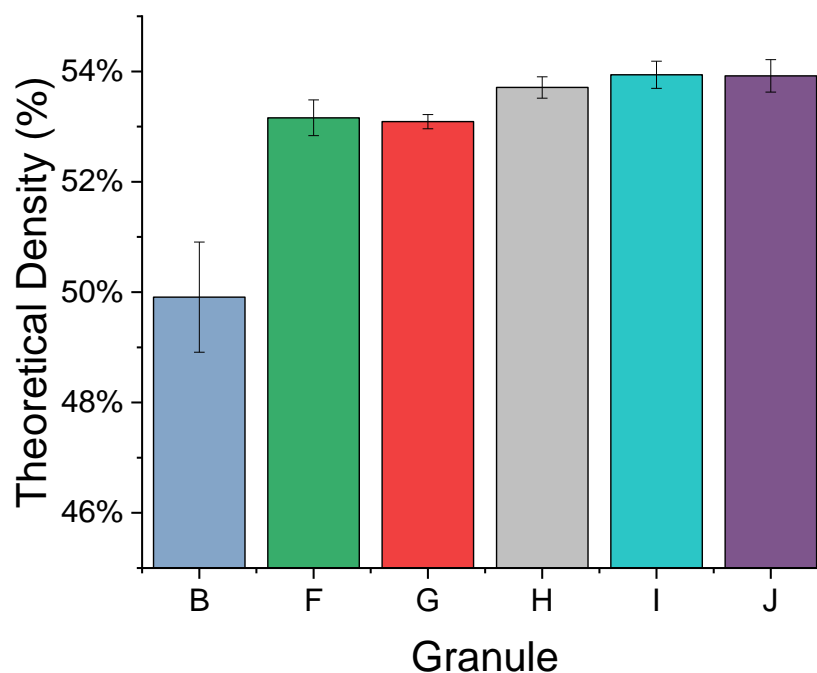
Figure 46. Theoretical density measurements based on the geometric density of the alumina compacts tested for modulus of rupture. Values are representative of three tested samples.

The geometric density calculations for the compacts were calculated based on four measurements of the thickness, width, and length of the tested specimen in the same regions across all samples. The highest densities calculated were for the compacts with the acrylic emulsion binder compacted at a moisture content of 1.93% (J) and the PVA binder compacted at a moisture content of 5.97% (I). The lowest densities as well as the largest density variation occurred with the specimens compacted with the PVA granules at zero percent moisture content (B). This trend was similar to what occurred with the compacted samples from the compaction curve analysis shown in Figure 34.
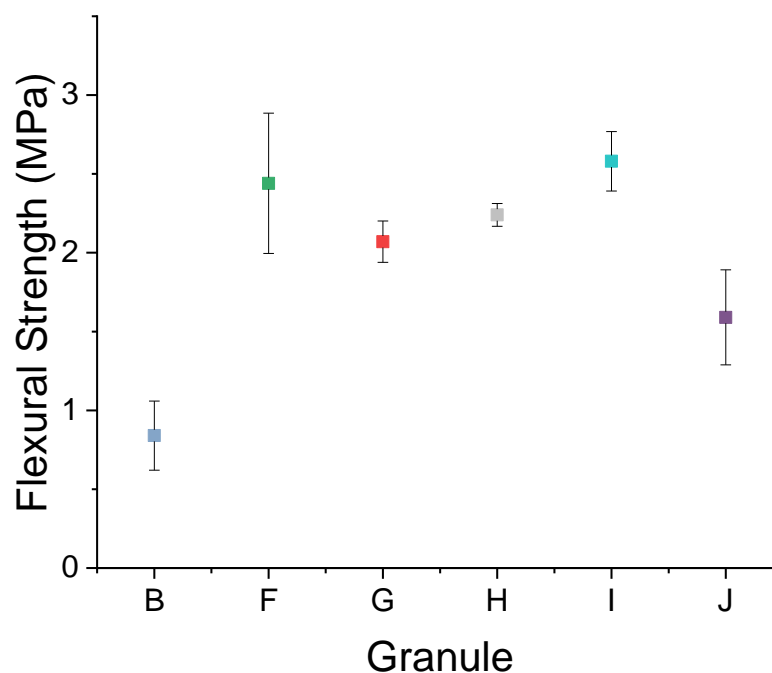
Figure 47. 3-point modulus of rupture (MOR) green flexural strength tests for the listed granule cases. Values shown are representative of three tested samples.

The highest average green flexural strength value was attributed to the PVA granules compacted at 5.97% moisture content (I). The highest flexural strength value was attributed to a specimen compacted with the acrylic emulsion binder (F) that also had the second highest average flexural strength. Despite having the highest geometric density average, the specimens compacted with J granules (acrylic at 1.93% moisture) resulted in the second lowest flexural strength measurement followed by the PVA granules (B) at zero percent moisture.

The observed behavior is likely attributed to the knitting characteristics of the spray-dried granules during compaction. Microstructures resulting in a higher microstructural uniformity and fewer microstructural defects in theory should result in

greater green strength values. Conducting further microstructural characterization of the fracture surface and bulk microstructure of these samples in objective three will likely employ the reasoning behind this behavior. The major trends observed included the green flexural strength increasing with increasing moisture content for the granules compacted with the PVA binder. In comparison, the acrylic emulsion granules compacted with zero moisture content (F) resulted in greater green flexural strength values when compared to the granules compacted with the PVA binder and zero moisture content (B). The F acrylic granules also resulted in higher green strength values in comparison to the acrylic granules compacted at the higher moisture content. This behavior justifies the theory that adding moisture to granules processed with PVA binder soften the granules and promote a higher degree of microstructural uniformity. In contrast, adding moisture to the acrylic emulsion granules actually may cause density gradients to arise, diminishing the green strength of the alumina compacts.

5.C. Summary

The conducted compaction analysis established a relationship between the mentioned slurry parameters and their effect on the compaction behavior and flexural green strength of the spray-dried alumina compacts. The impact slurry characteristics had on the morphology of the resultant spray-dried granules was explored, however, without further microstructural visualization of their morphology, the full impact cannot be evaluated.

The lowest viscosity alumina slurry resulted in the finest size of spray-dried granules generated. The overall trend for granule size seemed to follow what has been stated in the literature, that the binder type, degree of solids loading, and viscosity play a

significant role in the generated granule size. This is due to the size of the droplet formed when the alumina slurry is atomized within the drying chamber. The movement of the solid particles within the ceramic suspension relates to the formation of the droplet size and thus the generated granule morphologies.

The solids loading, binder type and amount had the largest impact on the resulting spray-dried granules tap density values. The highest tap density values were generated from the alumina slurries processed with the acrylic emulsion binders (the F granules). The lowest tap density values resulted from the spray-dried granules processed with the highest percentage of PVA binder, the E granules. Increasing the viscosity of the alumina slurries slightly altered the average tap density calculations but not to a significant degree. The higher solids loading slurry, processed at 60.0 wt. % alumina, resulted in the second highest tap density measurements. This behavior is similar to what has been previously noted in the literature.

The compaction behavior analysis was used as a tool to understand how the slurry parameters effected the granule morphology and their resultant knitting behavior. The effect moisture played as a plasticizer and its impact on the resultant compaction behavior as a function of the two varying binder types was also evaluated. This established a comparison between the experimental results of the slurry characteristics on a compaction scale. Evaluating the generated compaction curves using Mort's hybrid springback model accounted for the machine compliance and elastic springback of the alumina compact. It was found that that acrylic emulsion granules (F) resulted in higher compacted densities than the PVA granules. Adding 2.0% moisture to the acrylic granules resulted in slightly higher geometric densities. Adding moisture to the PVA granules significantly affected

their compaction behavior. The densification rate during compaction was increased and the spray-dried granules became softer due to the added moisture. By adding moisture, the glass transition temperature of the binder was lowered and the granules become softer. This increased densification rate resulted in increased compacted geometric densities as a function of increasing moisture content.

There was no significant difference in the calculated geometric densities for granules A through E, evaluating the viscosity and solids loading as a function of compaction characteristics. The only variation between these cases was the early stages of compaction and their respective deformation rates. This is likely due to the overall binder content and critical yield strength of the spray-dried granules promoting the deformation rate and knitting characteristics during stage II of compaction. As stated previously in section 4.B, the solids loading, viscosity, binder type and binder amount affected the overall granule morphology which strongly affects the critical yield pressures and early deformation characteristics of the granules during compaction. Processing the granules with the same type and amount of binder seemed to promote similar compacted densities, even by varying the solids loading and viscosities prior to spray-drying. The higher PVA binder content granules (E) resulted in the lowest compacted densities overall. This could be due to these granules having the lowest initial density values prior to compaction. Evaluating the compaction behavior analysis for the varying granule cases is an essential tool in establishing a relationship between what processing parameters promote microstructural uniformity. Understanding the initial density values of the varying granules as well as their compaction characteristics will further relate the experimental results to the obtained visualization results in the next objective. The developed microstructural

characterization techniques will further correlate these experimental results to the obtained visualization results by characterizing the green microstructures of the spray-dried granules and their resultant compacted microstructures as a function of the processing parameters.

6. OBJECTIVE 3: 2-D Microstructural Characterization of Processed Alumina

6.A. Experimental Procedures

The Spurr Low Viscosity Epoxy Kit contains four parts to the epoxy resin. The ratios of the resins are shown in Table 17. The epoxy was weighed out in a glass beaker and then was mixed on a magnetic stir plate at 125 rpm and a temperature of 60 ˚C for fifteen minutes. Samples were placed in a 32 mm diameter plastic mold with an applied release agent. Once the epoxy was finished being heated up to lower the viscosity, the sample and epoxy were placed under a vacuum to a pressure of 0.85 Bar. The epoxy is then poured over top of the sample, holding the sample under vacuum for an extended period to ensure full infiltration has been achieved.

Once embedded in the epoxy, samples were placed in an oven between 70 – 80˚C to cure the epoxy and sample for a minimum of eight hours. Once samples are cured in the epoxy, samples were mechanically polished down to 0.05 μm and were flat ion milled along the surface of the sample at a voltage of 6 kV for ten minutes and a slow rotational speed. Samples were then sputtered coated in gold to a thickness of 25 nm and were painted with silver paste along the epoxy surface to mitigate charging before microstructural characterization.

Table 17. The formulation for Spurr's Low Viscosity Epoxy Kit used for the infiltration process of porous ceramic materials.

Epoxy Formulation	
DMAE (dimethylaminoethanol)	0.70 wt. %
DER 736 (diglycidyl ether)	18.5 wt. %
ERL 4221 (cycloaliphatic epoxide resin)	23.1 wt. %
NSA (nonenyl succinic anhydride)	57.7 wt. %

Six varying spray-dried granules were characterized using a FESEM. Carbon tape was used to create a conductive path from the surface of the sample to the sample stud within the FESEM chamber. The six varying granules visualized are listed in Table 7, granules A – F, with their respective processing parameters. In an effort to visualize the compressibility of alumina granules along a compaction curve, granules were compacted at various pressures along their respective compaction curves to visualize the stages of compaction. Granules A – F and J were compacted at 10, 50, 100, and 175 MPa. Granules G through I were compacted to pressures of 3.5, 10, 50, 100, and 175 MPa. Compacts pressed to 175 MPa were also de-binded to visualize the microstructure after binder removal.

In an attempt to visualize the parallel and perpendicular direction of compaction, samples were prepared for microstructural characterization by a double infiltration method. Compacts were infiltrated in epoxy. After being cured in the epoxy, the compacts were cut using a diamond saw to expose the perpendicular direction of compaction. These sections were then re-infiltrated in epoxy and polished for microstructural characterization. A schematic of this process is shown in Figure 48.
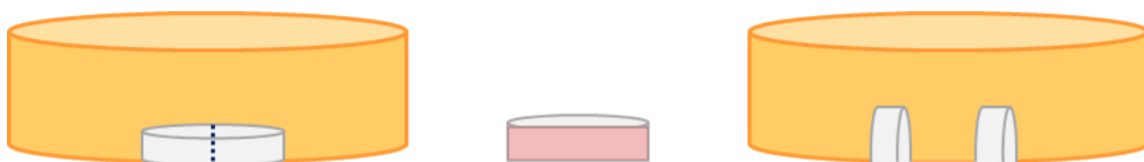
Figure 48. Schematic diagram showing the process to vacuum infiltrate the green alumina compact, cut along the center of the compact using a diamond saw, and re-infiltrate the compact to expose and visualize the perpendicular direction of pressing.

The fracture surfaces of the green strength samples were characterized as well. Sections of the compact along the center of the compact's fracture surface were cut out carefully with a serrated razor blade and prepared for characterization. Samples were sputter coated in 25 nm of gold. Silver paste and carbon tape were used as well to mitigate charging. Edge sections of the compact's fracture surface were cut out with the same serrated razor blade. These sections were infiltrated and polished to visualize the parallel and perpendicular direction of compaction. The compact that exhibited the highest force at break were the samples characterized for this analysis. All characterization of samples in this objective was carried out by use of a FESEM.

6.B. Results and Discussion

The spray-dried granules were characterized on the FESEM to evaluate and visualize the resultant granule morphologies for granule cases A through F. Micrographs of the mounted granules on carbon tape as well as the internal microstructures of the infiltrated and polished granules were taken. These micrographs are shown in Figure 49 through Figure 54 for granules A through F respectively. All samples were sputter coated with a nanolayer of gold to a thickness of 25 nm. Carbon tape and silver paste were used in order to mitigate charging issues during characterization on the FESEM. The use of a low viscosity epoxy resin coupled with a novel mechanical polishing and ion milling method was proved successful in visualizing green microstructural variations of spray-dried alumina granules and compacted green bodies. The conductive materials proved to be enough to counter and mitigate the charging effects that evolve from microscopy characterization of porous ceramic materials.

In comparison to the other methods mentioned in section 2.D, this process produced high resolution SEM micrographs to visualize the internal structure of the spray-dried granules. The liquid immersion method (LIM) allowed researchers to visualize the contrast differences between the organic binder and ceramic material while using an optical and confocal laser scanning microscope. This method was also able to visualize the segregated binder layers within alumina spray-dried granules as well as the organic binder locations within alumina compacts before binder burnout [5-19, 21, 22, 24-27, 31]. It has its limitations, which mainly center on the resolution and thus, the microstructural information gained throughout the porous ceramic. The work mentioned in Höhn *et al.* [82] of using a dual source ion beam to remove ceramic material and expose the internal structure of the

spray-dried granules proved sufficient to register high resolution SEM micrographs using a FIB. However, this method has its limitations of sample size and preparation, such as overheating of the specimen and having to integrate a cooling stage during the process.

In Figure 49, the A granules visualized showed an abundance of observed satellites on the surface of the granulated alumina as well as irregular shaped granules. This concludes what was visualized on the optical microscope in Figure 32 of section 5.B. During the droplet formation and drying stage of the process, clustering of smaller atomized droplets occurred when spray-drying at a low viscosity of 100 cP. Satellites were also visualized within the micrographs of the B granules as shown in Figure 50. These granules were spray-dried at a higher viscosity value of 250 cP, however, not much of a significant difference between the two cases was noted. The C granules are shown in Figure 51 and were spray-dried at the same solids loading as A and B but at the highest evaluated viscosity of 400 cP. Observed satellites on the surface of the spray-dried granules as well as irregular shaped granules were less abundant for the C granules when compared to the other two cases. The granules processed at the highest evaluated viscosity (C) resulted in a highest degree of circularity when compared to the lower viscosity granules (A and B).

The D and E granules visualized, shown in Figure 52 and Figure 53 respectively, showed the highest degree of circularity in comparison to granules A through C. The reason this occurrence was noted is likely due to the higher solids loading degree of the D granules (60 wt. %) and the highest percentage of PVA binder processed with the E granules (5.0 wt. % PVA). This relationship strongly suggests what previous researchers have noted, that the movement of the ceramic particles within the ceramic suspension prior to the spray-drying process relates to the droplet size and shape formation generated. The A and E

granules, spray dried at the lowest viscosity of 100 cP and the highest percentage of PVA binder respectively, showed the largest evidence of hollow coring and internal microstructural defects. Hollow coring was evident in all of the granules spray-dried with the PVA binder, with lager voids being observed in the lower viscosity and higher binder percentage (granules A and E).

The F granules spray-dried with the acrylic emulsion binder, shown in Figure 54, showed the highest degree of microstructural uniformity over all six cases evaluated. It is imperative to note that these granules resulted in the highest tap density values measured. This phenomenon occurred due to the acrylic organic species being insoluble. During the drying stage of the spray-drying process, this type of binder does exhibit binder migration to the outer surface of the granule. Polyvinyl alcohol being soluble, exhibits this phenomenon and migrates to the surface of the generated granule along with the evaporating water. A non-uniform binder layer is formed which causes an impedance for further evaporation to take place due to the low permeable segregated binder layer that formed. This segregated binder layer may be the reasoning that the hollow core structure forms, resulting in a ballooning effect from the remaining moisture inside the granule boiling. This causes the formation of an empty microstructural void and the resultant hollow core formation. This phenomenon could also be likely caused by the migration of the water soluble binder, migrating the binder species and ceramic particles to the surface of the spray-dried granule. This behavior is based off of the dispersed state of the suspension and the movement of the particles within the ceramic suspension, as previously noted by some researchers [39, 52].
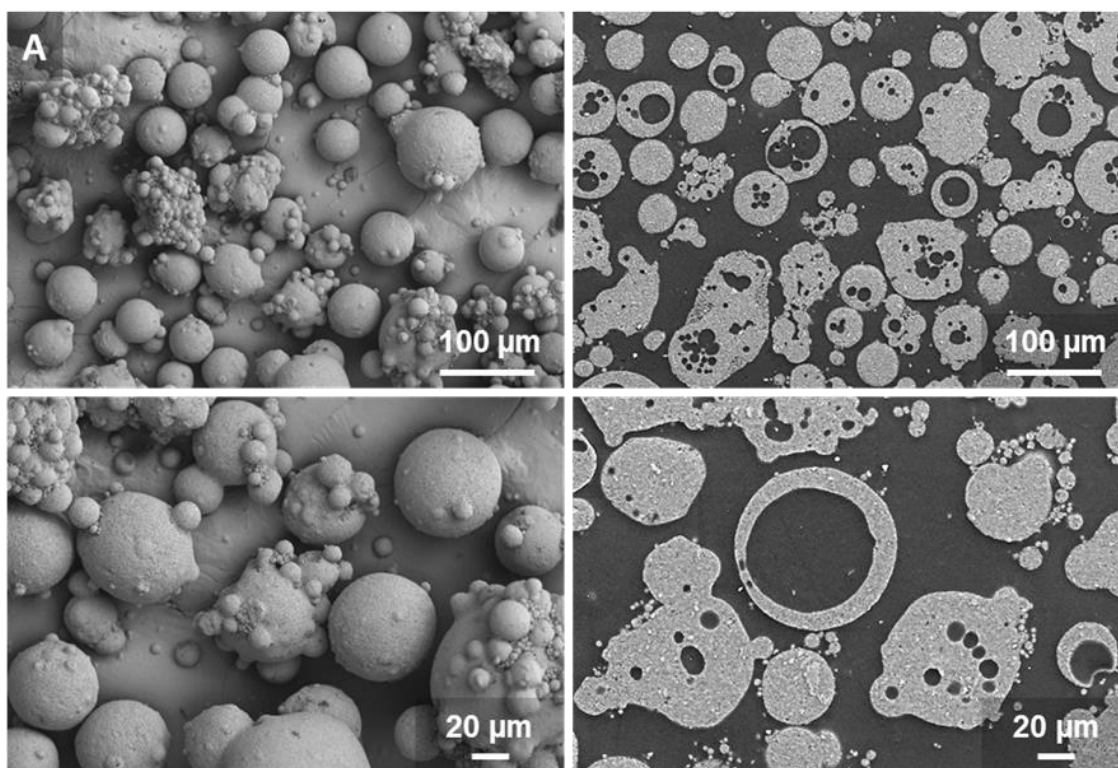
Figure 49. Micrographs of A granules (100 cP – 50 wt. % Alumina – 3.0 wt. % PVA.
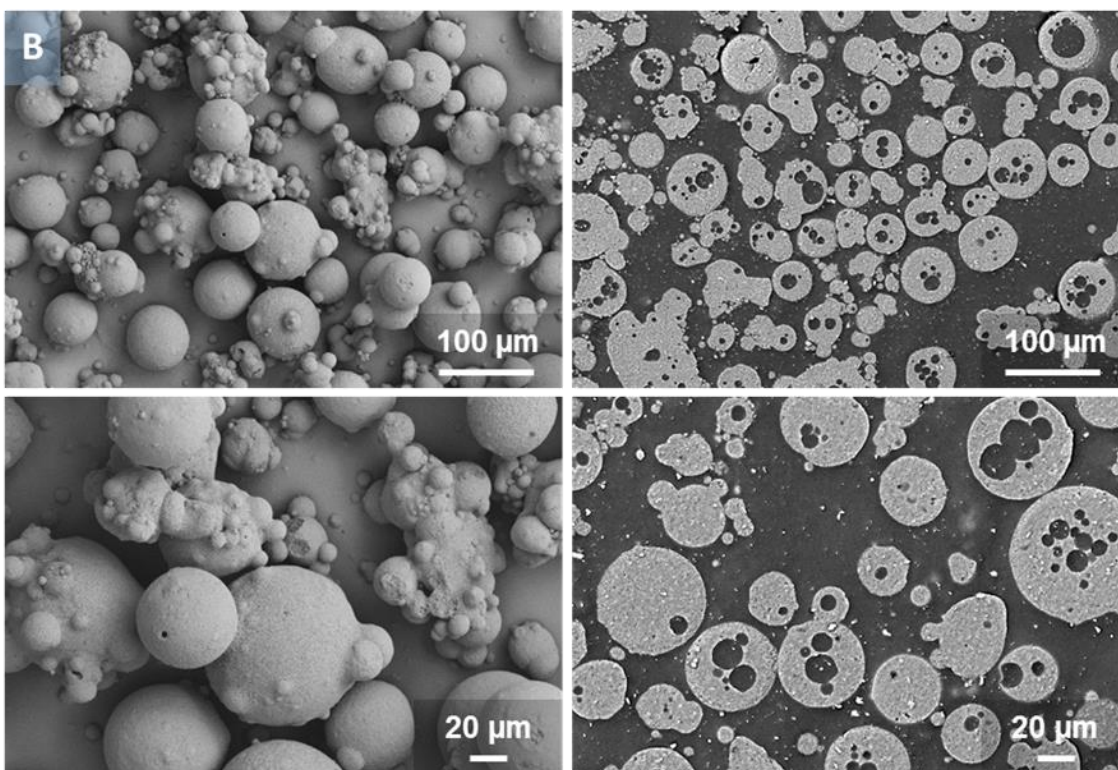
Figure 50. Micrographs of B granules (250 cP – 50 wt. % Alumina – 3.0 wt. % PVA).
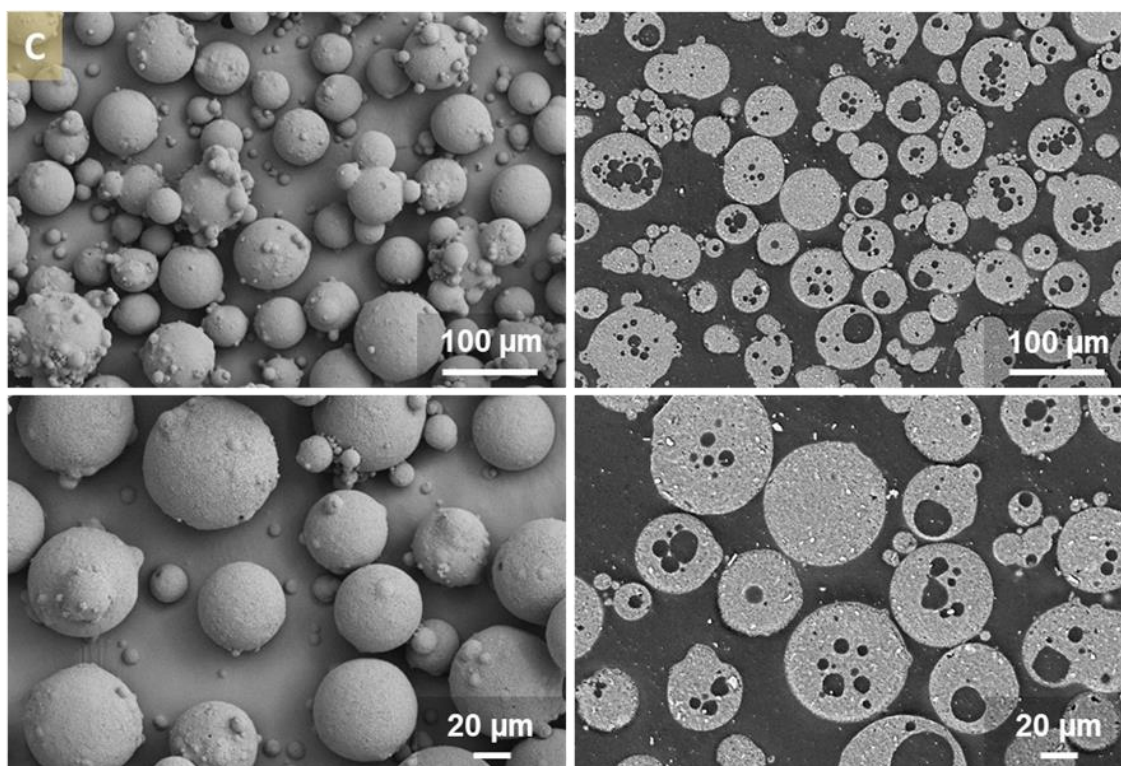
Figure 51. Micrographs of C granules (400 cP – 50 wt. % Alumina – 3.0 wt. % PVA).
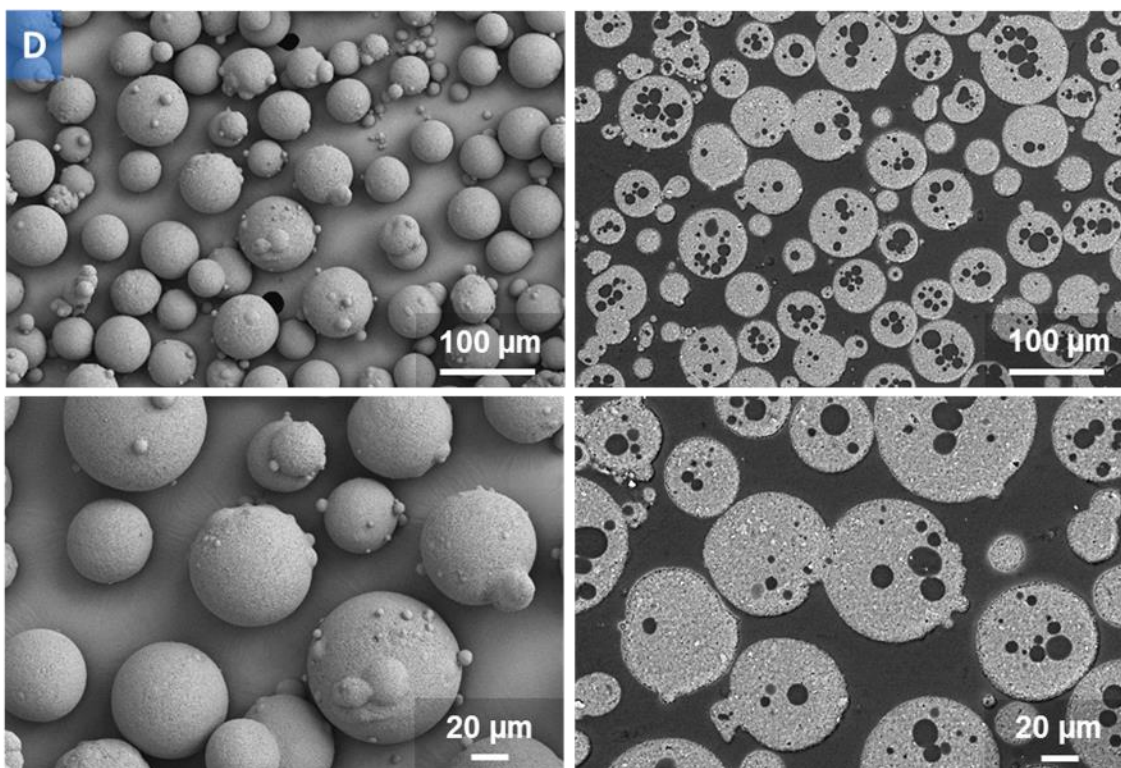
Figure 52. Micrographs of D granules (400 cP – 60 wt. % Alumina – 3.0 wt. % PVA).
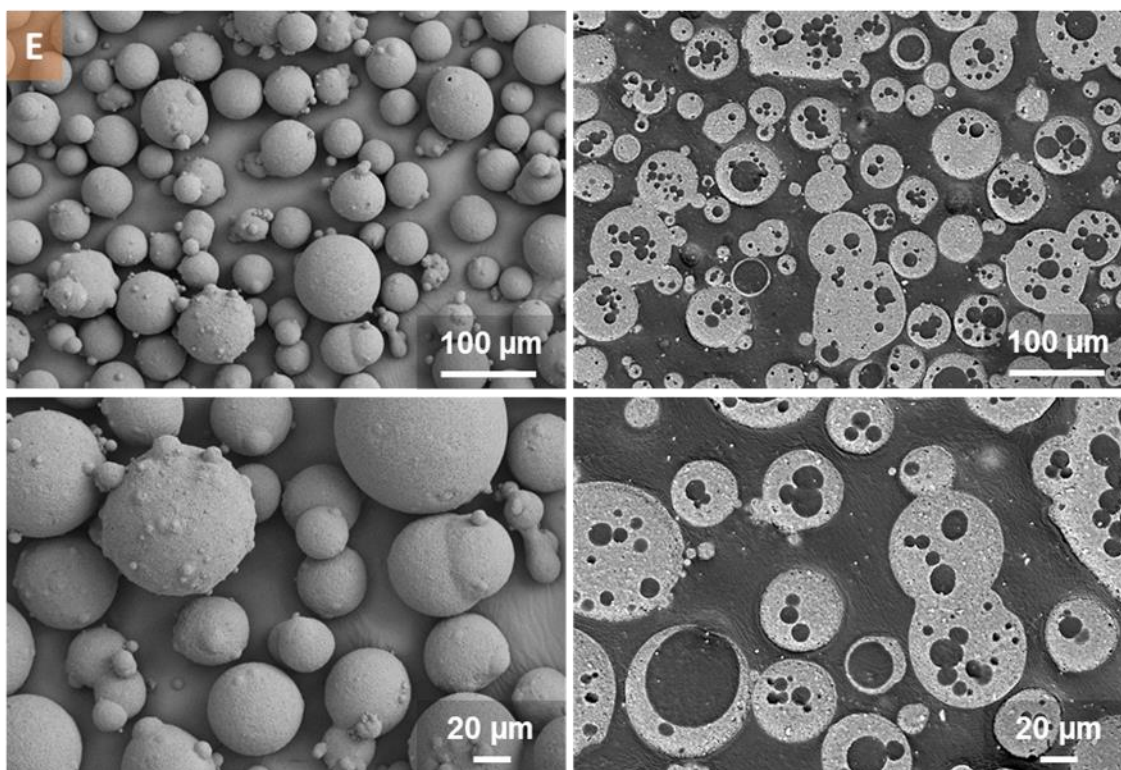
Figure 53. Micrographs of E granules (250 cP – 50 wt. % Alumina – 5.0 wt. % PVA).
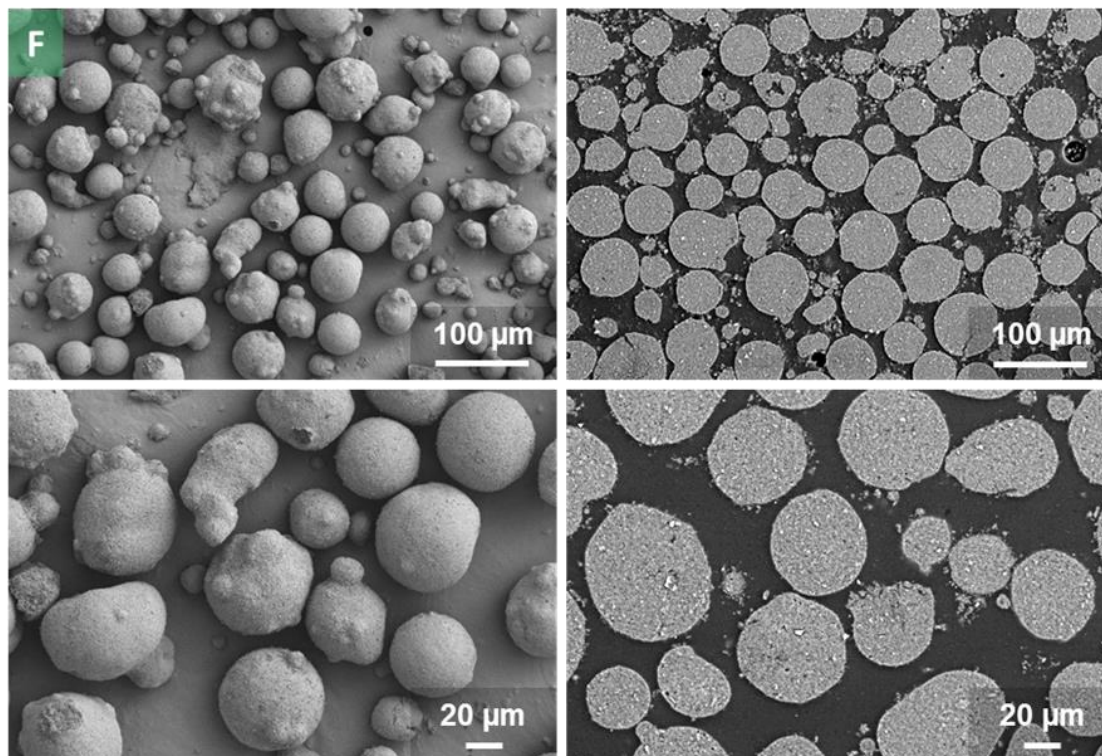
Figure 54. Micrographs of F granules (250 cP – 50 wt. % Alumina – 3.0 wt. % Acrylic).

The segregated binder layers formed from the PVA granules (A through E) generated a tougher surface layer than the acrylic granules (F). This layer caused an increase in the strength of the granulated powder, as shown in the critical yield pressure analysis in Figure 36 from the previous objective. The acrylic granules deformed at lower compaction pressures and were softer in comparison to the PVA granules. It is also possible that the hollow cores and microstructural defects act as stress concentrators, almost like a spring. This behavior may cause the increase in agglomerate strength and diminish achieving higher density parts at lower compaction pressures.

Micrographs were taken at specific uniaxial compaction pressures for all ten granule cases, A through J, to visualize the compaction behavior throughout their respective compaction curve. Four pressures were attempted for this analysis; 3.5, 10, 50, and 100 MPa. The only granules that formed compacts with sufficient green strength at a pressure of 3.5 MPa to support the strength needed to infiltrate and prepare the specimens for microstructural characterization were granules G through I (the B granules at moisture contents of 2.07%, 3.98%, and 5.97% respectively). The acrylic emulsion granules compacted with zero (F) and 1.93% moisture content (J) had a problem of sticking to the compaction die when attempting to eject the compact after the compaction run. The microstructures of these compacts as well as their respective compaction curves highlighting their critical yield pressures and joining points are shown in **Error! Reference s ource not found.** through **Error! Reference source not found.**.

This process was sufficient to compare the respective microstructures at specific compaction pressures over the varying processing parameters. The deformation behavior of the granules can be visualized throughout the compaction stages of II and III for all ten

of the varying granule cases. In terms of the differences noted between the granules processed with the PVA binder, granules A through E, there existed a variation in the resulting degree of granule remnants visualized. This occurred for all three of the listed compaction pressures. Comparing granules A through C, granule remnant boundaries were more abundantly observed within the microstructures of the compacts processed with the higher viscosity values prior to the spray-drying process. Comparing the microstructures of the compacts processed with the C and D granules, increasing the solids loading resulted in microstructures with a higher degree of granule remnants and boundaries. The same behavior was noted as well when comparing the B and E granules with the varying degrees of binder amount. With increasing viscosity, solids loading, and binder amount, there was an increasing degree of granule remnant boundaries visualized within the compact's microstructure. This could likely be due to the spray-dried granule's structure and shape. The higher degree of circularity observed for the spray-dried granules resulted in granule remnants that persisted throughout the compaction process. The deformation behavior of the granules is linked to their respective granule morphologies and relates to their final compacted microstructures. The resultant morphology seems to dictate the densification rate observed during the second stage of compaction. The binder species seems to dictate the final compacted green density, however, the granule morphology dictates the resultant alumina compact's microstructural characteristics. This visualization method gained insight on the differences that arise in dry-pressed alumina compacts processed at various processing parameters.
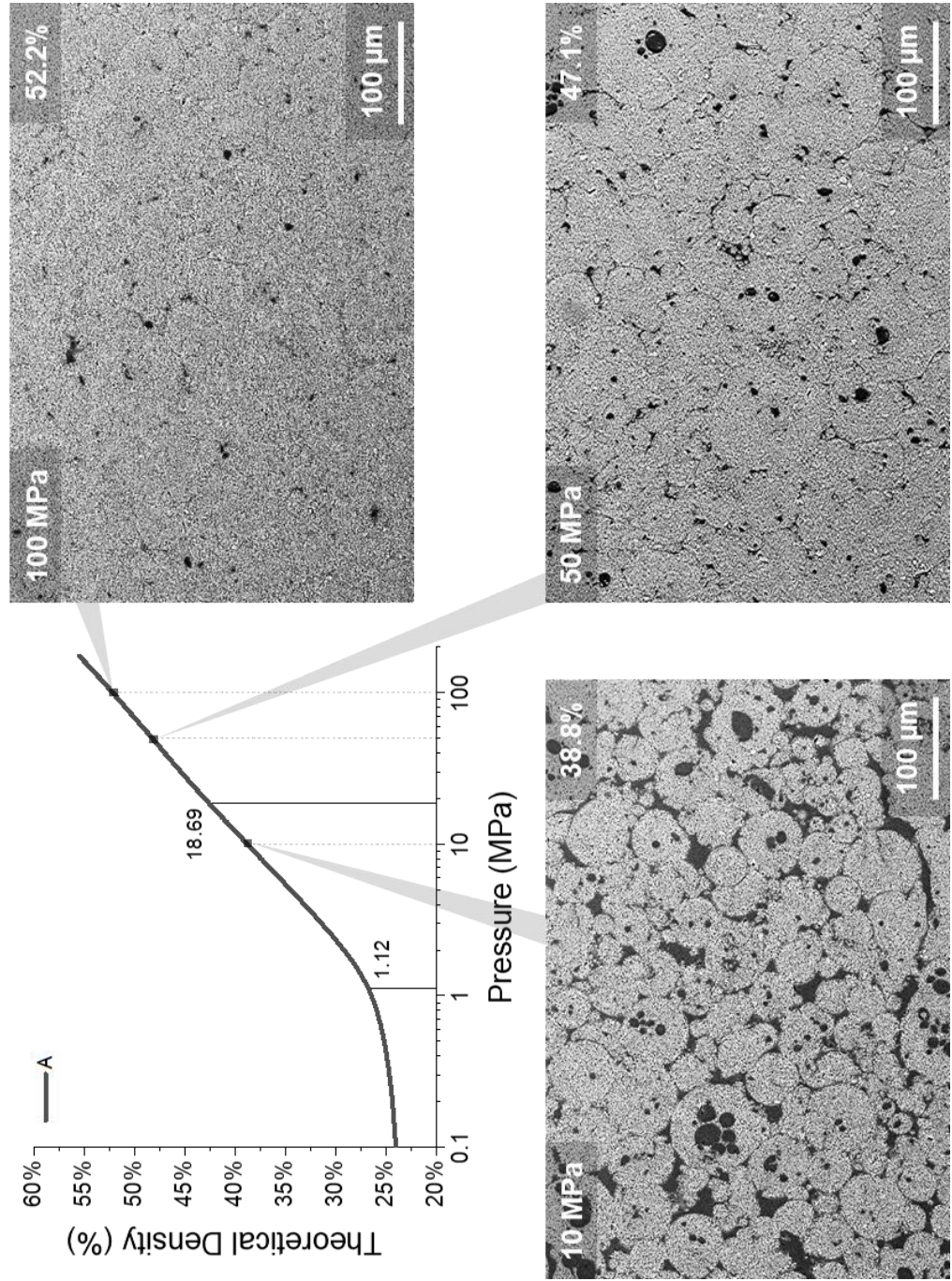
Figure 55. Micrographs of an alumina compact processed with the A granules at the various compaction pressures and respective theoretical density percentages. The compaction curve location is also shown for convenience.
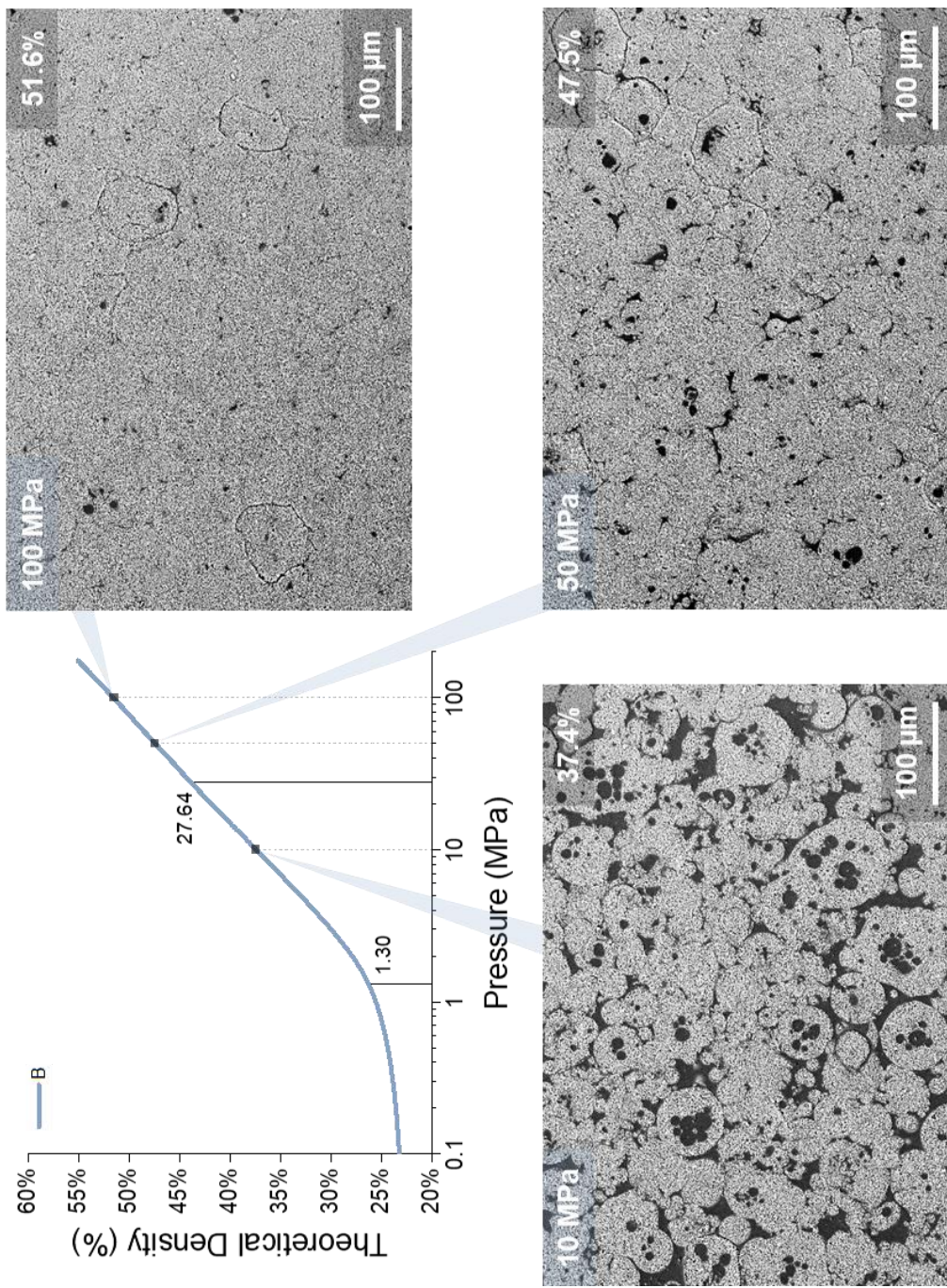
Figure 56. Micrographs of an alumina compact processed with the B granules at the various compaction pressures and respective theoretical density percentages listed. The compaction curve location is also shown for convenience.
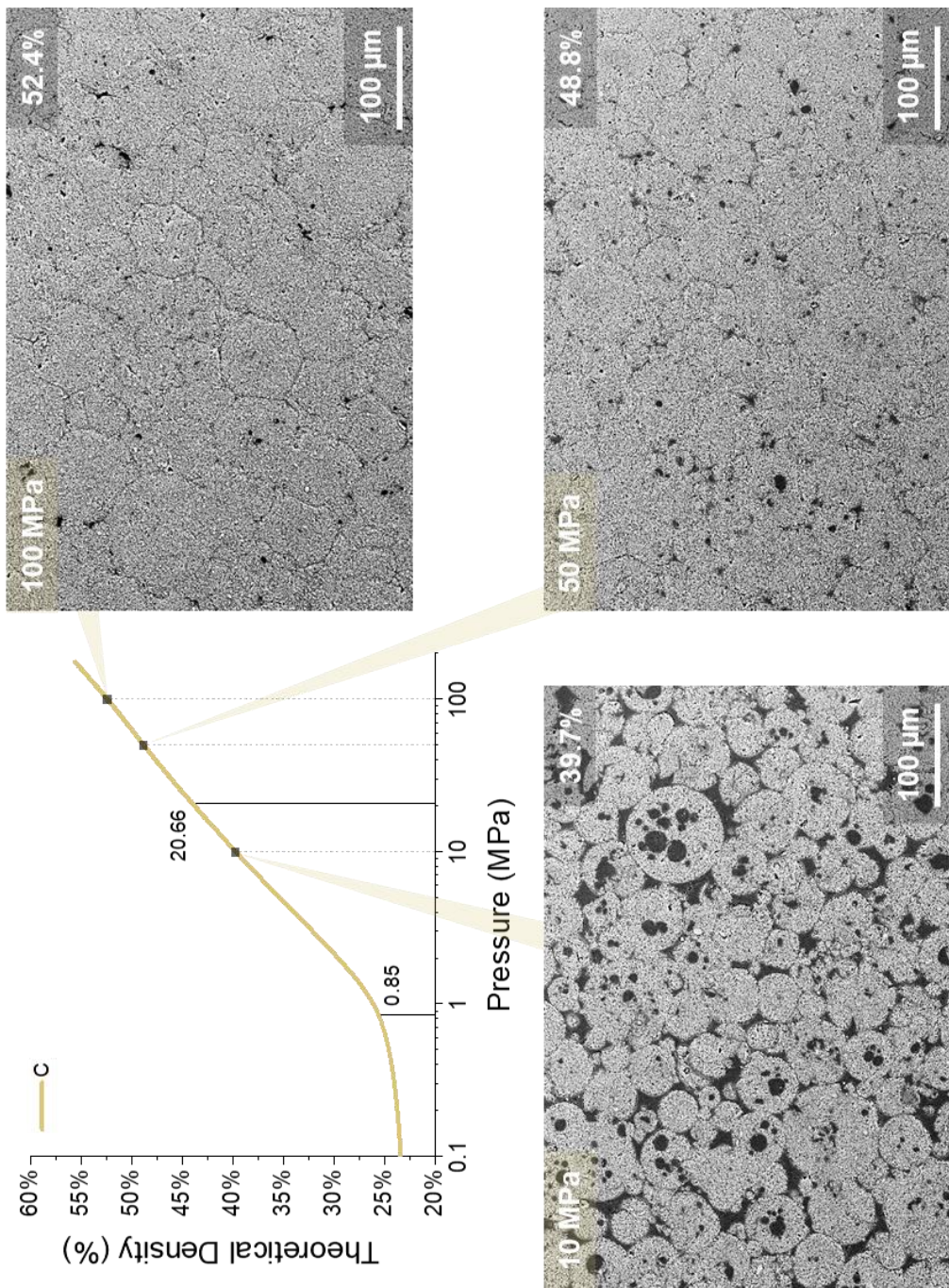
Figure 57. Micrographs of an alumina compact processed with the C granules at the various compaction pressures and respective theoretical density percentages. The compaction curve location is also shown for convenience.
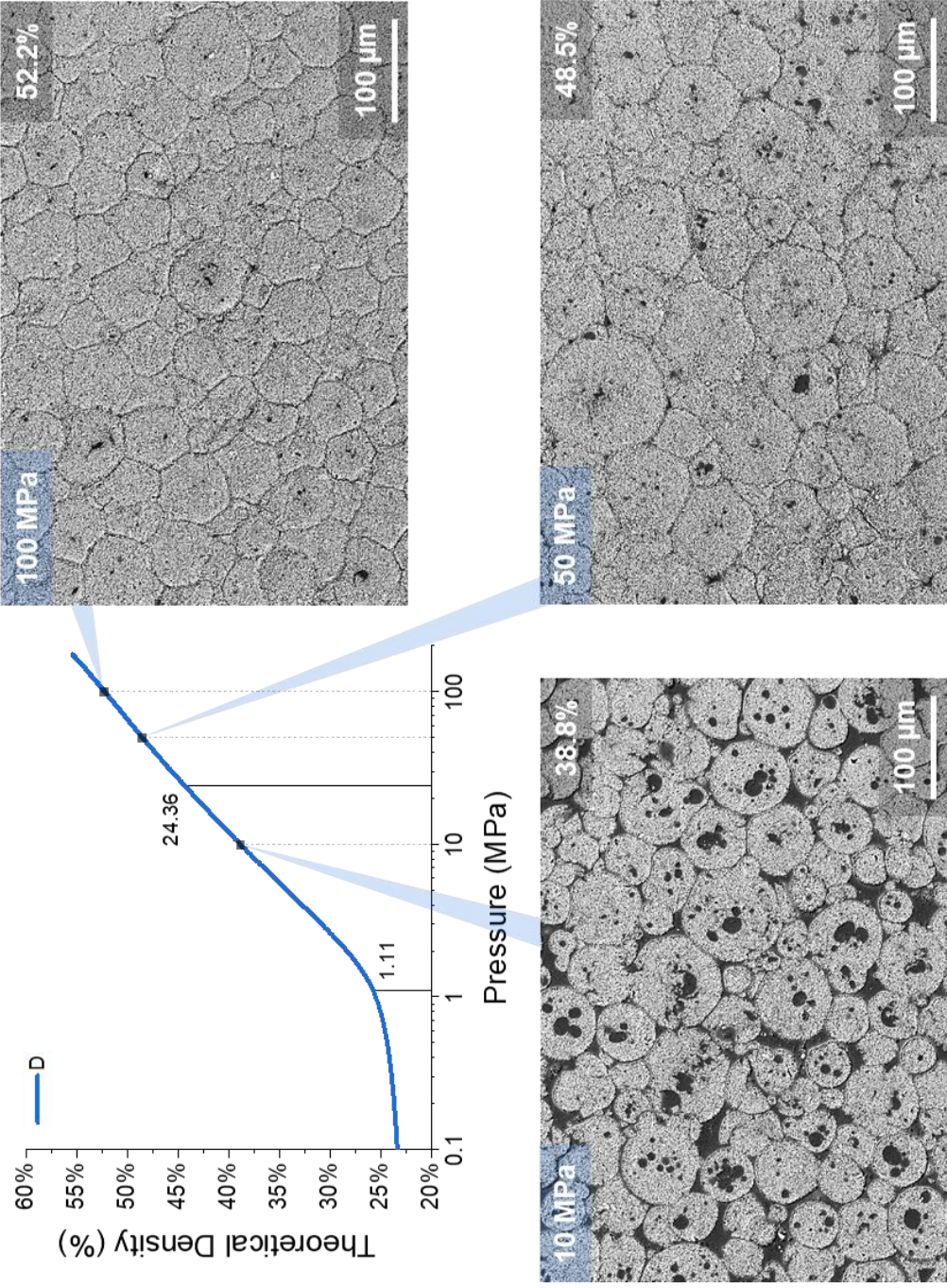
Figure 58. Micrographs of an alumina compact processed with the D granules at the various compaction pressures and respective theoretical density percentages listed. The compaction curve location is also shown for convenience.
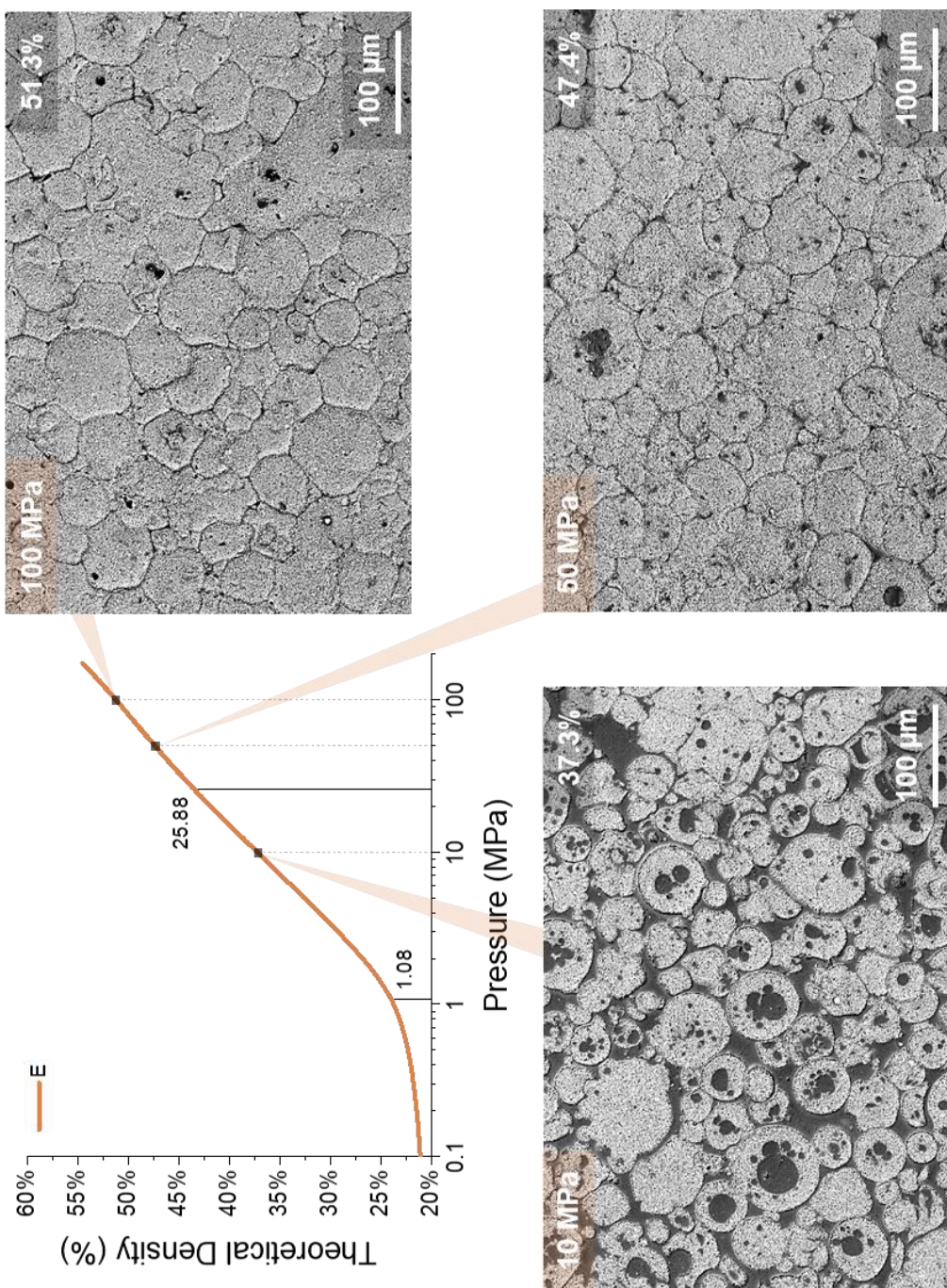
Figure 59. Micrographs of an alumina compact processed with the E granules at the various compaction pressures and respective theoretical density percentages listed. The compaction curve location is also shown for convenience.
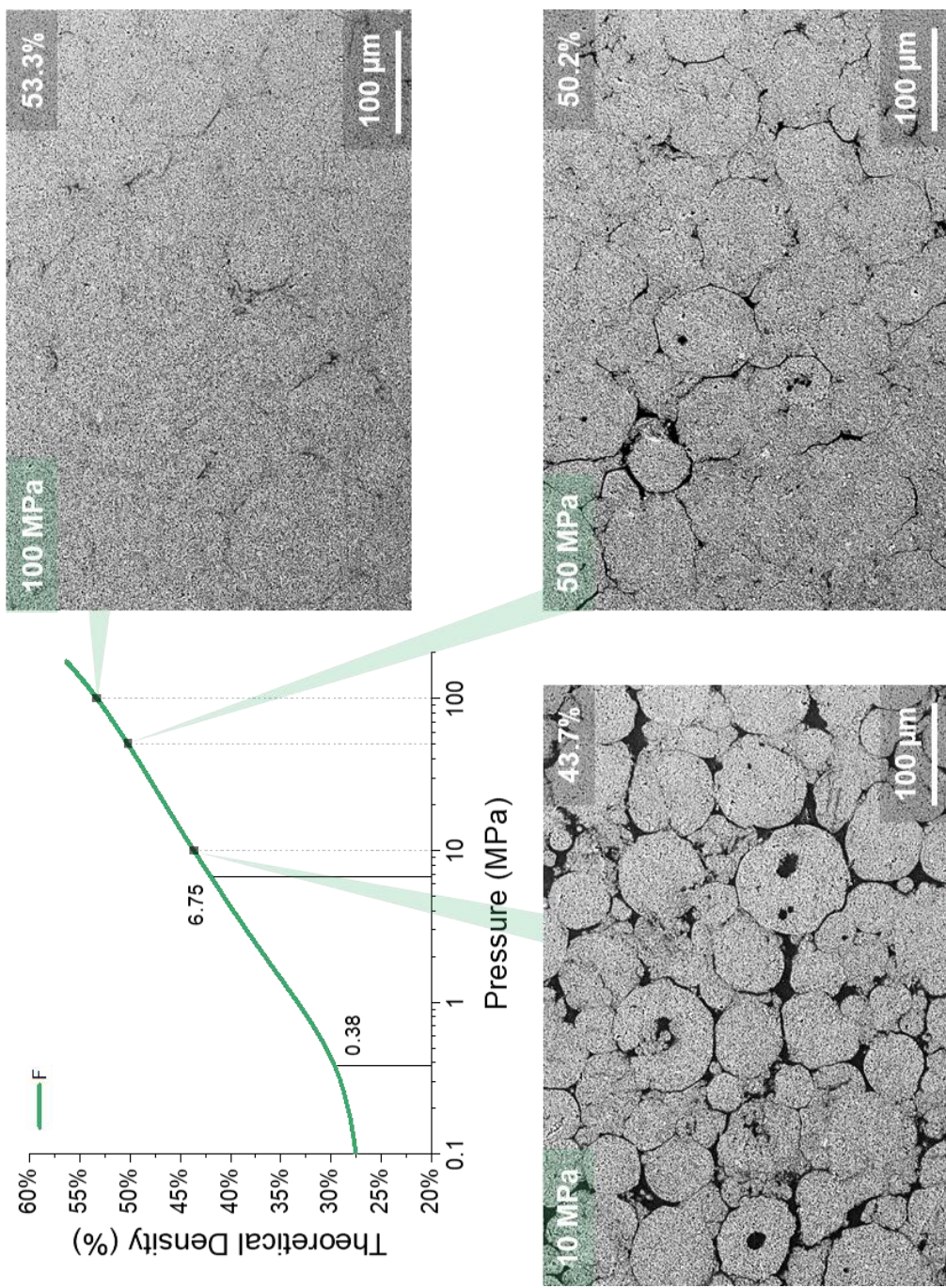
Figure 60. Micrographs of an alumina compact processed with the F granules at the various compaction pressures and respective theoretical density percentages listed. The compaction curve location is also shown for convenience.
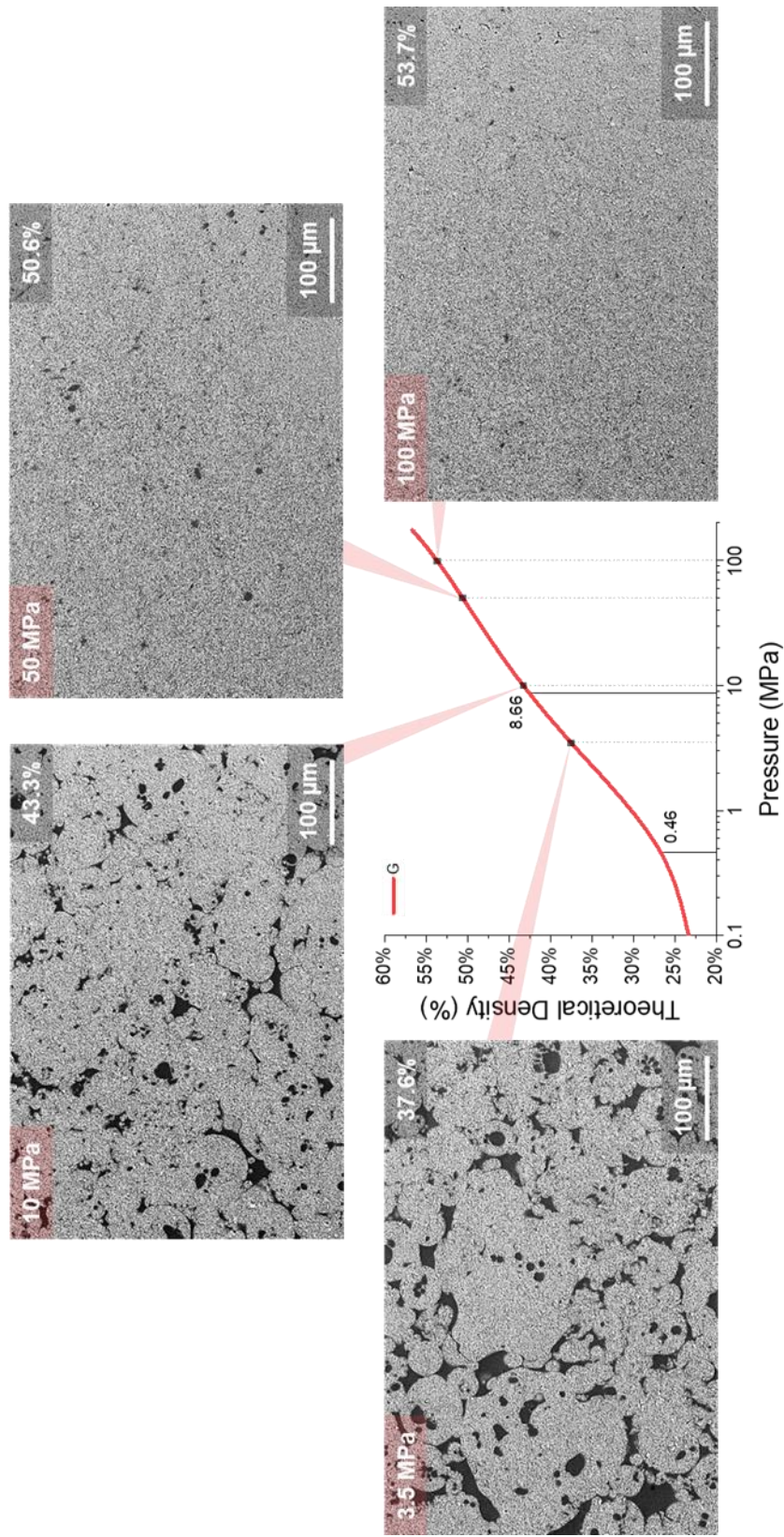
Figure 61. Micrographs of an alumina compact processed with the G granules at the various compaction pressures and respective theoretical density percentages listed. The compaction curve location is also shown for convenience.
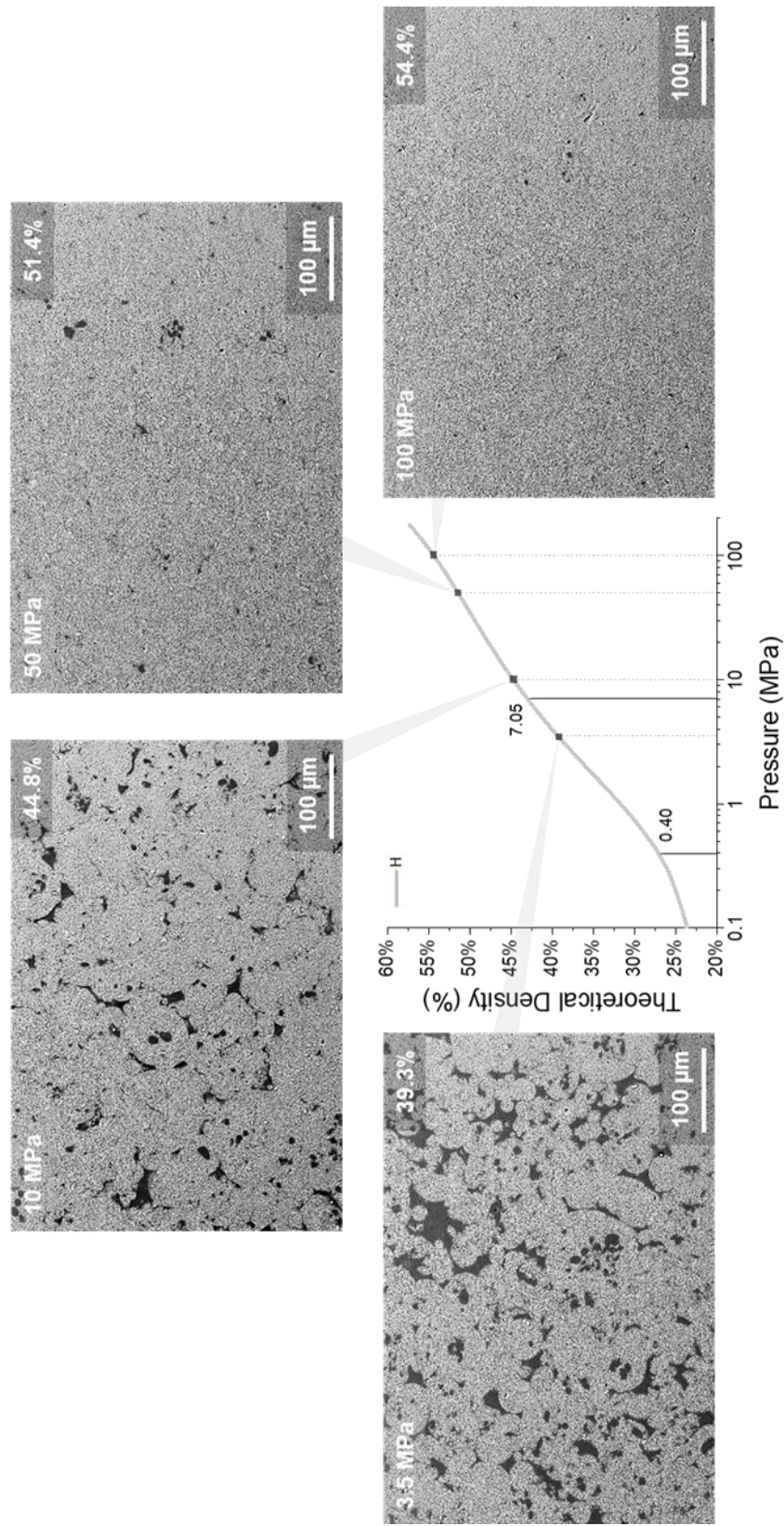
Figure 62. Micrographs of an alumina compact processed with the H granules at the various compaction pressures and respective theoretical density percentages listed. The compaction curve location is also shown for convenience.
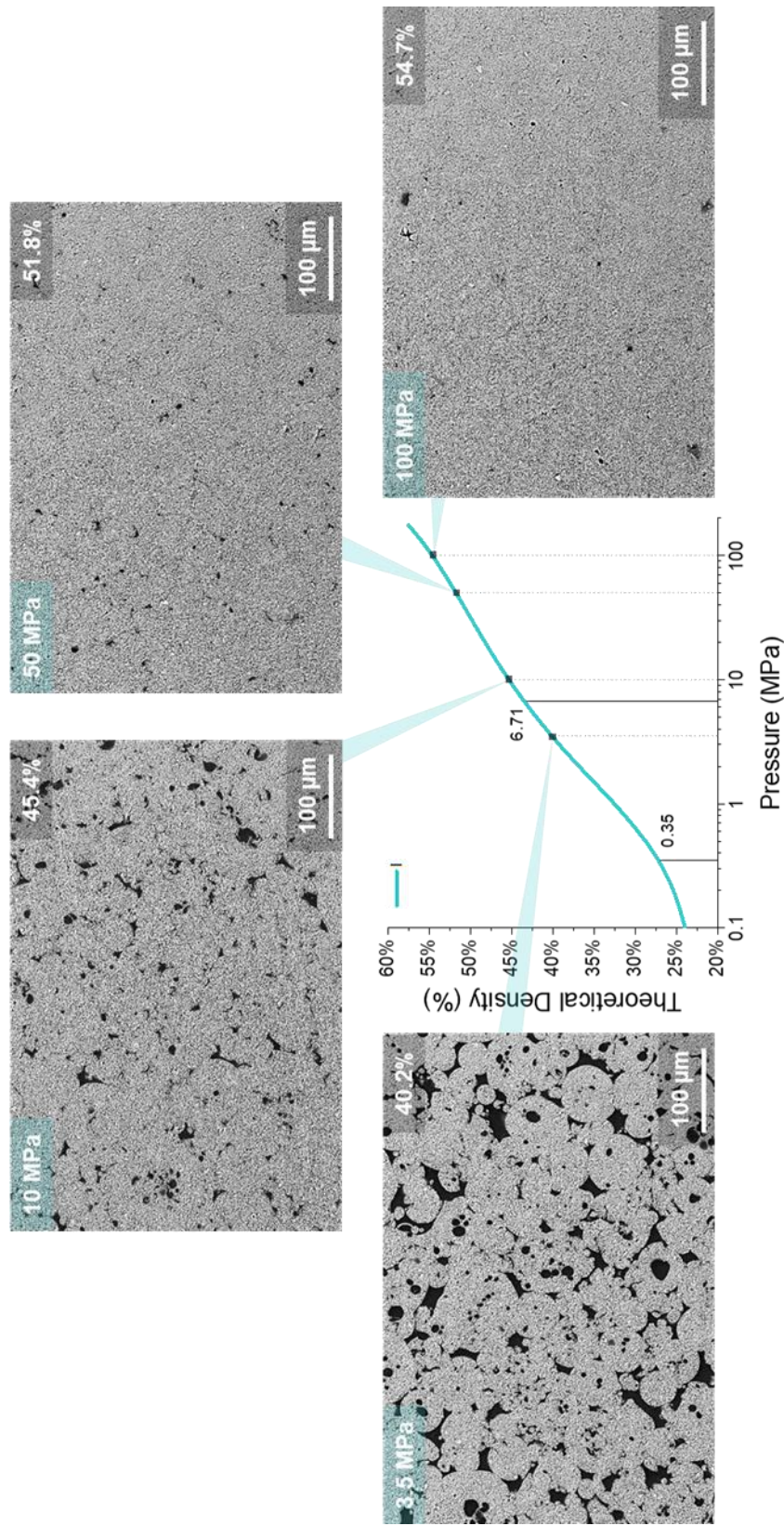
Figure 63. Micrographs of an alumina compact processed with the I granules at the various compaction pressures and respective theoretical density percentages listed. The compaction curve location is also shown for convenience.
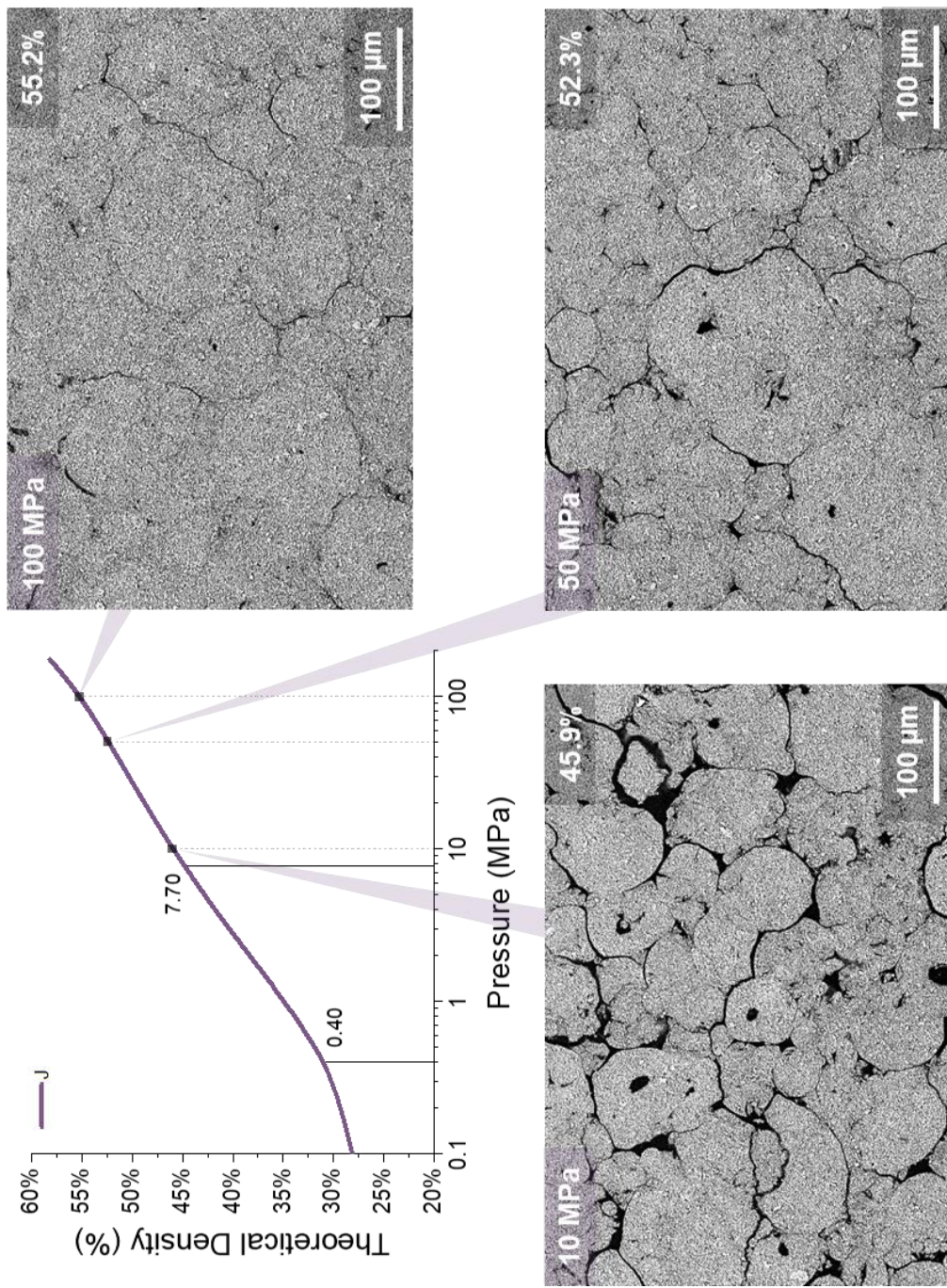
Figure 64. Micrographs of an alumina compact processed with the J granules at the various compaction pressures and respective theoretical density percentages listed. The compaction curve location is also shown for convenience.

A higher degree of microstructural uniformity was visualized within the compacts processed with the acrylic emulsion binder granules (F) as shown in **Error! Reference source not found.**. Comparing the alumina compact's microstructures of the PVA granules (A through E) to the acrylic emulsion granules (F), there was no visualized granule remnant boundaries observed. However, the porosity seemed localized along the region where the granule boundaries are located. Comparing the F granules with their acrylic binder counterpart compacted at 1.93% moisture (J), there seems to occur a slightly higher degree of the localized porosity along these granule boundary regions, even though the J compacts resulted in the highest relative density values. It is possible that the moisture resulted in density gradients within the alumina compact. This reason could also be what caused the decreased flexural green strength values for the tested specimens compacted with the J granules when compared to the acrylic granules compacted with zero percent moisture.

The microstructures of granules G through I, shown in **Error! Reference source not found.** through **Error! Reference source not found.** respectively, resulted in a higher degree of visualized microstructural uniformity when compared to the same granules compacted without a moisture content (B). This resultant observation was what was expected when adding moisture to a granule that was spray-dried with a water soluble binder. The moisture plasticized and softened the organic binder, resulting in microstructures that achieved higher densities at lower compaction pressures. Adding the moisture also gained the possibility of removing the microstructural defects and hollow cores within the internal structure of the spray-dried granules processed with the PVA binder. If removed, the closed porosity that is visualized within the compacts pressed from granules A through E would be minimized. Thus, sintering kinetics would be enhanced and

higher density parts may be achieved. There is a possibility of causing larger density gradients within the compacts pressed with higher levels of moisture content, however, this cannot be qualitatively analyzed without a needed method to visualize the compacts three-dimensionally.

The microstructures of the alumina compacts were also characterized at the final uniaxial compaction pressure of 175 MPa. The parallel and perpendicular direction of compaction were characterized for these samples using an InLens and back-scatter detector (BSD). The perpendicular direction of compaction was achieved by following the method described in Figure 48, to expose the internal structure of the compact. The alumina compacts were also de-binded and their resultant microstructures were characterized. These micrographs are shown in Figure 65 through Figure 74.

Using the InLens detector resulted in micrographs with a higher degree of surface information. This detector pronounced the granule boundaries that existed within the A and B compacts that were not picked up within the BSD micrographs. The BSD micrographs were useful in differentiating compositional differences within the compact, such as the alumina material and lower density regions. It is evident that increasing the viscosity, solids loading, and binder amount within the ceramic slurries resulted in more pronounced regions of porosity along the granule boundaries due to the enhanced granule remnants visualized within the BSD micrographs.

Similar observations were made when evaluating the micrographs of the varying alumina compacts. In terms of the PVA granules (A through E), with increasing viscosity, solids loading, and binder amount, there existed a higher degree of granule remnant boundaries. The acrylic compacts showed localized porosity along the granule boundaries

in both cases of with (J) and without (F) moisture contents. The InLens micrographs of granules G through I resulted in microstructures with higher degrees of microstructural uniformity when compared to the other granules compacted with zero percent moisture content (B). The granule boundaries visualized within the InLens micrographs of the B compacts are no longer visible within the H and I alumina compacts processed with moisture contents of 3.98% and 5.97% respectively. This is evidence of moisture softening the spray-dried granules processed with the PVA binder and promoting microstructural uniformity. This behavior is shown and evident when visualizing the parallel and perpendicular direction of compaction.

Evaluating the perpendicular direction of compaction can be a useful tool in attempt to visualize the density gradients within the internal microstructure of the green ceramic materials. Evaluating the de-binded microstructures were useful in evaluating the degree of closed porosity prior to sintering for each varying case. The lowest degree of closed porosity was visualized in the compacts processed with granules F through I. The J compacts, even though resulting in the highest relative density measurements, had larger regions of localized porosity along the granule boundaries rather than smaller pores resulting from closed porosity. These three different methods of visualizing the green compacts (the perpendicular and parallel direction of compaction as well as the microstructure of the de-binded compacts), observed different attributes of the final compacted microstructure. These attributes included the degree of uniformity, localized regions of porosity, and granule remnant boundary occurrence.
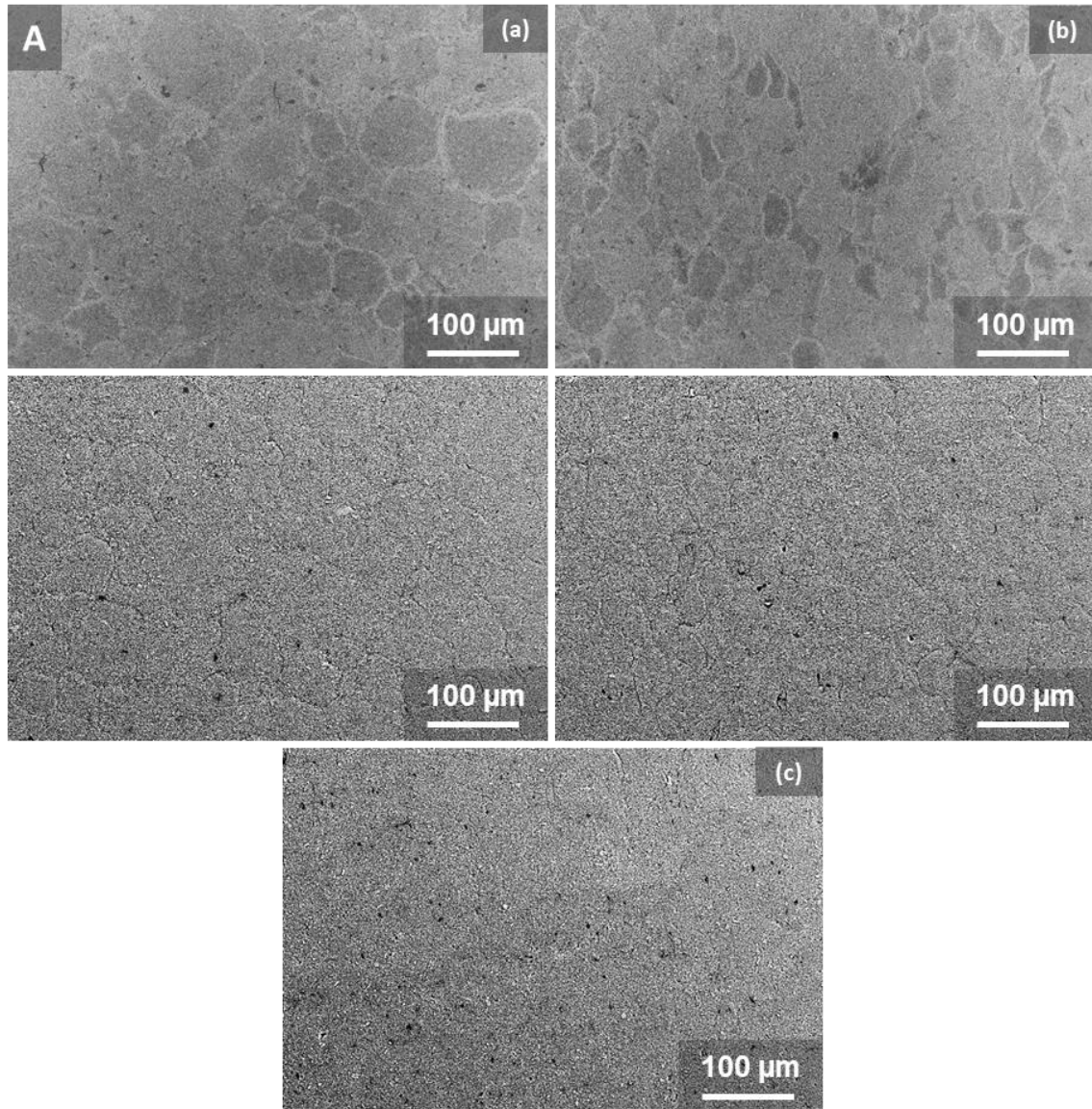
Figure 65. Micrographs of an alumina compact processed with the A granules at a uniaxial compaction pressure of 175 MPa. (a) Visualizing the parallel direction of compaction with an InLens and BSD images, (b) the perpendicular direction of compaction with an InLens and BSD image, (c) and the microstructure after binder burnout.
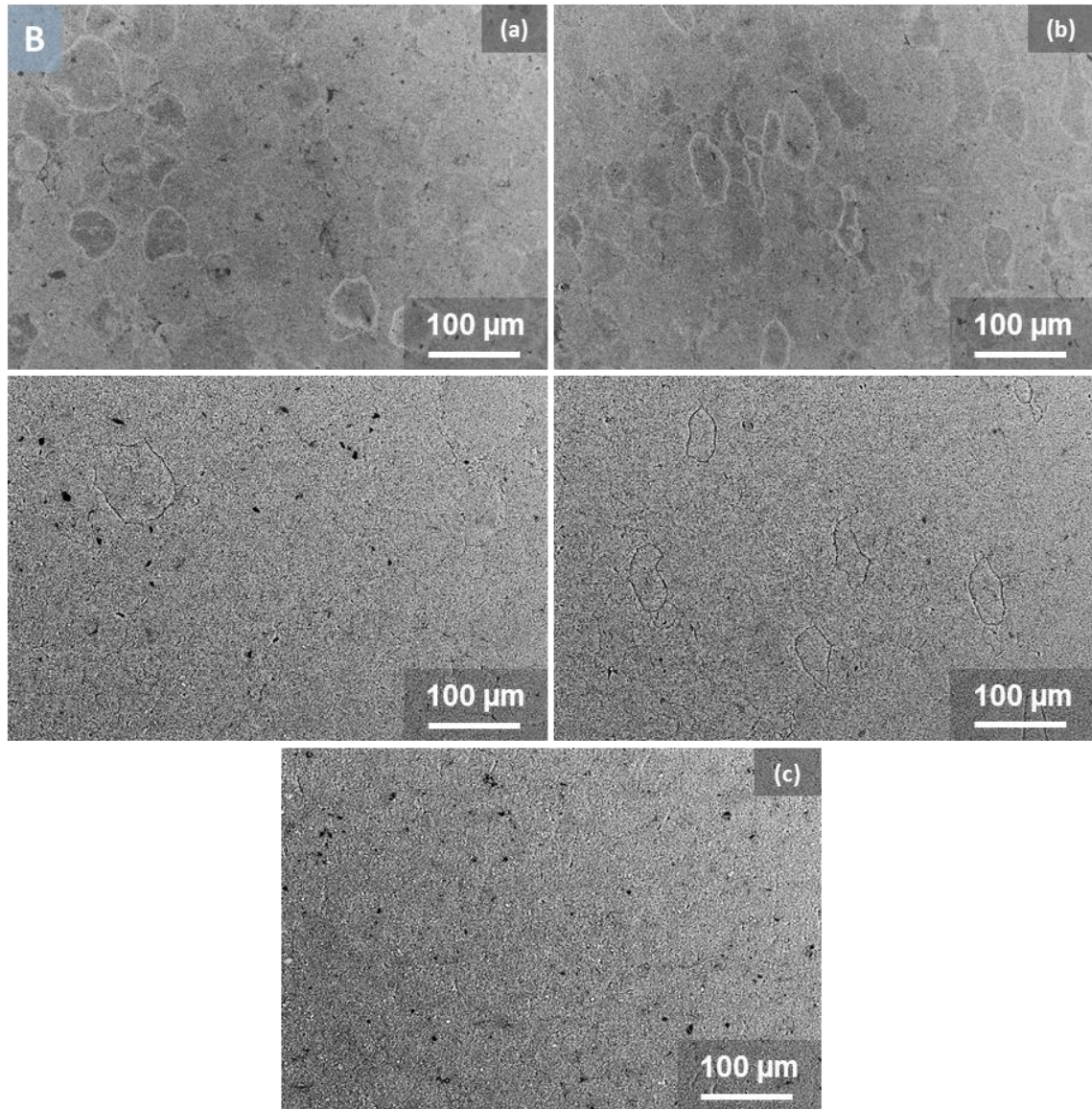
Figure 66. Micrographs of an alumina compact processed with the B granules at a
uniaxial compaction pressure of 175 MPa. (a) Visualizing the parallel direction
of compaction with an InLens and BSD images, (b) the perpendicular direction
of compaction with an InLens and BSD image, (c) and the microstructure after
binder burnout.
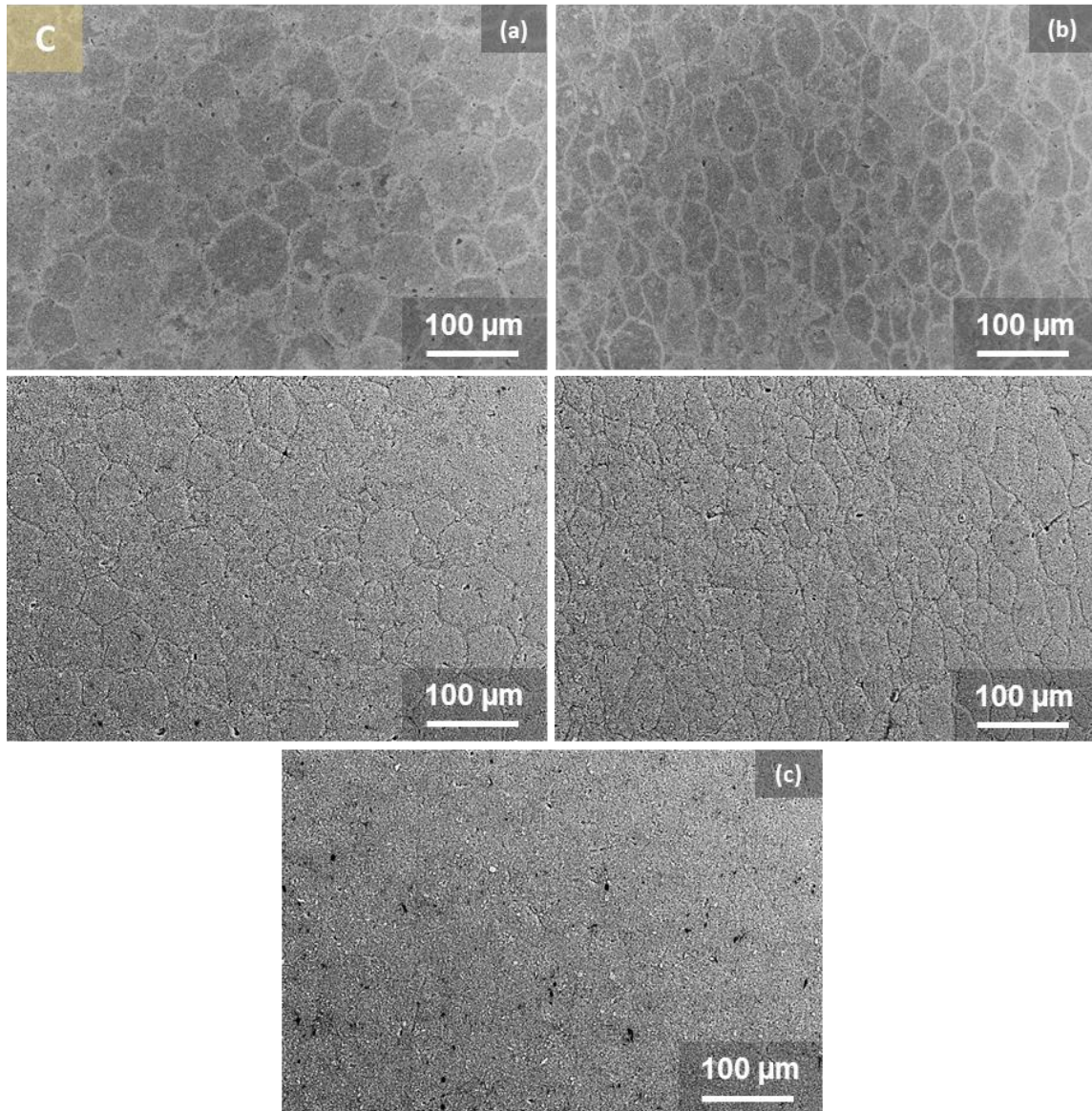
Figure 67. Micrographs of an alumina compact processed with the C granules at a
uniaxial compaction pressure of 175 MPa. (a) Visualizing the parallel direction
of compaction with an InLens and BSD images, (b) the perpendicular direction
of compaction with an InLens and BSD image, (c) and the microstructure after
binder burnout.
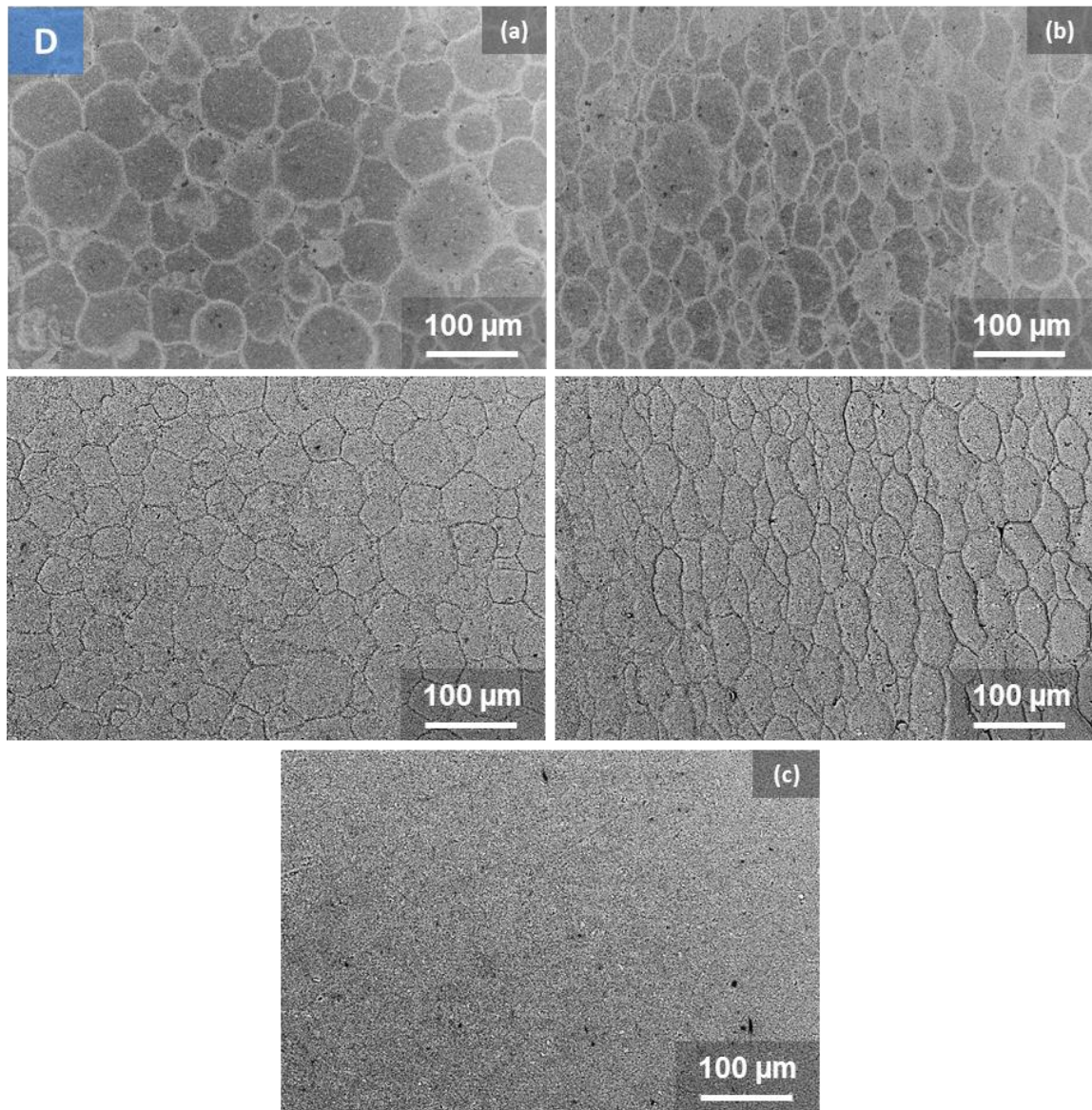
Figure 68. Micrographs of an alumina compact processed with the D granules at a uniaxial compaction pressure of 175 MPa. (a) Visualizing the parallel direction of compaction with an InLens and BSD images, (b) the perpendicular direction of compaction with an InLens and BSD image, (c) and the microstructure after binder burnout.
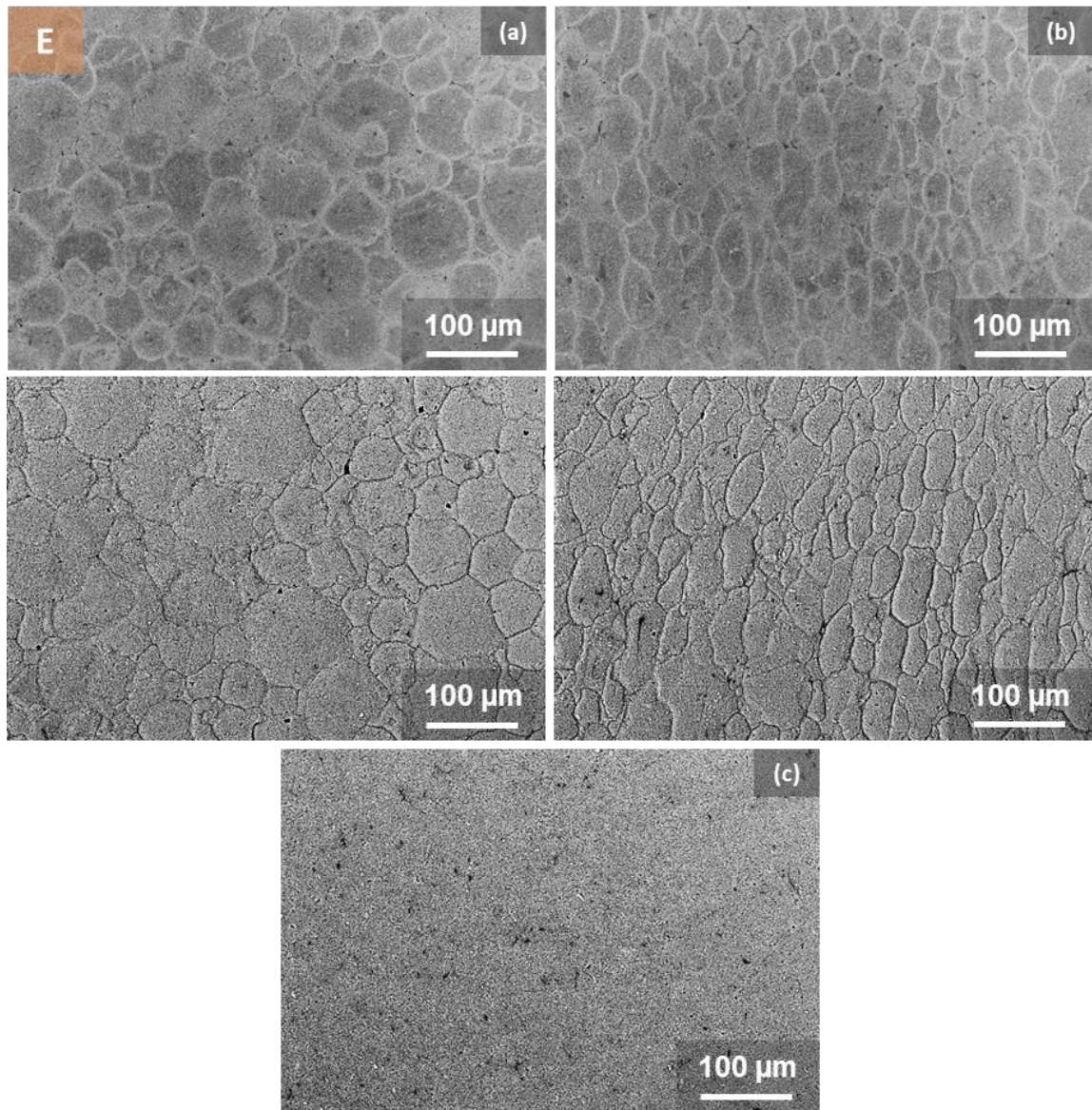
Figure 69. Micrographs of an alumina compact processed with the E granules at a
uniaxial compaction pressure of 175 MPa. (a) Visualizing the parallel direction
of compaction with an InLens and BSD images, (b) the perpendicular direction
of compaction with an InLens and BSD image, (c) and the microstructure after
binder burnout.
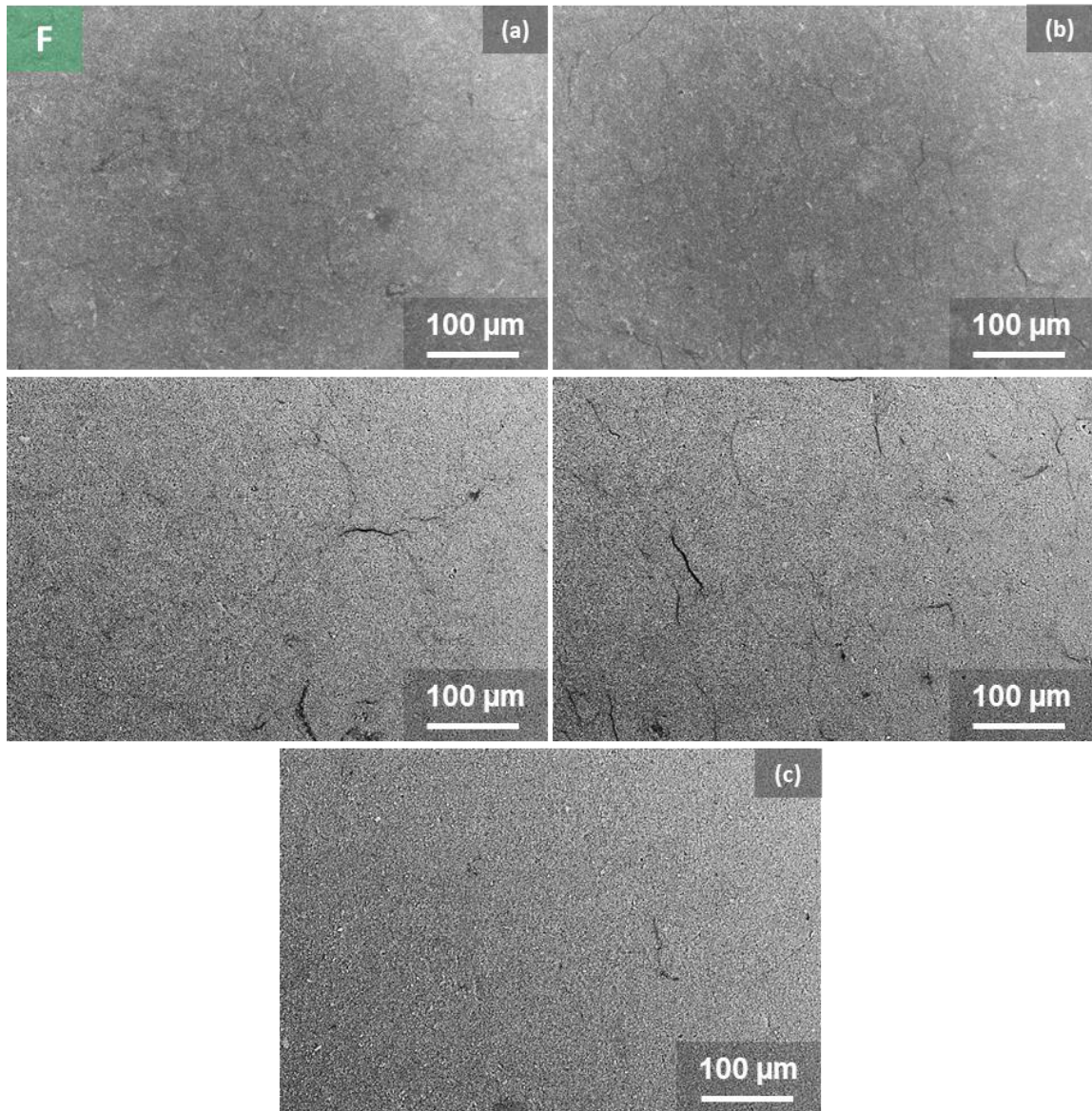
Figure 70. Micrographs of an alumina compact processed with the F granules at a
uniaxial compaction pressure of 175 MPa. (a) Visualizing the parallel direction
of compaction with an InLens and BSD images, (b) the perpendicular direction
of compaction with an InLens and BSD image, (c) and the microstructure after
binder burnout.
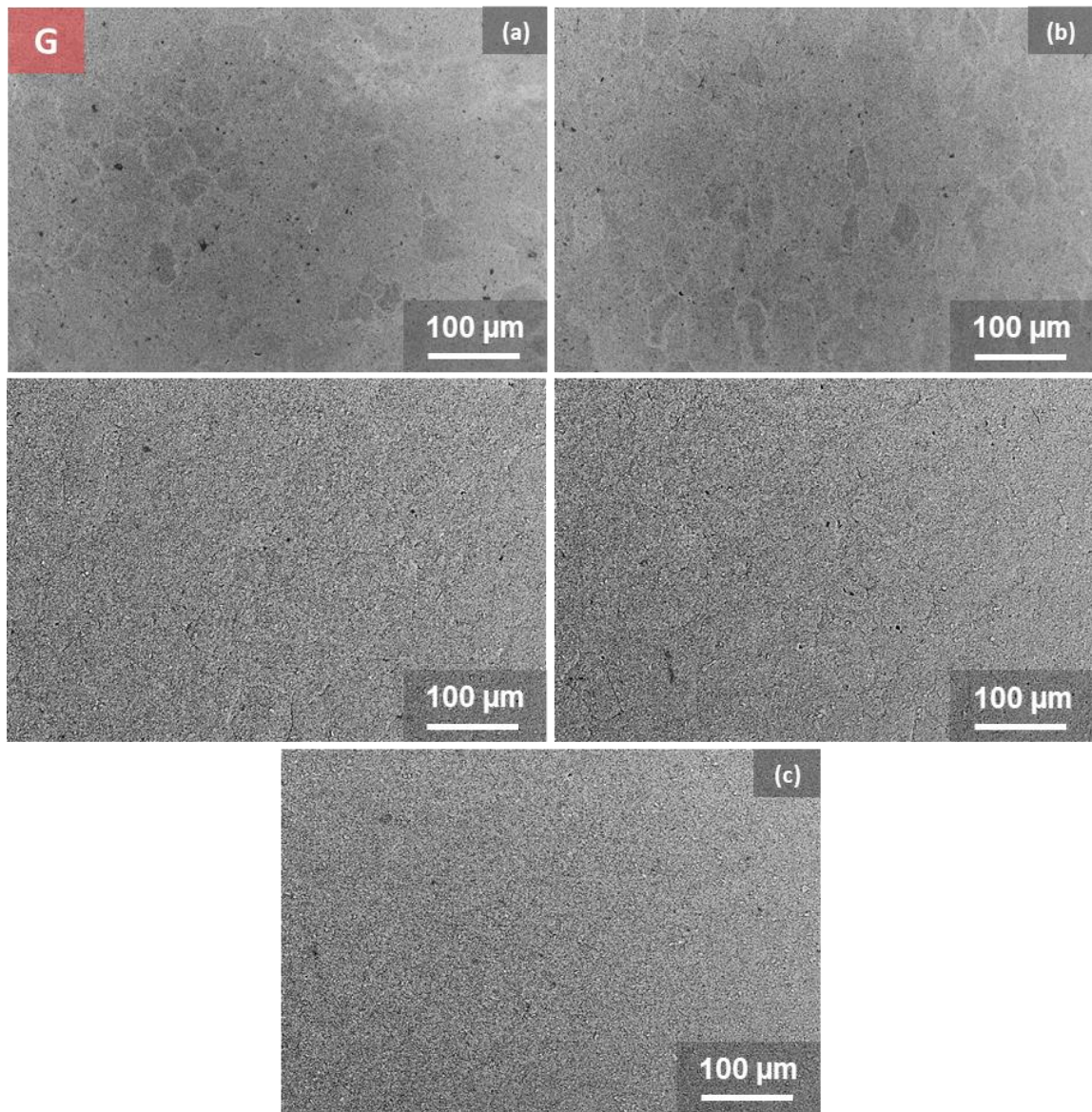
Figure 71. Micrographs of an alumina compact processed with the G granules at a uniaxial compaction pressure of 175 MPa. (a) Visualizing the parallel direction of compaction with an InLens and BSD images, (b) the perpendicular direction of compaction with an InLens and BSD image, (c) and the microstructure after binder burnout.
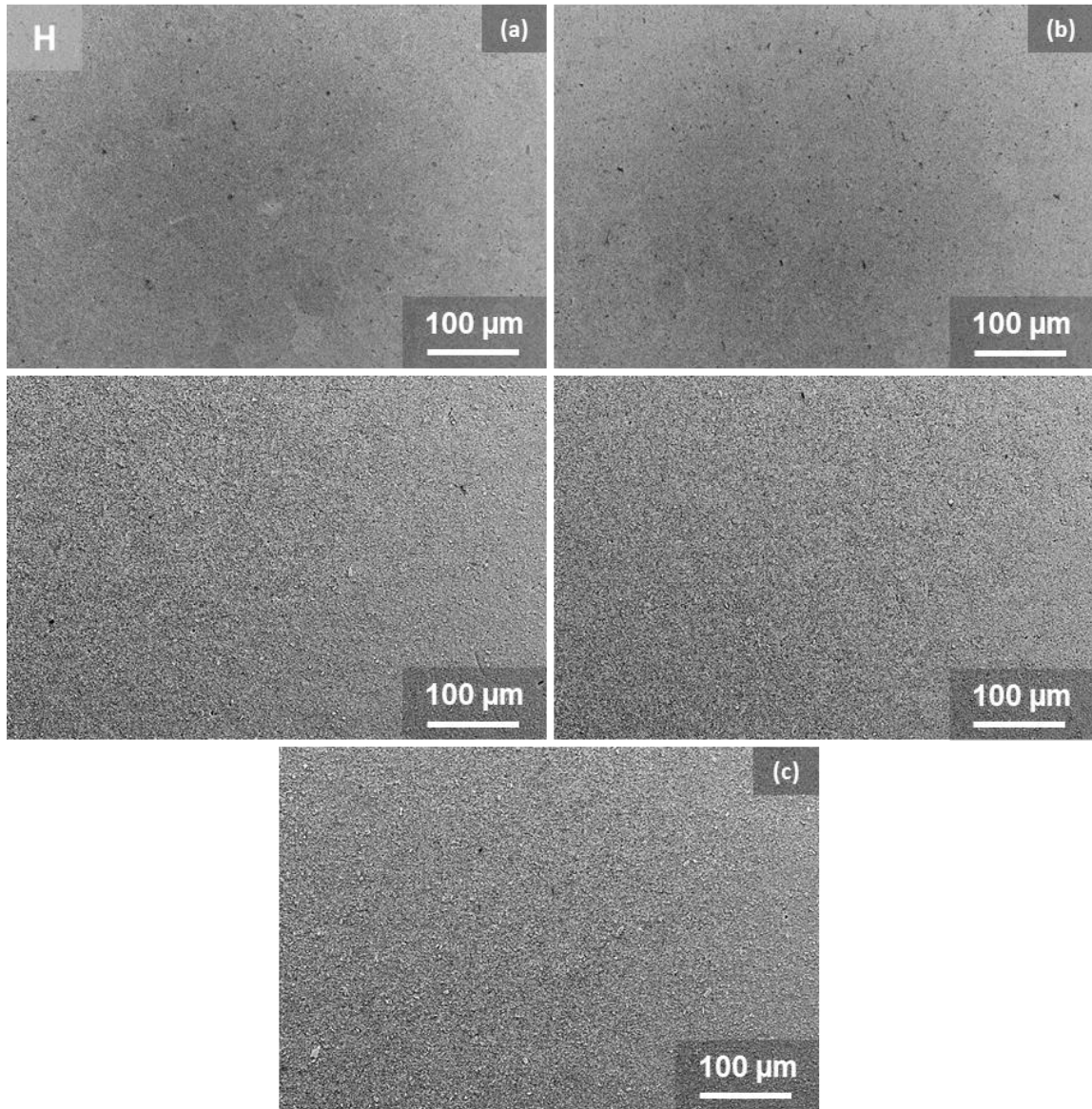
Figure 72. Micrographs of an alumina compact processed with the H granules at a
uniaxial compaction pressure of 175 MPa. (a) Visualizing the parallel direction
of compaction with an InLens and BSD images, (b) the perpendicular direction
of compaction with an InLens and BSD image, (c) and the microstructure after
binder burnout.
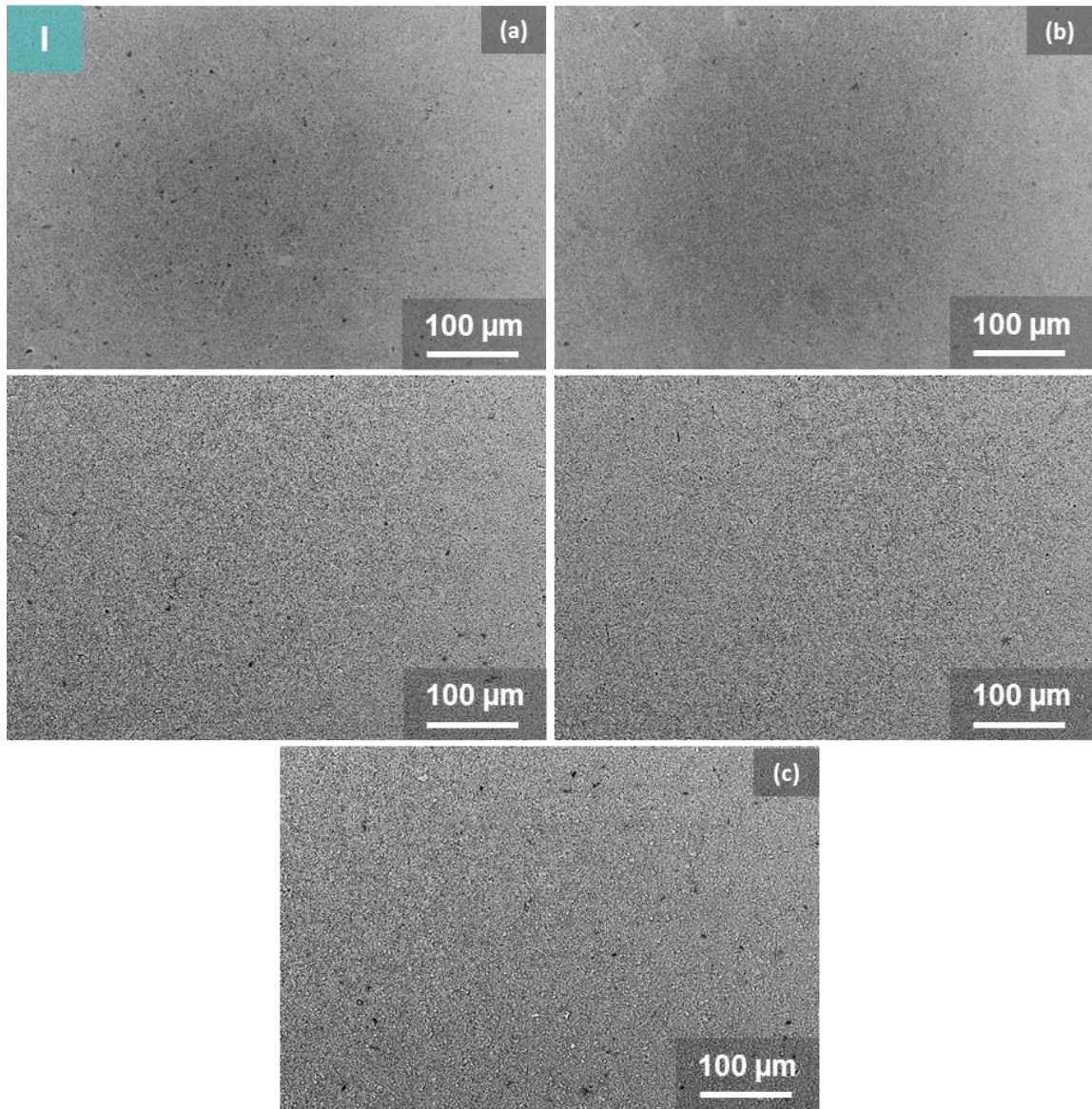
Figure 73. Micrographs of an alumina compact processed with the I granules at a uniaxial compaction pressure of 175 MPa. (a) Visualizing the parallel direction of compaction with an InLens and BSD images, (b) the perpendicular direction of compaction with an InLens and BSD image, (c) and the microstructure after binder burnout.
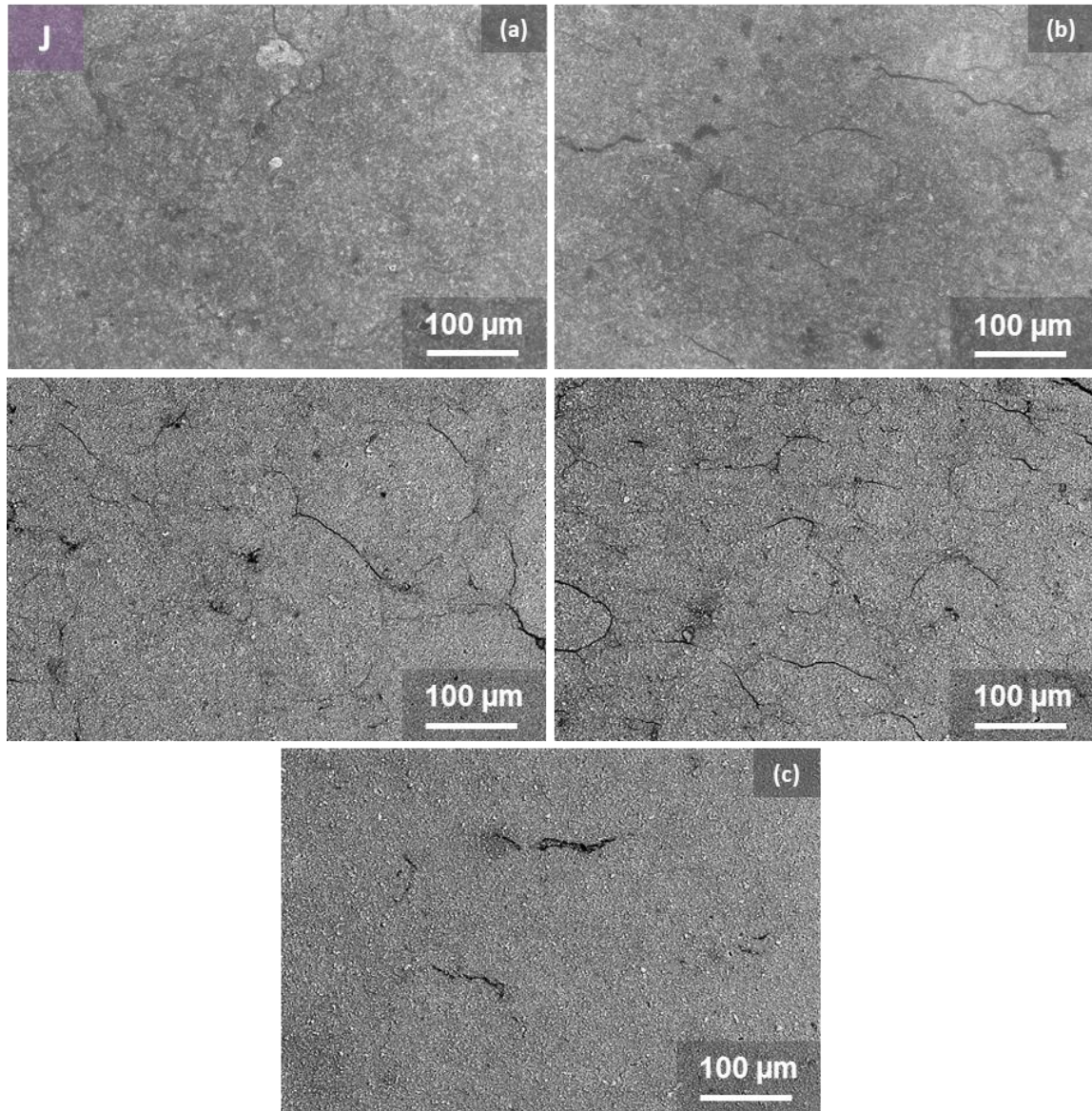
Figure 74. Micrographs of an alumina compact processed with the J granules at a uniaxial compaction pressure of 175 MPa. (a) Visualizing the parallel direction of compaction with an InLens and BSD images, (b) the perpendicular direction of compaction with an InLens and BSD image, (c) and the microstructure after binder burnout.

Microstructural characterization was conducted of the fracture surface for one the of the green strength samples that exhibited the highest flexural strength value for each of

the varying granule cases analyzed. The fracture surface and parallel direction of compaction were characterized on the FESEM in attempt to visualize the behavior observed in the modulus of rupture testing. The green bodies were sputtered coated with a nanolayer of gold to a thickness of 25 nm. The fracture surface samples were mounted on FESEM sample studs with carbon tape. Half of the sample's surface was covered with carbon tape to mitigate charging. As previously stated, these sections of the fracture surface were carefully cut out of the center of the sample with a serrated razor blade. The edge of the fracture surface was also cut out and infiltrated in preparation for mechanical polishing and microstructural characterization. These micrographs are shown in Figure 75 to Figure 81.

The lowest flexural strength samples were attributed to the specimens compacted with the B granules (50 wt. % alumina – 250 cP – 3.0 wt. % PVA). Observing the fracture surface micrograph in Figure 75, an abundance of granule remnants and boundaries that persisted throughout the compaction process can be visualized, which is likely where the stress localized during the rupture testing. Visual granule remnants were reduced with increasing moisture content added is seen when comparing Figure 77 through Figure 79, samples compacted with granules G through I respectively. As stated in section 6.B, the flexural strength increased with increasing moisture content. This is likely due to the higher degree of uniformity observed within the compacts processed with the I granules (5.97% moisture) in comparison to the compacts processed with the G and H granules (2.07% and 3.98% respectively).

The persistence of granule remnants remaining within the microstructures of the alumina compacts seems to be the governing factor in defining the flexural green strength

behavior. The higher degree of observed granule remnants resulted in lower green strength values. This is likely due to segregated binder layers formed along the granule boundaries of the PVA compacts, and when removed, form low density regions that act as stress concentrators and thus weaker alumina compacts. Also, due to the larger degree of hollow cores observed within the internal structure of the PVA granules, a higher degree of microstructural defects persisted within the microstructures and thus depleted the green strength of the sample. Adding moisture aided in removing these defects during the compaction process due to softening the granules. Therefore, the green strength increased with increasing moisture content during compaction for the PVA granules.

The acrylic emulsion compacts (F) had the second highest average flexural strength. This is likely due to the compaction characteristics observed in the previous section. The generated granules were softer than the PVA granules and promoted faster granule deformability and compact densities at lower compaction pressures. This phenomenon promoted the knitting behavior of the spray-dried granules that resulted in a higher degree of microstructural uniformity and thus higher green strength values. When evaluating the compacts processed with the acrylic emulsion granules at 1.93% moisture content (J), there were visible granule remnants on the fracture surface but not a significant amount more when compared to the compacts processed with the G and H granules, which exhibited higher green strength values. The reason the J compacts resulted in the highest relative density values but low green strength measurements could likely be due to the formation of density gradients within compact's microstructure. Coupling the other visualization results of the J compacts from this section, large localized porosity regions

located along the granule boundaries may act as stress concentrators, reducing the handability and green strength of the alumina compacts.

The micrographs shown in Figure 81 highlight granule remnants that persisted throughout the processing of alumina compacts made with B and I granules. Even adding 5.97% moisture (I) to soften the granules resulted in alumina compacts that exhibited persistent granule structures that were not removed during the compaction process. Processing dry-pressed compacts with a higher degree of microstructural uniformity are promoted from spray-dried granules that exhibit sufficient knitting behavior to remove these granule structures while increasing the handability and green strength of the ceramic. Coupling compaction curve analysis and the microstructural characterization of the processed spray-dried granules and resultant compacted microstructures allows one to gain an understanding of what processing parameters promote microstructural uniformity in dry-pressed ceramic parts.
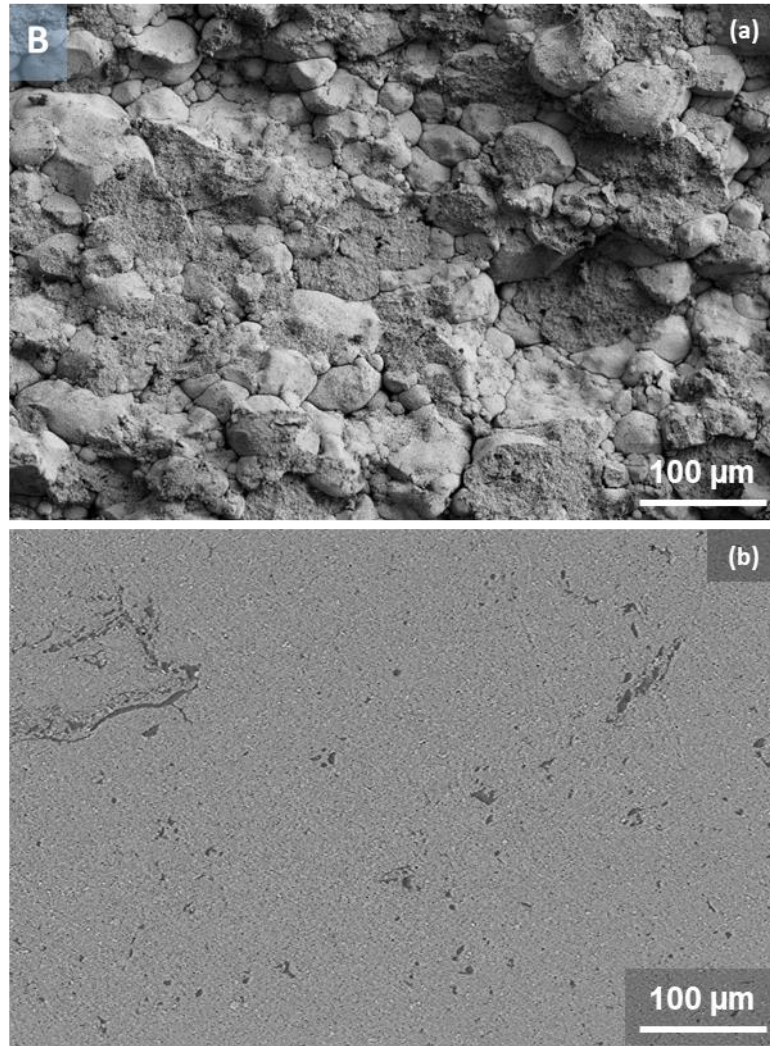
Figure 75. (a) FESEM micrograph of the fracture surface of a flexural strength sample compacted with the B granules and (b) a polished micrograph of the compact visualizing the parallel direction of compaction.
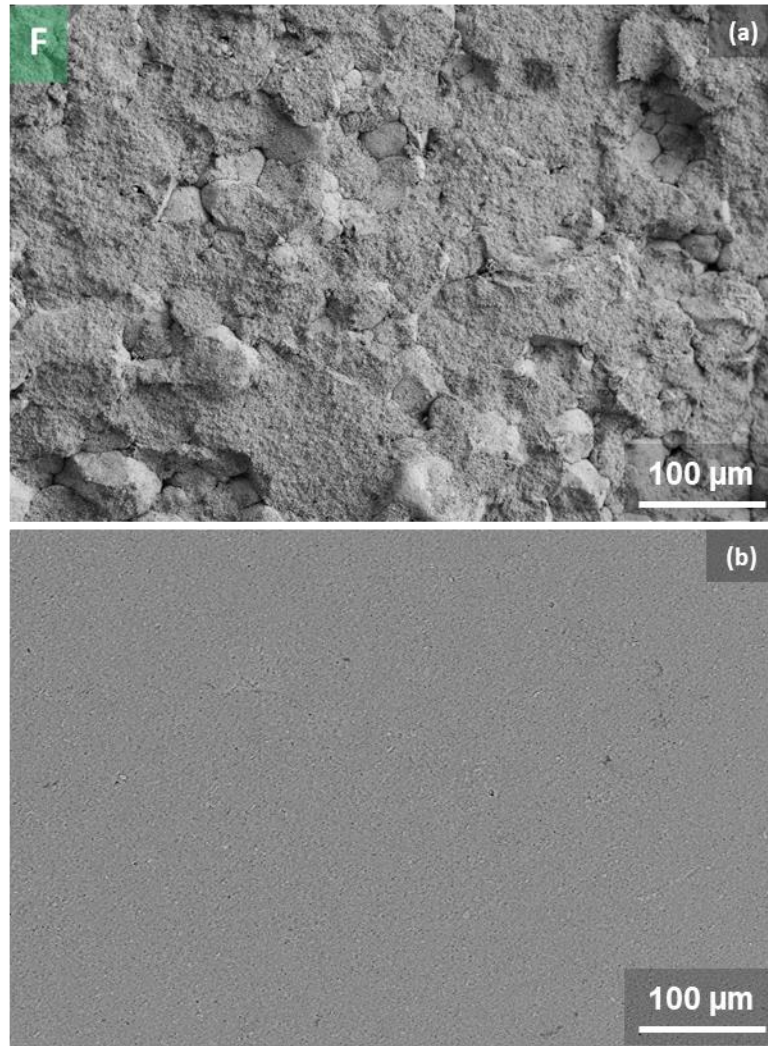
Figure 76. (a) FESEM micrograph of the fracture surface of a flexural strength sample compacted with the F granules and (b) a polished micrograph of the compact visualizing the parallel direction of compaction.
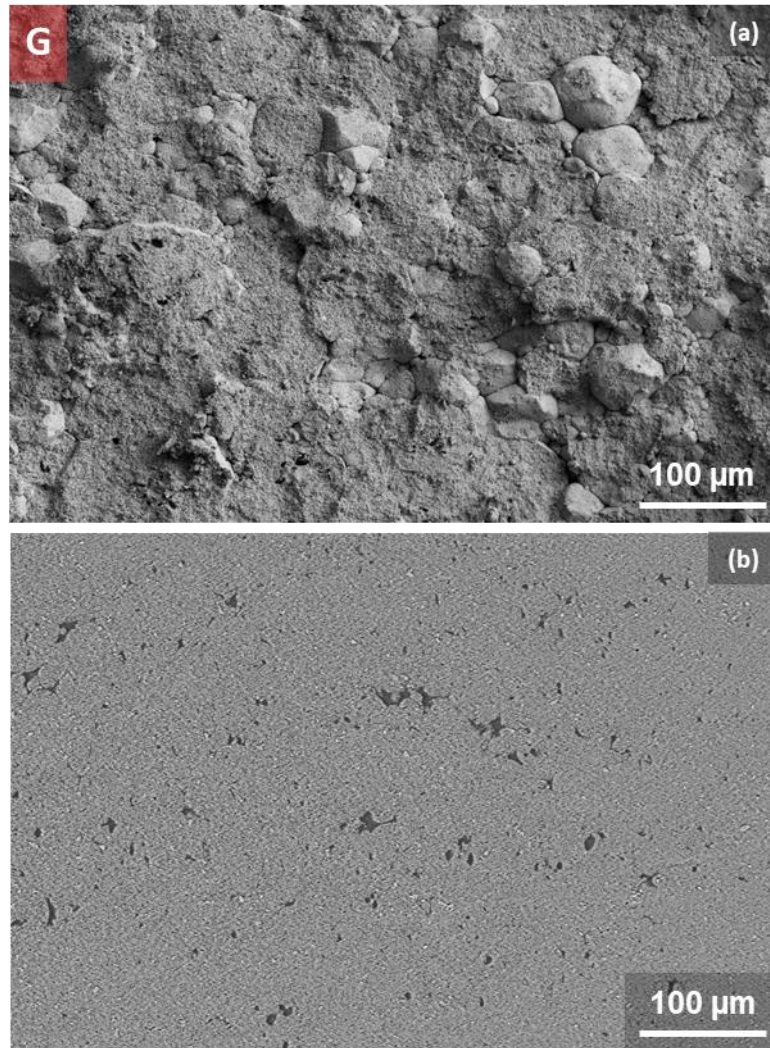
Figure 77. (a) FESEM micrograph of the fracture surface of a flexural strength sample compacted with the G granules and (b) a polished micrograph of the compact visualizing the parallel direction of compaction.
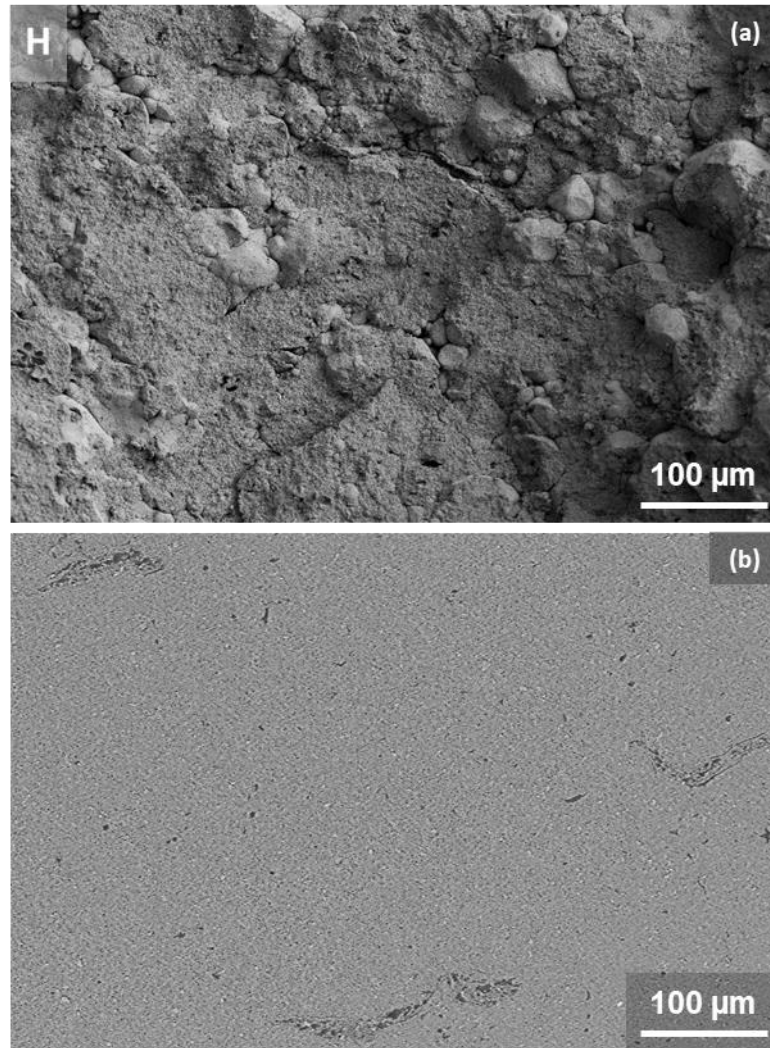
Figure 78. (a) FESEM micrograph of the fracture surface of a flexural strength sample compacted with the H granules and (b) a polished micrograph of the compact visualizing the parallel direction of compaction.
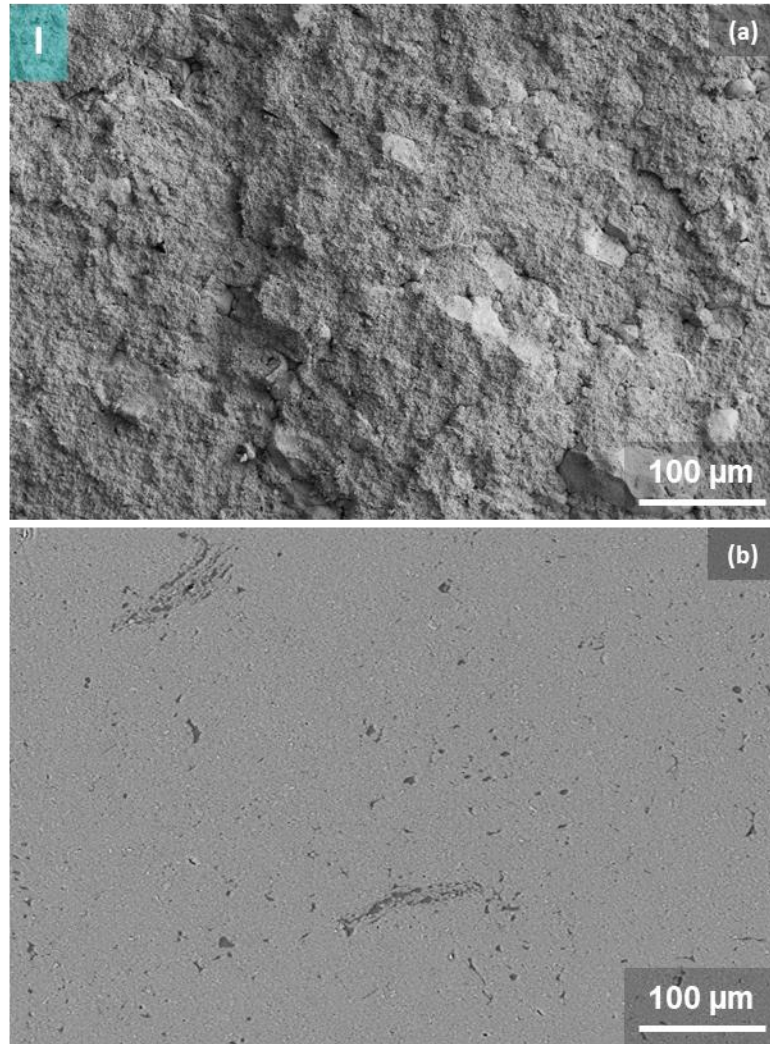
Figure 79. (a) FESEM micrograph of the fracture surface of a flexural strength sample compacted with the I granules and (b) a polished micrograph of the compact visualizing the parallel direction of compaction.
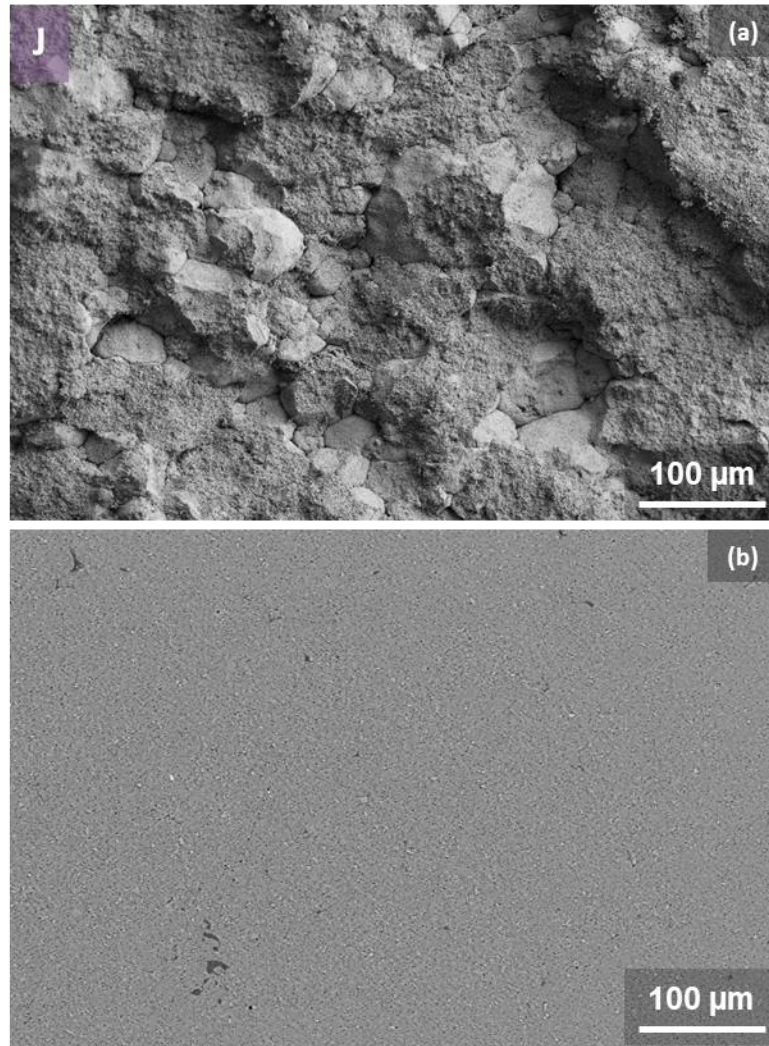
Figure 80. (a) FESEM micrograph of the fracture surface of a flexural strength sample compacted with the J granules and (b) a polished micrograph of the compact visualizing the parallel direction of compaction.
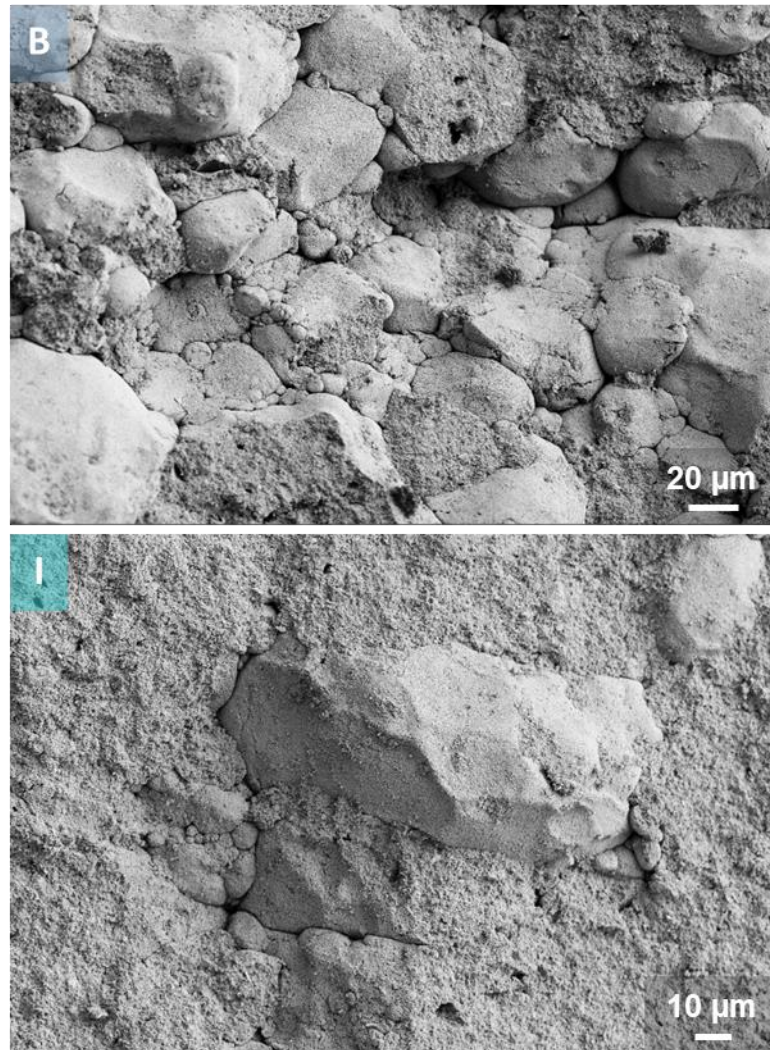
Figure 81. Higher magnification regions highlighting persistent granules remnants that remained throughout the compaction process on the fracture surfaces of B and I granules respectively.

6.C. Summary

Visualizing the microstructural variations as a function of what processing parameters, slurry properties, and spray-dried granule characteristics promote a higher degree of microstructural uniformity was imperative. Relating the visualization results to the previously mentioned compaction behavior and flexural green strength results was essential in developing tools to improve the characterization capabilities of green ceramic materials.

The spray-dried granules were characterized on a FESEM, visualizing the internal microstructures as well as the generated morphologies of the respective spray-dried granules. The spray-dried granules processed with the PVA binder resulted in an abundance of microstructural defects and hollow cores within their internal structures. This phenomenon was likely due to PVA binder migrating to the surface of the atomized droplets during the evaporation stage of the spray-drying process. This behavior occurred due to the PVA binder being water soluble. The acrylic emulsion binders resulted in a more uniform internal structure in comparison to the PVA granules. The reason behind this could be due to the acrylic binders being initially in emulsions that break during the drying stage of spray-drying, with the resultant organic species being insoluble. Therefore, binder migration during the evaporation stage does not occur. Fewer visualized microstructural defects within the internal structure of the acrylic emulsion binder (F) was the reason these granules obtained greater density values than the compared PVA granules (A through E).

The morphologies, or shapes, of the generated granules were governed by the viscosity, solids loading, binder type and amount. The lower the viscosity value of the alumina suspension, the more observed satellites were located on the surface of the spray-

dried granules. This behavior was noted due to the mobility of particles within the alumina suspension and during atomization, smaller atomized droplets form due to surface tension. These smaller droplets coalesce during the drying stage and result in clustered or satellite spray-dried granules with irregular shapes. It has been stated in previous research that the atomized droplet size is proportional to the slurry's viscosity. This behavior was visualized during the conducted work for this dissertation, with the lower viscosity granules (A – 100 cP and B – 250 cP) resulting in irregular shaped spray-dried granules in comparison to the other cases. The higher the viscosity, solids loading, and PVA binder amount (C, D, and E respectively) resulted in a higher degree of granule circularity than the lower viscosity granules. The acrylic emulsion granules (F) resulted in similar observed circularity to these cases as well.

Visualizing the microstructures as a function of compaction pressure was an important tool in visualizing the compaction characteristics of the varying process parameters. Correlating two-dimensional microstructural analysis as a tool in evaluating the compaction curves of the varying alumina granules gained insight and information on the differences between processing parameters during the compaction process. The higher the degree of circularity in the PVA granules, the higher the degree of observed granular interfaces and intergranular porosity. The higher degree of hollow coring within the spray-dried granules internal structure resulted in a higher degree of persistent closed porosity after the compaction process. As evident during the compaction behavior analysis, the acrylic emulsion granules, F and J, as well as the moisture granules, G through I, resulted in higher density compacts at lower compaction pressures. Adding moisture to the PVA granules resulted in softening the binder species and promoting higher densities. The added

moisture aided in removing the persistent closed porosity from the abundant hollow cores within the spray-dried granules.

This low viscosity infiltration process that visualized the parallel and perpendicular direction of compaction was an improved characterization technique to obtain high resolution cross-sectional micrographs of green alumina compacts. Comparing this visualization technique to other methods researched, higher resolution images were obtained therefore more microstructural information was gained. The green ceramic parts did not have to be thinned or reduced to a specific size for characterization like the liquid immersion technique (LIM). Specific regions of the green ceramic part can be evaluated since there was no need to thin the specimen prior to characterization. The improved visualization method correlated a relationship between processing parameters and experimental results during the forming process. This visualization relationship is essential to understand what processing parameters promote microstructural uniformity.

This method improved the capabilities of microstructural characterization of green ceramic materials while using a FESEM, however, it is limited in two-dimensional analysis. Visualizing the particle and pore arrangements in three-dimensions will further improve the capabilities of characterizing green ceramic materials. This established visualization method coupled with experimental compaction results is a tool in improving the capabilities of green microstructural variation. From the processing stage and the generated granule morphology, to the observed compaction characteristics and resultant microstructures, developing a relationship between experimental results and the observed visualization results was achieved and an improvement in understanding what processing phenomena promote varying microstructural characteristics was conducted.

7. OBJECTIVE 4: 3-D FESEM Visualization Method

7.A. Experimental Procedures

Initially, a registration material needed to be addressed. Different soft grades of aluminum, such as 1100, 3003, 2024, and 7025, were evaluated as well as soft plastics and cured epoxies. Vickers indents were evaluated on each of the tested samples using a Buehler Wilson VH3300. The relaxation behavior of the plastics and epoxies altered the geometry of the micro-indents and the depth was difficult to discern. The softest grades of aluminum, grades 1100 and 3003, showed evidence of differential pile-up and spalling after indentation. This became an issue when calculating the depth loss and polishing depth between layers. The hardest grade of aluminum, grade 7075, showed evidence of pullouts and artifacts on the green body's surface, therefore exhibited differential polishing behavior. This would become an issue during microstructural characterization. A soft 2024 T3 hardened aluminum was the registration material determined for this method. This aluminum had a similar polishing procedure as the infiltrated green ceramic and did not exhibit any issues during the layering process.

After deciding which registration material was best for the layering method, a layering technique needed to be determined. This included the placement of the indents for registration during microstructural characterization within the FESEM as well as the depth of the layer needed to gain sufficient information of the microstructure in three dimensions. Also, the geometry of the registration material was evaluated, between a hollow tube with the circular compact infiltrated within the aluminum tube, or a square piece of aluminum with the drilled hole in the middle to case the compact during infiltration and polishing. Similar behavior of polishing and layering was shown between the two different shapes of

aluminum, therefore, it was determined that for ease of testing, a hollow 2024 aluminum tube would be used for initial testing.

At first, for a small accurate precision of 0.5 μm layers, Vickers micro-indents coupled with Berkovich nano-indents were tested. Vickers indents were placed on the registration material using the Buehler Wilson VH3300 and the Berkovich nano-indents were placed using a Micro Materials NanoTest Vantage nanoindenter (Micro Materials Ltd., Wrexham, UK). The nanoindenter generated loading and unloading curves, shown in Figure 82. The depths of the nano-indents were determined based on the unloaded depth calculated from the equipment. The areas of the indents were measured and along with using the total area correction equation shown below, the unloaded depth of the indent was calculated by equations 16 and 17 in section 3.D.1. The a variable correlates to the side dimensions of the triangular Berkovich indent and h correlates to the depth of the indent. The angle θ, correlates to the half angle of the indentation, 65.3°. This unloaded depth calculation was compared to the generated unloaded depth obtained from the nanoindenter [96].

Projected Area:

$$A_p = \frac{\sqrt{3}}{4} \times a^2$$ 30

$$A_p = 3\sqrt{3} \times h^2 \times \tan\theta$$

Total Area:

$$A_t = \frac{1}{\sin\theta} \times \frac{\sqrt{3}}{4} \times a^2$$ 31

Using the unloaded depth as a calculation, nano-indents that ranged from 0.5 μm
to 3.0 μm were placed along a ring on the aluminum tube. Loading forces on the nano-
indenter ranged from 20 to 400 mN, with the depths of the nano-indents ranging from 0.5
– 3.0 μm. Vickers indents at a load of 2.0 kgf were placed in the corners and used as
registration marks for navigation purposes within the FESEM. A layer thickness of 0.5 μm
was removed via mechanical polishing. The infiltrated sample within the 2024 aluminum
tube was a 3.0 wt. % PVA compact spray-dried at 250 cP and 50 wt. % solids. The uniaxial
compaction pressure was 100 MPa. A schematic of this process is shown below in Figure
83.
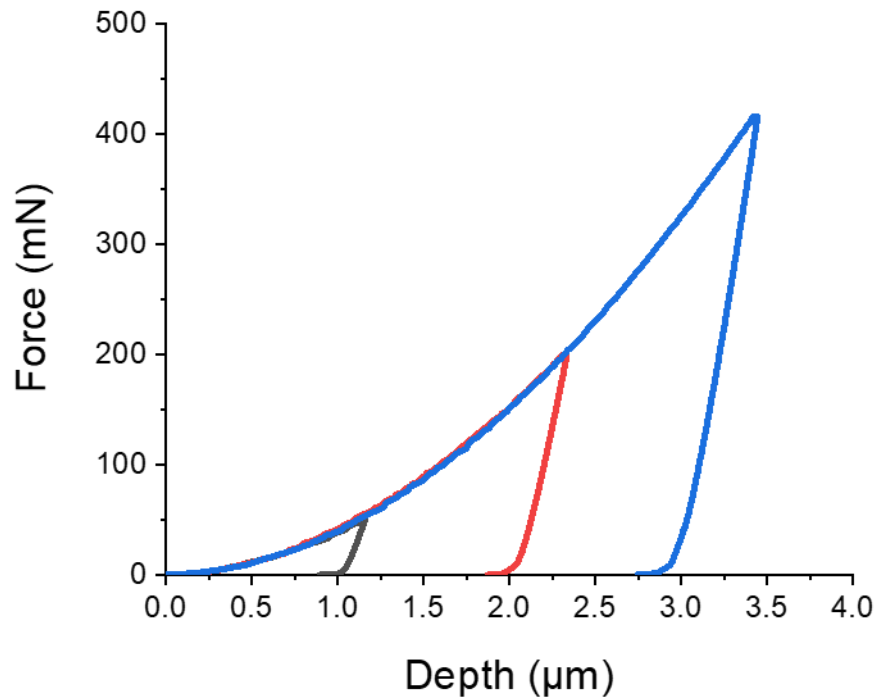
Figure 82. Generated loading and unloading curves from the nanoindenter conducted on a
tube of 2024 aluminum.
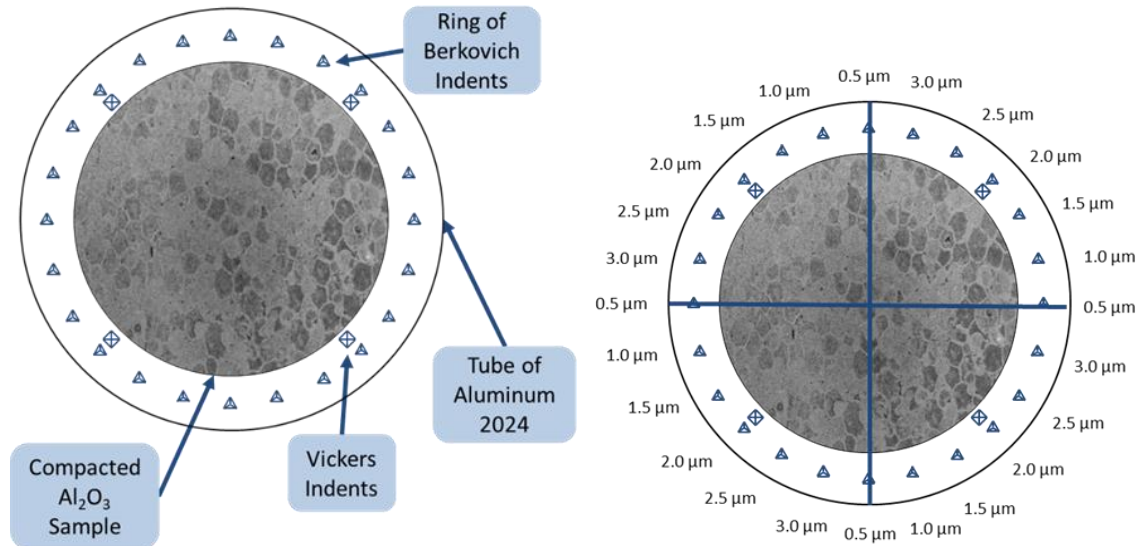
Figure 83. Schematic diagram showing the placements of the Berkovich nano-indents and
Vickers micro-indents.

Due to the small layered material removal, this method would have become time
sensitive for a larger level of material removal. Therefore, larger layered depths were
evaluated further for this dissertation. On a larger scale, layers ranging from 5–10 μm were
evaluated by use solely of Vickers micro-indents. The issue that arose with removing larger
depths was the accuracy of the depth lost. Upon removing the infiltrated sample from the
Buehler target holder and placing it in the FESEM, the placement of the sample back in
the target holder between layers was a concern as tilting or miss alignment from the
previous position would cause large variation. Since the target holder was integrated with
set screws, this helped place the sample back into the target holder in a similar position.
However, obtaining the same position to a micron sized accuracy proved difficult.

The intent process was to design a large stainless steel cylinder that would fit within
the target holder to a high tolerance and act as sample holder within the FESEM. Therefore,
the limiting factor of re-placing the sample into the same spot in the target holder each

layer would be minimized. Within the stainless steel cylinder, holes for the set screws were machined to ensure the sample was set into the target holder at the same spot. Since the diameter of the stainless steel cylinder was machined to a high tolerance of +/- 0.005 inches, and the height of the cylinder covered most of the target holder, tilting and miss alignment of the sample between layers was improved to a higher accuracy. On the base of the cylinder, a threaded insert was machined to insert a screw that acted as a stud to be placed into the sample holder of the FESEM. This screw was removed during layering and screwed in during microstructural characterization. The infiltrated green compact along with the registration material were adhered onto the stainless steel cylinder with the use of a Gorilla Super Glue Impact Tough Formula (Gorilla Glue Company, Cincinnati, OH). A schematic of the stainless steel cylinder used is shown in Figure 84.
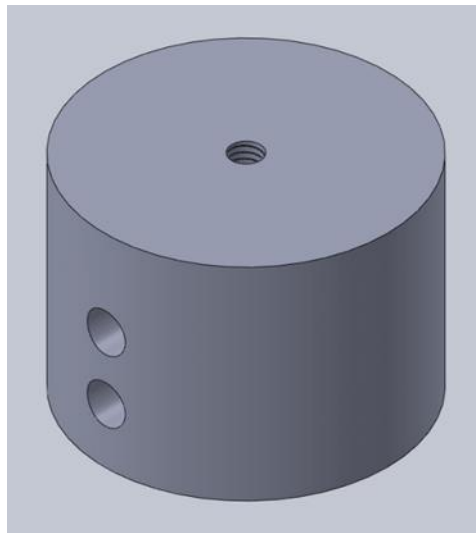
Figure 84. 3-D drawing from Solidworks of the stainless steel cylinder. The SEM stud would screw into the threaded insert on the top as shown. The target holder's set screws would screw into the hollow placements as shown on the side.

An accurate process to remove layers of 5-10 μm was determined. This included the placement of the Vickers indents, how many indents were placed each polishing cycle, and the polishing parameters used during the material removal process. The pile-up behavior of the material due to its soft nature was an issue to overcome. Due to differential pile-up occurring with the use of varying indent loads, a single indent load of 10 kgf was used. This was to account for any micron sized tilting caused by the varying indent pile-up height after indentation was placed.

It was determined that placing indents in a square or diamond shaped pattern proved the best method to keep an acceptable accuracy of one micron standard deviation of material removal. Therefore, four indents were placed at a time during the material removal. Twelve indents in total were used to account for the material removal during the mechanical polishing process. The location of the indents is shown below in Figure 85. Five indents were used per sample to calculate the material removed specific to that sample. All twelve indents were used to calculate the material removal for all of the four samples as a whole. Since 10 kgf indents on average are 45 μm in depth on the 2024 grade aluminum registration material, there is a limited depth that these Vickers indents can be used with this method. Therefore, when these indents were almost removed, a new set of indents was placed in a similar pattern to keep measurement locations similar and to continue the method across larger depths. It was imperative that these new indents were placed before the location indents were lost, to measure and calculate the new location indents coordinates from the previous location indents.
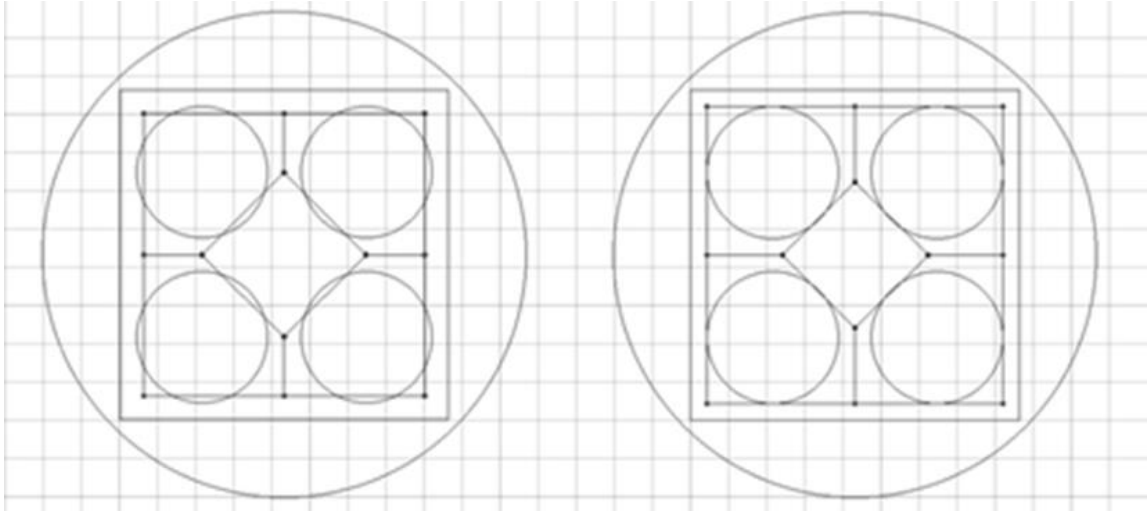
Figure 85. Schematic drawing from the AutoCAD software showing the placements of all twelve 10 kgf Vickers indents on the surface of the 2024 aluminum square registration material.

Since removing layers via mechanical polishing and visualizing the microstructure using an SEM is a time sensitive process, incorporating a method to visualize multiple green compacts that varied in processing parameters would be beneficial. A square shaped 2024 grade aluminum piece was machined to incorporate four compacts within the Buehler infiltration cup used with the vacuum infiltrator. A schematic of this aluminum registration material is shown in Figure 85. The four compacts were infiltrated using the Buehler Cast N' Vac 1000 vacuum infiltrator, holding the samples under vacuum for a time period of four hours to ensure proper infiltration with the EMS Spurr Low Viscosity Epoxy. Since a tight tolerance between the green alumina compacts and the wall of the aluminum existed, allowing proper infiltration time was essential. The infiltrated sample was then placed in an oven between 70 – 80°C to cure the epoxy and sample for a minimum of eight hours. The four samples infiltrated for this analysis mentioned previously in section 3.D.3. are listed below in Table 18.

Table 18. The characteristics of the four green alumina compacts used for the 3-D FESEM analysis. All four samples were compacted to a uniaxial pressure of 175 MPa.

Granule	Viscosity	Solids (Al_2O_3)	Binder (Al_2O_3 Solids wt.)	Moisture Content
B	250	50.0 wt. %	3.0 wt. % PVA	0.0 %
E	250	50.0 wt. %	5.0 wt. % PVA	0.0 %
F	250	50.0 wt. %	3.0 wt. % Acrylic (PAA)	0.0 %
I	250	50.0 wt. %	3.0 wt. % PVA	6.0 %

Due to the uneven nature of the cured epoxy, creating a flat surface to adhere the infiltrated sample onto the stainless steel cylinder was essential. The surface of the green alumina compacts and aluminum was adhered onto the cylinder by use of carbon tape for ease of removal. The cylinder was then set into the target holder with the set screws and the base of the infiltrated sample was mechanically polished to flatten the surface in-line with the target holder setting without harming the surface of the infiltrated alumina compacts. Using the Keyence VHX optical microscope, the surface variation of the infiltrated sample was analyzed by the Z stage measurement of the lens. The maximum and minimum z positions when the sample was in focus were taken. When the difference between the values was 20 μm or less, this was an acceptable value for flatness. The sample was then adhered to the stainless steel cylinder using the Gorilla Glue previously mentioned. A Teflon sleeve machined to the diameter of the infiltrated sample and stainless steel cylinder, ensuring proper alignment during the adhesion process. After adhering the sample to the stainless steel cylinder, samples were mechanically polished down to 0.05 μm.

The issue that needed to be overcome when incorporating more porous material within the infiltrated green sample was the higher degree of charging occurring during microstructural characterization. Specific locations of the green compacts were

characterized which included the edge and center of the compact, to visualize density and stress differences within these regions. The bulk of the sample was also exposed, removing five hundred microns prior to the start of the process using the measurements on the target holder. A diagram describing the two regions visualized as well as the bulk of the sample analyzed is shown in Figure 86.

To mitigate charging, carbon tape was used on top of the epoxy and the stainless steel cylinder was covered as well. Since the center and edge of the sample were the only regions characterized, carbon tape was used to cover partial areas of the sample and indented that did not need to be exposed. A schematic of the location indents and the location of the carbon tape is shown in Figure 87. Samples were then sputtered coated in gold to a thickness of 30 nm. After microstructural characterization was completed, the carbon tape was removed. The remaining nanolayer of gold on the surface of the samples was removed during the next cycle of polishing.
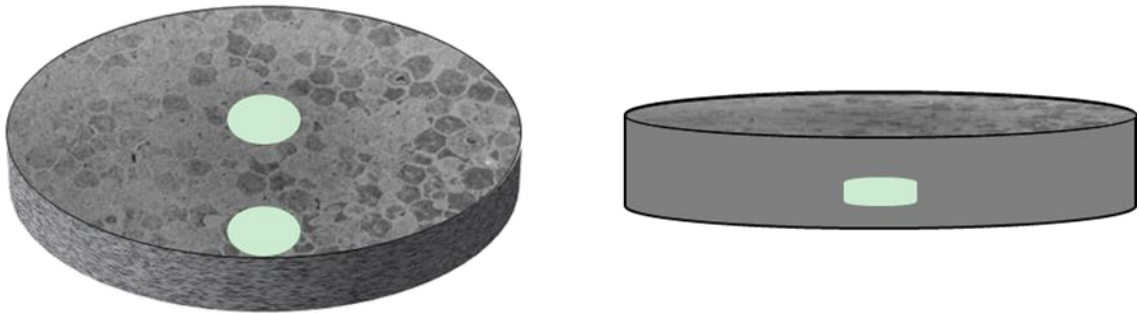
Figure 86. Schematic diagram showing the bulk region of the sample exposed during mechanical polishing as well as the center and edge regions visualized for each compacted sample.
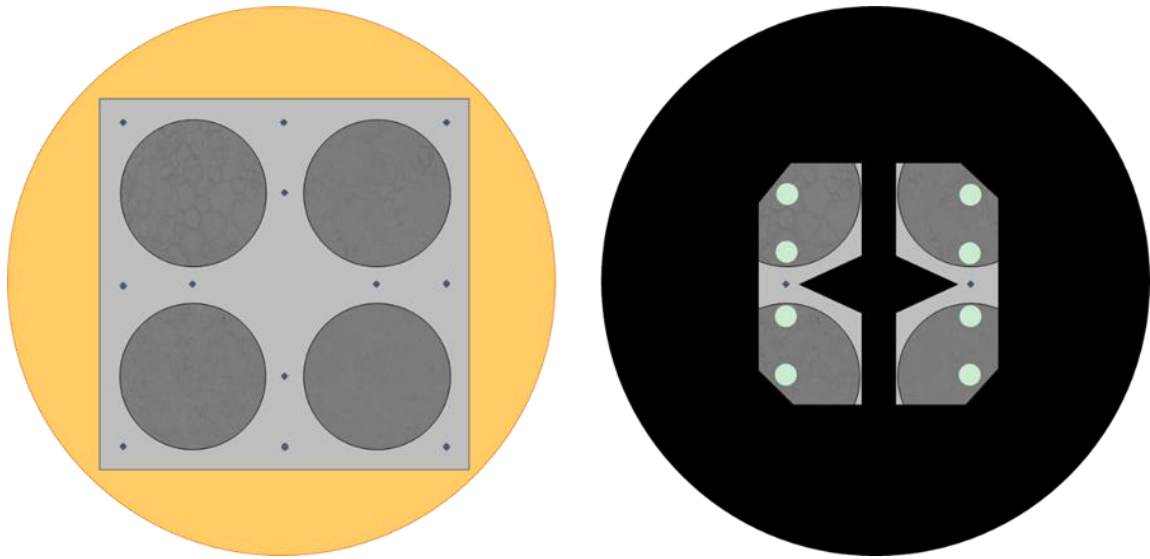
Figure 87. Schematic diagram showing the placement of carbon tape on the surface of the polished infiltrated sample. The two location indents are shown, exposed, plus the regions the FESEM micrographs were taken over a series of layers.

The two location indents were used to locate the same regions of the sample during microstructural characterization on the FESEM. The one indent on the left was used for the 5.0 wt. % PVA sample and acrylic emulsion binder sample. The other indent on the right was used for the dry and 6.0 % moisture content PVA sample. Using the diagonals of the Vickers indents as a guide, the stage of the FESEM was rotated to orient the sample in the same location within the FESEM. From the upper right corner of the Vickers indent and a magnification of 25kX, as shown in Figure 88, the X and Y coordinates of the indent were recorded. At the same magnification of 25kX, the X and Y coordinates of the region being characterized were input into the SmartSEM software. Then, the magnification was changed to 500X to record an image of the microstructure. It was essential not to increase the magnification after moving down to a magnification of 500X, otherwise the X and Y coordinates originally recorded will be changed. This is imperative to image the same area

of the compact repeatedly over multiple layers. When you relocate using the stage navigation tool within the SmartSEM software, the coordinates are preserved. As long as this movement occurs at the same navigation and you lower rather than increase the magnification, then the same area of the sample will be imaged.
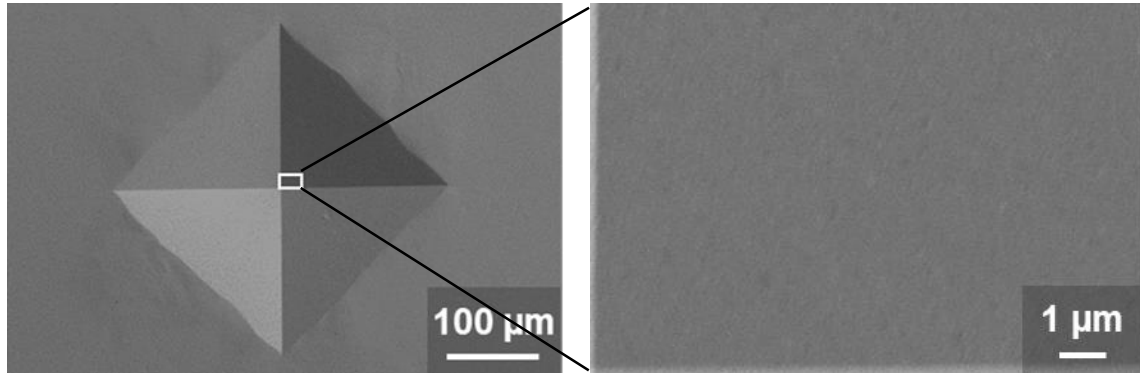
Figure 88. FESEM micrograph taken with an SE2 Detector showing a Vickers indent and the focused region at a high magnification to navigate the stage of the FESEM. This method was used to image the same area of the four compacted green samples.

FEI Houston's Avizo was the reconstruction software used to obtain three-dimensional images of the compacted alumina samples generated from FESEM micrographs. This software was also used for image processing across all micrographs. The micrographs needed to be processed and thresholded for segmentation analysis, separating the pixels of the images into two classes, porosity and material (or alumina for the case of this dissertation). The first stage of image processing dealt with matching the contrast across each FESEM image prior to the reconstruction process. The purpose behind this was to create a homogeneous contrast range for processing multiple images. This allows the same intensity based image analysis to be comparative across all micrographs.

Once the contrast was matched, a histogram equalization algorithm was used. This algorithm is a greyscale transformation module that widely distributes the greyscale histogram contrast range from 0 to 255 pixels. The aim of this was to make the greyscale histogram uniform to enhance the contrast for analysis purposes.

The last stage of image analysis was to segment the micrographs between material and porosity. An automatic thresholding algorithm was used with the Avizo software to separate the greyscale pixels into two classes of pixels, producing a binary image of porosity and material. The factorization module within the Avizo software was used, based off of Otsu's criterion. This criterion is based on clustering based image thresholding, reducing the greyscale image to a binary image. The algorithm assumes the image has two classes of pixels that follows a bi-modal histogram. The algorithm calculates the optimum threshold by separating the two classes of pixels so that the combined intra-class variance (within-class) is minimal and the inter-class variance (between-class) is maximum [97].

Minimizing the intra-class variance:

$$\sigma_W^2[t] = \omega_0[t] \times \sigma_0^2[t] + \omega_1[t] \times \sigma_1^2[t]$$

32

Where $\omega_0[t]$ and $\omega_1[t]$ are the probability occurrences and $\sigma_0^2[t]$ and $\sigma_1^2[t]$ are the variances of classes C_0 and C_1 respectively

Maximizing the inter-class variance:

$$\sigma_B^2[t] = \omega_0[t] \times \omega_1[t] \times (\mu_0[t] - \mu_1[t])^2$$

Where $\omega_0[t]$ and $\omega_1[t]$ are the probability occurrences and $\mu_0[t]$ and $\mu_1[t]$ are   33
the class means of classes C_0 and C_1 respectively

The algorithm computes a histogram and probabilities for each intensity level, sets up the initial class probabilities and means, and steps through all possible thresholds (t) to the maximum threshold. The desired threshold corresponds to the maximum of $\sigma_B^2[t]$. The Avizo software then produces an area computation of pixels that corresponds to the pixel size of the image. Using the z-displacement value, the volume of the segmented images can be calculated and thus the percentage of porosity and material in three-dimensions. This analysis was done for the two regions described previously, the center and edge of the sample, for roughly one hundred microns of the green alumina compact [97].

After image analysis is complete, a non-uniform stacking algorithm for 2-D SEM images was used to stack the micrographs in three dimensions. The code used is shown below, setting the total z-displacement value for each layer. These values are set to the depth loss calculations from the confocal laser scanning microscope for the average of five indents per sample, as previously described. If any post alignment between each micrograph layer was needed, the "Align Slices" module was used to manually set the micrographs by using the landmarks within the microstructure as guides. After the images were stacked and aligned, a "Volume Rendering" module was used within the Avizo software to visualize the three-dimensional reconstructed micrographs.

```
# Avizo Stacked Slices
pathname Images5Bind
pixelsize 0.587 0.587
5Bind.HE_00.tif 0
5Bind.HE_01.tif 8.078
5Bind.HE_02.tif 17.818
5Bind.HE_03.tif 22.543
5Bind.HE_04.tif 26.426
5Bind.HE_05.tif 33.711
5Bind.HE_06.tif 40.745
5Bind.HE_07.tif 46.658
5Bind.HE_08.tif 52.842
5Bind.HE_09.tif 58.510
5Bind.HE_10.tif 66.923
5Bind.HE_11.tif 78.739
5Bind.HE_12.tif 89.688
End
```

7.B. Results and Discussion

A method was developed to visualize green ceramic compacts with the use of a FESEM via conventional mechanical polishing and ion milling techniques. A detailed discussion follows as this is a new method developed during the work conducted for this dissertation. Initially, 24 Berkovich nano-indents were placed on a soft 2024 grade aluminum tube. This aluminum tube was infiltrated with the Spurr low viscosity epoxy resin along with an alumina compact placed in the center of the tube. The alumina compact was processed at 3.0 wt. % PVA spray-dried at 250 cP and 50 wt. % solids loading compacted to a uniaxial compaction pressure of 100 MPa. The ring of nano-indents consisted of four indents at depths of 0.5, 1.0, 1.5, 2.0, 2.5, and 3.0 μm. The four 2 kgf Vickers indents were used as registration marks to navigate the FESEM stage to the desired location of the compact. A schematic of the indent placements is shown in Figure 83. The indents were attempted to be polished away in stages of 0.5 μm or less per layer. After mechanical polishing, ion milling was conducted. A nanolayer of gold, carbon tape, and silver paste were used in between each layer to mitigate chagrining issues on the FESEM. The microstructure of the compact as well as each Berkovich indent for depth loss calculation purposes were imaged.

The nanoindentation software gives the user the load versus depth measurement during the indentation and calculates the loading and unloading curves based on electromagnetic force application and a capacitive depth measurement. This relaxed depth was averaged over the four indents at each load. The software ImageJ was used to measure the Berkovich indents respective sides, a, to calculate the total area correction (using equation 31) and thus the stiffness corrected unloaded depth (using equations 16 and 17)

for Berkovich indents. A micrograph was taken at layers 2, 3, and 4 and the removal process was repeated in between each layer. The comparison between the equipment's depth results with the corrected indent depth calculation are highlighted in Table 19. Using the corrected depths as a function of the depth polished off, the lost layering depth was assumed. These depth loss results between each layer are highlighted in Table 20. The three layers imaged are shown in Figure 89.

Table 19. Comparison between the nanoindenter's calculated unloaded depth of the indent and the stiffness correction unloaded depth for all of the Berkovich indents. Each force and respective depth measurements are an average of four indents.

Berkovich Force	Nanoindenter Depth	Total Area/Stiffness Correction
19.65 ± 0.60 mN	0.59 ± 0.01 μm	0.62 ± 0.01 μm
51.91 ± 1.65 mN	0.99 ± 0.02 μm	1.07 ± 0.01 μm
106.72 ± 1.57 mN	1.43 ± 0.02 μm	1.53 ± 0.01 μm
194.36 ± 3.87 mN	1.96 ± 0.04 μm	2.14 ± 0.01 μm
283.43 ± 4.23 mN	2.38 ± 0.03 μm	2.60 ± 0.00 μm
404.35 ± 11.52 mN	2.85 ± 0.02 μm	3.16 ± 0.01 μm

Table 20. Comparison between the depth loss between each layer calculated from the nanoindenter's unloaded depth and the stiffness correction unloaded depth. The first two depth loss layers are an average of 24 indents. The depth loss between layers 3 and 4 were an average of 18 indents.

Layer	Nanoindenter Depth Loss	Total Area Correction Depth Loss	Average Depth Loss
$1 - 2$	0.32 ± 0.07 μm	0.46 ± 0.14 μm	0.39 ± 0.13 μm
$2 - 3$	0.34 ± 0.13 μm	0.34 ± 0.13 μm	0.34 ± 0.13 μm
$3 - 4$	0.66 ± 0.43 μm	0.66 ± 0.44 μm	0.66 ± 0.43 μm
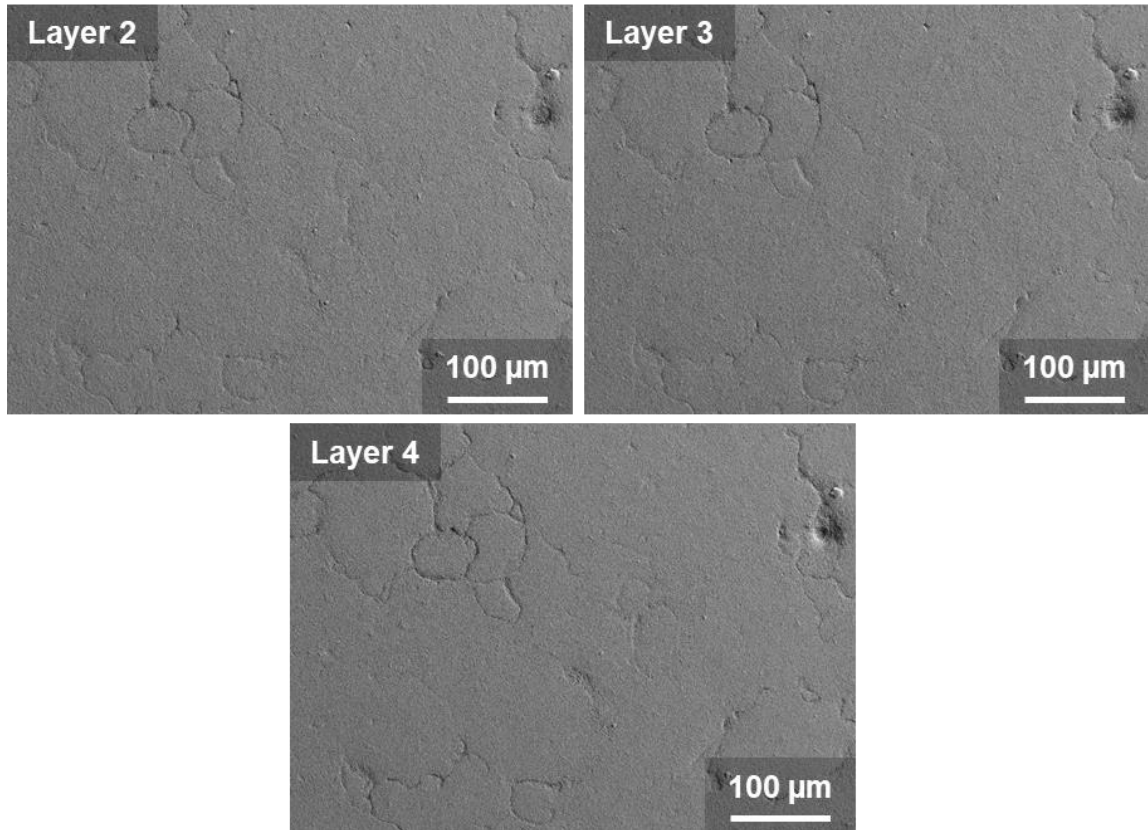
Figure 89. Micrographs of the green alumina compact obtained via the nanoindentation method.

The nanoindenter's resultant depth calculation and the total area/stiffness indent depth correction are based on the loading and unloading curves as a function of load and depth, therefore, the initial depth of the indent. Due to the fact that the only method available to calculate the depth loss in between each layer while the indent was not removed was to measure the area of the indent, based on equation 31, and calculate the difference between the initial corrected depth and the new polished area of the indent. Therefore, the calculations listed in Table 20 are based off of a baseline of the initial corrected depths (nanoindenter or stiffness) and the remaining geometry of the Berkovich indents as material was polished and milled away.

This method became time consuming, as removing sub-micron sized layers while preparing the sample for microstructural characterization in between each layer became impractical. The calculated depth was based solely on the geometry of the nano-indents and the size of the indent polished away. Also, the information gained three-dimensionally was minimal at this small removal rate. Therefore, removing larger depths that ranged from 5.0 to 10.0 um was decided as the best path forward.

As previously discussed, a method revolving around Buehler's target holder, larger material removal rates, a stainless steel sample holder, and a confocal laser scanning microscope was the optimal path forward. The stainless steel cylinder was imperative to set the infiltrated sample in the same spot during the polishing process. A series of twelve 10 kgf Vickers indents were placed in square and diamond patterns on the polished surface of the 2024 aluminum registration material. The reason behind this was to not cause any tilting or micron sized variation from the single force polishing arm. As the arm makes contact with the center of the infiltrated sample, the square and diamond patterns caused the smallest degree of variation in comparison to spherical patterns tested. The confocal laser scanning microscope was essential in calculating the depth loss in between each layer to a high accuracy. As shown in Figure 85 and Figure 87, the four compacted samples were infiltrated within the aluminum registration material. The four compacted samples chosen for this analysis are listed in Table 18 in the previous section.

This method resulted in a high accuracy depth loss observed for all of the alumina compacts evaluated. Table 21 highlights the calculated depth loss for each of the four alumina compacts observed. These listed depths are an average of five indents per sample, with the standard deviation from the mean listed. At a point in this process, the standard

deviation was calculated at three to four microns from the calculated mean across all four samples. The thought was this artifact may likely be due to the polishing procedure and the polishing arm causing a natural deviation based on the rotation of the polishing cycle. The rotation of the polishing cycle was altered to account for this issue occurring, however, the problem still arose. Removing layers at a micron sized accuracy was a difficult challenge to overcome. The other thought for the occurrence of this issue could be due to the orientation of the infiltrated sample being placed in the target holder and causing micron sized variations. However, the infiltrated sample was placed into the target holder with the same process each polishing layer, and it was concluded that there was no possible way to improve this section of the process. Rather than accepting the machine compliance issue and the possible micron sized variation of the sample placement, the next intent was to account for this issue by manually removing the deviation. Since the target holder has the twenty micron markings located on their sample mount, exposing the material to be polished is always done manually. As there was a deviation to a certain side, manually exposing the amount of material needed to be removed was conducted. The mount was then held manually to be polished, and force was applied by hand on the section needed to be removed. Using the target holder as an advantage throughout the process improved the accuracy of the depth loss over the removal process.

The confocal laser scanning microscope was an essential part of monitoring the depth loss throughout the process. Two indent profile scans obtained from the laser microscope are shown in Figure 90. When calculating the difference of the measured depth profiles obtained from the laser, the depth loss can be monitored and calculated with a high accuracy. The accuracy of the laser measurement is highlighted in equation 20. This

process is not very time consuming, with obtaining and calculating the depth loss in under an hour of time for the twelve indents. When the number of indents changes from twelve to 24, when adding the next stage of twelve indents before the original twelve indents are removed, the method becomes time consuming but necessary. The locations of the two indent placement methods are highlighted in Figure 85. Each of the 10 kgf Vickers indents are roughly 45 um deep, and each polished layer ranges from 5 to 10 um, therefore the transition of indent placements occurred every five layers and was conducted twice for this analysis.

Table 21. Depth loss accuracy comparing all of the characterized alumina compacts. The depth loss listed is an average of five indents per sample. The entire infiltrated sample statistics are an average of twelve indents.

Alumina Compact	Depth Loss
B – PVA 3.0 wt. %	51.3 ± 1.6 µm
	89.6 ± 3.7 µm
E – PVA 5.0 wt. %	52.3 ± 1.4 µm
	89.7 ± 2.5 µm
F – PAA 3.0 wt. %	53.9 ± 0.5 µm
	94.5 ± 2.0 µm
I – PVA 3.0 wt. % (6% Moisture Content)	53.0 ± 1.5 µm
	95.5 ± 2.1 µm
Entire Infiltrated Sample (All 4 Samples)	52.6 ± 1.6 µm
	92.3 ± 3.8 µm
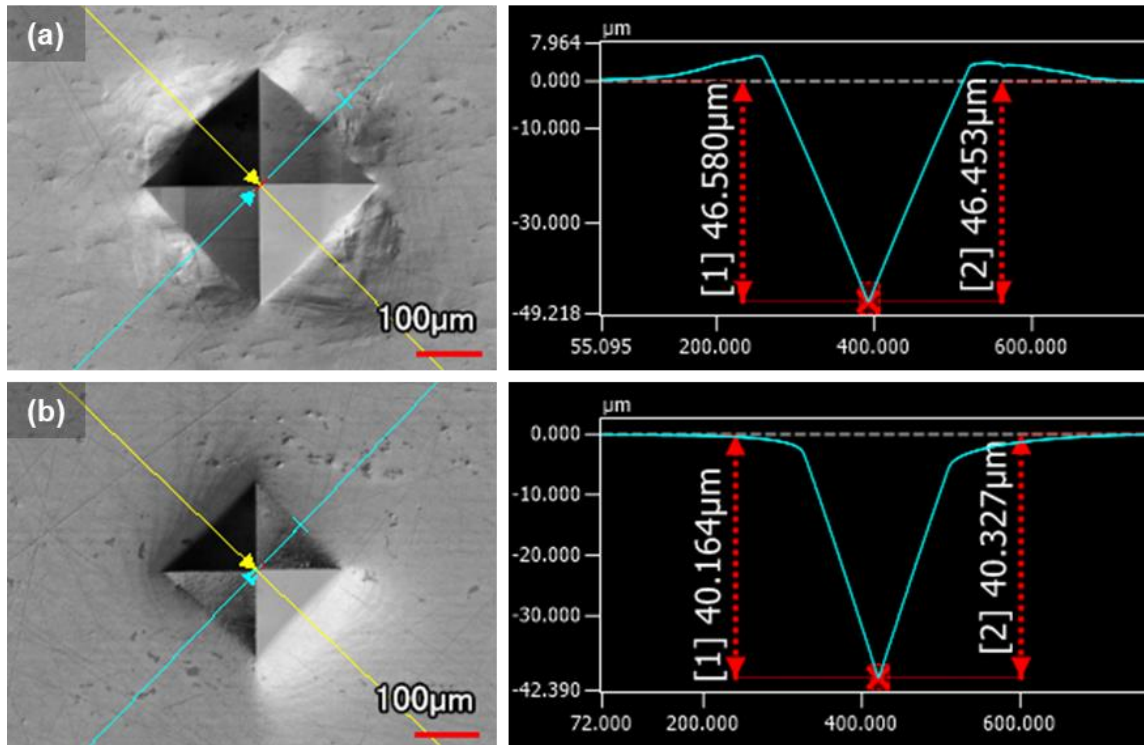
Figure 90. Confocal laser scanning microscope images and profiles showing (a) the initial Vickers indentation on the surface of the 2024 grade aluminum surface with visual pile-up and (b) the polished surface of the 2024 aluminum with the pile-up and roughly six microns removed.

As described previously, two location indents were used, each attributed towards two compacted samples. When adding the next stage of twelve indents at layers 5 and 10, the displacements between the original location indents to the next stage of location indents was measured using the FESEM's stage navigation tool. This process proved successful in measuring the same area of the compacted sample over the total number of thirteen layers characterized. Figure 91 highlights the process of focusing on the same region of the location indents geometry to navigate the same region to be imaged over each layer.
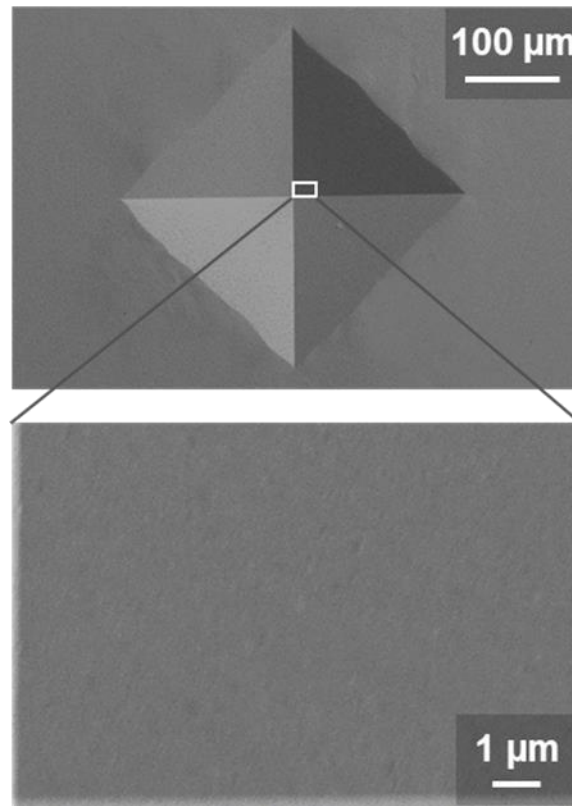
Figure 91. FESEM micrograph of a location Vickers indent, highlighting the region focused at a high magnification to navigate the same region of the compact with a high accuracy.

The micrographs were processed with the Avizo software to match the contrast between each layer for segmentation purposes. The histogram of these micrographs was equalized, maximizing the histogram distribution across all micrographs analyzed. Otsu's automatic thresholding criteria was used to segment the back-scatter electron detected images into a binary phase image. This process is highlighted in Figure 92 to Figure 94. The histogram of the thresholded micrograph is shown, highlighting the pixels attributed to porosity in red. The overall volume segmentation analysis was conducted by the Z height of each micrograph layer. The thirteen layers imaged and their respective micrographs for each of the varying compacts are shown in **Error! Reference source not found.** to **Error! Re**

ference source not found.. Taking the two-dimensional segmentation results by area of the micrograph and multiplying the pixel area by the height of each layer, the volume of porosity and material attributed to each layer was calculated. This process was conducted for both of the sections analyzed per sample, the edge and center of the alumina compact. An overall average porosity percentage was calculated over the two regions per alumina compact and the results are listed in Table 22, with the respective geometric porosity measurement listed for comparison.

These layers were then stacked non-uniformly with the Avizo software to reconstruct the micrographs three-dimensionally according to their respective depth loss measurements from the laser microscope. The three-dimensional reconstructed micrographs for the edge regions characterized are shown in Figure 99 to Figure 102 for each of the four compacts. This process proved to be fast and practical with the Avizo software, and a three-dimensional microstructure of the green alumina compact was obtained.
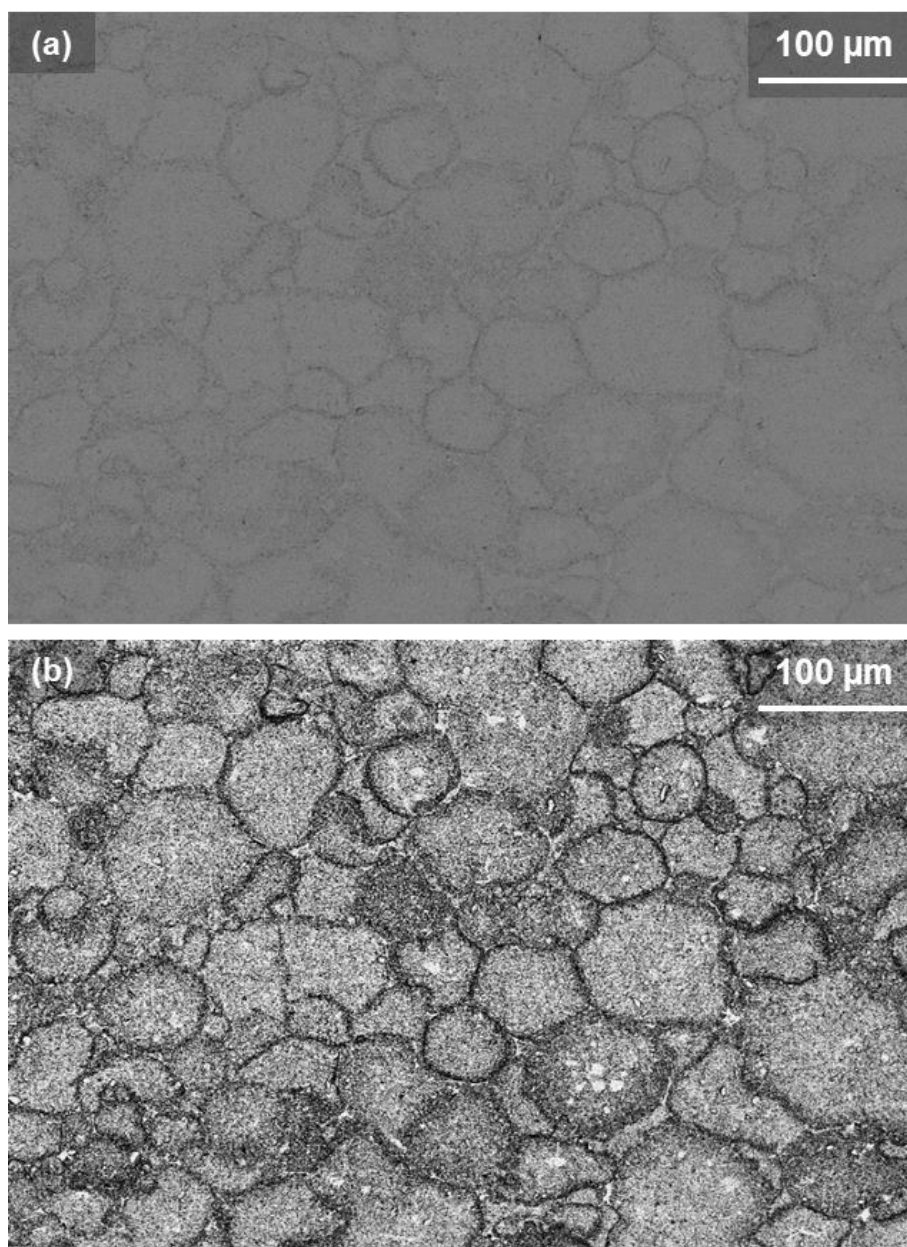
Figure 92. FESEM micrographs of an alumina compact processed with 5.0 wt. % PVA binder (compact E). (a) The FESEM micrograph was matched in contrast with all of the micrographs analyzed. (b) The same micrograph that was histogram equalized for thresholding and segmentation.
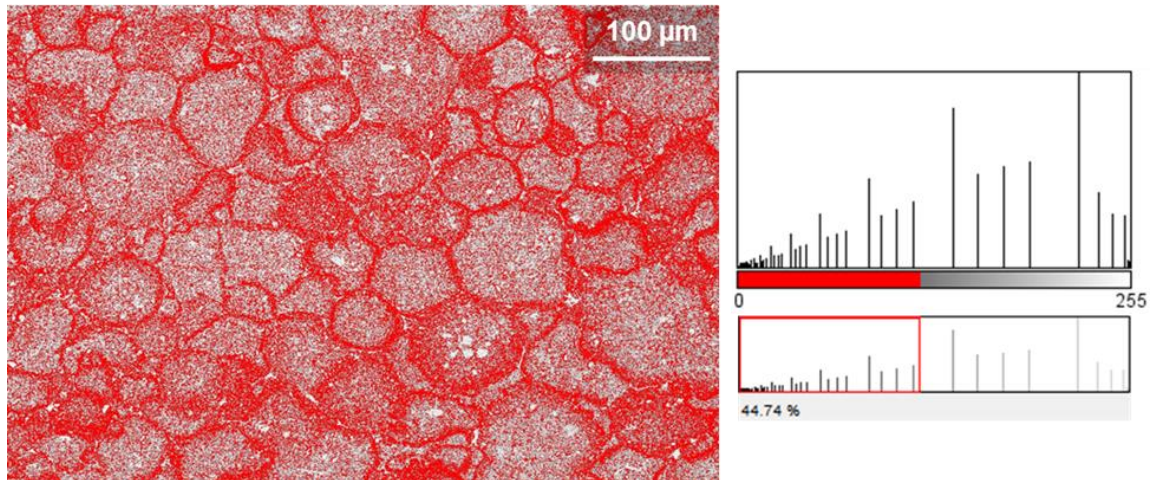
Figure 93. Thresholded FESEM micrograph by using Otsu's automatic criterion. The resultant equalized histogram and segmentation values are highlighted on the right. The red pixels correspond to porosity.
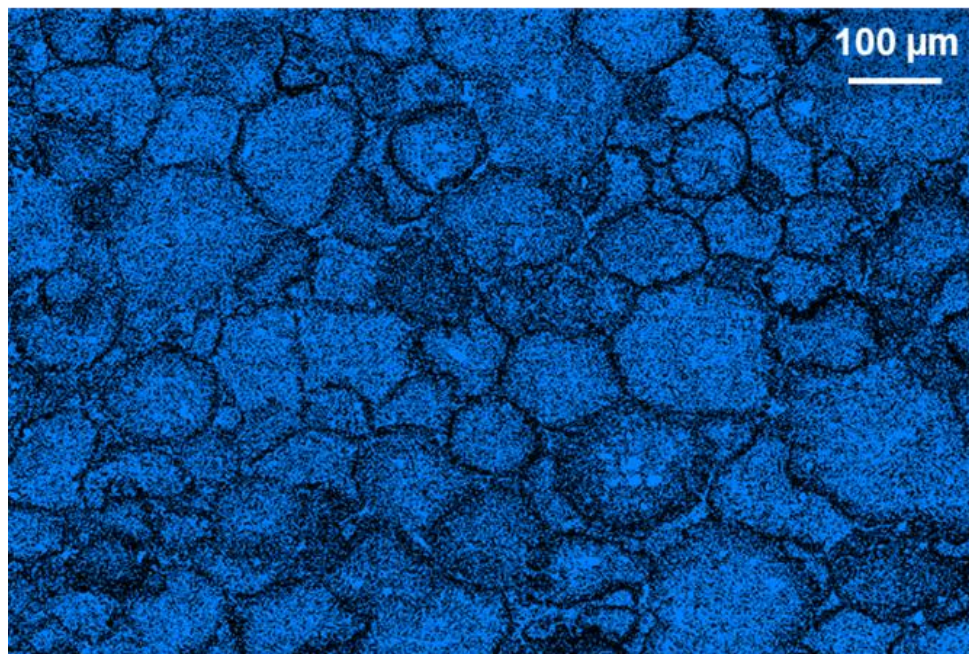
Figure 94. FESEM micrograph that has been segmented into a binary image of alumina ceramic (blue) and porosity (black).
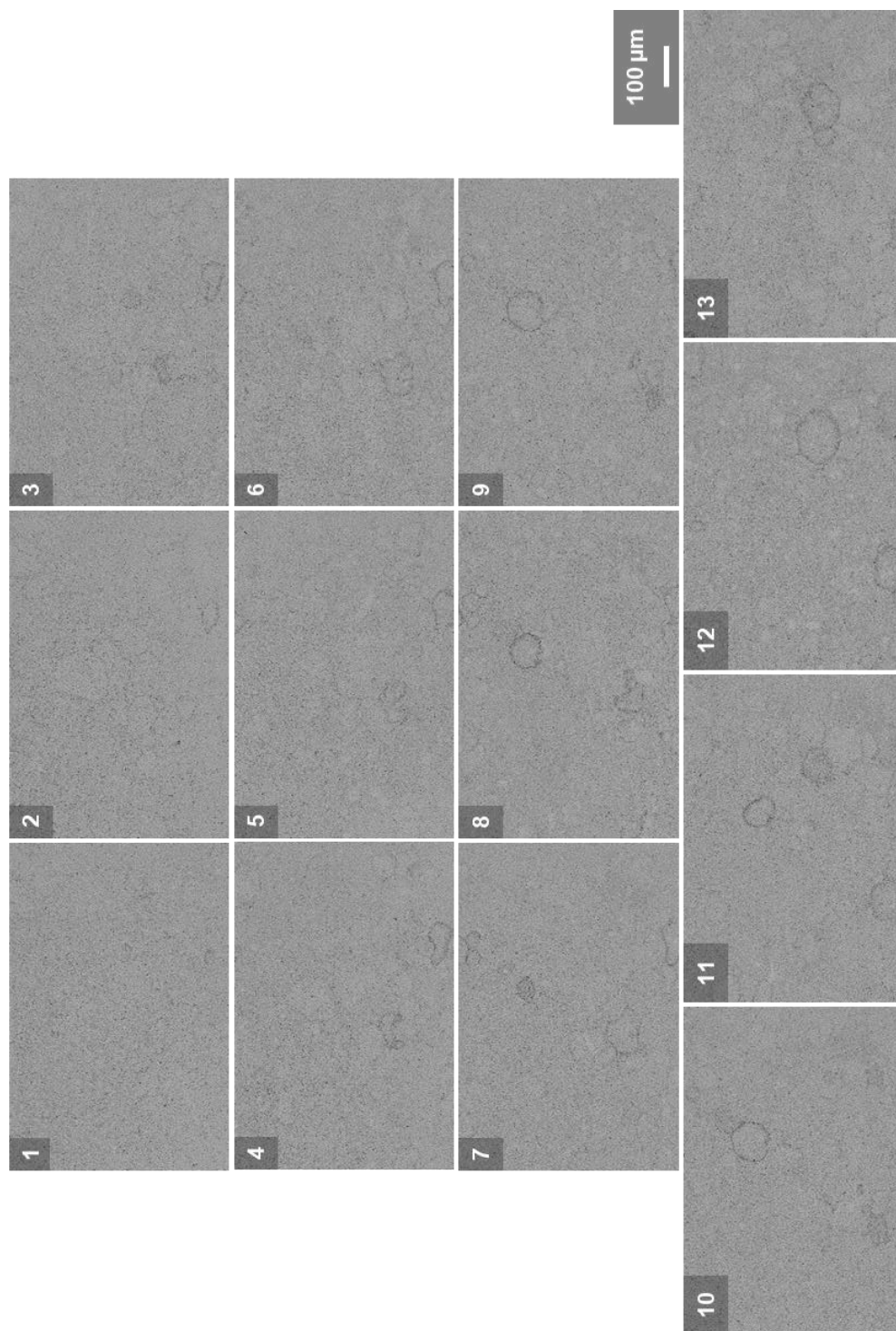
Figure 95. FESEM micrographs matched in contrast for all thirteen layers of alumina compact B processed with 3.0 wt. % PVA binder and spray-dried at 250 cP and 50.0 wt. % solids loading. The compact was pressed to a uniaxial pressure of 175 MPa.
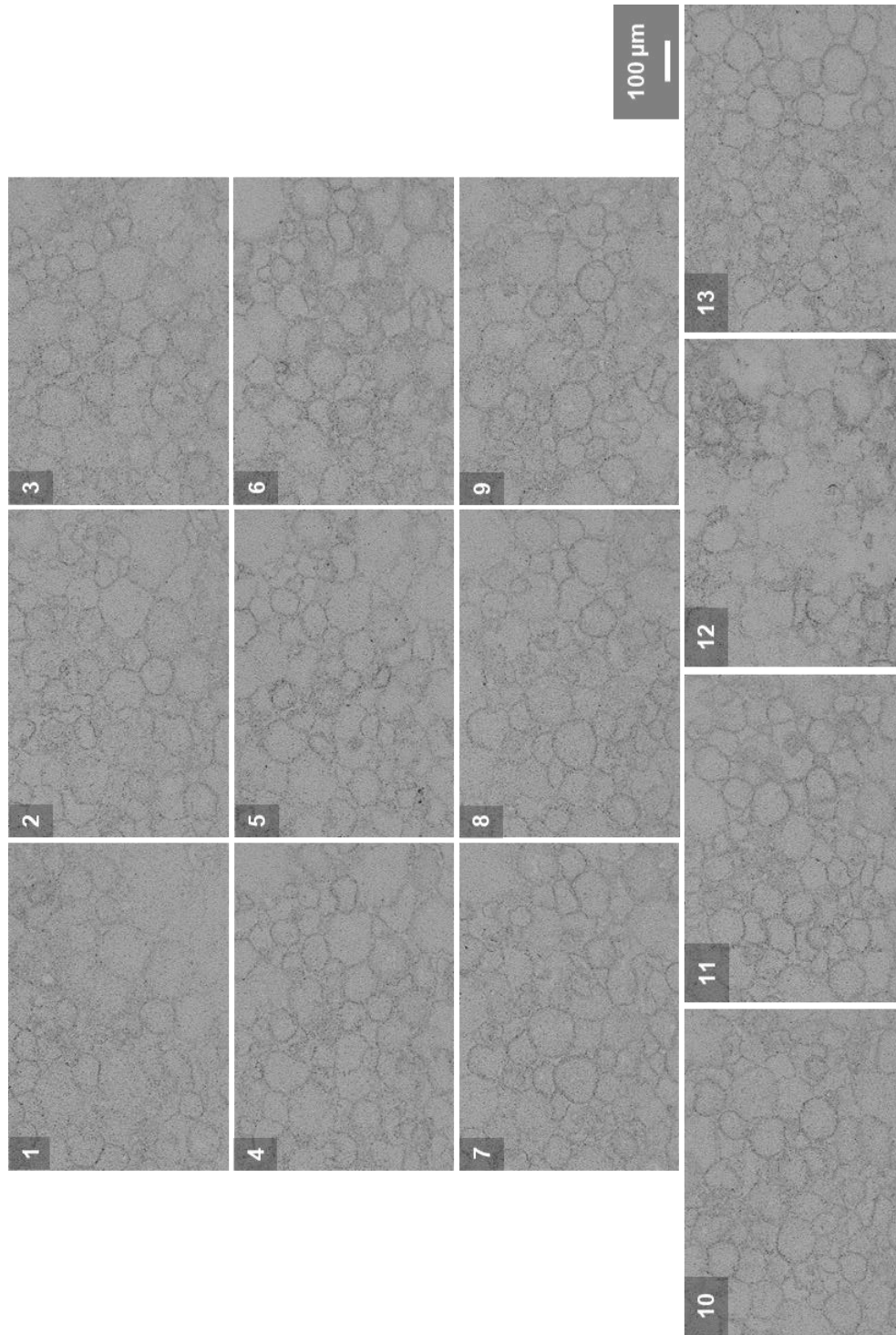
Figure 96. FESEM micrographs matched in contrast for all thirteen layers of alumina compact E processed with 5.0 wt. % PVA binder and spray-dried at 250 cP and 50.0 wt. % solids loading. The compact was pressed to a uniaxial pressure of 175 MPa.
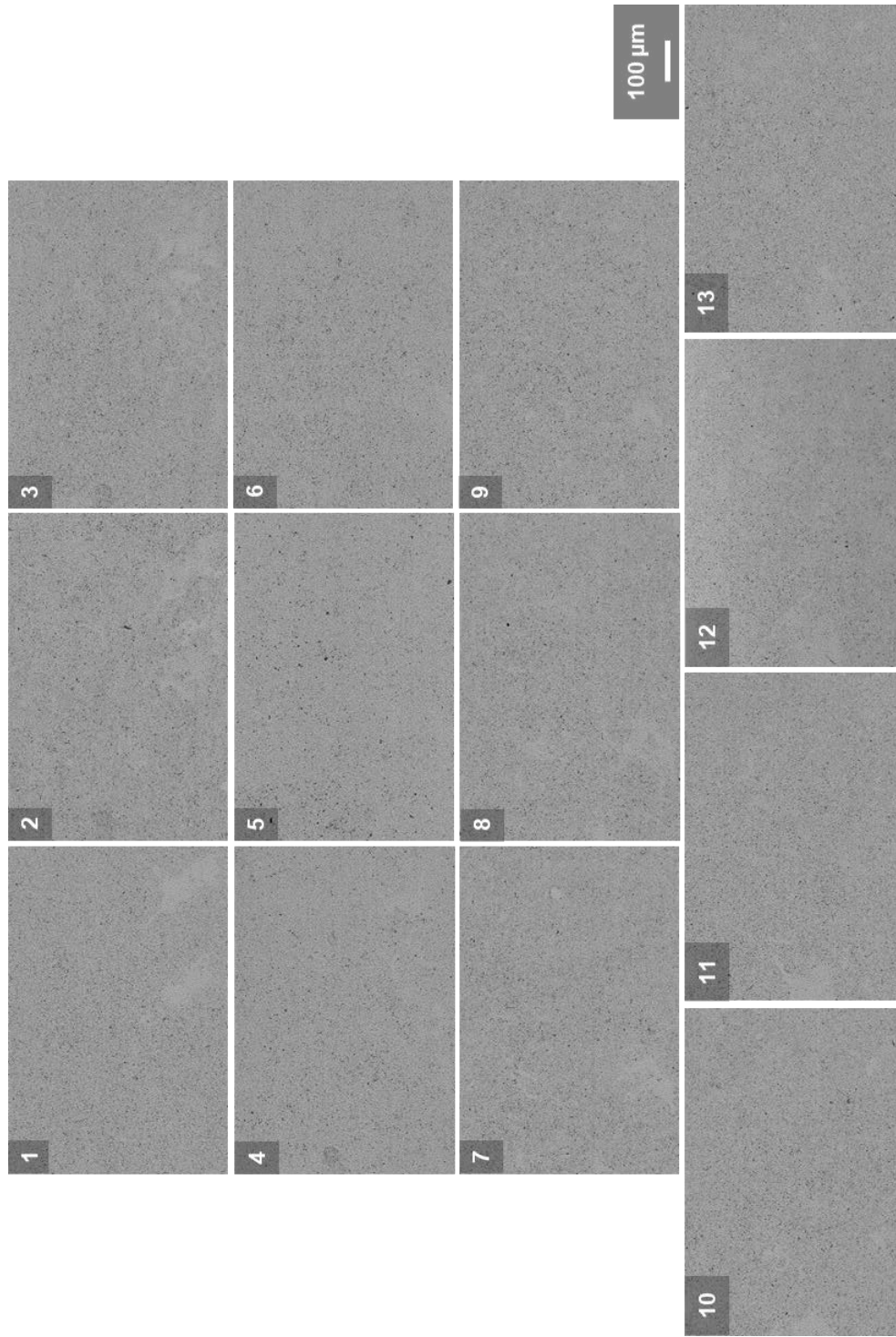
Figure 97. FESEM micrographs matched in contrast for all thirteen layers of alumina compact F (3.0 wt. % acrylic binder and spray-dried at 250 cP and 50.0 wt. % solids loading). The compact was pressed to a uniaxial pressure of 175 MPa.
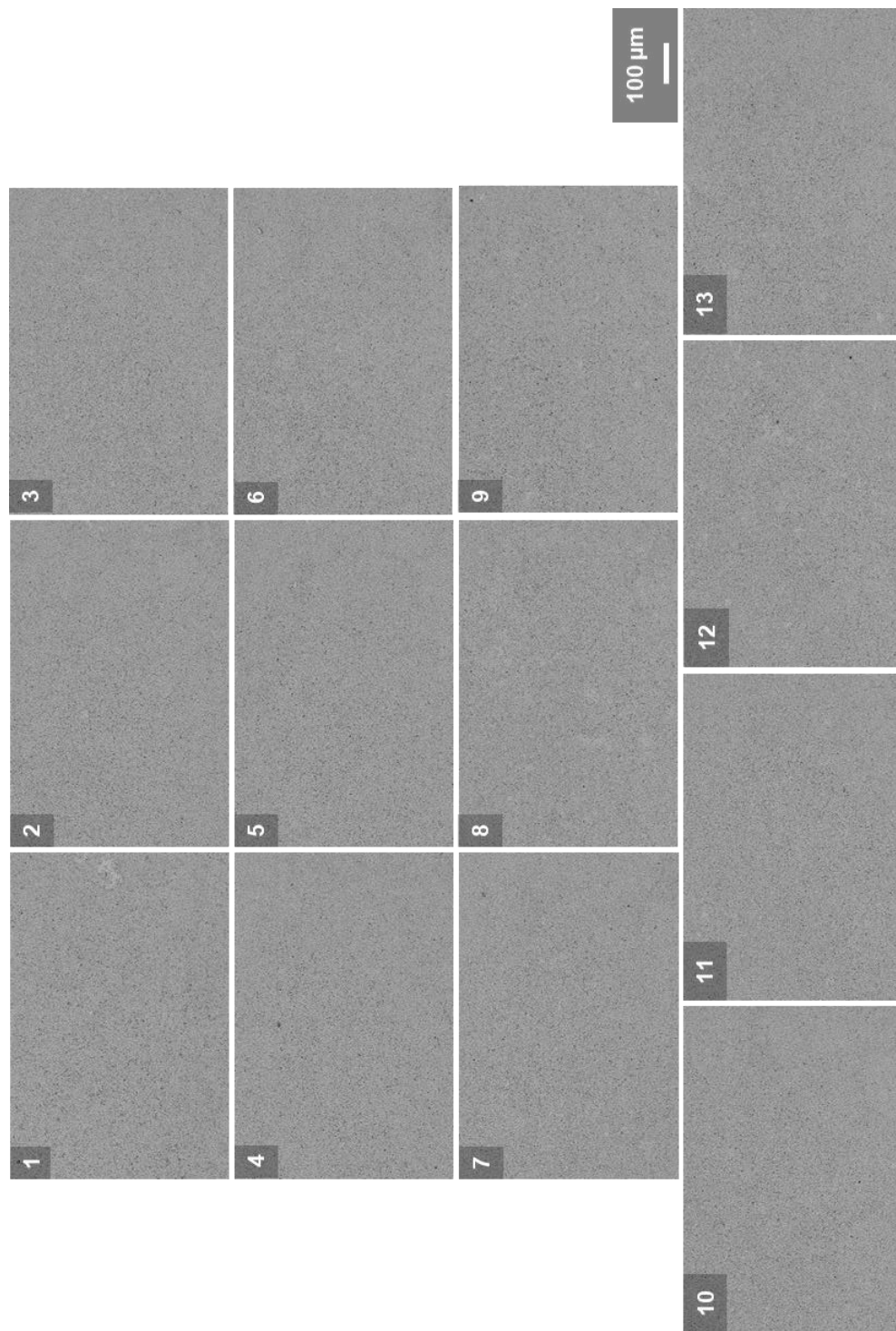
Figure 98. FESEM micrographs matched in contrast for all thirteen layers of alumina compact I (3.0 wt. % PVA binder (5.97% moisture) and spray-dried at 250 cP and 50.0 wt. % solids loading). The compact was uniaxially pressed to 175 MPa.
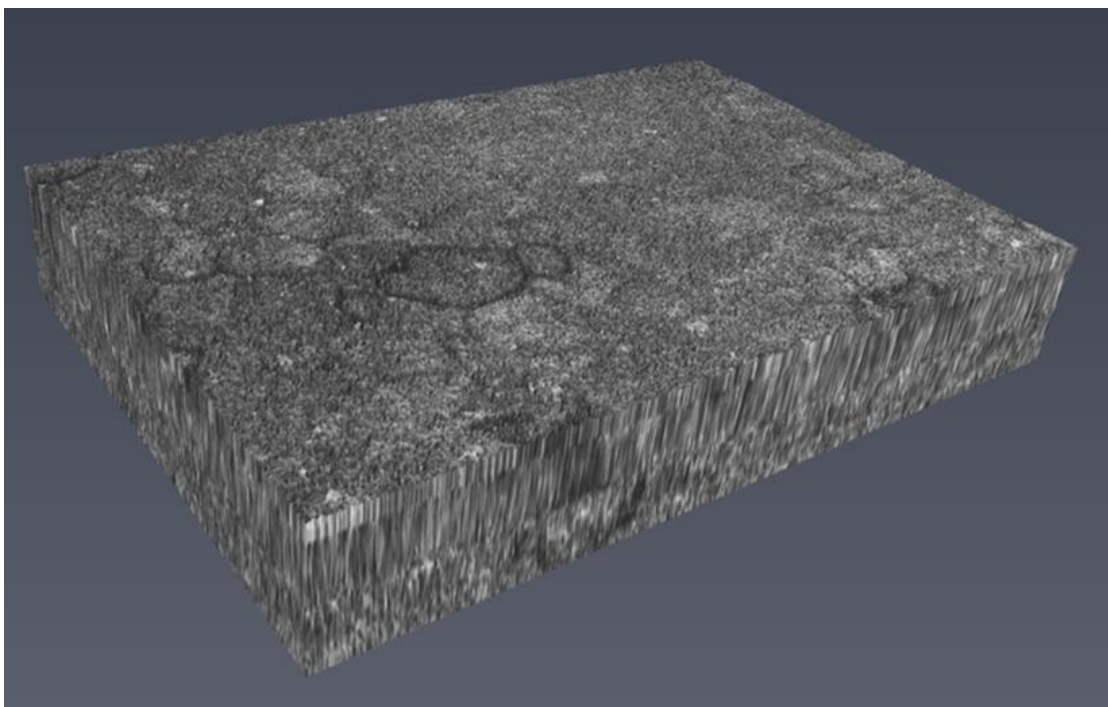
Figure 99. 3-D FESEM microstructure of alumina compact B processed with 3.0 wt. % PVA binder and spray-dried at 250 cP and 50.0 wt. % solids loading.
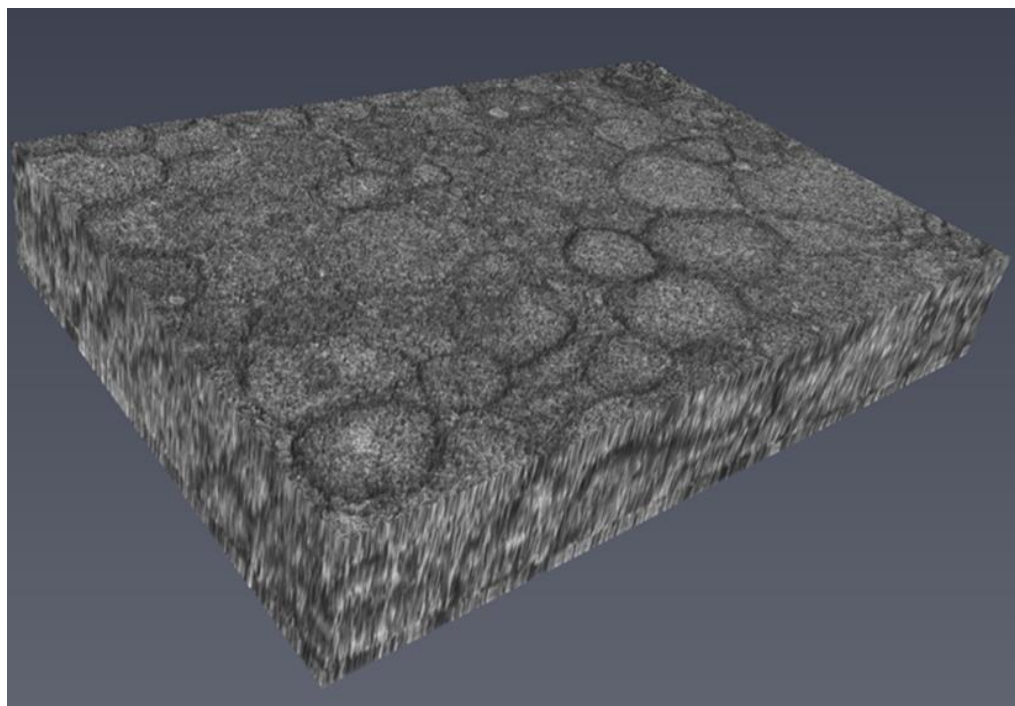
Figure 100. 3-D FESEM microstructure of alumina compact E processed with 5.0 wt. % PVA binder and spray-dried at 250 cP and 50.0 wt. % solids loading.
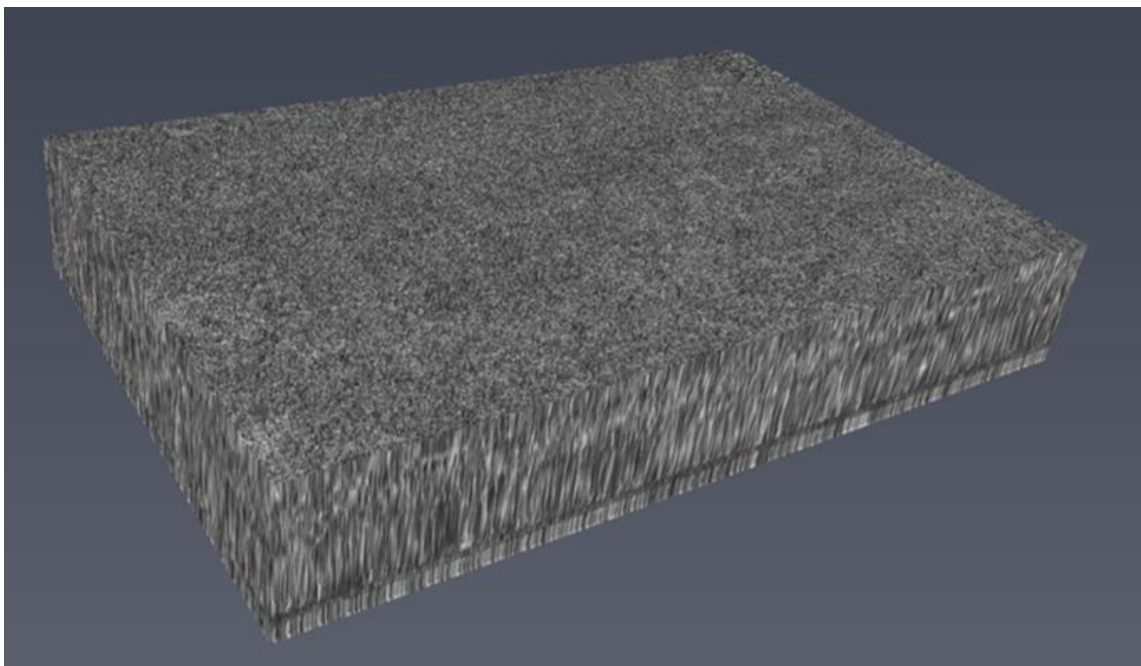
Figure 101. 3-D FESEM microstructure of alumina compact F processed with 3.0 wt. % acrylic emulsion binder and spray-dried at 250 cP and 50.0 wt. % solids loading.
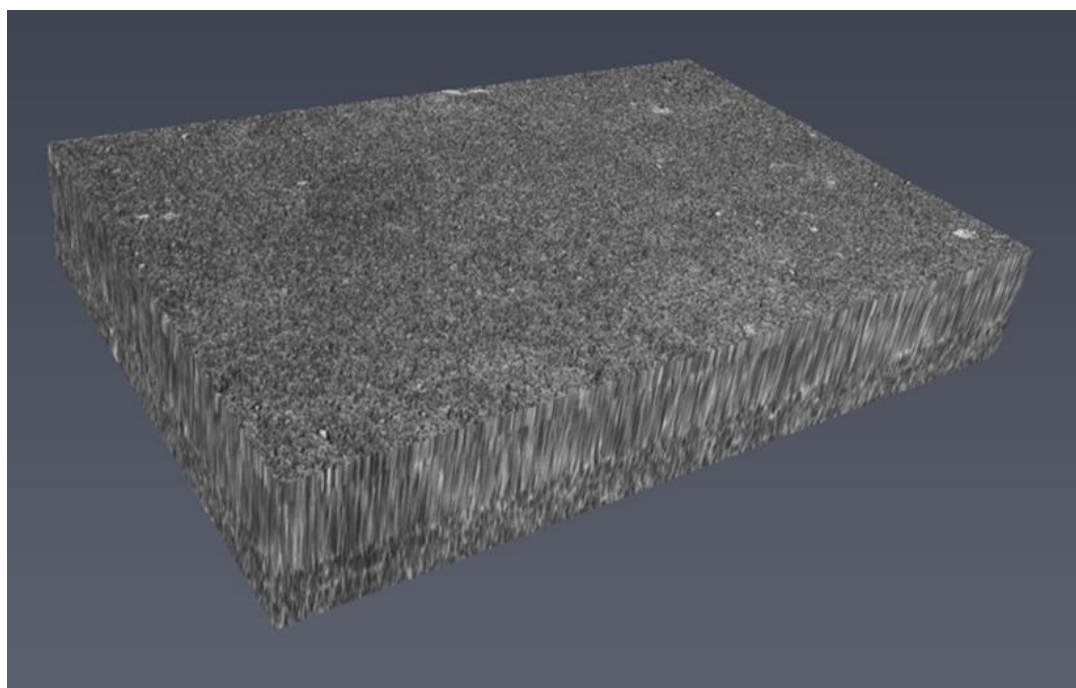
Figure 102. 3-D FESEM microstructure of alumina compact I processed with 3.0 wt. % PVA binder and spray-dried at 250 cP and 50.0 wt. % solids loading. This compact was pressed with a 5.97% moisture content.

Table 22. 3-D FESEM segmented porosity results for both of the regions analyzed in this
work and their resultant average value.

Compact	3-D FESEM (Edge)	3-D FESEM (Center)	3-D FESEM (Average)
B – PVA 3.0 wt. %	48.5%	47.1%	47.8%
E – PVA 5.0 wt. %	47.9%	49.0%	48.4%
F – PAA 3.0 wt. %	44.9%	45.1%	45.0%
I – PVA 3.0 wt. % (6% Moisture Content)	47.1%	47.8%	47.5%

The micrographs and three-dimensional microstructures reflect what has been
noted in the previous objective results in relation to the processing parameters. The highest
binder content of PVA, compact E, resulted in a higher degree of granule remnant
boundaries observe when compared to the lower binder content within compact B. The
acrylic emulsion binder and the compact processed with 6.0% moisture, compacts F and I
respectively, resulted in the highest degree of uniformity amongst the three dimensional
reconstructed microstructures. These results are similar to the microstructural
characterization and compaction analysis discussed in the previous objective results.

When comparing the two regions analyzed, the volume porosity measurement was
greater in the center regions than the edge regions, except for the case of compact E. This
is likely due to the stress distribution along the edge of the compact being the greatest along
the edges, as shown in Figure 5. Compact E could have deviated from this behavior due to
possible density gradients created from the spray-dried granules processed with the highest
concentration of PVA binder. The highest binder concentration resulted in the lowest
compacted theoretical geometric density measurement across all ten varying cases. These
compacts have resulted in a higher degree of intergranular voids and microstructural

defects that are observed within the microstructures in comparison to the other compacts. The closest segmented porosity values calculated in proximity over the two regions analyzed was attributed to the acrylic emulsion binder granule, compact F, only varying by 0.2% porosity between the maximum and minimum over the two regions. This is likely due to the knitting characteristics of the spray-dried granules resulting in a higher uniformity green compact compared over the other cases.

This three-dimensional visualization method was sufficient in visualizing the particle and pore arrangements within four varying cases of alumina compacts. The knitting characteristics of the spray-dried granules were able to be visualized and compared across all of the four varying cases. Otsu's automatic thresholding overestimated the porosity percentage in comparison to the geometric measured porosity of the alumina compact. This is likely due to the resolution of the SEM images and the pixel information gained from each of the micrographs. Even though the porosity segmentation was overestimated, the automatic thresholding algorithm was a useful tool to compare the segmented porosity measurement across all of the alumina compacts. The calculated average segmented porosity over all four samples followed a similar trend as shown with the geometric porosity measurements listed in Table 23 in the next experimental procedures section for objective 5. The reason the segmented porosity calculations resulted in an overestimation of the porosity when compared to the geometric porosity is likely due to the resolution of the micrographs analyzed. The resolution and pixel information is the limiting factor in this type of analysis. The important factor is the segmented porosity results followed a similar trend to the final geometric porosity measurements of the compact.

This type of analysis is useful for understanding localized regions of porosity as a function of processing parameters. This software made it possible to visualize the microstructure of the porous ceramic three-dimensionally, showing the porosity interconnectivity throughout the microstructure. Further analysis to separate the porosity and measure the pore sixe distribution proved difficult as the resulting three-dimensionally images had an interconnected network of pores. To achieve this analysis, further research into image processing algorithms was needed to smooth out the voxels of the three-dimensional pores and separate them into specific sizes. This type of analysis would be possible when analyzing ceramic foams that exhibit coarser pore size distributions rather than an interconnected network of pores. This analysis would be achievable through image processing techniques such as separating objects and a watershed segmentation. However, without an advanced knowledge of image processing with the Avizo software, this type of analysis for an interconnected network of pores proved difficult.

7.C. Summary

Developing a three-dimensional visualization method to section the green alumina compacts and quantify the depth loss in-between each sectioned layer was essential in improving the characterization capabilities of compacted green microstructures. Using this method with the capabilities of higher resolution FESEM micrographs to visualize the particle and pore arrangements within the alumina compacts was the focal point of this work. This developed method visualized the granule remnant and porosity network three-dimensionally, while visualizing the resultant compaction behavior of the varying spray-dried granules as a function of processing parameters. The developed method proved it was

possible to visualize and characterize the same area of the green alumina compact over a specific volume range with an accepted layering accuracy. This was achieved by tracing the depth change of the micro-indents over the volume range.

Microstructural differences were determined by comparing the different binder systems, binder amounts, and moisture contents of the spray-dried granules prior to the compaction process. Similar observations were noted as observed during the two-dimensional microstructural characterization in section 6.B. The acrylic emulsion granules (F) and higher moisture content PVA granules (I) resulted in the highest degree of microstructural uniformity as observed in the regions characterized. The PVA granules compacted at a dry moisture content showed evidence of a few persistent granular interfaces remaining after the compaction process. The higher amount of PVA binder resulted in the highest degree of microstructural defects and persistent granular interfaces. This is likely due to the segregated layers of PVA binder being localized along the surface of the spray-dried granules, which made it difficult to deform. This behavior increased the granule strength of the PVA granules and resulted in granular interfaces that were difficult to remove. The moisture content added to the PVA granules resulted in softening this binder layer and removing microstructural defects that occurred. The uniform distribution of acrylic binder resulted in a uniform compacted microstructure visualized.

The segmented porosity measurements of the four varying alumina compacts followed a similar trend in comparison to the geometric porosity measurements. Using the same automatic thresholding algorithm was imperative to compare and quantify the visualization results. Overall, the segmented porosity measurements were an overestimation based on the geometric porosity measurements. The highest porosity was

attributed to the highest content of PVA binder (E). This was likely due to the segregated binder layers impeding densification as well as the hollow cores within the internal structures of the spray-dried granules persisting throughout the compaction process. The lower PVA binder compact (B) was the next highest segmented porosity calculation, followed by the PVA compact processed at the higher moisture content (I) and the acrylic emulsion compact (F).

Three-dimensional microstructures were achieved by stacking two-dimensional FESEM micrographs at specific volumes. The downside to this method however was the small volume of 100 µm conducted for microstructural characterization. Specific regions of the alumina compact were able to be analyzed over a range of layers, however, the practicality of characterizing a larger volume of green ceramic material comes into question. Comparing the data analyses of the developed three-dimensional FESEM method to other three-dimensional characterization techniques was needed to further explore the possibilities of improving microstructural characterization capabilities of green ceramic materials. Comparing the developed method with other techniques will improve in developing the relationship between experimental and visualization results.

8. OBJECTIVE 5: Relating Processing Parameters to Visualization Results

8.A. Experimental Procedures

Micro X-ray computed tomography was conducted to compare the visualization results of the developed 3-D FESEM method to an established characterization tool. However, as explained in section 2.D.3, the difficulty with analyzing porous materials with a micro X-ray CT is gaining sufficient contrast information between loose packing structures and porosity due to the similar degrees of X-ray absorbency and attenuation coefficients. In order to analyze the green alumina compacts, a contrast agent was needed. A 0.9 M (16.5 w/v%) potassium iodide solution was vacuum infiltrated into a similar set of the four samples investigated with the FESEM 3-D method. A comparison of the geometric densities between the two sets of samples is shown below in Table 23.

The potassium iodide solution was vacuum infiltrated in four stages, each lasting ten minutes at a vacuum pressure of 0.85 Bar. Two sets were conducted on one side of the sample before the surface was saturated. Then the sample was flipped along the edge to conduct the final two sets on the opposite side of the sample, saturating that surface as well. This was to ensure full infiltration of the contrast agent through all the interconnected pores of the green alumina compact. After infiltration was finished, the sample was dried with a wipe and was left in an oven at a temperature of 80°C for an hour. The samples were then left in a desiccator overnight before testing the next day.

Each sample was analyzed at a voltage and current of 100 kV and 100 µA respectively. The pixel size of the X-rays was set to 6.99 µm using a 1 mm aluminum/copper filter. These scan parameters were kept similar to what Hondo *et al.* [30] performed to analyze a thinned unfired isostatically compacted alumina sample. The

resulting CT images were already matched in contrast from the micro X-ray CT equipment. A histogram equalization algorithm was used to widely distribute the greyscale histogram of the images. Due to the rotation of the micro X-ray CT during evaluation, ring artifacts appeared in the CT images near the top and bottom of the alumina compacts. The top and bottom slices were removed so that the observed ring artifact would not alter the segmentation analysis of the alumina compacts. Figure 103 shows the observed evidence of the ring artifact for all of the four samples.

Table 23. Percent theoretical density calculations based on the geometry and de-binded weight of the alumina compacts used for the listed characterization (ρth = 3.95 grams/cm3).

Compact's Geometric Density – Percent Theoretical Density

Granule	3-D FESEM	Micro X-ray CT	Mercury Porosimetry
B	54.6 %	54.6 %	54.8 %
E	54.1 %	54.2 %	54.2 %
F	55.8 %	56.1 %	55.9 %
I	57.1 %	57.0 %	57.2 %

The CT images were uploaded into Photoshop CS3 to remove the contrast differences within the background of the images. This was needed for segmentation purposes to be able to remove the background before the analysis. The sample within the image was cropped, the background was removed, and a new background was set to a single color of black, creating a background with one intensity. Therefore, on a greyscale histogram, the lowest intensity value would be attributed to the background of the image and can be easily removed. This process is highlighted in Figure 104 below.

After implementing a histogram equalization algorithm on the cropped images, the CT images were segmented using the same process as described previously, using Otsu's

criterion and an automating thresholding algorithm. The CT images were then stacked uniformly, with a voxel size of 6.99 μm. Using the histogram as a tool, the background was removed for the segmentation analysis. After the images were stacked and aligned, a "Volume Rendering" module was used within the Avizo software to visualize the three-dimensional reconstructed CT images.

The resultant percentage of porosity based on the segmentation analysis results were compared to the FESEM results of 100 μm. Since the CT images were evaluated for 2 mm of the sample rather than 100 μm, a similar region was evaluated for the CT images as was evaluated for the FESEM images to evaluate the same volume of 100 μm for the green alumina compacts. All values were compared to the geometric porosity calculated from the geometric densities of the alumina compacts.

The mercury porosimetry calculations were conducted using the same penetrometer for all samples analyzed. The penetrometer had a bulb size of 3 mL and a stem volume of 4.1. An initial calibration run was conducted along with a blank test of the empty penetrometer. The reason behind this was to calculate the volume and weight of the mercury within the blank penetrometer for analysis purposes. The blank test was run to a pressure of 60,000 psi absolute. During sample analysis, the intrusion rate of mercury varied depending on the test conducted and was altered to account for the porous nature of the specimen. It was imperative to slowly intrude the sample so that the mercury intrusion would not break the structure of the soft green alumina compact. Each test ranged from pressures of 10,000 to 60,000 psi absolute. The reason the test pressures ranged were to account for the issue of possibly breaking apart the structure of the green compact and not achieving sufficient results for the porosity analysis.
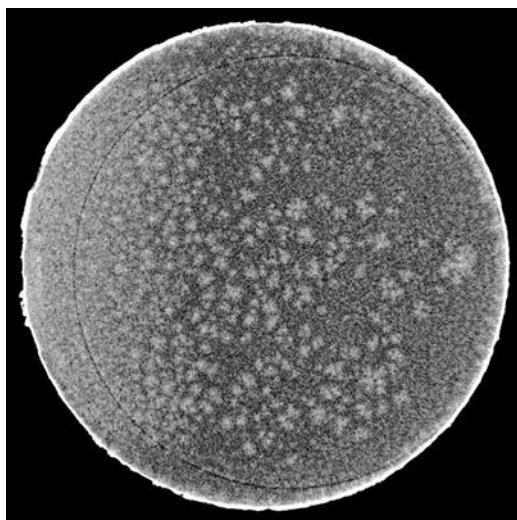
Figure 103. A micro CT image showing the appearance of a ring artifact in the microstructure of the green alumina compact that appears due to the rotation of the CT scan.
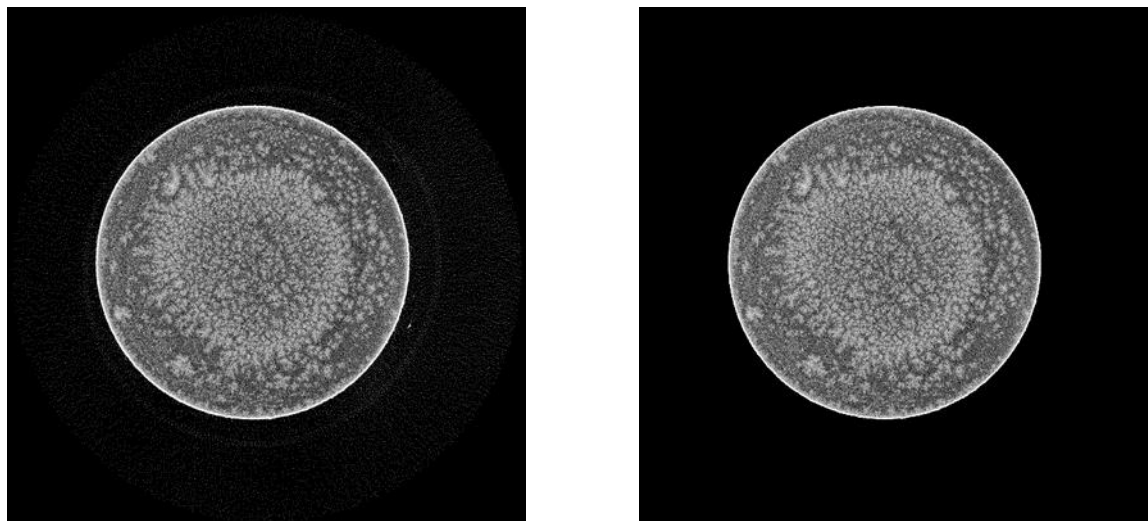
Figure 104. Micro CT images showing the removal of the background to create a single intensity background of black pixels that are easily removed during segmentation analysis.

8.B. Results and Discussion

Relating the processing results to the obtained three-dimensional visualization data was needed to be conducted by comparing the results to established characterization techniques. The three-dimensional data obtained via the new established FESEM method was compared to conventional techniques for three-dimensional visualization and porosity measurement analyses. Micro X-ray computed tomography (CT) was conducted to compare the micrographs of the FESEM images stacked in a three-dimensional microstructure to the image data obtained from a micro X-ray CT. Mercury porosimetry analyses were conducted to compare the segmented porosity calculations from the FESEM, micro X-ray CT, and geometric porosity calculations. For the three different types of analyses, three different compacts of the same processing parameters were used. The geometric porosity listed is an average over the three compacts per process parameter with the standard deviation listed. The geometric porosity comparisons amongst the three varying compacts are highlighted in Table 23.

In order to overcome the X-ray absorbency issues that arise when characterizing porous materials with micro X-ray CT, a 0.9 M solution of potassium iodide was vacuum infiltrated within all four compacts analyzed. After the solution was dried, the compacts were analyzed the following day. Each sample was analyzed at a voltage of 100 kV and current of 100 µA. The pixel size of each scan was 6.99 µm using a 1 mm aluminum/copper filter. The bright regions were attributed to the alumina material and the darker regions were attributed to porosity. This is because the contrast agent, now dried, is coated along the alumina ceramic material. A total of 250 images were analyzed for each of the four varying compacts. Each image was uploaded into Photoshop CS3 to remove the contrast

differences of the background for segmentation purposes. These images were then histogram equalized and thresholded using Otsu's automatic criterion. Based on the pixel intensity information of the black border and compact, the border was removed before calculating the segmentation results. To do this, the histogram of the images needed to be analyzed in order to account for the black border. The micro X-ray CT images were also cropped to remove the black border and compare the segmentation results of the full X-ray CT images, the cropped micro X-ray CT images, and the FESEM images discussed in the previous results section. This process is highlighted in Figure 104 to Figure 107. For comparison reasons, 100 µm of the full and cropped micro X-ray CT images were compared to the FESEM results of roughly 90 µm. The same bulk regions of the compacts, shown in Figure 86, were segmented for this analysis.

The resultant three-dimensional microstructures were stacked uniformly at their respective voxel sizes of 6.99 µm. The resultant CT microstructures of the four compacts are shown in Figure 108 to Figure 111. Due to the CT images being stacked uniformly, the Avizo software calculated the resultant segmentation results by volume and area, therefore there was no need to calculated the results per layer as a function of the layer height as was conducted for the FESEM results. The segmentation results over the four analyses conducted are shown in Table 24 for comparison.
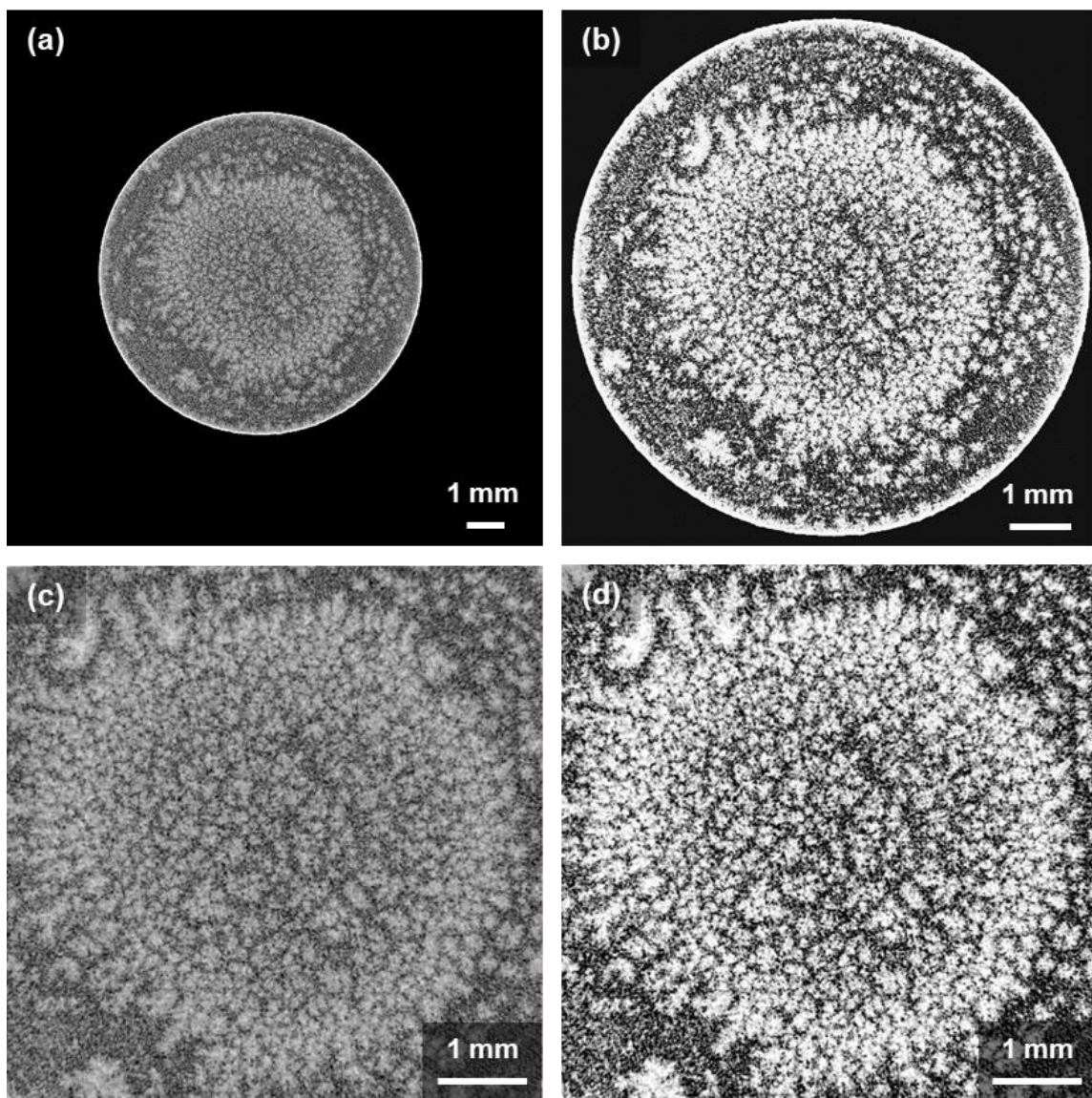
Figure 105. (a) A micro X-ray CT image of compact E, processed at 5.0 wt. % PVA binder and (b) the same image cropped and histogram equalized for thresholding purposes. The images in (c) and (d) highlight the same process for a cropped image removing the black border.
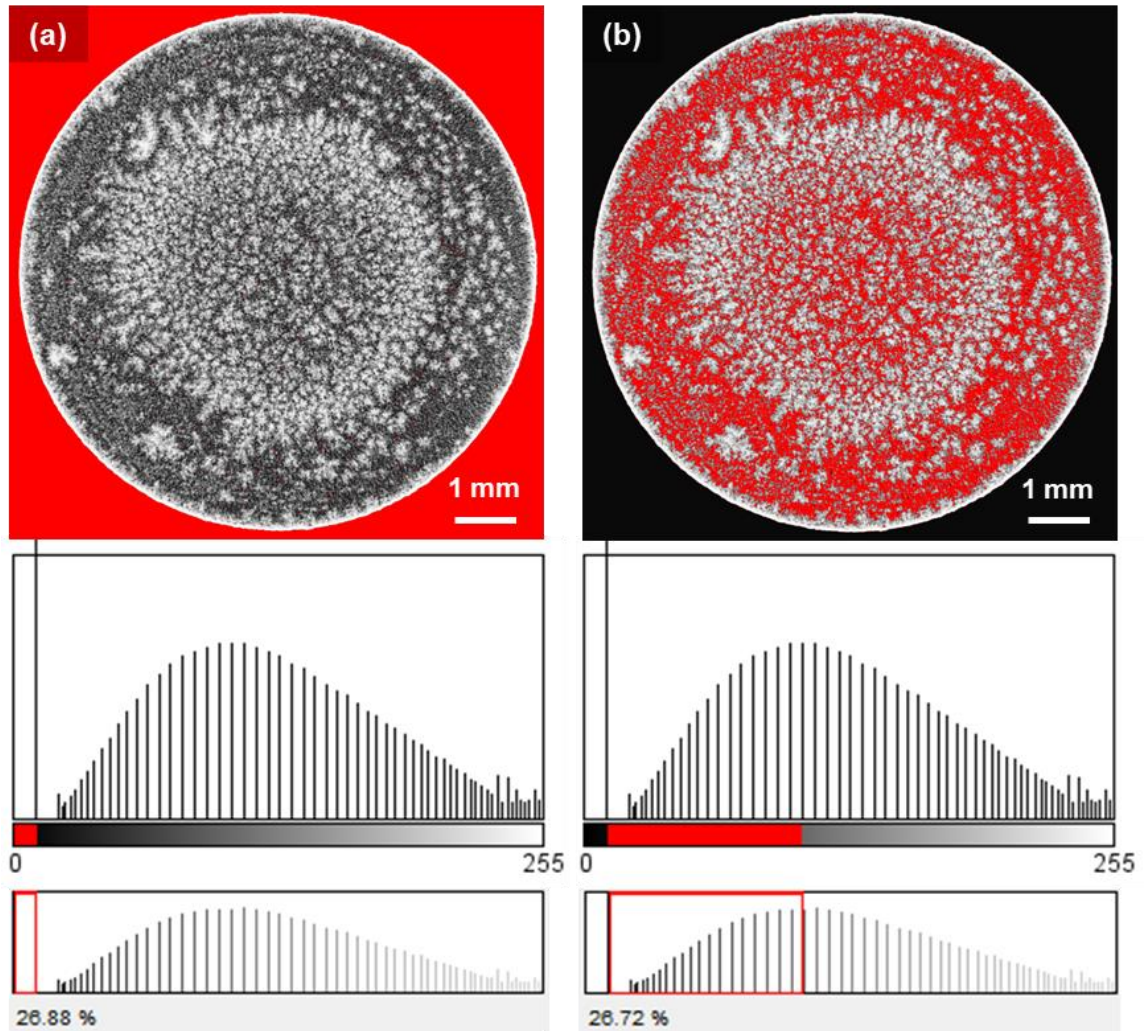
Figure 106. Otsu's automatic thresholding and respective histograms in (a) removing the black border from the analysis and (b) accounting for the porosity of the alumina compact solely.
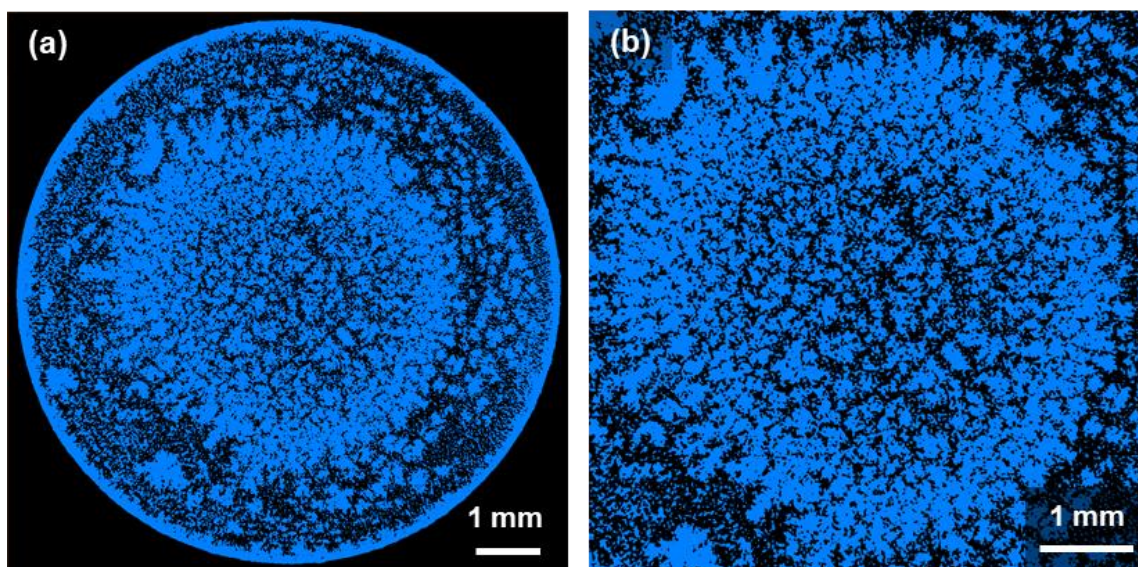
Figure 107. Binary images of the segmented micro X-ray CT microstructures of (a) the full compact and (b) the cropped microstructure removing the black border. The blue pixels correspond to alumina and the black pixels correspond to porosity.

Table 24. Micro X-ray CT segmented porosity results for the full 8.5 mm diameter compact as well as the cropped images. Both sets were evaluated at 100 μm in the same bulk region of the compact the FESEM micrographs were taken. The 3-D FESEM average segmented porosity measurements are listed for comparison.

Compact	Full X-ray	Full (100 μm)	Cropped X-ray	Cropped (100 μm)	3-D FESEM
B – PVA 3.0 wt. %	37.5%	35.3%	48.5%	46.3%	47.8%
E – PVA 5.0 wt. %	38.6%	37.6%	49.6%	48.9%	48.4%
F – PAA 3.0 wt. %	37.8%	40.2%	48.0%	46.4%	45.0%
I – PVA 3.0 wt. % (6% Moisture Content)	37.8%	37.6%	48.6%	49.1%	47.5%
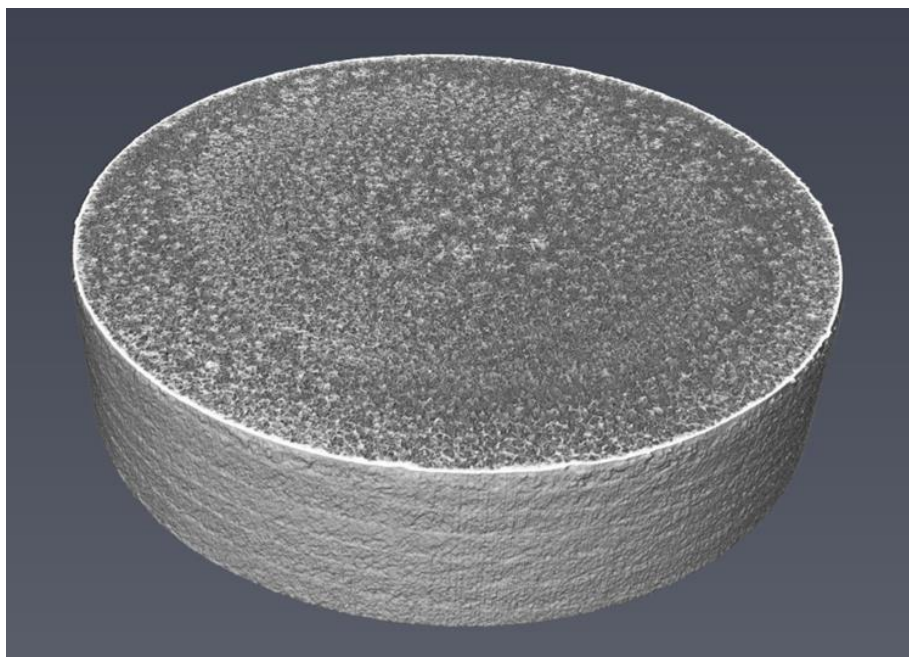
Figure 108. 3-D reconstructed microstructure of compact B (processed at 3.0 wt. % PVA) from the Avizo software. Micro X-ray CT images were stacked uniformly at the voxel size of 6.99 μm.
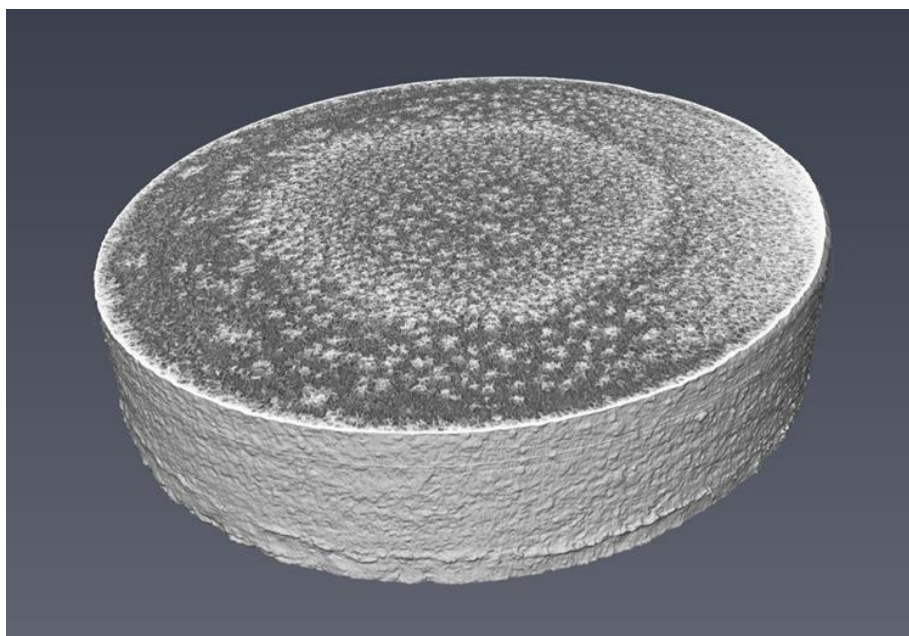
Figure 109. 3-D reconstructed microstructure of compact E (processed at 5.0 wt. % PVA) from the Avizo software. Micro X-ray CT images were stacked uniformly at the voxel size of 6.99 μm.
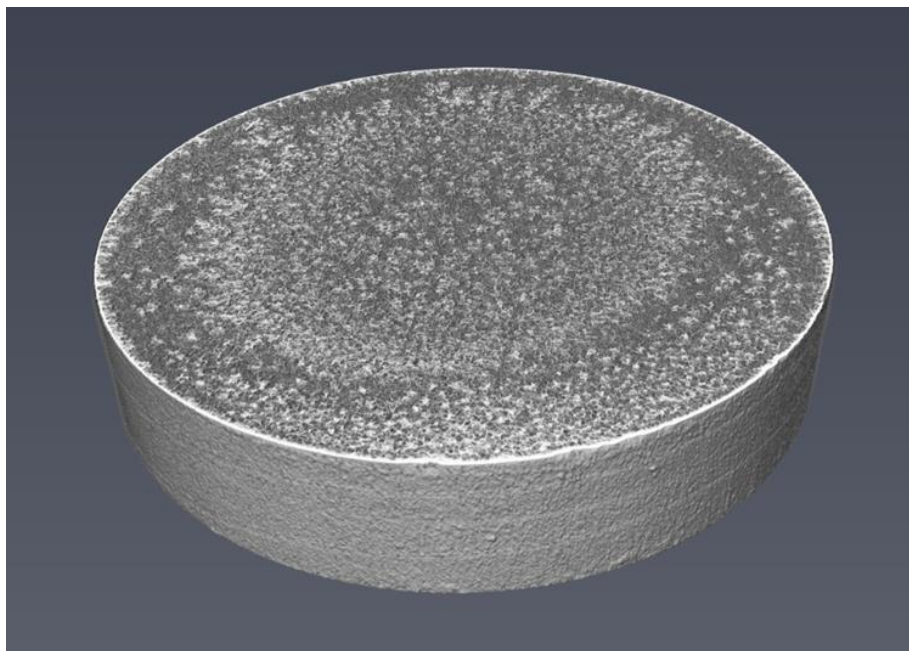
Figure 110. 3-D reconstructed microstructure of compact F (processed at 3.0 wt. % acrylic emulsion binder) from the Avizo software. Micro X-ray CT images were stacked uniformly at the voxel size of 6.99 µm.
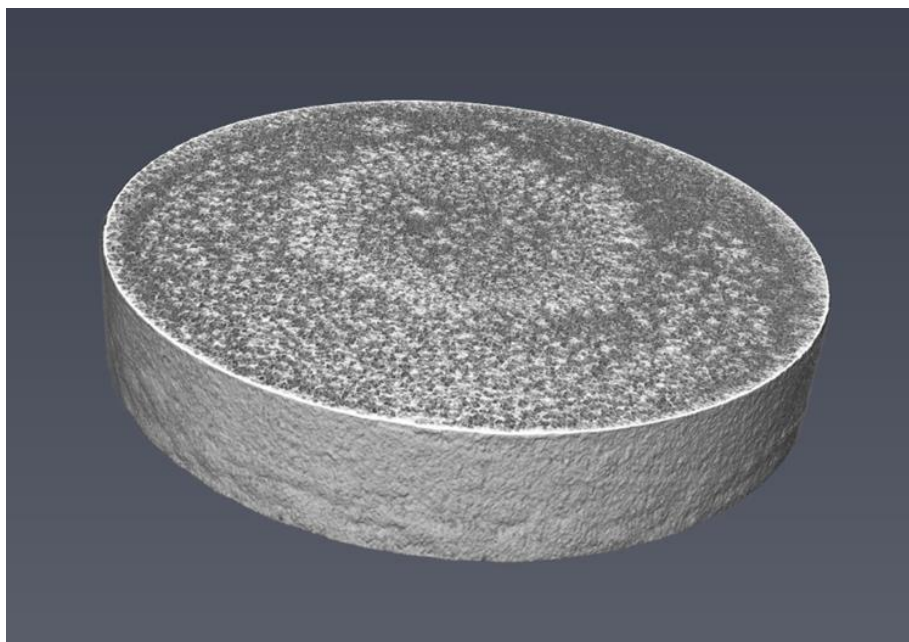
Figure 111. 3-D reconstructed microstructure of compact I (processed at 3.0 wt. % PVA and compacted with 5.97% moisture content) from the Avizo software. Micro X-ray CT images were stacked uniformly at the voxel size of 6.99 µm.

Calculating the segmentation results over the full CT sample resulted in porosity results that underestimated the porosity in comparison to the geometric porosity. In comparison to the 3-D FESEM results, the full sample CT images underestimated the segmented porosity results based on the resolution of the images. The FESEM micrographs have a higher resolution than the micro X-ray CT results due to the equipment capabilities. For the images processed, the FESEM micrographs were taken at a magnification of 500X which resulted in a pixel size of 0.59 µm/pixel (1.70 pixels/µm). In comparison, the micro CT scans were achieved at a pixel size of 6.99 µm/pixel (0.14 pixels/µm). Therefore, the FESEM micrographs at that magnification level resulted in a resolution twelve times greater than the micro X-ray CT images. It is also imperative to note that a magnification of 500X is on the coarser end of the capabilities of the FESEM and can be improved at higher magnifications.

As removing the border surrounding the full CT sample images is strongly dependent on the pixel intensity information per layer, variation may occur based on how well the background is cropped and replaced. As shown in Figure 106, the segmented porosity results are dependent on the subtraction and removal of this background. In comparison of the full CT sample segmented results, the CT images were also cropped and evaluated for the center of the compact as shown in Figure 105 and Figure 107. The segmented porosity for these images resulted in a closer trend observed for the FESEM results, with the highest porosity attributed to compact E, processed with the higher binder concentration of PVA. The trend followed with compacts I, B, and F in the order of highest porosity to lowest porosity. These results were closer in proximity to the 3-D FESEM results and the geometric porosity results calculated. The reason behind this could be due

to the density distribution on the edge of the compacts visualized over all of the four compacts tested.

The 100 µm segmentation analysis for the CT images followed a similar trend when compared to the analysis conducted over all 250 CT layers. The segmentation results for the full sample resulted in volume porosity percentages that underestimated the porosity when compared to the geometric porosity even more so then the segmentation results for all 250 layers. This is likely due to only characterizing a specific region and the respective density distribution within that bulk region of the compact. The 100 µm of the cropped images resulted in a similar trend observed for all of the cropped 250 layers, with slightly less of a porosity percentage for these layers as opposed to the values calculated for the whole compact. This is likely due to the same reason previously mentioned, the density distribution due to the uniaxial compaction process in that bulk region of the alumina sample.

Segmenting the porosity of the visualized compacts in both two and three dimensions is solely dependent on the image processing techniques used. However, this type of analysis does visualize closed porosity and other microstructural characteristics. Larger intergranular voids and closed porosity were visualized within the compact processed with the higher binder concentration of PVA, compact E. Compact B, processed with 3.0 wt. % PVA, resulted in a few visualized microstructural defects, closed porosity, and granule remnants. This is what was also observed in section 6.B., with the higher values of viscosity, solids loading, and binder concentration granules resulting in a higher degree of circularity and resultant granule remnants observed within the microstructure.

Due to the phenomenon of hollow coring within the granules processed with PVA resulting to a higher degree of closed porosity within the compact's microstructure, these remaining hollow cores visualized would be difficult to remove during the densification process. Adding moisture content to the PVA granules did benefit the removal of granules remnants and the closed porosity visualized in the prior cases, as shown with compact I. The highest degree of microstructural uniformity visualized three-dimensionally were the compacts processed with the acrylic emulsion binder. When comparing the center and edge regions analyzed with the 3-D FESEM data, similar segmented porosity results were obtained in both regions as discussed in section 7.B. The acrylic emulsion compacts resulted in the lowest porosity measurement over both segmented porosity comparisons, except for the full sample CT segmentation results. This information relates to what was observed during the green strength modulus of rupture study, microstructural characterization across various compaction pressures, and the compaction analysis conducted. There was a smaller degree of closed porosity visualized for these compacts, with the majority of the porosity attributed along the granule boundaries.

The interconnected pore network was also visible across all of the varying compacts by both visualization methods. The micro X-ray CT images made it possible to visualize the density distribution throughout regions of the alumina compact. For all four varying cases, there was a trend observed on the degree of porosity and density within the compacts shown. It seemed in some images near the bottom resulted in a larger degree of porosity when compared to their opposing side. Since the contrast agent was infiltrated into both sides of the alumina compact for the same amount of time (ten minutes) until the surface was saturated with the contrast agent, this wasn't attributed to a contrast issue with the use

of the equipment. It is possible this is due to the stress distribution of uniaxial compacted ceramics. When looking at Figure 5, the stress distributions exhibited during uniaxial compaction are highlighted. **Error! Reference source not found.** highlights this p henomenon observed over all four cases characterized. Although this method resulted in a lower spatial resolution when compared to the 3-D FESEM method, the interconnected pore network throughout the whole alumina compact was made visible in a short period of a few hours. This could be beneficial when evaluating the tortuosity of varying ceramic materials during the processing stage. The size, shape, and location of the pore network as a function of processing parameters could be characterized in a short period of time with X-ray CT techniques.

Evaluating the above micro CT images, it is clear this phenomenon occurred for all of the various compacts. The top side that was in contact with the compaction die resulted in a region of maximum density. This method visualized the density distribution during uniaxial compaction, where the highest pressure during the forming process localizes at the top of the compact. When evaluating the bottom of the compact, this region resulted in a minimum density in comparison. The highest uniformity visualized along the top and bottom surfaces of the compact was observed in compact F. Compact I showed a higher degree of density gradients along the top surface of the compact. Compact B resulted in the second highest uniformity when comparing between all four cases. Compact E resulted in a similar trend as shown with compact I.
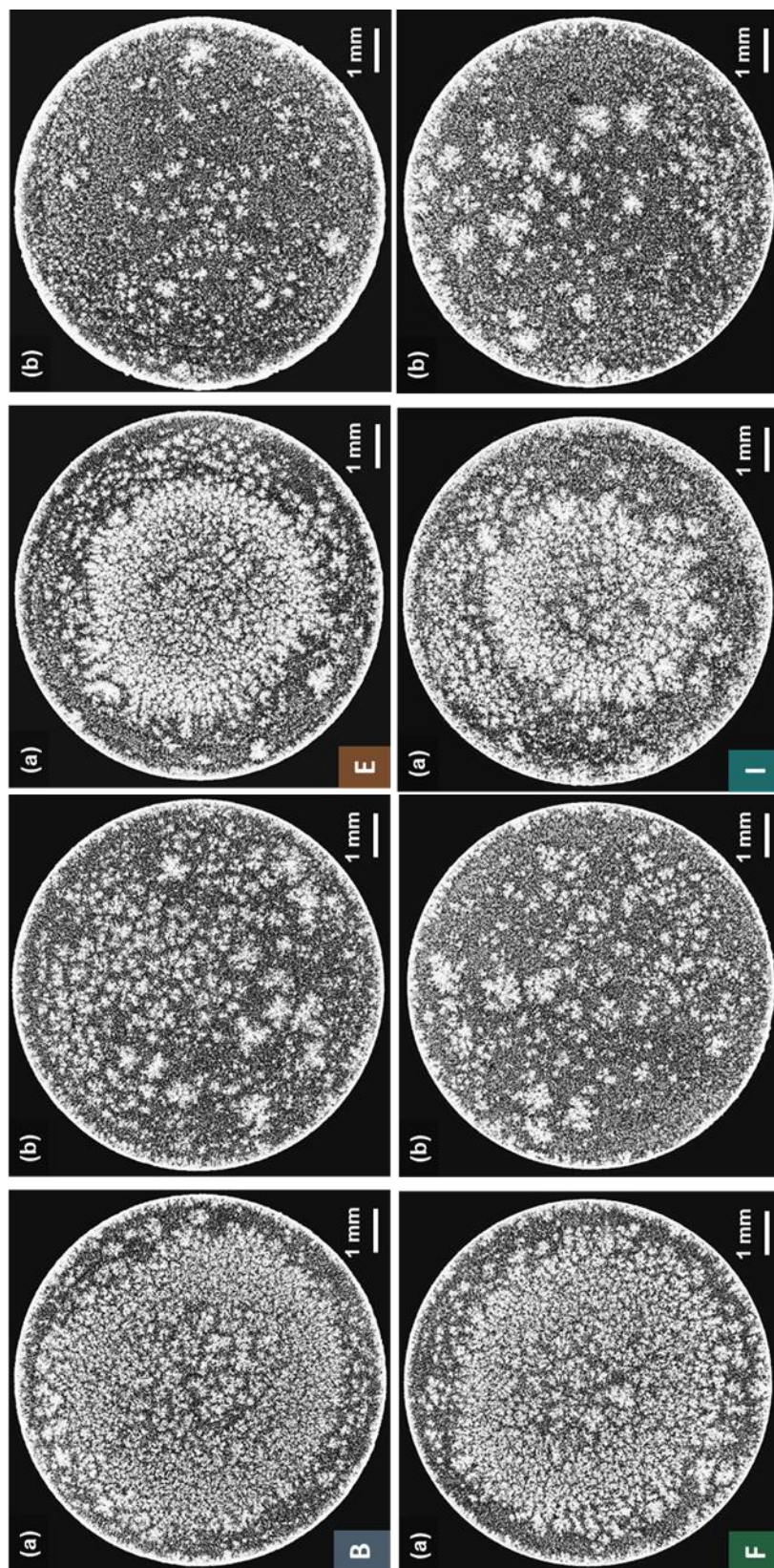
Figure 112. Micro X-ray CT images for all four varying compacts highlighting the (a) top, in contact with the die punch and (b) bottom of the compact, visualizing the density distributions during uniaxial compaction. The four varying cases included compact B (3.0 wt. % PVA), E (5.0 wt. % PVA), F (3.0 wt. % acrylic emulsion binder), and I (3.0 wt. % PVA compacted with 6.0% moisture content).

The observed density distribution is likely due to the knitting characteristics of the respective granules as well as how that behavior relates to the stress distribution within the compact during the uniaxial compaction process. As this behavior can be understood by using compaction curve analysis as a tool to understand the characteristics of the spray-dried granules, it can also be visualized with both mentioned 3-D visualization methods. This behavior is highlighted in the compaction curve analysis shown in Figure 34. Evaluating the compaction and densification rates during analysis gains insight into the knitting behavior of the spray-dried granules. Visualizing the microstructures at various uniaxial compaction pressures allows one to visualize the particle and pore orientations throughout the compaction process. Coupling that by visualizing the resultant microstructures three-dimensionally gains the capability of visualizing the interconnected pore network throughout the compact, formed density gradients, and microstructural defects as a function of processing parameters.

The 3-D FESEM method was beneficial in characterizing specific regions to a higher spatial resolution in comparison to micro X-ray CT results and improved porosity segmentation results due to this increase in resolution. The limiting factor for this process is the time it takes to remove micron sized layers of the material, measure the depth loss, and characterize the green microstructure. Even though it is a more time consuming process, its three-dimensional visualization capabilities are an improvement. It is imperative to note that X-ray CT technology is improving and the resolution capabilities are improving as well, therefore this type of analysis may be possible in the future and can also be achieved in a timely manner.

Unfortunately, sufficient data was not collected for the mercury porosimetry analysis. Initially, compacts processed with the acrylic emulsion binder were tested. The reason behind this was because these compacts returned the highest flexural strength results compared to the other compacts analyzed during the modulus of rupture testing in section 5.B. Unfortunately, all of the compacts broke apart during the mercury porosimetry analysis. The rate of mercury intrusion was decreased to account for this issue, however, no successful run was achieved. All of the compacts returned porosity measurements that could not be calculated based on the volume measurement achieved during the blank penetrometer runs and the weight of the added compact during analysis. The only run that achieved a porosity value was the first acrylic emulsion compact tested. It returned a porosity value of 1.8% porosity, which is a known underestimation for the green alumina compacts. Further analysis was deemed difficult with the other alumina compacts and did not occur due to the insufficient results obtained initially. It is imperative to note that this type of mercury intrusion analysis for porosity calculations of unfired or green ceramic materials is difficult due to the soft nature of the samples. This reason reflects the advantages of image segmentation analysis for porosity calculations of three-dimensionally visualized green ceramic materials with the use of a FESEM or X-ray computed tomography.

When evaluating the degree of intergranular voids and porosity, the compacts processed with the highest percentage of PVA binder (E) showed the largest evidence of these observed voids. A clear network of granule boundaries is present in all visualized data, in both two and three dimensions. It is evident that these compacts resulted in microstructures that will contain persisted residual defects from the higher degree of PVA

binder. These defects included persistent closed porosity from the hollow cores within the granular microstructure as well as low density regions remaining along the intergranular boundaries present. The highest degree of microstructural uniformity was observed in the compacts processed with the acrylic emulsion binder (F) and compacted with the PVA binder at a moisture content of 5.97% (I). The compact processed with the B granules resulted in less observed granule boundaries and intergranular voids present in comparison to the E compact, however, there still existed evidence of these characteristics. These observed characteristics for all varying compacts were similar to the observed microstructural characteristics in the two-dimensional micrographs from section 6.B. As previously stated, the three-dimensional information gained from the 3-D FESEM microstructural imaging gained visualization knowledge of the knitting characteristics of these compacts as a function of processing parameters. Similar information was gained by the two-dimensional analysis when comparing the processing parameters, however, the three-dimensional analysis gained more information on the resultant structure and the characteristics of the spray-dried granules during compaction.

Relating the processing parameters to the observed visualization results will be evaluated for all granule cases. Based on the binder systems evaluated for this dissertation, granules processed with the polyvinyl alcohol binder resulted in tougher granules to deform in comparison to the acrylic emulsion binders. The acrylic spray-dried granules resulted in higher density and degree of microstructural uniformity in comparison to the PVA granules. This is also evident during the compaction analysis and resultant microstructures of the binder systems. The acrylic granules resulted in higher density compacts at lower compaction pressures. Fewer observed microstructural defects resulted in the acrylic

compacts when compared to the PVA compacts. The pore network observed three-dimensionally was considered more uniform as well, and could be the reason higher green strength compacts were processed with this binder system in comparison to the PVA binder system. This microstructural uniformity could relate to the higher green strength values as well as final sintered hardness and flexural strength properties researched [19].

The viscosity of the ceramic slurries spray-dried with the same binder system seemed to govern the droplet formation during the drying stage of the process and thus the resultant particle orientation and morphology of the spray-dried granule. This is likely due to the movement of particles within the suspension correlated to the movement of particles during the droplet formation and thus the generated spray-dried granule. A higher degree of circularity was observed for the granules with the highest viscosity evaluated. These granules resulted in lower critical yield pressures when compared to the lower viscosity granules evaluated. This could be due to fewer microstructural voids and defects within the internal structure of the higher viscosity granules (C) being present when compared to the lower viscosity granules (A and B). These defects may act as stress concentrators, increasing the strength of the granules and reducing the deformation rate during compaction. This could be the reason the higher viscosity granules (C) resulted in higher compacted densities when compared to the other two viscosity cases. The resultant microstructures

The higher solids loading, or specific gravity, of the alumina slurries prior to spray-drying (granule case D) resulted in granules that exhibited a higher critical yield pressure but similar compaction characteristics otherwise when compared to the lower solids loading case (C). The higher solids loading slurries generated granules that exhibited a

greater density measurement due to the higher degree of alumina solids processed and thus a variation in particle orientation due to the higher degree of solids loading processed. Other than the granule density affecting the overall critical yield pressure exhibited, there was no other variation noticed during compaction analysis or characterization between the two varying solids loading slurries. The compaction characteristics were categorized as similar. The resultant two-dimensional micrographs characterized resulted in similar characteristics when compared. The final compacted densities varied by a theoretical density percentage of 0.2%. Therefore, the solids loading seems to have an effect on the overall density and the resultant particle packing and orientation of the generated spray-dried granule. The viscosity of the alumina suspension, as it relates to the overall charge differences within the system, seems to play a major role in the movement and orientation of the formed droplets and therefore the overall spray-dried granule characteristics and resultant observed microstructural characteristics.

In terms of evaluating the binder percentages of the polyvinyl alcohol binder system, the higher degree of binder (granule case E) within the alumina slurry prior to spray-drying resulted in spray-dried granules with a lower density and a greater degree of internal microstructural defects when compared to the lower binder percentage case (B granules). The critical yield pressure decreased with the increasing moisture content and this could be due to the larger degree of generated microstructural defects producing weaker spray-dried granules. However, these granules do not seem to easily deform, with large intergranular voids and boundaries persisting throughout the compacted microstructure in comparison to the lower binder percentage case (B). These observations can be made when evaluating the two-dimensional micrographs. When observing the

microstructures in three-dimensions, the observation is the same, with larger intergranular porosity regions and voids being produced with the greater binder percentage. The density distribution observed when evaluating the micro X-ray CT data set seemed greater in the higher PVA amount. This could be likely due to the lower density granules generated with the higher polyvinyl alcohol percentage. These lower density compacts produced with the higher percentage of PVA binder may result in lower density sintered microstructures that deplete the properties and reliability of the alumina part. However, without further investigation of this behavior, this statement is only based on speculation that uniform green microstructures will produce more reliable sintered ceramic parts.

Adding varying levels of moisture content does aid in the removal of the observed microstructural defects within the internal structure of the spray-dried granules processed with the PVA binder. As moisture is a plasticizer for polyvinyl alcohol, the critical yield pressure decreases with increasing moisture content. Green strength and handability increase with increasing moisture content by promoting higher density parts at lower compaction pressures. However, in terms of the practicality of this process, adding moisture in manufacturing processes can become costly and time restrictive. Even though it aided in the compaction and deformation behavior of the granules, increasing the green strength of the alumina compacts, and promoted a higher degree of uniformity in both two and three dimensions, similarly to the acrylic emulsion binder system evaluated, it can become an impractical processing parameter on a larger scale. Adding moisture to the acrylic granules (J) decreased the green strength of the compact due to the observed abundance of porosity localized along the granule boundaries within the microstructure.

8.C. Summary

It was important to compare the results of the developed three-dimensional method using FESEM micrographs to an established method used for visualizing samples three-dimensionally. The difficult aspect of using micro X-ray computed tomography to characterize green or porous ceramics is distinguishing between loose packing structures and porosity within the material's microstructure. Overcoming the X-ray attenuation differences of these attributes is imperative to be able to conduct this analysis on green ceramics. Micro X-ray CT has lower resolution capabilities and gaining enough information to adequately visualize the different attributes of the microstructure may prove difficult.

Potassium iodide as a contrast agent proved successful in distinguishing the porosity, loose packing structures, and alumina material during the analysis. The resolution of the FESEM three-dimensional analyses were twelve times greater than the pixel size of the micro X-ray CT analysis (6.99 μm). The FESEM analysis can always be improved to be conducted at higher magnifications then the conducted resolution for this dissertation. The other downside to this analysis is the specimen size being analyzed. The sample has to fit into the chamber to be able to rotate and gain information. Most specimens are thinned to a specific size to achieve this type of characterization. The positive attribute to this method is the time scale on achieving a larger volume range in comparison to the three-dimensional FESEM method.

Although the micro X-ray CT analysis achieved less sub-micron information in comparison to the FESEM method, it was able to visualize density gradients throughout the alumina compacts. Visualizing the variation in density gradients as a function of

processing parameters was an improvement from the small amount of volume characterized with the FESEM method. The visualized density gradients highlight the effect the processing parameters had on the microstructure as a whole throughout the whole compact. Although the density gradients observed were representative of the uniaxial compaction process and the location of pressure regions during compaction, varying attributes were noticed amongst the varying processing parameters. Although the added moisture content to the polyvinyl alcohol granules (I) improved the densification and removal of coarse microstructural defects within the compact, the density distribution observed seemed to be greater than the polyvinyl alcohol binders compacted without moisture content (B). This evidence showed that even though moisture improved the green strength and overall densification process during compaction, green bulk density variation was still an issue. The higher polyvinyl alcohol content granules (E) resulted in a similar observed phenomenon as the moisture content granules (I). The acrylic emulsion compacts observed had the highest degree of uniformity throughout the bulk of the green alumina compact. This behavior was constant throughout the experimental and visualized data sets.

Similar visual observations were made as previously stated in section 6.B. In terms of relating all of the visualization results to the obtained experimental results, it seems polyvinyl alcohol binder causes microstructural defects during the spray-drying process that persist throughout compaction. This behavior of persistent closed porosity, granular interfaces and remnants, as well as segregated binder layers, deplete the green strength of the alumina compact and may persist during sintering and deplete the overall reliability of the ceramic compact. Adding moisture to the polyvinyl alcohol binders aided in the removal of these defects, resulting in stronger alumina compacts that showed a higher

degree of microstructural uniformity. This higher uniformity will enhance sintering kinetics and possible promote highly reliable ceramic parts. However, the downside is the impractical nature of using moisture as a compaction aid during large scale manufacturing processes. Acrylic emulsion binders promoted higher green strength compacts without moisture and promoted higher density parts at lower compaction pressures. These compacts showed higher degrees of microstructural uniformity throughout the compact in two and three-dimensions.

The segmented porosity results of the full alumina compacts resulted in porosity measurements that were underestimations in comparison to the geometric porosity measurements. The trend was not similar to the geometric measurements as well, with the lowest porosity calculation attributed to the compact with the lower PVA binder amount (B). This was likely due to the resolution capabilities of the micro X-ray CT system, as most of the generated measurements for the varying compacts were close in proximity. Cropping the micro X-ray CT micrographs to only evaluate the bulk of the compact resulted in segmented porosity results similar to the obtained FESEM analysis. The trend of these porosity values were similar to the trend of the FESEM results as well. This was likely due to removing the edge regions of the compact during the analysis. These regions had higher degrees of density distributions due to the exhibited compaction pressures localized along these regions of the compact during uniaxial compaction.

Mercury porosimetry analysis was difficult to conduct with the soft green alumina compacts. All of the tested compacts broke apart during the initial stage of mercury intrusion. The correct bulb and stem sized were used for the range of porosity the alumina compacts were based on the geometric porosity. The rate of mercury intrusion was varied,

however, no improvements were noted when this rate was decreased. Due to the amount of mercury used during the failed tests, no further testing was completed. Due to the difficulty of this analysis with green ceramic materials, image processing is a sufficient alternative method for porosity analysis.

Image processing for segmented porosity analysis is dependent on the tools and methods used as well as the resolution of the obtained micrographs. High resolution micrographs, such as the FESEM micrographs and stacked three-dimensional FESEM micrographs, obtained microstructural information that is difficult to account for with other methods. That is what makes this analysis technique important in characterizing green ceramic materials. The ability to visualize these microstructural variations and compare them to experimental data analyses is imperative to improve the reliability of processed ceramic materials. Coupling the developed three-dimensional FESEM method with micro X-ray CT analysis developed a visualization relationship to the experimental results on what processing parameters affect microstructural variations in dry-pressed alumina compacts.

9. CONCLUSIONS

The work conducted for this dissertation centered on correlating a relationship between experimental and visualization results of spray-drying and compacted alumina as a function of processing parameters. The varied processing parameters included the slurry characteristics prior to spray-drying and the granule characteristics prior to compaction. The viscosity, solids loading, binder type and amount were investigated to understand what characteristics altered granule morphologies after the spray-drying process as well as what characteristics affected the compaction behavior of the generated granules.

The solids loading affected the overall density of the spray-dried granules. The higher the solids loading, the higher the densities of the spray-dried granules. The viscosity of the alumina suspension affected the overall granule morphologies generated. The lower the viscosity values, the higher the degree of irregular shaped granules and microstructural defects were observed. The binder type affected the movement of the particles within the atomized droplets as well as the drying behavior of the generated droplets during the spray-drying process. The acrylic and polyvinyl alcohol binders tested showed a variation in binder segregation during the spray-drying process. Polyvinyl alcohol segregated to the surface of the spray-dried granules during the evaporation stage due to being water soluble. This behavior affected the distribution of the binder within the spray-dried granule. A higher amount of polyvinyl alcohol was evaluated, and it was found the higher the polyvinyl alcohol content, the lower the density of the generated granules. These granules resulted in higher degrees of microstructural defects within the granules internal structure. The acrylic emulsion binder generated higher density granules that consisted of a more uniform internal structure of alumina particles. The viscosity of the alumina slurries prior

to spray-drying did not alter the density of the generated granules to a significant amount. The viscosity only affected the overall morphology of the granules.

The compaction characteristics were evaluated as a tool in differentiation the compaction differences as a function of processing parameters. Mort's hybrid springback model was sufficient in accounting for the elastic springback and machine compliance during the compaction process. The acrylic granules resulted in lower critical yield pressures and promoted higher density parts at lower pressures. Similar critical yield pressures were noted for all of the varying polyvinyl alcohol binders. The higher the solids loading resulted in slightly higher critical yield pressures. The higher the binder amount resulted in lower critical yield pressures in comparison to the lower binder amount. Adding moisture content to the spray-dried granules resulted in lower critical yield pressures and promoted higher density parts at lower compaction pressures. The compacted density increased with increasing moisture content. Adding moisture to the acrylic emulsion binder increased the density of the alumina compact but did not lower the critical yield pressure.

Modulus of rupture green flexural strength testing was also conducted on the varying binder systems as a function of moisture content during compaction. The higher the moisture content during compaction with the polyvinyl alcohol binders, the higher the green strength values calculated. The acrylic emulsion binders with no moisture content exhibited the second highest green strength values, however, adding moisture content to these granules lowered the green strength. This was due to acrylic emulsion binders not being sensitive to humidity or moisture content. The fracture surfaces of these samples were further explored during microstructural characterization on a FESEM. Fewer granular interfaces or remnants were observed with the compacts that exhibited the higher green

strength values. This shows that the stress localized along the granular boundaries and these lower density regions were the initial flaws that caused the failure during analysis. Fewer granular interfaces and a higher degree of microstructural uniformity increased the green strength and handability of the processed ceramic.

Visualizing the compacted microstructures aided in the understanding of the observed compaction results. Higher degrees of microstructural defects were observed for the granules processed with the polyvinyl alcohol binder. The highest degree of these defects was observed for the compacts processed with the higher amount of binder. Closed porosity was an issue due to the abundance of hollow cores visualized within the internal structure of the polyvinyl alcohol. These hollow cores are difficult to remove and persist throughout the compaction process. Adding moisture to the granules prior to compaction aided in the removal of these defects and improved the degree of coarse pores being evident within the microstructure. The acrylic compacts exhibited higher microstructural uniformity due to not exhibiting a high degree of hollow cores within the internal structure of the spray-dried granules. Visualizing these differences in the parallel and perpendicular direction of compaction improves the characterization capabilities of processing the alumina compacts with the low viscosity infiltration method.

The method was developed to visualize green alumina compacts in three-dimensions with the use of a FESEM, a registration material, micro-indents, and calculating the depth change of these indents throughout a cycle of material removal via mechanical polishing. This method returned accurate material removal calculations across a volume of nearly 100 microns. High resolution FESEM micrographs were stacked and a three-dimensional reconstructed microstructure was achieved. Analysis techniques were

used to analyze these microstructures and quantify the visualized porosity differences amongst the varying alumina compacts. This method was compared to another three-dimensional visualization method in micro X-ray CT. The FESEM method obtained more microstructural information than the micro X-ray CT micrographs. However, the micro X-ray CT analysis was quicker and had the ability to visualize the density variations throughout the bulk of the green alumina compact.

A relationship was established between experimental and visualization results to improve the characterization capabilities of green ceramic materials. This improved methodology will aid in the understanding of what processing parameters promote reliability or microstructural variations. Image processing of these green ceramic materials used as a tool to correlate a further fundamental relationship of what forming methods and processing systems promote the reliability needed for a specific application is the key moving forward in improving the capabilities of green microstructural characterization.

10. FUTURE WORK

This project and has multiple paths it could follow going forward. In terms of following the research work conducted in this dissertation, looking into the same candidate system of spray-dried alumina and compacted green bodies, the three-dimensional FESEM visualization method could be used to generate three-dimensional microstructures of single spray-dried granules. This would evaluate the particle orientations, hollow coring or defect size, and potentially binder location within the internal structure of the spray-dried granules. As improvements are being made on the technology of X-ray computed tomography, higher resolution X-ray CT analysis could be conducted as well. Nano X-ray

CT could be used to evaluate the density distribution of the green alumina compacts as a function of processing parameters, furthering improving the characterization capabilities of green ceramic materials.

In terms of image processing, tortuosity quantification methods could be further explored. Tortuosity is defined as the differences in pore size and pore length throughout a porous medium. When segmented, each pixel or voxel within the image is attributed to material or porosity. For the case of compacted alumina, the pore network within the compact is interconnected. Therefore, in terms of image processing, calculating the pore size distribution is difficult throughout an interconnected network three-dimensionally. There are algorithms and image processing methods that can calculate a numerical value for tortuosity based on the segmented voxel location and the nearest location of a similar voxel. There are three algorithms that could be used: hydraulic, diffusional, and geometric. These algorithms calculate a tortuosity value by taking different paths throughout the three-dimensional pore network. Tortuosity is calculated based on the longest path over the shortest path for a porosity pixel to lineup with a corresponding pixel throughout all of the N layers of the three-dimensional data set. The closest the calculated number for tortuosity is to a value of one, the higher the uniformity of the pore network. Further research into this type of analysis would be beneficial for binder removal models and similar modeling related projects within ceramic processing research.

In terms of visualization aspects, continuing the three-dimensional FESEM method on other forming methods, such as additive manufacturing or extrusion, would be plausible. Visualizing the effect of different processes within these methods could be explored. Another material candidate system could also be evaluated. This system could be another

ceramic material, such as silicon carbide, boron carbide, silicon nitride, or zirconia. This

other system could even be other materials such as metals. Using nano X-ray CT

technology as well would be valuable for these forming methods or other candidate

systems.

11. REFERENCES

[1]   A. Jillavenkatesa, S. J. Dapkunas, and L.-S. H. Lum, "Particle size characterization," *NIST Special publication,* 2001.
[2]   S. W. Smith, "Influence of granule characteristics on the compaction behavior of granulated ceramic powders," Rutgers University, 2000.
[3]   N. A. Golomb, "Compaction Behavior of Spray Dreied Alumina," Rutgers University, 1997.
[4]   D. J. Shanefield, *Organic Additives and Ceramic Processing: With Applications in Powder Metallurgy, Ink, and Paint*, 2nd ed.: Kluwer Academic Publishers, 1999.
[5]   K. Uematsu, J. Y. Kim, M. Miyashita, N. Uchida, and K. Saito, "Direct Observation of Internal Structure in Spray-Dried Alumina Granules," *Journal of the American Ceramic Society,* vol. 73, pp. 2555-2557, 1990.
[6]   Y. Saito, S. Tanaka, N. Uchida, and K. Uematsu, "Direct Evidence for Low-Density Regions in Compacted Spray-Dried Powders," *Journal of the American Ceramic Society,* vol. 84, pp. 2454-2456, 2001.
[7]   Y. Saito, S. Tanaka, and N. Uchida, "CLSM for Ceramic Green Microstructure," *American Ceramic Society Bulletin,* vol. 81, pp. 35-38, 2002.
[8]   K. Uematsu, M. Miyashita, J. Y. Kim, and N. Uchida, "Direct Study of the Behavior of Flaw-Forming Defect in Sintering," *Journal of the American Ceramic Society,* vol. 75, pp. 1016-1018, 1992.
[9]   Y. Zhang, N. Uchida, and K. Uematsu, "Direct observation of non-uniform distribution of PVA binder in alumina green body," *Journal of materials science,* vol. 30, pp. 1357-1360, 1995.
[10]   K. Uematsu, "Immersion microscopy for detailed characterization of defects in ceramic powders and green bodies," *Powder Technology,* vol. 88, pp. 291-298, 1996.
[11]   Y. Zhang, X. Tang, N. Uchida, and K. Uematsu, "Binder surface segregation during spray drying of ceramic slurry," *Journal of materials research,* vol. 13, pp. 1881-1887, 1998.
[12]   T. Hotta, K. Nakahira, M. Naito, N. Shinohara, M. Okumiya, and K. Uematsu, "Origin of strength change in ceramics associated with the alteration of spray dryer," *Journal of materials research,* vol. 14, pp. 2974-2979, 1999.
[13]   N. Shinohara, M. Okumiya, T. Hotta, K. Nakahira, M. Naito, and K. Uematsu, "Formation mechanisms of processing defects and their relevance to the strength in

alumina ceramics made by powder compaction process," *Journal of materials science,* vol. 34, pp. 4271-4277, 1999.

[14]   N. Shinohara, M. Okumiya, T. Hotta, K. Nakahira, M. Naito, and K. Uematsu, "Seasonal Variation of Microstructure and Sintered Strength of Dry-Pressed Alumina," *Journal of the American Ceramic Society,* vol. 82, pp. 3441-3446, 1999.

[15]   K. Uematsu, N. Uchida, Z. Kato, S. Tanaka, T. Hotta, and M. Naito, "Infrared microscopy for examination of structure in spray-dried granules and compacts," *Journal of the American Ceramic Society,* vol. 84, pp. 254-256, 2001.

[16]   N. Shinohara, S. Katori, M. Okumiya, T. Hotta, K. Nakahira, M. Naito*, et al.*, "Effect of heat treatment of alumina granules on the compaction behavior and properties of green and sintered bodies," *Journal of the European Ceramic Society,* vol. 22, pp. 2841-2848, 2002.

[17]   Y. Saito, J. Nyumura, Y. Zhang, S. Tanaka, N. Uchida, and K. Uematsu, "Kinetics of property change associated with atmospheric humidity changes in alumina powder granules with PVA binder," *Journal of the European Ceramic Society,* vol. 22, pp. 2835-2840, 2002.

[18]   Y. Saito, J. Nyumura, K. Fukai, Y. Zhang, N. Uchida, and K. Uematsu, "Moisture diffusion in alumina green compact containing polyvinyl alcohol binder," *Journal of the Ceramic Society of Japan,* vol. 110, pp. 237-242, 2002.

[19]   S. Tanaka, C. C. Pin, and K. Uematsu, "Effect of Organic Binder Segregation on Sintered Strength of Dry-Pressed Alumina," *Journal of the American Ceramic Society,* vol. 89, pp. 1903-1907, 2006.

[20]   S. Jiang, T. Matsukawa, S. Tanaka, and K. Uematsu, "Effects of powder characteristics, solid loading and dispersant on bubble content in aqueous alumina slurries," *Journal of the European Ceramic Society,* vol. 27, pp. 879-885, 2007.

[21]   S. Tanaka, C. Chia-Pin, Z. Kato, and K. Uematsu, "Effect of internal binder on microstructure in compacts made from granules," *Journal of the European Ceramic Society,* vol. 27, pp. 873-877, 2007.

[22]   M. Imran Zainuddin, S. Tanaka, and K. Uematsu, "Effect of Segregation of a Polyacrylic Acid (PAA) Binder on the Green Strength of Dry-Pressed Alumina Compacts," *Journal of the American Ceramic Society,* vol. 91, pp. 3896-3902, 2008.

[23]   Z. M. Imran, S. Tanaka, and K. Uematsu, "Effect of polyacrylic acid (PAA) binder system on particle orientation during dry-pressing," *Powder Technology,* vol. 196, pp. 133-138, 2009.

[24]   M. I. Zainuddin, S. Tanaka, R. Furushima, and K. Uematsu, "Correlation between slurry properties and structures and properties of granules," *Journal of the European Ceramic Society,* vol. 30, pp. 3291-3296, 2010.

[25]   S. Tanaka, Z. Kato, N. Uchida, and K. Uematsu, "Direct observation of aggregates and agglomerates in alumina granules," *Powder technology,* vol. 129, pp. 153-155, 2003.

[26]   S. Tanaka, "Design of packing structures through direct characterization of ceramics green bodies," *Journal of the Ceramic Society of Japan,* vol. 114, pp. 141-146, 2006.

[27]   Z. Kato, S. Tanaka, N. Uchida, and K. Uematsu, "Observation of the granule packing structure using a confocal laser-scanning microscope," *Journal of the European Ceramic Society,* vol. 26, pp. 683-687, 2006.

[28]   S. Tanaka, Y. Kuwano, and K. Uematsu, "Packing structure of particles in a green compact and its influence on sintering deformation," *Journal of the American Ceramic Society,* vol. 90, pp. 3717-3719, 2007.

[29]   K. Sato, H. Abe, M. Naito, T. Hotta, and K. Uematsu, "Structure of strength-limiting flaws in alumina ceramics made by the powder granule compaction process," *Advanced Powder Technology,* vol. 17, pp. 219-228, 2006.

[30]   T. Hondo, Z. Kato, and S. Tanaka, "Enhancing the contrast of low-density packing regions in images of ceramic powder compacts using a contrast agent for micro-X-ray computed tomography," *Journal of the Ceramic Society of Japan,* vol. 122, pp. 574-576, 2014.

[31]   T. Hondo, Z. Kato, K. Yasuda, F. Wakai, and S. Tanaka, "Coarse pore evolution in dry-pressed alumina ceramics during sintering," *Advanced Powder Technology,* vol. 27, pp. 1006-1012, 2016.

[32]   T. Hondo, K. Yasuda, F. Wakai, and S. Tanaka, "Influence of binder layer of spray-dried granules on occurrence and evolution of coarse defects in alumina ceramics during sintering," *Journal of the European Ceramic Society,* vol. 38, pp. 1846-1852, 2018.

[33]   P. Ramavath, M. Swathi, M. B. Suresh, and R. Johnson, "Flow properties of spray dried alumina granules using powder flow analysis technique," *Advanced Powder Technology,* vol. 24, pp. 667-673, 2013.

[34]   S. R. James, "Principles of Ceramics Processing," 2nd ed: Wiley, New York, 1995.

[35]   W. H. Rhodes, "Agglomerate and particle size effects on sintering Yttria-stabilized Zirconia," *Journal of the American Ceramic Society,* vol. 64, pp. 19-22, 1981.

[36]   F. Lange, "Sinterability of agglomerated powders," *Journal of the American Ceramic Society,* vol. 67, pp. 83-89, 1984.

[37]   K. Masters, "Spray drying handbook," *Spray drying handbook.,* 1985.

[38]   S. J. Lukasiewicz, "Spray-Drying Ceramic Powders," *Journal of the American Ceramic Society,* vol. 72, pp. 617-624, 1989.

[39]   W. J. Walker, J. S. Reed, and S. K. Verma, "Influence of Slurry Parameters on the Characteristics of Spray-Dried Granules," *Journal of the American Ceramic Society,* vol. 82, pp. 1711-1719, 1999.

[40]   H. Takahashi, N. Shinohara, and K. Uematsu, "Influence of spray-dry slurry flocculation on the structure of sintered silicon nitride," *Journal of the Ceramic Society of Japan,* vol. 104, pp. 59-62, 1996.

[41]   G. Bertrand, C. Filiatre, H. Mahdjoub, A. Foissy, and C. Coddet, "Influence of slurry characteristics on the morphology of spray-dried alumina powders," *Journal of the European Ceramic Society,* vol. 23, pp. 263-271, 2003.

[42]   G. Bertrand, P. Roy, C. Filiatre, and C. Coddet, "Spray-dried ceramic powders: A quantitative correlation between slurry characteristics and shapes of the granules," *Chemical Engineering Science,* vol. 60, pp. 95-102, 2005.

[43]   W. Walker and J. Reed, "Green testing of pressed compacts," *A Collection of Papers on Engineering Aspects of Fabrication of Ceramics: Ceramic Engineering and Science Proceedings, Volume 14, Issue 11/12,* pp. 43-57, 1993.

[44]   X. K. Wu, D. W. Whitman, W. L. Kaufell, W. C. Finch, and D. I. Cumbers, "Acrylic binders for dry pressing ceramics," in *98th Annual Meeting and the Ceramic Manufacturing Council's Workshop and Exposition: Materials & Equipment/Whitewares: Ceramic Engineering and Science Proceedings, Volume 18, Issue 2*, 1997, pp. 422-438.

[45]   R. DiMilia, "Dependence of compaction on the glass transition temperature of the binder phase," *Am. Ceram. Soc. Bull.,* vol. 62, pp. 484-488, 1982.

[46]   Y. Zhang, T. Suga, M. Kawasaki, X. X. Tang, N. Uchida, and K. Uematsu, "Effect of poly (vinyl alcohol) adsorption on binder segregation during drying," *Journal of the American Ceramic Society,* vol. 79, pp. 435-440, 1996.

[47]   W. Walker Jr and J. Reed, "Polyethylene Qlycol Binders for Advanced Ceramics," 1992.

[48]   F. Shaw, "Spray drying: a traditional process for advanced applications," *American Ceramic Society Bulletin,* vol. 69, pp. 1484-1489, 1990.

[49]   G. W. J. J. o. t. A. C. S. Scherer, "Theory of drying," vol. 73, pp. 3-14, 1990.

[50]   D. E. Niesz, "A review of ceramic powder compaction," *KONA Powder and Particle Journal,* vol. 14, pp. 44-51, 1996.

[51]   H. Liang, K. Shinohara, H. Minoshima, and K. Matsushima, "Analysis of constant rate period of spray drying of slurry," *Chemical Engineering Science,* vol. 56, pp. 2205-2213, 2001.

[52]   J. TSUBAKI and H. YAMAKAWA, "Optimization of granules and slurries for press forming," *Journal of the Ceramic Society of Japan,* vol. 110, pp. 894-898, 2002.

[53]   S. Lukasiewicz and J. Reed, "Character and compaction response of spray-dried agglomerates," *AM. CERAM. SOC. BULL. Am. Ceram. Soc. Bull.,* vol. 57, p. 798, 1978.

[54]   N. Ku, *Evaluation of the behavior of ceramic powders under mechanical vibration and its effect on the mechanics of auto-granulation*: Rutgers The State University of New Jersey-New Brunswick, 2015.

[55]   N. Venugopal, "Aggregate breakdown of nanoparticulate titania," Rutgers University-Graduate School-New Brunswick, 2008.

[56]   T. Kumagai, "Isostatic compaction behavior of yttria-stabilized tetragonal zirconia polycrystal powder granules," *Powder Technology,* vol. 329, pp. 345-352, 2018.

[57]   G. L. Messing, C. J. Markhoff, and L. G. McCoy, "CHARACTERIZATION OF CERAMIC POWDER COMPACTION," 1982.

[58]   W. J. Walker, J. S. Reed, and S. K. Verma, "Influence of granule character on strength and Weibull modulus of sintered alumina," *Journal of the American Ceramic Society,* vol. 82, pp. 50-56, 1999.

[59]   S. Baklouti, P. Coupelle, T. Chartier, and J. Baumard, "Compaction behaviour of alumina powders spray-dried with organic binders," *Journal de Physique III,* vol. 6, pp. 1283-1291, 1996.

[60]   R. G. Frey and J. Halloran, "Compaction Behavior of Spray-Dried Alumina," *Journal of the American ceramic Society,* vol. 67, pp. 199-203, 1984.

[61]   D. Niesz, M. SNYDER, and R. BENNETT, "Strength characterization of powder aggregates," *American Ceramic Society Bulletin,* vol. 51, pp. 677-&, 1972.

[62]   C. Nies and G. Messing, "Effect of glass-transition temperature of polyethylene glycol-plasticized polyvinyl alcohol on granule compaction," *Journal of the American Ceramic Society,* vol. 67, pp. 301-304, 1984.

[63]   B. J. Briscoe and N. Özkan, "Compaction behaviour of agglomerated alumina powders," *Powder Technology,* vol. 90, pp. 195-203, 1997.

[64]   H. Tanaka, S. Fukai, N. Uchida, K. Uematsu, A. Sakamoto, and Y. Nagao, "Effect of moisture on the structure and fracture strength of ceramic green bodies," *Journal of the American Ceramic Society,* vol. 77, pp. 3077-3080, 1994.

[65]   S. Balasubramanian, D. J. Shanefield, and D. E. Niesz, "Effect of Externally Applied Plasticizer on Compaction Behavior of Spray-Dried Powders," *Journal of the American Ceramic Society,* vol. 85, pp. 749-754, 2002.

[66]   H. Al-Jewaree and H. Chandler, "Air entrapment: a source of laminations during pressing," *British ceramic. Transactions and journal,* vol. 89, pp. 207-210, 1990.

[67]   A. B. Van Groenou, "Compaction of ceramic powders," *Powder technology,* vol. 28, pp. 221-228, 1981.

[68]   B. Briscoe and P. Evans, "Wall friction in the compaction of agglomerated ceramic powders," *Powder Technology,* vol. 65, pp. 7-20, 1991.

[69]   S. Balasubramanian, D. J. Shanefield, and D. E. Niesz, "Effect of Internal Lubricants on Defects in Compacts Made from Spray-Dried Powders," *Journal of the American Ceramic Society,* vol. 85, pp. 134-138, 2002.

[70]   R. A. DIMILIA and J. S. REED, "Stress Transmission During the Compaction of a Spray-Dried Alumina Powder in a Steel Die," *Journal of the American Ceramic Society,* vol. 66, pp. 667-672, 1983.

[71]   R. A. J. C. B. Thompson, "Mechanics of powder pressing: I. Model for powder densification," vol. 60, pp. 237-243, 1981.

[72]   D. Niesz, "Structure and properties of agglomerates," *Ceramic processing before firing,* 1978.

[73]   W. Duckworth, "Discussion of ryshkewitch paper by winston duckworth," *J. Am. Ceram. Soc.,* vol. 36, pp. 68-69, 1953.

[74]   E. Ryshkewitch, "Compression strength of porous sintered alumina and zirconia," *Journal of the American Ceramic Society,* vol. 36, pp. 65-68, 1953.

[75]   K. G. Ewsuk, "Compaction science and technology," *MRS Bulletin,* vol. 22, pp. 14-18, 1997.

[76]   J. Amorós, V. Cantavella, J. Jarque, and C. Felíu, "Fracture properties of spray-dried powder compacts: effect of granule size," *Journal of the European Ceramic Society,* vol. 28, pp. 2823-2834, 2008.

[77]   M. Järveläinen, A. Kaleva, A. Kaitajärvi, J. Laakso, U. Kanerva, and E. Levänen, "Compression curve analysis and compressive strength measurement of brittle granule beds in lieu of individual granule measurements," *Particuology,* vol. 29, pp. 60-68, 2016.

[78]   P. R. Mort, R. Sabia, D. E. Niesz, and R. E. Riman, "Automated generation and analysis of powder compaction diagrams," *Powder technology,* vol. 79, pp. 111-119, 1994.

[79]   R. L. J. J. o. t. A. C. S. Matsumoto, "Generation of powder compaction response diagrams," vol. 69, pp. C-246-C-247, 1986.

[80]   R. L. Matsumoto, "Analysis of powder compaction using a compaction rate diagram," *Journal of the American Ceramic Society,* vol. 73, pp. 465-468, 1990.

[81]   R. Moreno-Atanasio, R. A. Williams, and X. Jia, "Combining X-ray microtomography with computer simulation for analysis of granular and porous materials," *Particuology,* vol. 8, pp. 81-99, 2010.

[82]   S. Hohn, S. Eckhard, M. Fries, B. Matthey, M. Herrmann, and A. Michaelis, "Methods of quantification of the internal structures of spray granules," *Journal of Ceramic Science and Technology,* vol. 2, pp. 75-88, 2011.

[83]   T. A. Deis and J. J. Lannutti, "X-ray Computed Tomography for Evaluation of Density Gradient Formation during the Compaction of Spray-Dried Granules," *Journal of the American ceramic Society,* vol. 81, pp. 1237-1247, 1998.

[84]   S. Cottrino, Y. Jorand, E. Maire, and J. Adrien, "Characterization by X-ray tomography of granulated alumina powder during in situ die compaction," *Materials Characterization,* vol. 81, pp. 111-123, 2013.

[85]   S. Eckhard and M. Nebelung, "Investigations of the correlation between granule structure and deformation behavior," *Powder technology,* vol. 206, pp. 79-87, 2011.

[86]   P. Lu, J. J. Lannutti, P. Klobes, and K. Meyer, "X-ray Computed Tomography and Mercury Porosimetry for Evaluation of Density Evolution and Porosity Distribution," *Journal of the American Ceramic Society,* vol. 83, pp. 518-522, 2000.

[87]   S. Eckhard, M. Fries, S. Antonyuk, and S. Heinrich, "Dependencies between internal structure and mechanical properties of spray dried granules–Experimental study and DEM simulation," *Advanced Powder Technology,* vol. 28, pp. 185-196, 2017.

[88]   M. K. Alazzawi, S. Murali, and R. A. Haber, "Visualizing the Effect of Extrusion Velocity on the Spatial Variation of Porosity in a Titanium Dioxide/Binder System," *Materials Sciences and Applications,* vol. 8, p. 933, 2017.

[89]   I. P. Maher, R. A. J. M. S. Haber, and Applications, "Green Microstructural Visualization of Dry-Pressed Spray-Dried Alumina (Al2O3)," vol. 9, 2018.

[90]   J. C. Hay, A. Bolshakov, and G. Pharr, "A critical examination of the fundamental relations used in the analysis of nanoindentation data," *Journal of materials Research,* vol. 14, pp. 2296-2305, 1999.

[91]   G. Pharr, W. Oliver, and F. J. J. o. m. r. Brotzen, "On the generality of the relationship among contact stiffness, contact area, and elastic modulus during indentation," vol. 7, pp. 613-617, 1992.

[92]   B. Hendrix, "The use of shape correction factors for elastic indentation measurements," *Journal of materials research,* vol. 10, pp. 255-257, 1995.

[93]   W. C. Oliver and G. M. Pharr, "Measurement of hardness and elastic modulus by instrumented indentation: Advances in understanding and refinements to methodology," *Journal of materials research,* vol. 19, pp. 3-20, 2004.

[94]   R. A. Haber, ed. Rutgers University: Personal Communication, 2017.

[95]   M. K. Alazzawi, F. F. Maniaci, B. Beyoglu, and a. R. A. Haber, "Title," unpublished|.

[96]   V. Domnich, ed. Rutgers University: Personal Communication, 2018.

[97]   N. Otsu, "A threshold selection method from gray-level histograms," *IEEE transactions on systems, man, and cybernetics,* vol. 9, pp. 62-66, 1979.